

# **ANNEX: INDIVIDUAL REPORTS**

Published on the CD-ROM and attached to the hard copy



## TOPIC 2: RESULTS ACHIEVED

### 2.1. INVESTIGATION OF OXIDE-DISPERSED-STRENGTHENED STEELS

Author	Affiliation	Title of the paper
<a href="#">Balagurov, A.</a>	Joint Institute for Nuclear Research (JNIR), Russian Federation	Investigation of Precipitation-Hardened Steels using TOF Neutron Diffraction
<a href="#">Coppola, R.</a>	National Agency for New Technologies, Energy and Sustainable Economic Development (ENEA), Italy	Characterization of Y <sub>2</sub> O <sub>3</sub> particle distribution in Oxide Dispersion Strengthened Eurofer steel for nuclear applications by means of small-angle neutron scattering (SANS) and of neutron diffraction

### 2.2. RESEARCH ON ZIRCONIUM BASED MATERIALS (INCLUDING HYDROGEN UPTAKE)

<a href="#">Bourke, M.A.M.</a>	Los Alamos National Laboratory (LANL), United States of America	Neutron scattering activity at Los Alamos National Laboratory
<a href="#">Grosse*, M.</a>	Institut für Materialforschung, Germany	In-situ neutron radiography investigations of the hydrogen re-distribution during DHC
<a href="#">Grosse**, M.</a>	Institut für Materialforschung, Germany	Post-test examination of the hydrogen distribution in zirconium claddings after LOCA tests
<a href="#">Grosse***, M.</a>	Institut für Materialforschung, Germany	Small angle neutron scattering investigations of hydride precipitations in Zircaloy-4
<a href="#">Lehmann*, E.</a>	Paul Scherrer Institut, Switzerland	Final report about activities at PSI, Switzerland
<a href="#">Santisteban*, J.</a>	Comisión Nacional de Energía Atómica (CNEA); Argentina	Preliminary Round Robin on the determination of crystallographic texture of Zr components by neutron diffraction
<a href="#">Santisteban**, J.</a>	Comisión Nacional de Energía Atómica (CNEA); Argentina	Crystallographic phases, texture and dislocation densities of ZR2.5%NB pressure tubes at different stages of manufacturing

### 2.4. RESULTS WITH IRRADIATED MATERIALS

<a href="#">Kozlov, A.</a>	Institute of Nuclear Materials, Russian Federation	Examination of austenitic steels microstructure change induced neutron irradiation by using of neutron scattering methods
<a href="#">Liu, Y.</a>	China Institute of Atomic Energy, (CIAE), Republic of China	Development, Characterization and Testing of Materials of Relevance to Nuclear Energy Sector Using Neutron

<a href="#">Shikama, T.</a>	Tohoku University, Japan	Neutron beam analysis on materials for nuclear applications, being irradiated in fission reactors and having radioactivity
<a href="#">Török, G.</a>	Wigner Research Institute, Institute of Solid State Physics. Hungary	Investigation of irradiation RPV and ODS steels by SANS and residual stress

## 2.5. OPTIMIZATION OF INSTRUMENTS FOR RESIDUAL STRAIN/STRESS MEASUREMENTS

<a href="#">Carr, D.</a>	Australian Nuclear Science and Technology Organisation (ANSTO) Australia	Final report on evaluating residual stresses and internal defects in nuclear materials at the Opal reactor at ANSTO, Australia.
<a href="#">Mikula, P.</a>	Nuclear Physics Institute (NPI), Czech Republic	Development and optimization of high-resolution neutron scattering instruments dedicated to characterization and testing of materials of relevance to nuclear energy sector and related experiments in SANS, residual strain/stress and texture studies
<a href="#">Sutiarso, S.</a>	National Nuclear Energy Agency (BATAN) Indonesia	Optimization of Neutron Beam Techniques for Characterization of Structural Materials

## 2.6. EFFORTS TOWARDS STANDARDIZATION OF NEUTRON IMAGING

<a href="#">Pugliesi, R.</a>	Instituto de Pesquisas Energeticas e Nucleares (IPEN) Brazil	Improvement of a neutron tomography facility
<a href="#">Radebe, M.</a>	South African Nuclear Energy Corp. (NECSA) South Africa	Towards standardization of digital neutron radiography and tomography: Setup characterization and application porous media quantification
<a href="#">Sim, C.</a>	Korea Atomic Energy Research Institute Republic of Korea	Neutron tomography Standardization using NTR and NTC Phantom for industry application

**2. RESULTS ACHIEVED**  
**2.1. INVESTIGATION OF OXIDE-  
DISPERSED-STRENGTHENED STEELS**



## 2.1. Investigation of oxide-dispersed-strengthened steels

### INVESTIGATION OF PRECIPITATION-HARDENED STEELS USING TOF NEUTRON DIFFRACTION

A.M. BALAGUROV, G.D. BOKUCHAVA, V.V. SUMIN, I.V. PAPUSHKIN

Frank Laboratory of Neutron Physics, Joint Institute for Nuclear Research,  
Joliot-Curie 6, 141980 Dubna, Moscow region  
Russia  
Email: [bala@nf.jinr.ru](mailto:bala@nf.jinr.ru); [gizo@nf.jinr.ru](mailto:gizo@nf.jinr.ru)

#### **Abstract.**

In the frame of current CRP activity series of austenitic and ferritic dispersion-hardened steels, which are used as various structural reactor components, were investigated using high resolution neutron diffraction. The effect of temperature and duration of heat treatment on the precipitation of dispersion-hardened phase particles, as well as lattice parameter changes and microstrain during high temperature creep was studied.

## 1. INTRODUCTION

Increasing the strength of constructional materials allows one to reduce the amount of material used in the manufacturing of various machinery parts and mechanisms and significantly increase their lifetime. In addition to improving strength properties during the creation of materials for the nuclear industry (steel, structured alloys, etc.) the actual problem is to improve their radiation resistance too, i.e. to reduce their tendency to embrittlement and vacancy swelling. One of the most promising ways to solve this problem is to use the effect of metal or alloy hardening due to the formation of chemically stable non-metallic dispersed phases of submicron size, which inhibit the dislocations movement in the material. Accordingly, the most important task of material science is to understand the processes that occur during precipitation hardening in steels and alloys that can help to create materials purposefully with the desired mechanical properties.

Precipitation strengthening process can take place in the hardened material as a result of annealing at a certain temperatures or under irradiation. It is well known that the strength, creep resistance and radiation resistance of hardened material depend on the dispersed phase state: the degree of its crystal lattice coherence with matrix lattice, the location of nanoparticles precipitation and their size. In addition, the precipitation of second-phase particles is accompanied by a lattice spacing changes in the matrix phase and, thus, the appearance of microstrain, which has a significant effect on the material characteristics.

Important role in the study of dispersion hardening processes occurring in structural materials play nuclear physics methods and, in particular, the diffraction of thermal neutrons. Constructed in various research centers high resolution neutron diffractometers have unique capabilities to determine the materials microstructure due to the high accuracy of the results, the possibility of analysis of multiphase materials, and especially the deep penetration length of neutrons, which is hundred times greater than the penetration length of X rays.

This paper presents the results of high-resolution neutron diffraction and SANS studies of some types of austenitic and ferritic steels which are mainly used as structural materials for nuclear reactor components.

## 2.1. Investigation of oxide-dispersed-strengthened steels

## 2. METHODS AND SAMPLES

### 2.1. Microstrain studies in precipitation-hardened austenitic steels

The studied cylindrical samples with 6 mm diameter were made from austenitic steels H16N15M3T1 and N26H5T3 with Ni<sub>3</sub>Ti hardening phase and 40H4G18F2 with VC hardening phase (hereinafter labeled as S1, S2 and S3, respectively). In the initial state, all samples were annealed at 450°C for 2 hours, and then quenched in water. Then the samples were subjected to aging at different temperatures. Subsequent heat treatment temperature and aging duration were selected taking into account the results of Ref. [1]. In this work the kinetic curves of Ni<sub>3</sub>Ti precipitation in quenched Fe-Ni-Ti alloy during isothermal annealing were presented. It was also shown that the characteristic size of precipitates during isothermal annealing at 650°C ranged from 3 to 10 nm when the aging time varied from 2 to 12 hours.

Neutron diffraction experiments for microstrain analysis were conducted on the HRPT instrument [2], operating at the SINQ neutron source in the Paul Scherrer Institute (Switzerland). HRPT is the constant wavelength high resolution diffractometer (with resolution value of  $\Delta d/d \approx 0.001$  at the minimum of the resolution curve), which allowed to perform detailed analysis of the microstructural characteristics of the samples.

Before investigating the microstress influence on the radiation resistance as well as modification of microstress under irradiation, it was necessary to clarify the possibility of using high resolution neutron diffraction for these purposes. Correct definition of microstresses in polycrystalline samples on a neutron diffractometer is possible if it has a sufficiently high resolution and its resolution function dependence versus interplanar distance  $d_{hkl}$  is well known. Therefore, at first the resolution function of the HRPT diffractometer was investigated. This was done by measuring the diffraction patterns from a standard polycrystalline sample Na<sub>2</sub>Al<sub>2</sub>Ca<sub>3</sub>F<sub>14</sub> (NAC), recommended by the International Union of Crystallography for instrument calibration and definition of the resolution function with good accuracy. Thus, using the obtained calibration parameters for further patterns processing from working samples by the help of the Rietveld method it was possible to obtain the precise lattice parameters, as well as the microstrain and the average crystallite size.

In Fig.1 diffraction peak widths for two 40H4G18F steel samples tempered at 600°C and 700°C measured on HRPT in comparison with instrument resolution function are shown. As it can be seen from this figure on the HRPT diffractometer the diffraction peak broadening effects can be measured easily and with high accuracy.

For quantitative estimates we use the formula relating the width of the diffraction lines with the characteristics of the microstructure of the material - the microstrain  $\varepsilon = \Delta a/a_0$ , where  $a_0$  is stress-free unit cell parameter, and the characteristic size of coherent scattering domains  $D$ . Respective contributions to the peak width are (see, e.g. [3]):

$$\beta_D = k \cdot \lambda / (D \cdot \cos \theta), \quad \beta_\varepsilon = 4 \cdot \varepsilon \cdot \tan \theta, \quad (1)$$

where  $\beta$  is integral width in radians in the scale of the scattering angle, i.e. peak area divided by its amplitude,  $k$  is dimensionless coefficient depending on both the symmetry and the shape of the crystal, and, in general, close to 0.9 [4],  $\lambda$  is the neutron wavelength,  $\theta$  is Bragg angle. Usually, the broadening due to crystallites size gives Lorentz contribution to the line width, while the microstrain contribution has a Gaussian form. More important is the fact that the angular dependences of these two contributions are significantly different, and, by

## 2.1. Investigation of oxide-dispersed-strengthened steels

analysing a wide range of Bragg angles, one can confidently share them. The experimental practice on HRPT showed that the peak broadening effects can be reliably detected at the microstrain values  $\varepsilon \geq 10^{-4}$  and the average crystallite size of the  $D \leq 2000 \text{ \AA}$ .

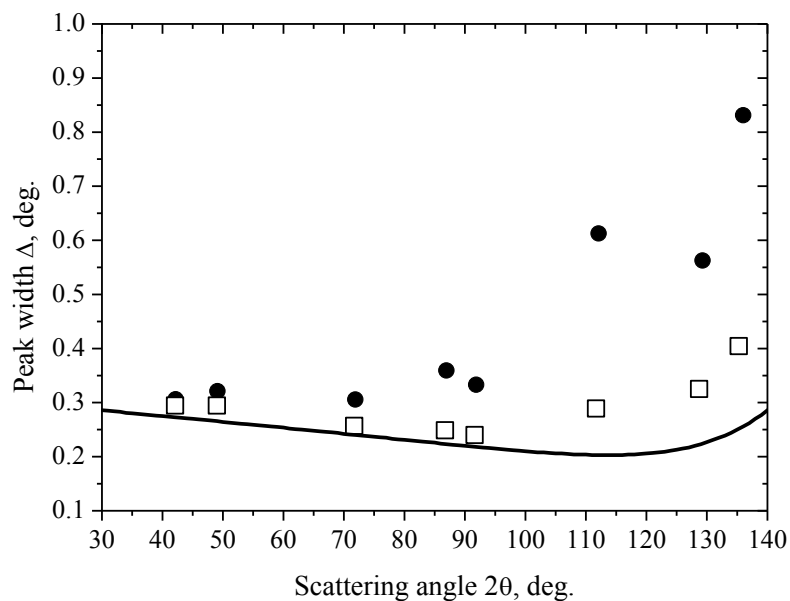


FIG. 1. Diffraction peak widths for two 40H4G18F steel samples tempered at 600°C (squares) and 700°C (circles) measured with HRPT at  $\lambda = 1.494 \text{ \AA}$  in comparison with instrument resolution function (solid line).

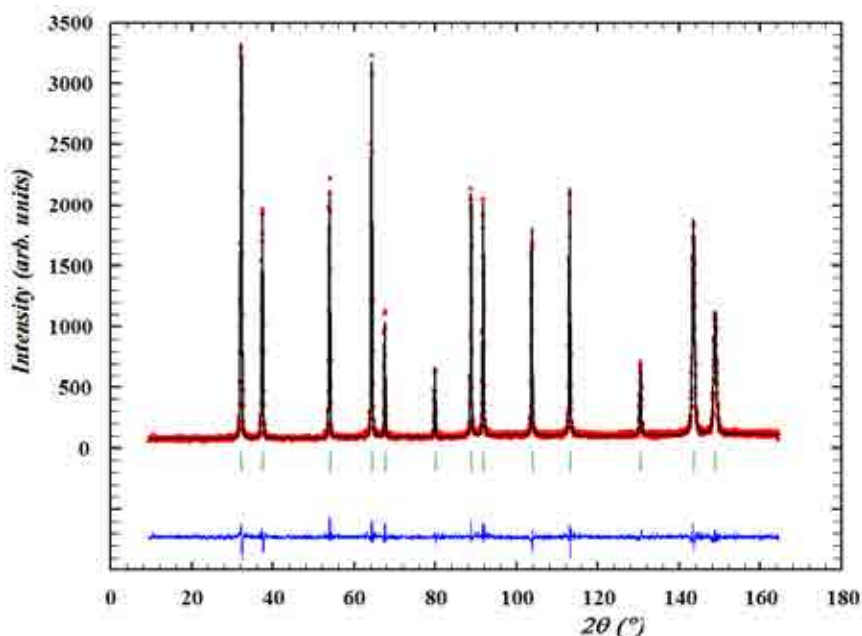


FIG. 2. A typical diffraction pattern from the H16N15M3T1 steel sample (S1) measured on HRPT at  $\lambda = 1.1545 \text{ \AA}$  and processed by the Rietveld method. The experimental points, calculated profile (bottom) and peak positions (vertical bars) are shown. The diffraction peaks correspond to the  $d$ -spacing interval  $0.55 - 2.15 \text{ \AA}$ .

Our experimental data were obtained for steel S1, annealed for 1, 6 and 12 hours at 600°C and 700°C for steel S2, annealed under the same conditions, except at 700°C, 6 hours,

## 2.1. Investigation of oxide-dispersed-strengthened steels

and for steel S3, annealed under the same conditions except at 700°C, 1 hour and 6 hours. The neutron diffraction patterns were measured at room temperature for two wavelengths of the primary beam ( $\lambda = 1.1545$  and  $1.494 \text{ \AA}$ ). Processing of diffraction data were done according to the Rietveld method using the software package FullProf [5], which has the opportunity to analyze the peak width dependence on the scattering angle and to estimate the contributions to the peak broadening due to lattice microstrain and the average size of the coherently scattering domains. It was found that the size effect contribution to the peak width is negligible, i.e.  $D \gg 2000 \text{ \AA}$ . Conversely, microstresses contribute significantly and, therefore, in further considerations the peak broadening is attributed to the microstress presence only. All main diffraction peaks in the patterns are indicated in the face-centered cubic space group Fm3m with a lattice parameter  $a_0 \approx 3.6 \text{ \AA}$ . A typical diffraction pattern processed by the Rietveld method is shown in Fig. 2.

Experimental values of the lattice parameter and microstrain obtained for two neutron wavelengths are in good agreement with each other for each sample; therefore, their average value was used in further considerations. The obtained results are shown in Fig.3 and Fig.4 and in Table 1. The standard deviations for lattice parameters obtained with Full Prof software are very small (the relative error is much smaller than  $10^{-4}$ ). Microstrain error values calculation is rather complicated and is not yet implemented in FullProf. The error of the experimental microstrain values was evaluated based on the spread between the results obtained for two different wavelengths, and was about  $0.5 \cdot 10^{-4}$ . In Fig. 3, the lattice parameter dependence on the isothermal annealing duration for all three steels is shown. It can be clearly seen that except for the point 700°C for S3 sample depending on the parameter of temperature and time of annealing does not have any features, so here only the behavior of microstrain in the samples is analysed.

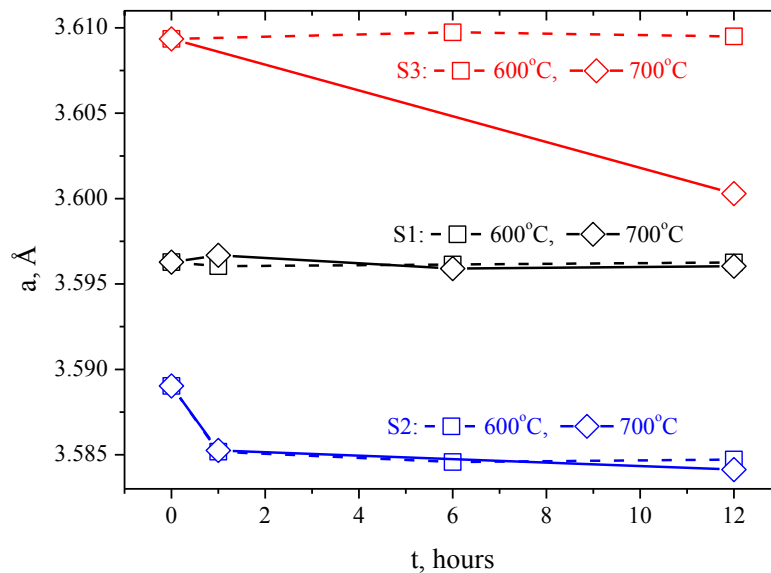


FIG. 3. Lattice parameter changes versus isothermal annealing time. The lattice parameter value for the initial state is shown at  $t=0$ . Error bars for data points are smaller than symbols.

## 2.1. Investigation of oxide-dispersed-strengthened steels

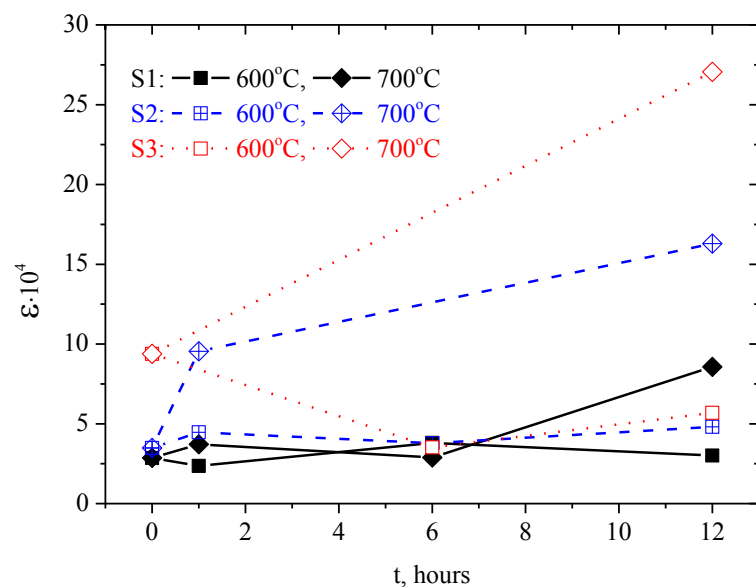


FIG. 4. The experimental values of the microstrain depending on the isothermal annealing duration. The value for the initial state is shown at  $t=0$ .

TABLE 1. LATTICE PARAMETER AND MICROSTRAIN FOR S1, S2 AND S3 STEELS QUENCHED AND AGED AT 600°C AND 700°C (1, 6, 12 HOURS)

Heat treatment	S1	S2	S3	S1	S2	S3
	$a, \text{\AA}$			$\epsilon \cdot 10^4$		
annealing						
450°C, 2 h	3.59628(2)	3.58903(2)	3.60935(4)	2.9	3.5	9.4
600°C, 1 h	3.59604(2)	3.58518(3)	-	2.4	4.5	-
600°C, 6 h	3.59614(2)	3.58457(3)	3.60974(3)	3.8	3.8	3.5
600°C, 12 h	3.59626(2)	3.58472(3)	3.60950(3)	3.0	4.8	5.7
700°C, 1 h	3.59668(2)	3.58525(3)	-	3.7	9.5	-
700°C, 6 h	3.59590(2)	-	-	2.9	-	-
700°C, 12 h	3.59604(3)	3.58413(5)	3.60029(7)	8.6	16.3	27.1

Microstrain behavior depending on the isothermal annealing duration is shown in Fig. 4. It can be seen that after annealing at 600°C microstrain is approximately constant or even slightly decreases. On the contrary, annealing at 700°C leads to a significant increase in microstrain. Let us discuss the obtained results in more detail.

1. *Chromium-nickel austenite with 1 wt% Ti*. Data analysis for the H16N15M3T1 steel annealed at 600°C showed that microstrain remains at the level of  $3.9 \div 4.1 \cdot 10^{-4}$ , while Brinell hardness at the same time increases from 1300 to 1400 MPa. Annealing at 700°C led to an increase in microstrain from  $3.7 \cdot 10^{-4}$  to  $9.9 \cdot 10^{-4}$  and to a small increase in Brinell hardness from 1360 to 1490 MPa. In the neutron patterns diffraction peaks from metastable  $\gamma'$ -Ni<sub>3</sub>Ti phase were not observed even for the annealing at 700°C, 12 hours, for which a sharp increase in microstrain was registered. Probably, this can be explained by its small volume content (less than 1%).

## 2.1. Investigation of oxide-dispersed-strengthened steels

2. *FCC N26H5T3 alloy with 3 wt% Ti.* For fcc alloy N26H5T3 with 3 wt% Ti after annealing at 600°C Brinell hardness increases from 1360 to 1880 MPa, and microstrain remains at the level of  $4.0 \cdot 10^{-4}$  for all annealing durations. At the same time after annealing at 700°C hardness increases from 1360 to 3160 MPa, and microstrain up to  $18 \cdot 10^{-4}$ , i. e. four times. In the neutron diffraction pattern of this alloy the diffraction peaks of  $\gamma'$ -Ni<sub>3</sub>Ti phase at both annealing temperatures are observed (Fig.5). However, after annealing at 600°C (and 700°C, 1 hour), they exhibit Lorentz type of broadening, which points to small particle size of this phase. These results are in good agreement with transmission electron microscopy (TEM) and electron diffraction [1] data – the  $\gamma'$ -Ni<sub>3</sub>Ti phase particles were observed only after annealing at 700°C, 6 and 7 hours. After annealing at 600°C (and 700°C, 1 hour) tweed contrast is clearly seen, which indicates a stress field change in the solid solution of the matrix due to the precipitation of the coherent  $\gamma'$ -Ni<sub>3</sub>Ti phase nanoparticles.

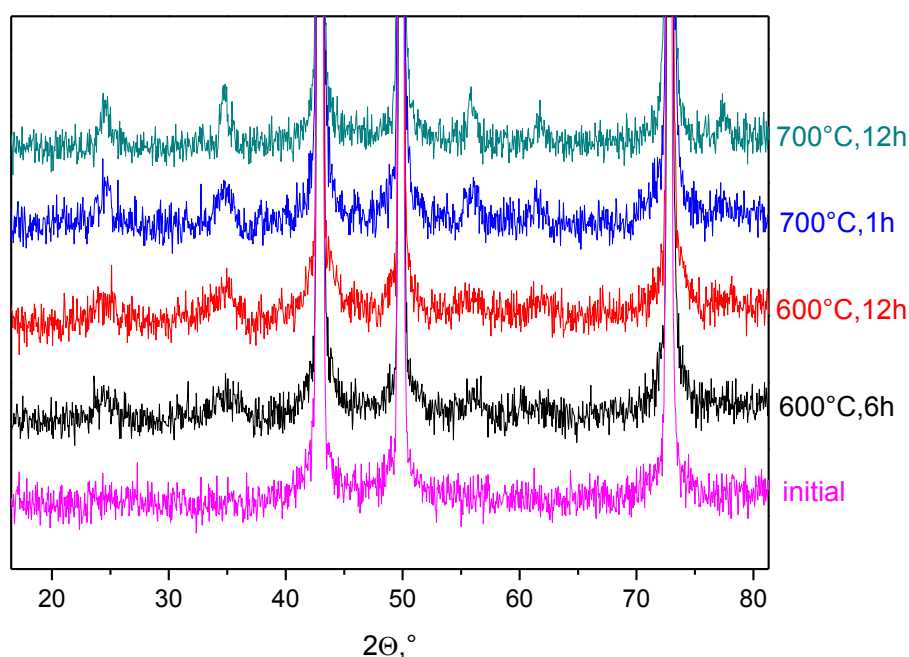


FIG. 5. Precipitation kinetics of the  $\gamma'$ -Ni<sub>3</sub>Ti phase (the additional peaks appearance in the patterns), depending on the temperature and annealing duration of hardened alloy H26X5T3 (alloy S2). Three strong diffraction peaks from matrix phase of the alloy are clearly visible at  $2\theta \approx 42^\circ$ ,  $49^\circ$  and  $73^\circ$ , the low intensity peaks belong to the  $\gamma'$ -Ni<sub>3</sub>Ti phase.

3. *Vanadium-carbide austenite 40H4G18F2.* For carbon austenite 40H4G18F2 vanadium carbide precipitation after annealing at 600°C, 12 h reduces microstrain from  $11 \cdot 10^{-4}$  to  $5.58 \cdot 10^{-4}$ . The micro-hardness, however, is growing from 2210 to 3130 MPa, and then decreases slightly to 2820 MPa. At the same time, the lattice parameter of the fcc matrix is almost constant. TEM data shows tweed ripples for hardened and annealed samples up to 12 h annealing duration [6]. At this annealing temperature in its initial stage (1 h), a relaxation of a solid solution of austenite with simultaneous forming of a coherent vanadium-carbon clusters occurs, which leads to the stress relaxation in the hardened matrix with a random distribution of interstitial and substitutional atoms. Consequently, the microstrain level drops. However, the formation of vanadium carbides does not occur as it can be concluded from TEM data and from the absence of changes in the matrix lattice parameter.

## 2.1. Investigation of oxide-dispersed-strengthened steels

The similar behavior was observed during decay of the nitrous austenite [7]. Hardness increase at these heat treatment regimes we explain by the proximity of the studied steel to the Hadfield steel, in which  $\gamma \rightarrow \varepsilon$  martensitic transformation occurs easily during deformation, in our case, during the hardness test.

As a result of the destabilizing “high-temperature” (700-750°C) aging, passing with the release of relatively large (up to 9-10 nm) incoherent vanadium carbide particles, austenitic matrix is depleted in carbon and vanadium. These results do not contradict the neutron structural data. At the “high-temperature” (700°C) aging (Fig.3 and Table 1) due to the formation of the second phase – precipitation of relatively large (up to 9-10 nm) incoherent vanadium carbide particles – lattice parameter decreases from 3.60956 to 3.60050 Å, i. e. by 0.00906 Å, or in terms of 1 at% of carbon atom it is 0.0054 Å. This value is typical for lattice parameter changes during the dissolution of carbon in the fcc transition metals.

In accordance with popular opinion the microstress level around precipitation-hardening particles should decrease at the failure of coherence (due to the precipitation of the second phase). However, our measurements have shown that they remain at the level of microstrain produced by coherent vanadium carbides nanoparticles up to  $30 \cdot 10^{-4}$  for the 40H4G18F2 steel and slightly lower for coherent precipitates in the case of  $\gamma'$ -Ni<sub>3</sub>Ti phase in N26H5T3 steel at 700°C, 6 and 12 h (Fig.4). If we use the simplest approximation [6] for estimation of microstress values from measured microstrain  $\sigma = E \cdot \varepsilon$ , where  $E$  - Young's modulus of steel, from our data follows that for the N26H5T3 alloy  $\sigma \approx 300$  MPa, and for the vanadium-carbide austenite  $\sigma \approx 640$  MPa, which is quite close to the yield point of these materials.

## 2.2. H26X5T3 austenitic steel behavior under applied load

The experiments were performed on the MEREDIT neutron powder diffractometer in Nuclear Physics Institute of the Czech Academy of Sciences in Řež near Prague (<http://neutron.ujf.cas.cz/meredit>). The instrument is placed on the horizontal channel number 6 in the reactor hall of LWR15 light water reactor and it is mainly dedicated to the study of the crystalline and/or magnetic structure of the powder or polycrystalline samples. To enhance the possibility to measure the samples at different conditions there are several sample environments available for practical use: close cycle cryostat and vacuum furnace for temperature dependent studies in the range between 10 up to 1300 K, automatically exchangeable sample carousel for up to 6 samples, deformation rig with tensile/pressure load up to 20 kN for mechanical testing, an Euler goniometer for texture measurements available.

Three H26X5T3 alloy samples were chosen for uniaxial loading, which were austenized beforehand at 1100°C during one hour and quenched in water. One sample was measured in quenched form, two other passed through preliminary thermal treatment at 600°C and 700°C for 12 hours to precipitate the strengthening Ni<sub>3</sub>Ti  $\gamma'$ -phase.

In order to precipitation of strengthening  $\gamma'$ -phase particles remained constant the temperature of 500°C was chosen for this experiment. Uniaxial load value varied from 0 to 350 or 500 MPa by means of the LM-20 testing machine in steps of 50 MPa. Totally, four measurement cycles were performed. Macro deformation of studied samples was determined by the travel distance of movable element of testing machine without taking into consideration the system rigidity (Fig.6). As follows from this figure, mechanical properties of quenched sample and quenched and tempered at 700°C, 12 h sample are quite close. The quenched and tempered (600°C, 12 h) sample is more rigid, especially during the second load cycle. This sample demonstrates plastic flow at load value of 500 MPa (see red line in Fig.6).

## 2.1. Investigation of oxide-dispersed-strengthened steels

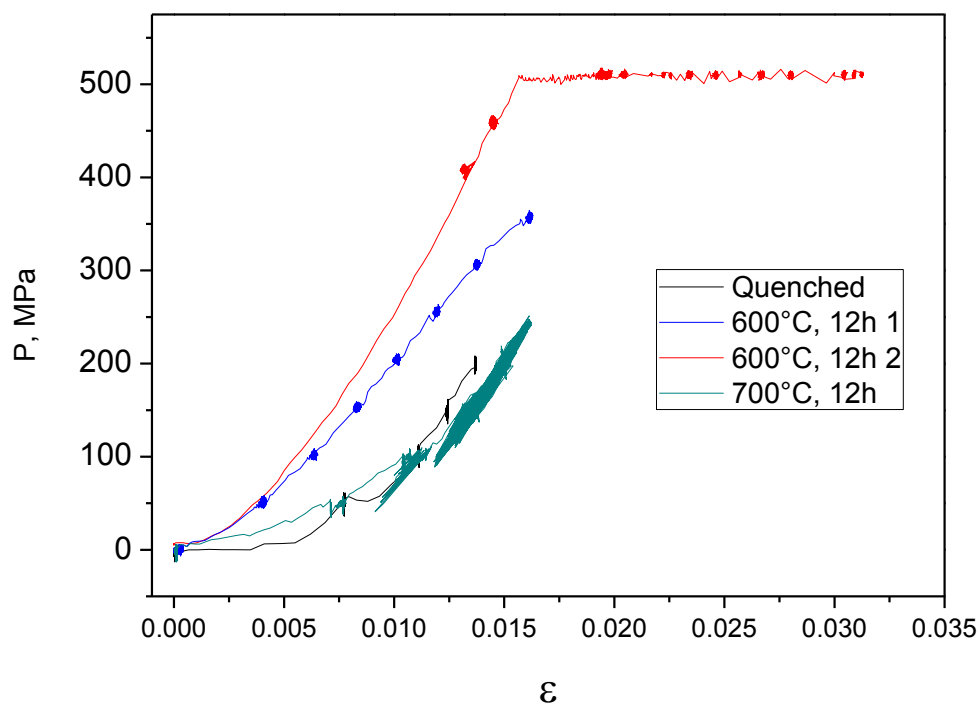
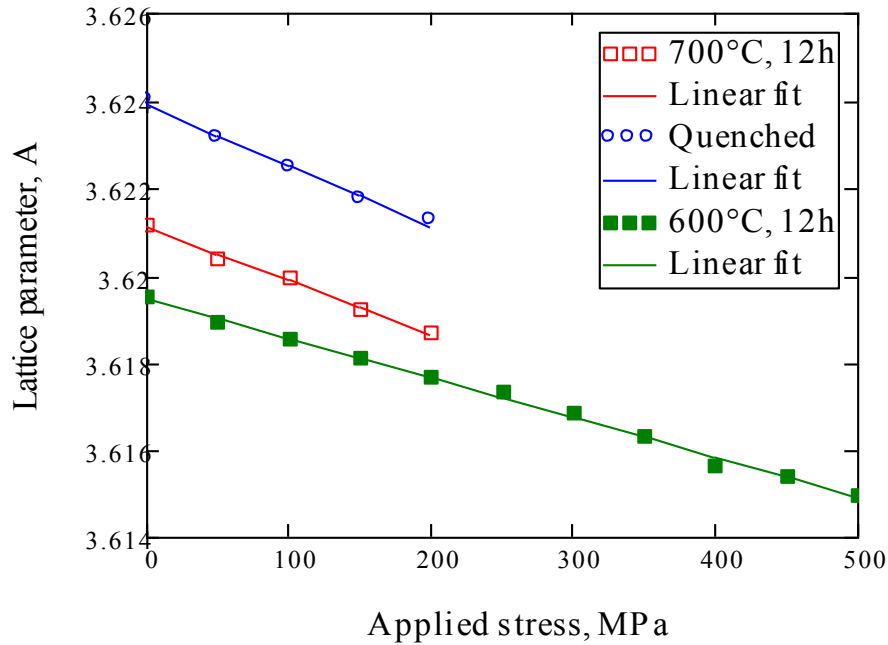


FIG. 6. Sample macro deformation as a function of uniaxial load at test temperature of 500°C: black line – quenched sample of H26X5T3 alloy; green line – quenching + tempering at 700°C (12 h); blue line - quenching + tempering at 600°C (12 h, first cycle); red line - quenching + tempering at 600°C (12 h, second cycle).

Neutron diffraction patterns of all samples were measured *in situ* simultaneously with the sample macro deformation measurement. Lattice parameter dependence of the studied samples as a function of applied load is shown in Fig.7. As in case of mechanical deformation, micro deformation (Figs. 7, 8) exhibits greater rigidity for the sample annealed at 600°C. It was caused obviously by smaller precipitation of Ni<sub>3</sub>Ti  $\gamma'$ -phase and this can be judged by the diffusion of diffraction peaks (see Fig.5).

## 2.1. Investigation of oxide-dispersed-strengthened steels



H26X5T3 steel samples

FIG. 7. The fcc lattice parameters of H26X5T3 alloy as a function of external load at various tempering after quenching:  $\circ$  – alloy after quenching,  $\blacksquare$  - quenching + tempering 600°C, 12 h,  $\square$  - quenching + tempering 700°C, 12 h.

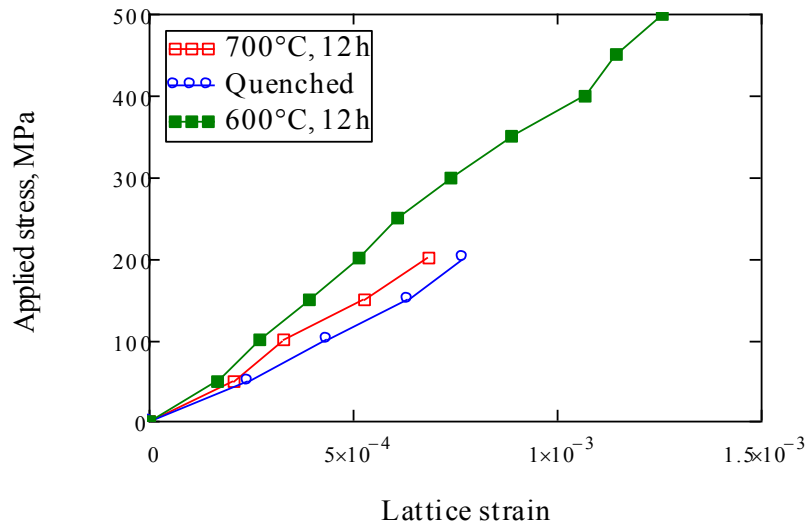


FIG. 8. Microstrain in H26X5T3 alloy as a function of applied load at various tempering after quenching (legend is the same as for the previous figure).

Formal determination of Young's modulus based on microstrain data yields conservative values and greater spread:  $E_{700} = 88.9$  GPa,  $E_{600} = 119.6$  GPa,  $E_{\text{Quench}} = 77.5$  GPa (Fig.9). For example, the work [8] for  $T = 600^\circ\text{C}$  for steel 316 FR gives the value 165 GPa. One of reasons of the spread consists obviously in the measurement of transversal micro deformation, which are by  $\mu^{-1}$  less than longitudinal micro deformation, where  $\mu$  is Poisson's ratio. Micro deformations versus applied load for various  $(hkl)$  (Fig.10) have a typical character. As usual, the plane (002) is the most compliant plane, and (111) is the most rigid plane, this is caused by slip band hierarchy.

## 2.1. Investigation of oxide-dispersed-strengthened steels

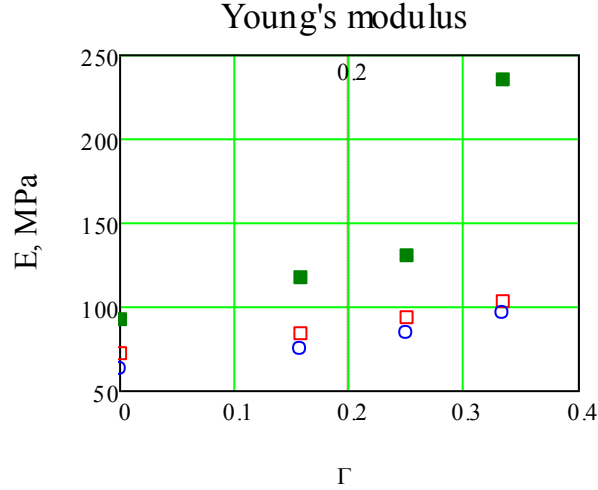


FIG. 9. Effective modulus of elasticity based on neutron diffraction pattern data of H26X5T3 alloy at 500°C (legend is given in Fig.7).

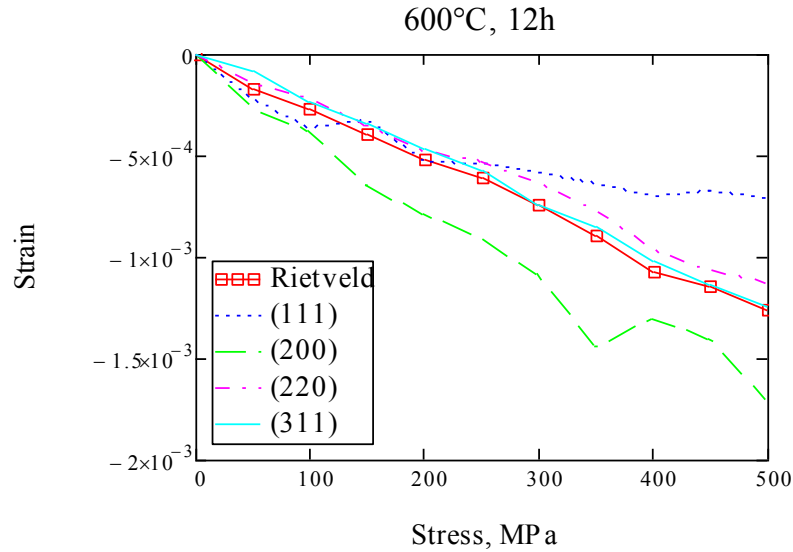


FIG. 10. Microstrain in H26X5T3 alloy as a function of applied load at 600°C for various (hkl). Additionally, the fcc-lattice parameter dependence obtained by Rietveld method is shown.

At the external load values up to 350 MPa, the neutron reflections line widths do not change practically (Fig.11). And as stated above, peak broadening is observed only above this value, then at load value exceeding 500 MPa the alloy starts to flow. If we attribute this broadening to increased dislocation density, as it takes place especially, and if the average values of peak widths below 350 MPa are assumed as a reference point, then it is possible to evaluate microstrain  $\epsilon$  and dislocation density  $\rho$  in this sample (Fig.12) [9] according to the relation:

$$\rho = K \langle \epsilon^2 \rangle / Fb^2, \quad (2)$$

where  $\langle \epsilon^2 \rangle$  - mean squared value of microstrain,  $b$  - Burgers vector,  $K$  and  $F$  - constants.

2.1. Investigation of oxide-dispersed-strengthened steels

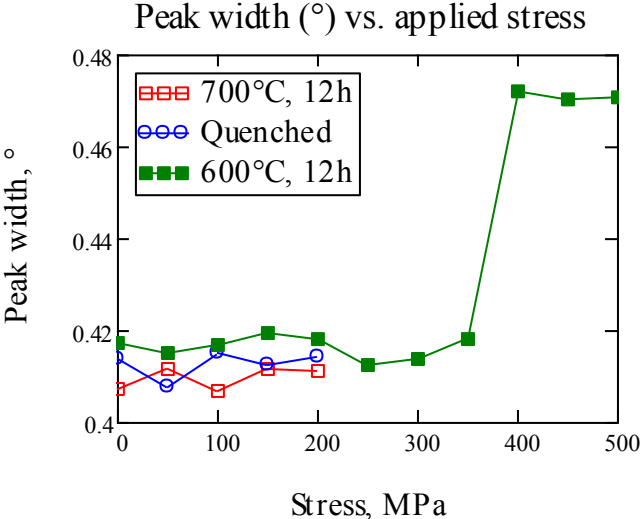


FIG. 11. Diffraction line width of H26X5T3 alloy as a function of applied stress at various tempering after quenching (legend is given in Fig.7).

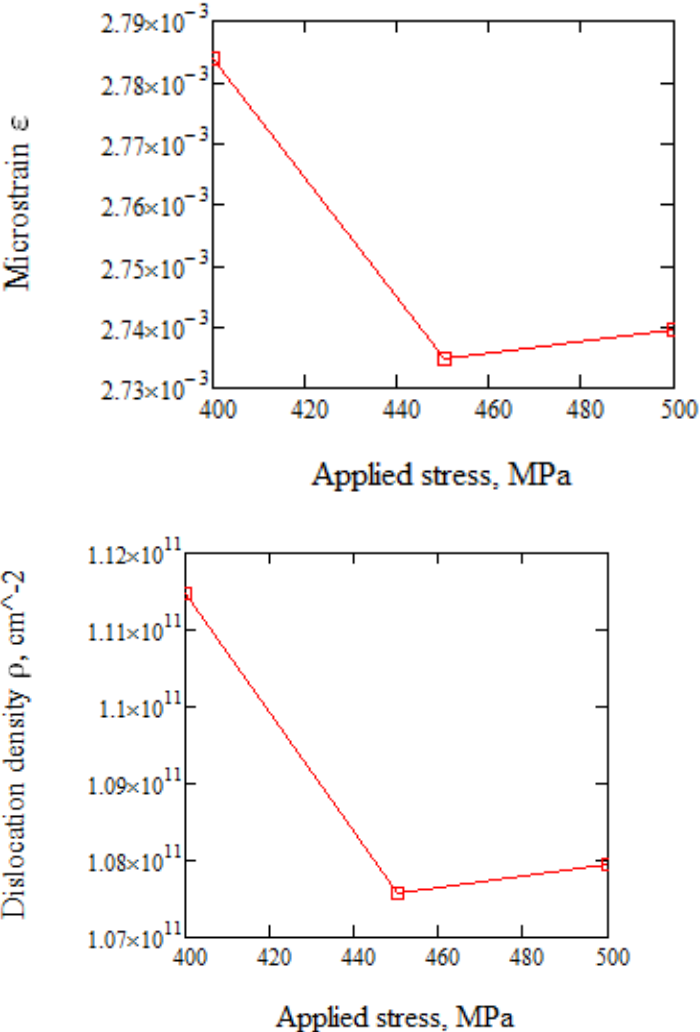


FIG. 12. Microstrain (left) and calculated dislocation density values (right) of H26X5T3 alloy as a function of applied stress.

## 2.1. Investigation of oxide-dispersed-strengthened steels

## 2.3. Investigation of new heat-resistant ferrite-martensite steels 10H9K3V2MFBR and 10H9MFB by neutron diffraction and SANS

Heat-resistant pipeline components (elements of steam and boiler superheaters, turbines, blades, etc.) of thermal power plants operating in the creep range at temperatures up to 650°C are often made from tempered ferrite-martensite steels with approx. 10 %wt chromium content. Therefore, it is important to improve their thermal efficiency and mechanical properties. The heat treatment of tempered ferrite-martensite steels usually consists of two stages: austenization and tempering. It is well known that chromium in steels delays the formation of carbides, and that martensite phase forms in such steels after slow air cooling [10]. Ferrite-martensite steels have a complex microstructure which consists of fine micro grains separated by different kinds of interfaces (austenite grain boundaries, block boundaries and twin boundaries) and carbides which are precipitated near these boundaries. Additionally, these steels exhibit a very high dislocation density after heat treatment [11, 12]. Dislocations are produced in the parent phase during the martensitic transformation due to the associated martensite shear. As it well known from literature the dislocation density strongly drops in the early stages of tempering and then gradually further decreases with further aging. Ferrite-martensite steels with high dislocation densities exhibit specific mechanical properties. Thus they show cyclic softening when exposed to strain controlled fatigue testing and a strong decrease of creep rate during primary creep. The decrease of the high dislocation density in such material during tempering and creep accounts for the formation of subgrain boundaries that represent a dominant feature of ferrite-martensite steel microstructures.

Therefore new ferrite-martensite steels are of great interest for nuclear industry due to their unique heat- and radiation-resistant properties. To this end two newly developed in Russia heat-resistant ferrite-martensite steels 10H9K3V2MFBR and 10H9MFB (similar to P91 steel, Russ. grading) were investigated on FSD diffractometer at the IBR-2 pulsed reactor in wide range of tempering temperatures. These steels revealed good results in the long-term heat resistance which is by about 10% as compared with the previously developed steels of this type. This gives hope for its use in thermal power units at supercritical conditions ( $P = 30$  MPa and  $T = 620^\circ\text{C}$ ). Hereinafter 10H9K3V2MFBR and 10H9MFB steels are designated as K3 and P91, accordingly.

Using TOF neutron diffraction it is possible to estimate *in situ* microstrain and coherent domain size in material from diffraction peak broadening and their changes with temperature and external load. Both mentioned phenomena are closely related to the dislocation structure inside the grain of polycrystalline materials. The obtained information will be useful for better understanding of the heat-resistant properties of investigated steels, as well as high embrittlement at low and high temperatures. This approach will give a possibility to optimize thermomechanical treatment of the steels to improve their properties.

The studied steels have the following chemical composition: K3 steel - 0.1% C, 9.36% Cr, 2.93% Co, 1.85% W, 0.45% Mo, 0.2% V, 0.05% Nb, 0.048% N, 0.005% B, the rest – Fe; P91 steel - 0.1% C, 9.36% Cr, 0.85-1.05% Mo, 0.2% V, 0.06-0.1% Nb, 0.25-0.5% Si, 0.3-0.6% Mn, the rest - Fe. The studied samples were normalized at 1050°C and tempered for 3 hours at temperature of 750°C.

## 2.1. Investigation of oxide-dispersed-strengthened steels

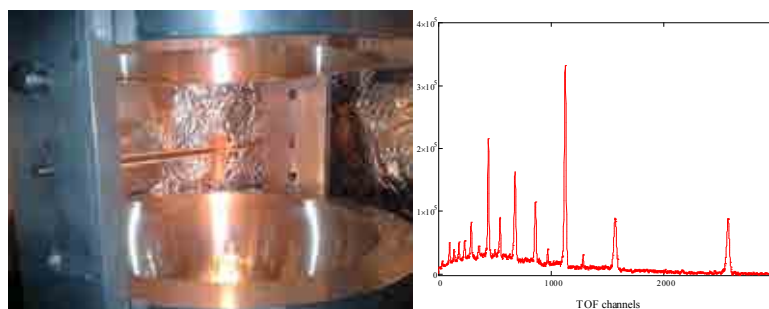


FIG. 13. Left: Studied K3 steel sample inside the mirror furnace (1 kW,  $\sim 1000^\circ\text{C}$ ) during experiment. Right: Typical neutron diffraction spectrum from K3 ferrite-martensite steel sample heated at  $200^\circ\text{C}$ .

Two series of experiments were performed on FSD diffractometer at the IBR-2 reactor. In first measurement initially quenched K3 steel sample was heated *in situ* in the mirror furnace from room temperature to  $600^\circ\text{C}$  and at the same time the neutron diffraction spectra were recorded (Fig.13 and Fig.14). All the main diffraction peaks are indicated within the body-centered cubic group  $\text{Im}\bar{3}\text{m}$  with lattice parameter  $a_0 \approx 2.87 \text{ \AA}$ . The diffraction data has been processed routinely by the Rietveld method in order to evaluate main crystal structure parameters changes with temperature (Fig.15). The lattice parameter dependence vs. temperature allowed estimating the linear thermal expansion coefficient of the material, which has a value typical for this class of steels  $\alpha = (10.9 \pm 0.5) \cdot 10^{-6} \text{ }^\circ\text{C}^{-1}$  (Fig.15, left). The neutron spectra measured on FSD diffractometer have shown significant diffraction peak broadening in comparison with reference sample (Fig.15).

In order to analyze peak broadening effects due to the crystal lattice microstrain and finite size of coherently scattering crystallites the individual diffraction peaks were fitted. Detailed analysis of peak widths revealed anisotropic character of peak broadening at which some reflection deviate from linearity (especially for (200) and (310) peaks). This deviation is usually associated with the dislocation contrast factor variation, repeatedly has been observed previously in the literature as well as in our earlier neutron experiments. The observed anisotropic peak broadening effect is expressed quite strongly and can be readily registered due to quite good instrument resolution of FSD. For correct microstrain evaluation this peak width anisotropy should be taken into account during fitting procedure which can be done using the model proposed in [13] (Fig. 17 and 18, left). The dislocation density behavior during heat treatment for both studied steels is presented in Fig. 18, right. It can be clearly seen that main changes occur in the temperature interval from  $500^\circ\text{C}$  to  $600^\circ\text{C}$  where sharp decrease of dislocation density is observed.

In addition, outlined above neutron diffraction measurements heat-resistant 10H9MFB (P91) steel samples were investigated at the SANS instrument “Yellow Submarine” in the Budapest Neutron Center, Hungary (Fig.19). Heat-treated steel plates of thickness of 1.8 mm were measured by SANS with the position of the PSD detector at 1 m ( $\lambda = 6 \text{ \AA}$ ) and 6 m ( $\lambda = 6 \text{ \AA}$  and  $12 \text{ \AA}$ ). In the same positions a standard sample of the water and the background of fast neutrons were measured. The measurements were performed with magnetic saturation field of  $H = 1.4 \text{ T}$  perpendicular to the scattering vector and without the field. The intensity of the SANS was analyzed by standard method with separation of nuclear and magnetic contributions (Fig.20). The nuclear SANS data were fitted using approach [14] in order to evaluate main structural parameters of the studied systems (Fig.22).

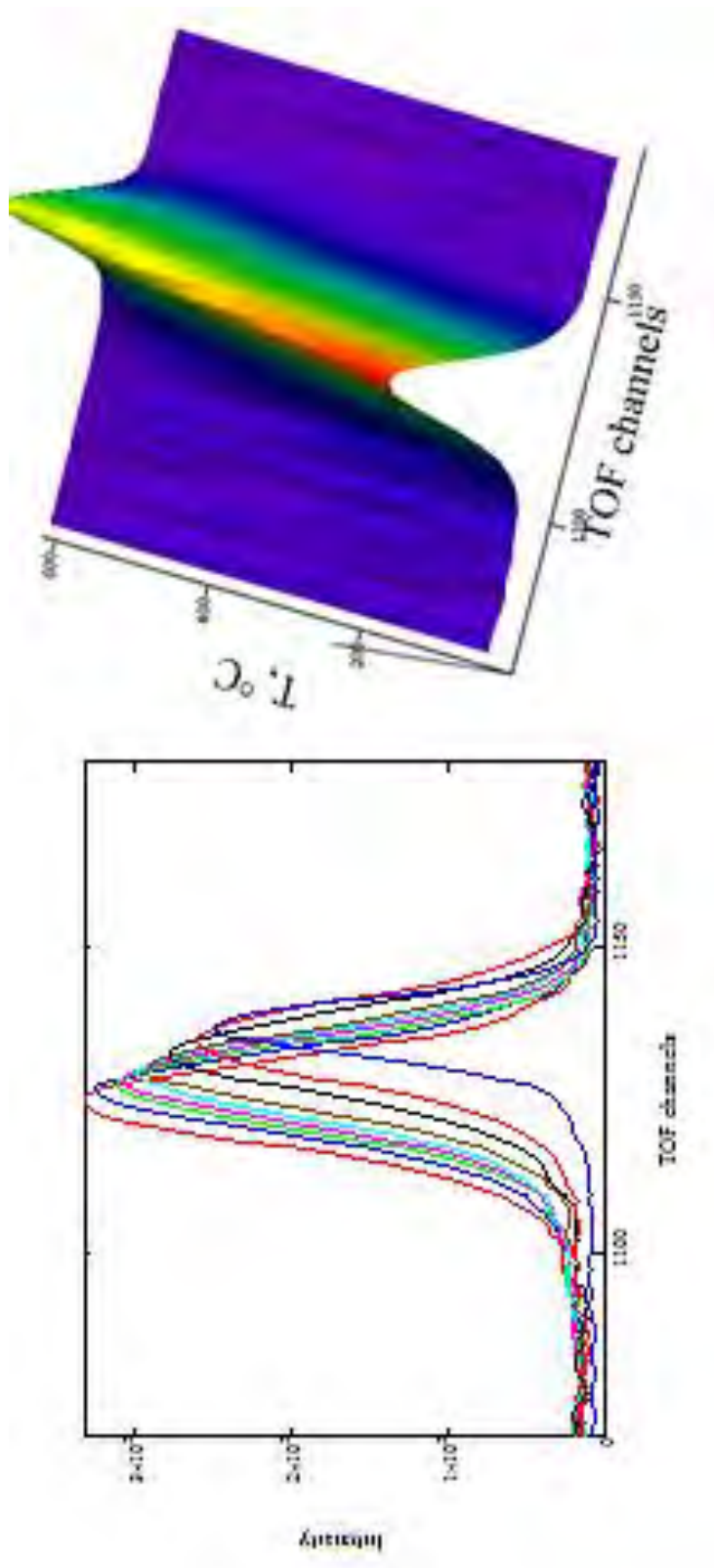


FIG. 14. Diffraction peak (211) position and width changes vs. temperature for the K3 ferrite-martensite steel.

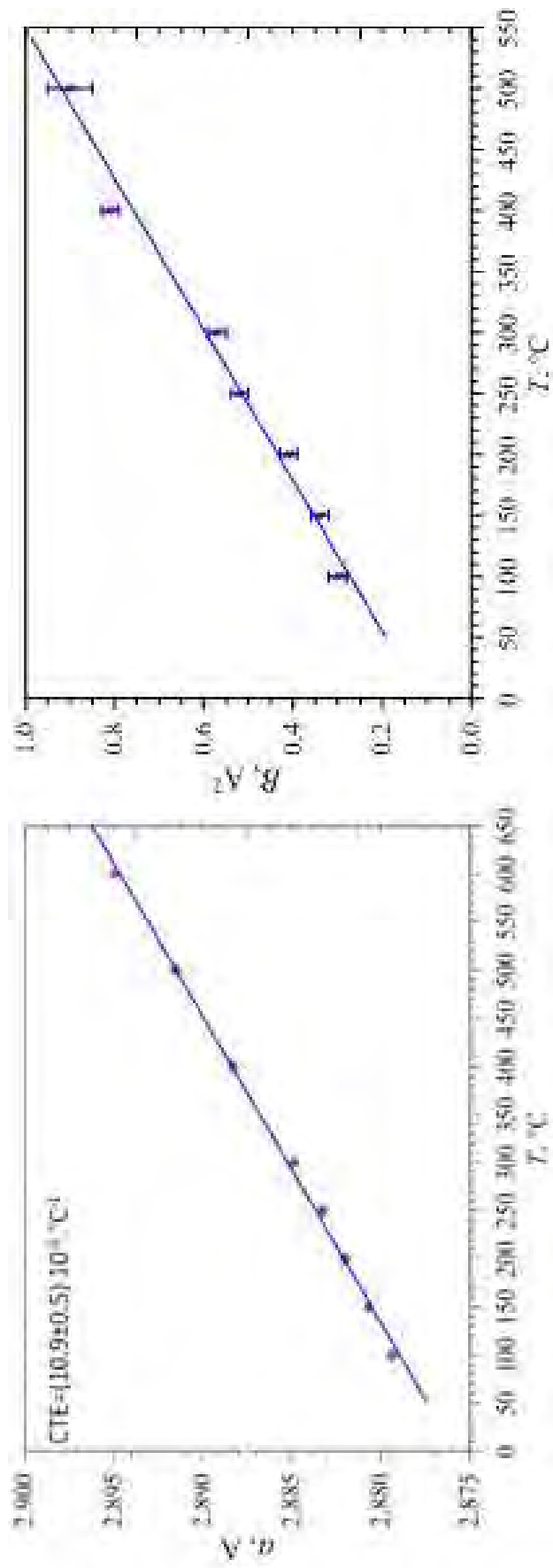


FIG. 15. Lattice parameter (left) and Debye–Waller factor (right) dependence vs. temperature for the K3 ferrite-martensite steel.

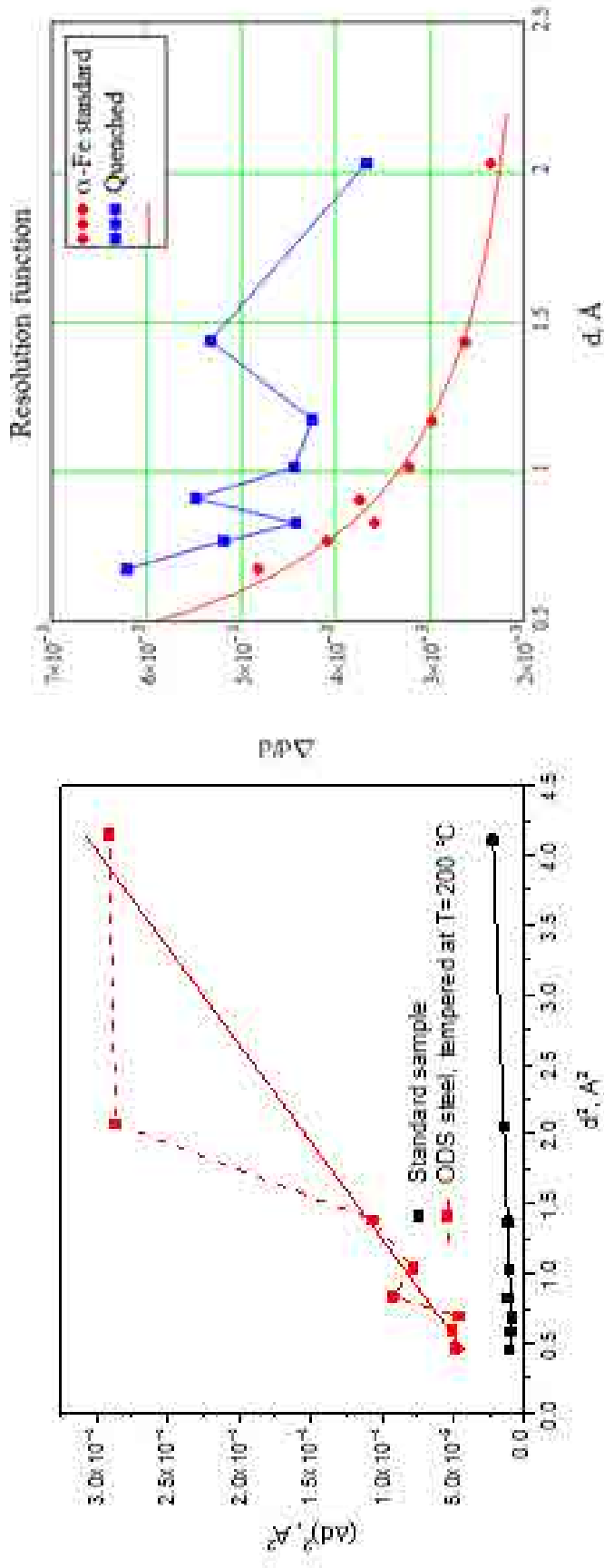


FIG. 16. Comparison of squared peak width  $(\Delta d)^2$  vs. squared interplanar spacing  $(d_{hkl})^2$  dependences (left) and the resolution function (right) for standard sample and for the K3 ferrite-martensite steel sample tempered at 200 °C.

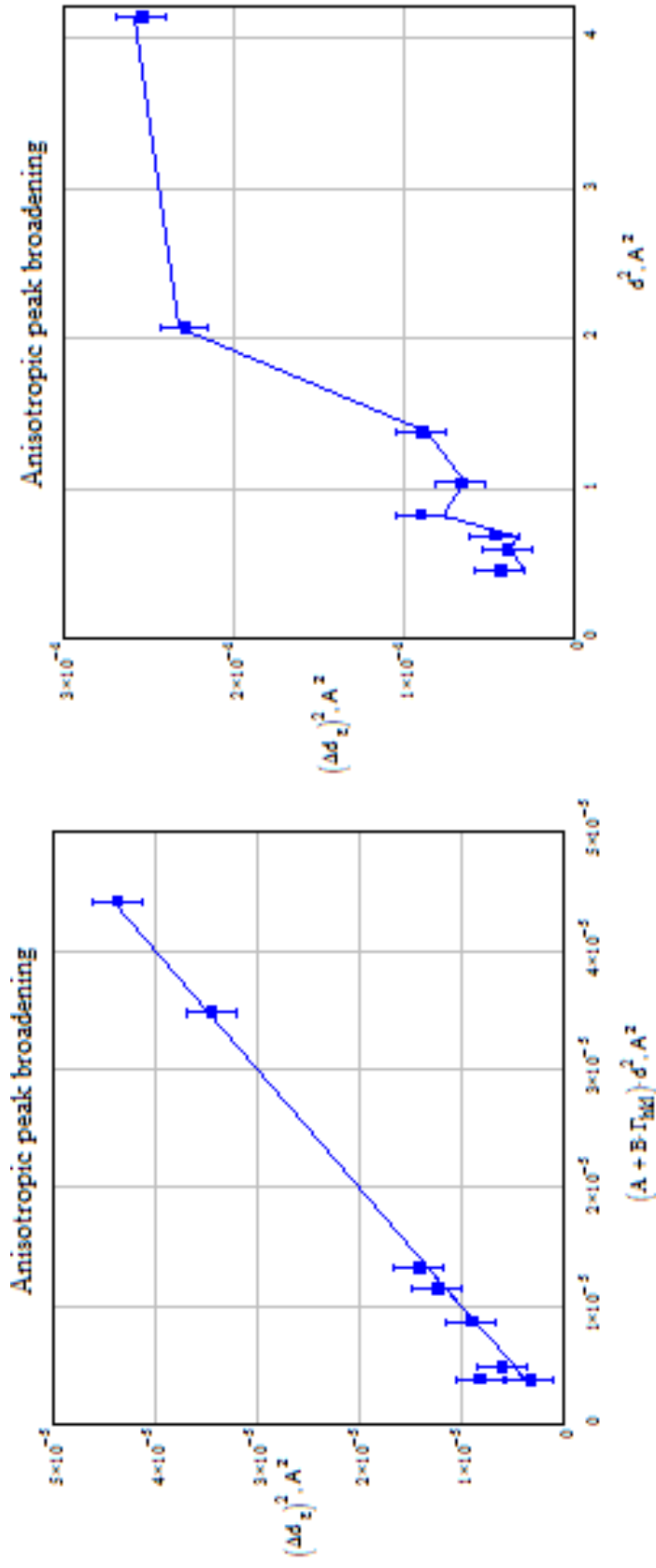


FIG. 17. Fitting of anisotropic peak broadening: comparison of squared peak width  $(\Delta d)^2$  dependence vs.  $(A+B\Gamma_{MK}) \cdot d^2$  (left) and squared interplanar spacing  $d^2$  (right) for the tempered the K3 ferrite-martensite steel sample.

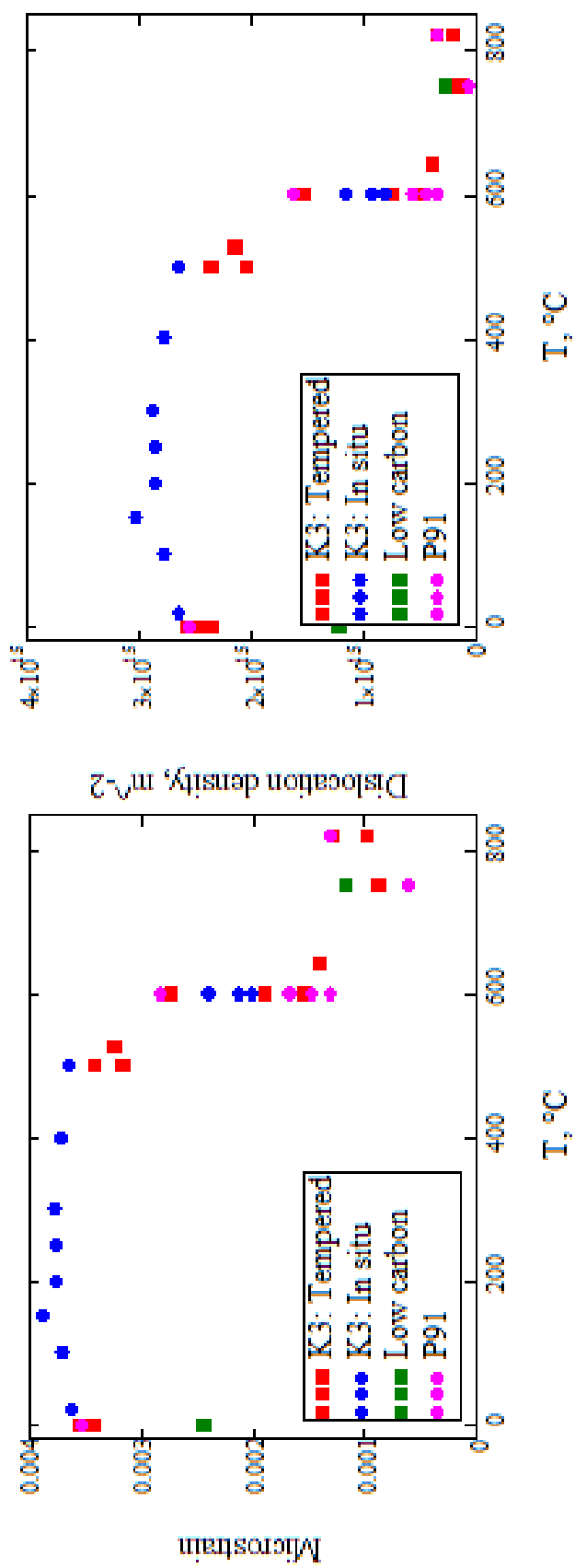


FIG. 18. Lattice microstrain (left) and estimated dislocation density (right) dependence vs. tempering temperature for both K3 and P91 studied steels.

## 2.1. Investigation of oxide-dispersed-strengthened steels

According to the nuclear SANS data the nature of neutron scattering changes from surface fractals to the volume fractals, which also indicates the mass appearance of carbonitrides, packages and other surfaces, which probably suppress the scattering from surfaces. It should be noted that after the mass precipitation of carbonitrides from martensite lattice and their coarsening, the scattering spectrum from these objects is shifted to the low Q region, which is not reachable at the “Yellow Submarine” spectrometer. However, at the same time the scattering by surface fractals is restored again.

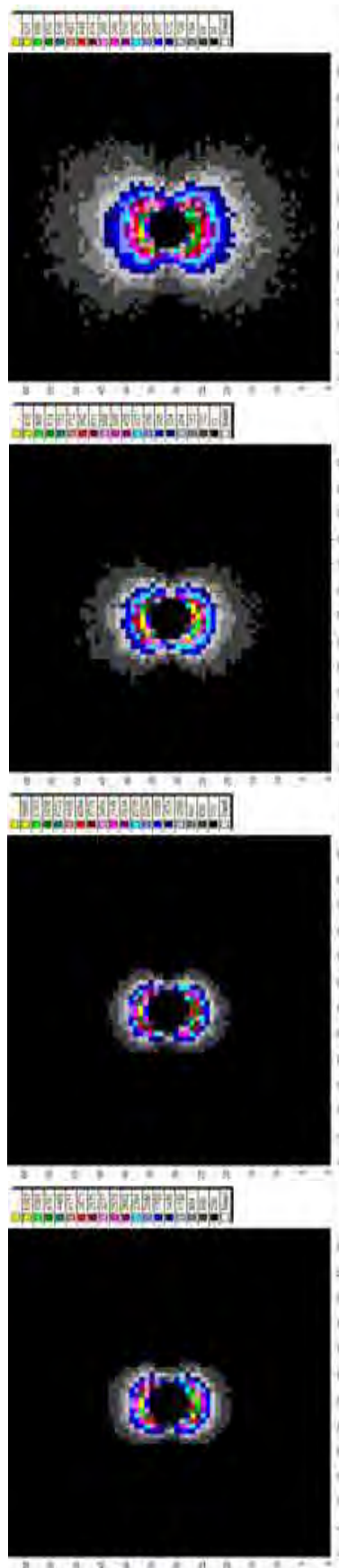
## 3. CONCLUSIONS

The behavior of the hardness and lattice parameter of the fcc H16N15M3T1 steel after tempering does not provide valuable information about changing of materials structure. At the same time our analysis indicates an increase in the lattice microstrain after annealing at 700°C, 12 h, caused most likely by formation of Ni<sub>3</sub>Ti type clusters. At the increase of the titanium concentration in the N26H5T3 alloy up to 3 wt% the early precipitation and precipitation stages of the second phase are observed. Joint diffraction and TEM analysis indicate that  $\gamma'$ -Ni<sub>3</sub>Ti phase is formed after annealing 700°C and the heat treatment duration of about 6 hours. During the growth of number of the precipitated particles at 600°C microstrain does not increase, while the hardness increases. In addition, we see that with the growth of intermetallic nanoparticles, coherently coupled with the crystal lattice, the level of hardness and microstrain increases.

Unlike the previous steel, where the lattice parameters for the dispersion-hardening phase and for the matrix are almost equal, the lattice parameter of vanadium carbide nanoparticles is by 15.5% higher than in the matrix for the 40H4G18F2 steel. However, even in this case, at the failure of coherence caused by the second phase appearance there is a significant increase in microstrain, and not decrease, as is sometimes stated in the literature [15].

The dislocation density value obtained in our experiment with H26X5T3 alloy (Fig.12) is comparable with dislocation density in ferrite-martensite steels. However, in our case the dislocation density drops sharply at prolonged high temperature creep tests. This fact as well as a sharp drop of Young’s modulus at increased temperature obviously complicates the use of this steel at high temperatures.

Neutron diffraction study of K3 and P91 steels performed in a wide temperature range revealed high microstrain level due to dislocations. The sharp decrease of dislocation density was observed during tempering in the range from 500°C to 600°C for both steels. From SANS measurements results it was concluded that for the studied steels (K3 and P91) scattering occurs from the highly developed surface of the laminated martensite. For the sample Nr. 4 tempered at 600°C, 1 h, main contribution to the scattering is due to the presence of carbides.

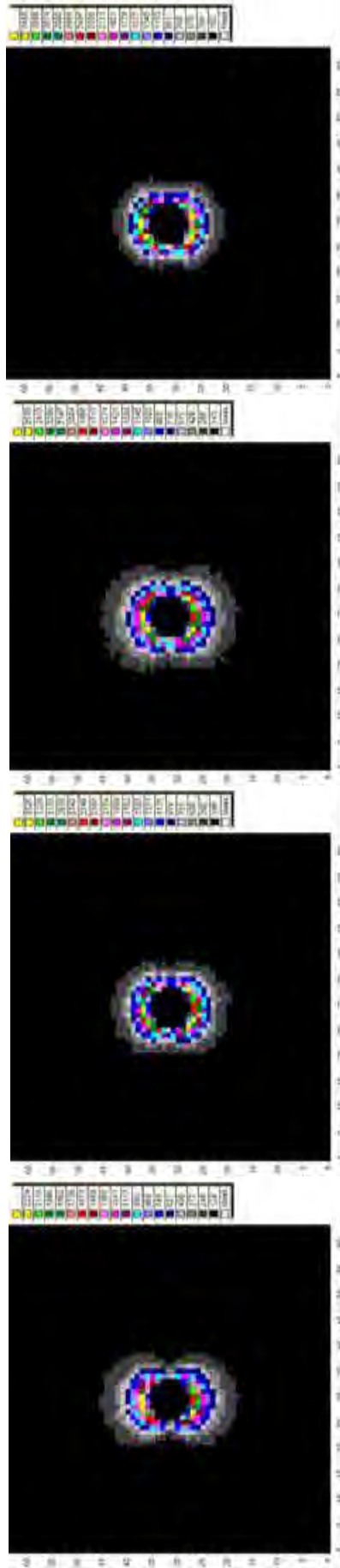


Sample Nr. 1 2:  
(initial) quenching at 1050°C

Tempering: 500°C, 1 h

3: 500°C, 100 h

4: 600°C, 1 h



5: Tempering: 525°C, 3 h

6: 640°C, 5 h

7: 600°C, 24 h

8: 750°C, 3 h

FIG. 19. Maps of scattering SANS intensity measured on studied P91 steel samples under applied horizontally magnetic field ( $H=1.4 T$ ).

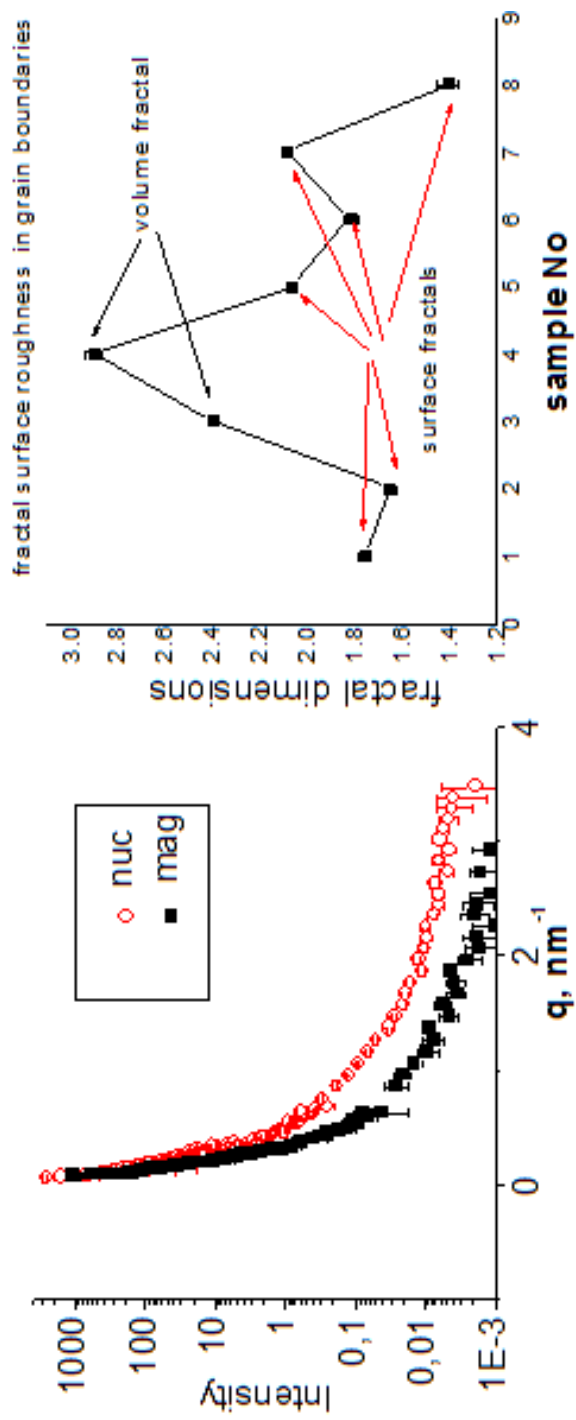


FIG. 20. The comparison of nuclear and magnetic scattering for sample Nr.1.

FIG. 21. Surface and volume fractals of nuclear SANS.

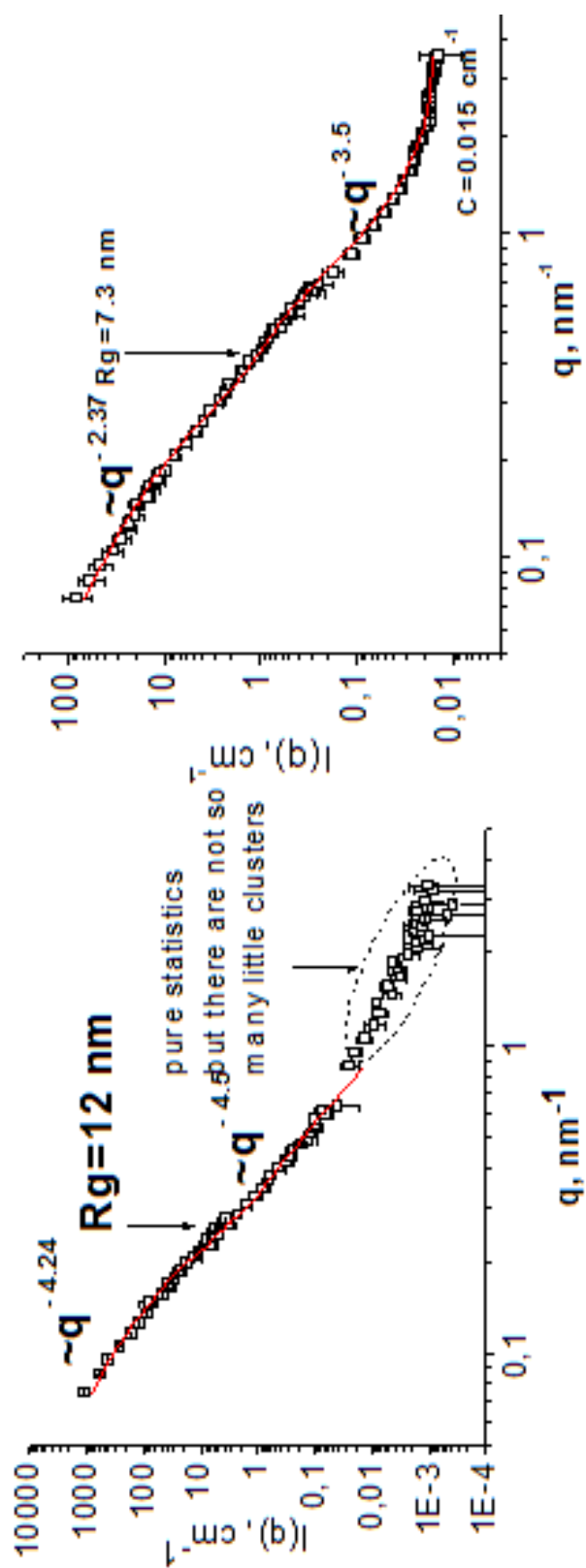


FIG. 22. Nuclear SANS data fit for initial quenched sample Nr. 1 (left) and sample Nr. 4 tempered at 600°C (right).

## 2.1. Investigation of oxide-dispersed-strengthened steels

### ACKNOWLEDGEMENTS

This work was supported by IAEA research contract Nr. 16000. The authors are grateful to Dr. D. Sheptyakov, Dr. P. Lukáš, Dr. P. Mikula, Dr. P. Beran and Dr. Gy. Török for their assistance in conducting experiments and useful discussions.

### COOPERATION WITHIN THE CRP PARTNERS

**1) Institute of Nuclear Materials, Zarechny, Russia (A. Kozlov).** The main task of this collaboration was investigation of residual microstresses in the radiation-resistant steels with BCC and FCC lattices which are used for reactor vessels, components of inter-reactor structures and fuel element shells during the process of formation, growth and coagulation of second-phase disperse particles. Microstress level was estimated in iron-based alloys with precipitates of coherent intermetallides Ni<sub>3</sub>Ti (type 16Cr-15Ni-3Mo-Ti and 36Ni-3Ti steels) and coherent carbides VC (type 15Cr-2Ni-Mo and 0.2C-18Mn-V steels).

**2) Nuclear Physics Institute, Řež near Prague, Czech Republic (P. Mikula).** Austenitic H26X5T3 steel with  $\gamma'$ -Ni<sub>3</sub>Ti precipitation-hardening phase behavior under applied load was studied on the MEREDIT neutron powder diffractometer in Nuclear Physics Institute of the Czech Academy of Sciences in Řež near Prague. The properties of quenched and tempered at various temperatures samples were compared: from measured strain-stress dependencies Young's moduli were estimated as well as microstrain and dislocation density values from diffraction line broadening as a function of applied stress.

**4) Research Institute for Solid State Physics and Optics, Budapest, Hungary (Gy. Török).** New ferritic-martensitic steels are of great interest for nuclear industry due to their unique heat- and radiation-resistant properties. To this end two newly developed in Russia heat-resistant martensitic steels 10H9K3V2MFBR and 10H9MFB (similar to P91 steel) were investigated at the SANS instrument in the Budapest Neutron Center. The SANS spectra measured on quenched and annealed samples exhibit a large surface fractal scattering in these steels. At the annealing temperature of 600°C, 1 hour, an intensive precipitation of bulk fractal carbides and nitrides particles is observed. With further annealing carbides are enlarged in size and cannot be observed by SANS. This process restores the surface scattering on fractals up to high annealing temperature.

**5) Institute of Nuclear Research, Pitesti, Romania (I. Ionita).** The aging behavior of the Incoloy 800HT alloy and OL 304C austenitic stainless steel was studied at the Fourier Stress Diffractometer (FSD) in the Frank Laboratory of Neutron Physics of the JINR, Dubna, Russia. The samples were subjected to heat treatment for 60 days at 450°C, 500°C, 550°C, 600°C. Totally 10 samples in two series (Incoloy 800HT and OL 304C) were investigated. Both materials are going to be used in nuclear power industry due to their advanced properties. The 304-L alloy is an austenitic stainless steel with high ductility, good corrosion resistance, low yield stress and relatively high ultimate tensile strength. Incoloy 800 HT is a nickel based alloy with good mechanical properties and excellent corrosion resistance in water at high temperatures. For this reason Incoloy 800 HT alloy is exceptionally useful for many applications involving long term exposure to elevated temperature and corrosive atmosphere. Recently, this alloy starts to be studied as candidate material for fuel cladding in supercritical water reactors.

**6) Centro Atómico Bariloche, Comisión Nacional de Energía Atómica, Argentina (J. Santisteban).** In collaboration with Centro Atómico Bariloche (Argentina) the experiments for residual stress and texture studies in Zr-2.5 wt% Nb pressure tubes samples were started in

## 2.1. Investigation of oxide-dispersed-strengthened steels

FLNP JINR, Dubna. Zr-2.5 wt% Nb can be used as the pressure tube material for nuclear reactors due to its good mechanical strength, high corrosion and creep resistance. The final goal of these experiments is to estimate the macroscopic and intergranular residual stresses appearing after various technological processes; and optimize the annealing treatment required to relieve them to acceptable levels.

### REFERENCES

- [1] SAGARADZE, V., et al., *The Physics of Metals and Metallography*, **112** (2011) 543-551.
- [2] FISCHER, P. et al., *Physica B* **276-278** (2000) 146.
- [3] MITTEMEIJER, E.J., WELZEL U., *Zeitschrift für Kristallographie* **223** (2008) 552-560.
- [4] HOLZWARTH U., GIBSON N., *Nature Nanotechnology* **6** (2011) 534.
- [5] RODRÍGUEZ-CARVAJAL, J., *Physica B* **192** (1993) 55-69.
- [6] SAGARADZE, V., et al., *The Physics of Metals and Metallography* **111** (2011) 82-92.
- [7] BANNYH O.A. et al., *Russian Metallurgy (Metally)* **5** (2002) 55-59.
- [8] H. CHOO, D.W. BROWN, “Intergranular Strain Evolution during High-Temperature Tensile Deformation”, SNS-HFIR User Meeting, Oak Ridge (2005).
- [9] WILLIAMSON, G.K., SMALLMAN, R.E., III. Dislocation Densities in Some Annealed and Cold-Worked Metals from Measurements on the X ray Debye-Scherrer Spectrum, *Philosophy Magazine* **1**, 1 (1956) 34-46.
- [10] KAYBYSHEV, R.O., et. al., New martensitic steels for fossil power plant: Creep resistance, *The Physics of Metals and Metallography*, **109**, No. 2 (2010) 186-200.
- [11] PESICKA, J., et al., The evolution of dislocation density during heat treatment and creep of tempered martensite ferritic steel, *Acta Materialia* **51** (2003) 4847-4862.
- [12] KIPELOVA, A.Yu., et al., Tempering-induced structural changes in steel 10KH9K3V1M1FBR and their effect on the mechanical properties. *Metal Science and Heat Treatment*, **52**, 3-4 (2010) 100-110.
- [13] UNGAR, T., et al., The contrast factors of dislocations in cubic crystals: the dislocation model of strain anisotropy in practice, *J. Appl. Cryst.* **32** (1999) 992-1002.
- [14] HIRSCH, P.B., et al., *Electron microscopy of thin crystals*, Butterworths, London, 1968.
- [15] BEAUCAGE G., Small-angle scattering from polymeric mass fractals of arbitrary mass-fractal dimension, *J. Appl Cryst.* **29** (1996) 134-149.

### CRP related publications and presentations

- 1) G.D. BOKUCHAVA, A.M. BALAGUROV, V.V. SUMIN, I.V. PAPUSHKIN, “Neutron Fourier diffractometer FSD for residual stress studies in materials and industrial components”, *Journal of Surface Investigation. X-ray, Synchrotron and Neutron Techniques*, **4**, 6, (2010) 879-890.
- 2) A.M. BALAGUROV, G.D. BOKUCHAVA, I.V. PAPUSHKIN, V.V. SUMIN, A.M. VENTER, “Neutron diffraction potentialities at the IBR-2 pulsed reactor for non-destructive testing of structural materials”, JINR Preprint E13-2010-84, Dubna, 2010.
- 3) V.V. SUMIN, G.D. BOKUCHAVA, I.V. PAPUSHKIN, A.M. BALAGUROV, A.M. VENTER, “Exploitation the Potentialities of Neutron Diffraction for Non-Destructive Testing of Constructive Materials”, The 10<sup>th</sup> European Conference on NDT, June 7-11,

2010, Moscow, Russia. [www.ndt.net/search/docs.php3?MainSource=-1&id=9138](http://www.ndt.net/search/docs.php3?MainSource=-1&id=9138);  
<http://www.ecndt2010.ru/>

## 2.1. Investigation of oxide-dispersed-strengthened steels

- 4) I.V. PAPUSHKIN, V.V. SUMIN, G.D. BOKUCHAVA, A.M. BALAGUROV, D.V. SHEPTYAKOV, “Determination of residual stresses in precipitation hardening steels by neutron diffraction”, STI-2011: The International Conference “Stress and Texture Investigations by Means of Neutron Diffraction”, <http://sti2011.jinr.ru>, Dubna (2011), JINR E14-2011-41 (2011) 49.
- 5) G.D. BOKUCHAVA, “Neutron Fourier diffractometer FSD for residual stress studies in advanced materials and industrial components”, in: The International Conference “Stress and Texture Investigations by Means of Neutron Diffraction 2011 (STI-2011)”, <http://sti2011.jinr.ru>, 6-9 June 2011, Dubna, Russia, Abstracts book, JINR E14-2011-41, 2011, 37.
- 6) G.D. BOKUCHAVA et al., “Anisotropic peak broadening studies on the RTOF diffractometer”, NSCFI-2012: XXII International Workshop on Neutron Scattering in Condensed Matter Investigations, Gatchina (2012).
- 7) I.V. PAPUSHKIN et al., “Microstrain in dispersion-hardened steels”, NSCFI-2012: XXII International Workshop on Neutron Scattering in Condensed Matter Investigations, Gatchina (2012).
- 8) V.V. SUMIN, “Investigation of the martensite decay in ferritic-martensitic steels by SANS method”, NSCFI-2012: XXII International Workshop on Neutron Scattering in Condensed Matter Investigations, Gatchina (2012).
- 9) G.D. BOKUCHAVA, V.V. Sumin, I.V. Papushkin, “Microstrain studies in ferrite-martensite steel using TOF neutron diffraction, FLNP Annual Report (2012).
- 10) G.D. BOKUCHAVA et al., “Microstrain in dispersion-hardened steels”, Particles and Nuclei, Letters, Nr. 2-179, **10**, 2 (2013) 157-161.

## 2.1. Investigation of oxide-dispersed-strengthened steels

### CHARACTERIZATION OF Y<sub>2</sub>O<sub>3</sub> PARTICLE DISTRIBUTION IN OXIDE DISPERSION STRENGTHENED EUROFER STEEL FOR NUCLEAR APPLICATIONS BY MEANS OF SMALL-ANGLE NEUTRON SCATTERING (SANS) AND OF NEUTRON DIFFRACTION

R. COPPOLA\*, M. VALLI\*\*

\*ENEA-Casaccia, Via Anguillarese 301, 00123 Roma, Italy

\*\* ENEA-Faenza, Via Ravennana 186, 48018 Faenza (RA), Italy

Email: [roberto.coppola@enea.it](mailto:roberto.coppola@enea.it)

#### Abstract.

This report summarizes the scientific results obtained in the frame IAEA Agreement No. 16200/R0 4/5/2010 until May 2013. Small-angle neutron scattering (SANS) and neutron diffraction measurements have been carried out on Oxide Dispersion Strengthened (ODS) Eurofer97 and 14 Cr ferritic/martensitic steels, obtaining relevant information on their microstructure. Collaborative results have also been obtained with other CRP participants, concerning the optimization of SANS data analysis, compared SANS measurements on ODS material at different neutron sources and the characterization of H-loaded Zr tubes.

## 1. INTRODUCTION

This report refers to the experimental activities carried out until May 2013 to characterize by means of small-angle neutron scattering (SANS) and neutron diffraction the microstructure of Oxide Dispersion Strengthened (ODS) Eurofer97 and 14 Cr ferritic/martensitic steels, based on the following originally proposed work plan:

Year 1

1.1 SANS measurements of polycrystalline and nano-structured Eurofer-ODS.

1.2 SANS data analysis.

Year 2

2.1 Neutron diffraction measurements of polycrystalline and nano-structured Eurofer-ODS.

2.2 Neutron diffraction data analysis.

Year 3

3.1 Correlation of neutron diffraction and SANS results.

3.2 Preparation of a technical report summarizing the obtained results and outlining their relevance to the metallurgical characterization and optimisation of the investigated material.

The objectives of this work plan have up to now been mostly fulfilled (except 3.2), a considerable amount of SANS and neutron diffraction experimental data has been collected on different ODS ferritic/martensitic steels and data analysis has been carried out or is underway. However, a deep and complete metallurgical characterization of microstructural evolution in such complex materials will require collaborative efforts well beyond the deadline of this CRP, as it was also discussed during the 2<sup>nd</sup> RCM (Beijing, September 2011). More specifically, the results obtained by neutron techniques are being correlated with other microstructural information, obtained by other techniques and some scientific papers are in preparation or submitted for presentation at international conferences.

In addition to these individual achievements, collaborative work has been carried out with BNC (“round-robin” SANS measurements, development of SANS data analysis), with KIT and

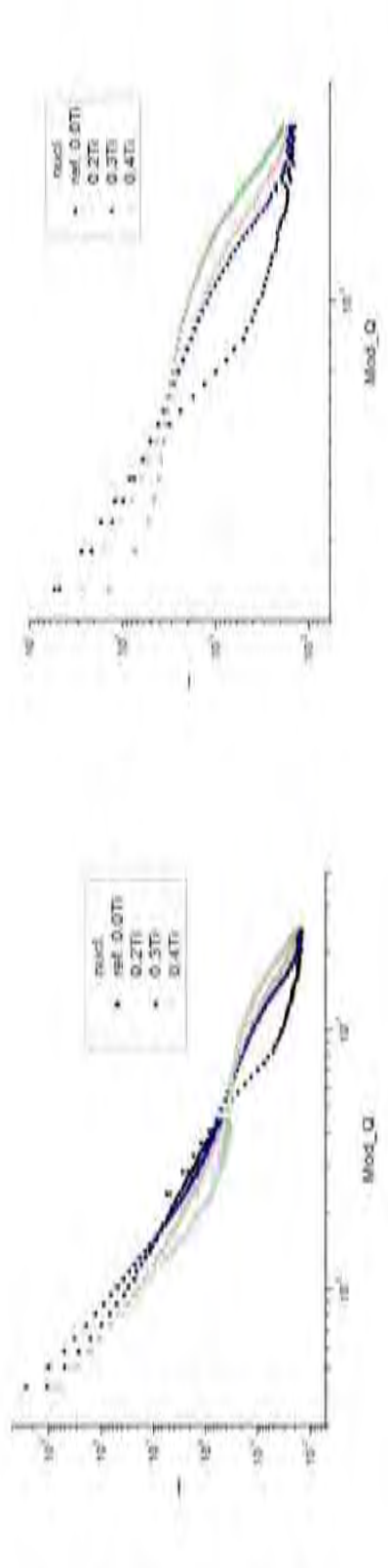
## 2.1. Investigation of oxide-dispersed-strengthened steels

CNEA on H-loaded Zr tubes SANS characterization, obtaining quite recently very promising SANS results. Finally, this CRP has allowed strengthening the collaboration with JRC, already established in the frame of the “NeT – Network on Neutron Techniques Standardization for Structural Integrity”.

## 2. INDIVIDUAL PROGRESS REPORT ON THE WORK CARRIED OUT AND RESULTS OBTAINED

SANS measurements have been carried out on 14 Cr ODS  $Y_2O_3$  0.35 wt% ferritic martensitic steel with Ti contents ranging from 0.2 wt% to 0.4 wt%, provided by KIT, where such promising laboratory heats are being produced and characterized, both mechanically and by TEM and ATP. A reference 14 Cr ODS sample, with no Ti, and three samples with respective Ti contents of 0.2, 0.3 and 0.4 wt% were investigated by SANS at the D22 instrument at the High Flux Reactor of the Institut Max von Laue – Paul Langevin (ILL) in Grenoble, France. Sample-to-detector distances of 2 m and 11 m were utilized with a neutron wavelength of 6 Å, giving an experimental range corresponding to particle sizes ranging between 10 and 300 Å in size approximately. A saturating magnetic field of 1 T was utilized to separately measure the nuclear and magnetic SANS components.

The SANS results are shown in fig. 1 (a-b): it is evident that adding Ti promotes the growth of a new population of microstructural defects, 20 Å approximately in average size, and that at the same time significant changes in SANS cross-section are detected also in the low  $Q$  region. Based the ratio of nuclear plus magnetic to magnetic SANS cross-sections (Fig. 2) as well as on TEM and ATP results [1,2], the smaller inhomogeneities can be tentatively identified Y-Ti-O complexes, while the SANS variations observed at smaller  $Q$ -values should be attributed to the evolution of large Cr carbides. The Rietveld analysis of the high resolution neutron diffraction data [3] indicate the contribution corresponding to  $Y_2O_3$  is comparable to the experimental error, so the real stoichiometry has to be clarified; traces of the TiN, well above the experimental error, have been detected [3], which could also contribute in the total SANS effect observed at high  $Q$ -values.



a

b

FIG. 1. Nuclear SANS cross-sections ( $\text{cm}^{-1}$  vs  $\text{\AA}^{-1}$ ) of 14 Cr ODS  $\text{Y}_2\text{O}_3$  0.35 wt% ferritic / martensitic steel with different Ti contents (a) whole spectrum, b) 2 m sample-to-detector distance.

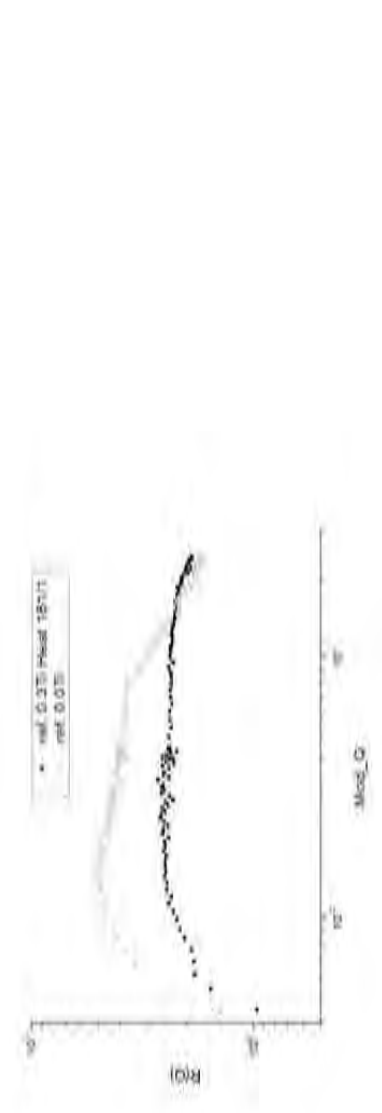


FIG. 2.  $R(Q)$  ratio of nuclear plus magnetic to magnetic SANS cross-sections for 14 Cr ODS with no Ti and 0.4 Ti (non-magnetic particles?).

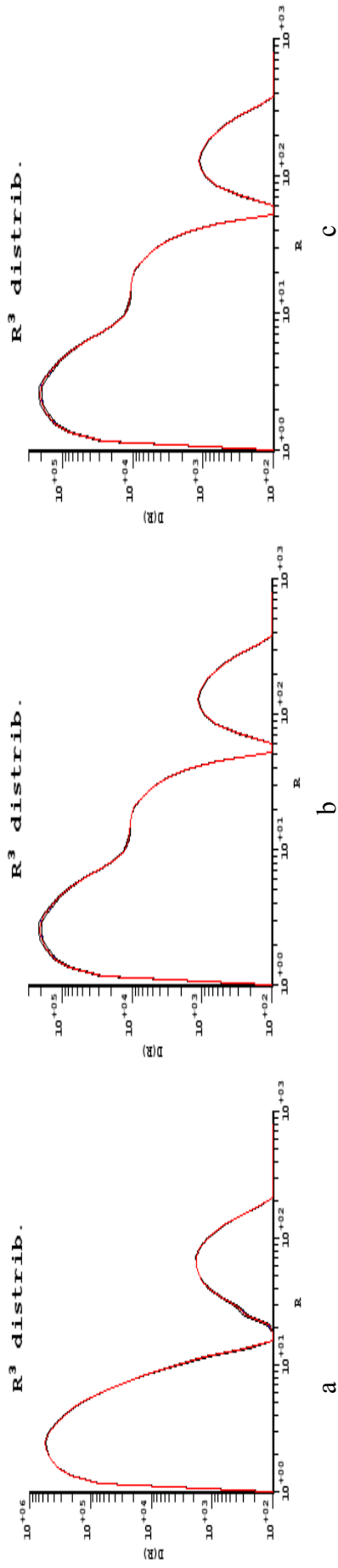


FIG. 3. Number distribution functions (number of particles per unit volume with size between  $R$  and  $R+dR$ ) for 14Cr ODS without 0 (a) 0.3 (b) and 0.4 (c) wt% Ti; the uncertainty band is 15-20%.

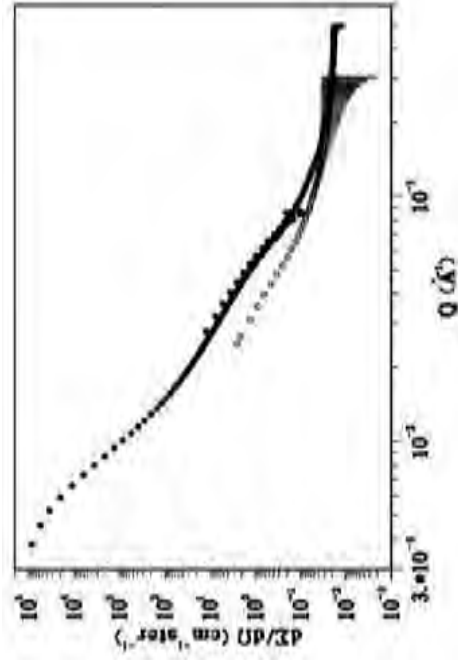


FIG. 4. Nuclear SANS cross-sections ( $\text{cm}^{-1}$  vs  $\text{\AA}^{-1}$ ) of nano-structured 9Cr Eurofer ODS (empty dots) 14Cr ODS  $\text{Y}_2\text{O}_3$  0.35 wt% (full dots) ferritic/martensitic steels.

## 2.1. Investigation of oxide-dispersed-strengthened steels

The size distribution functions obtained by the method described in ref.s [4,5] for Ti contents varying between 0 and 0.4 wt% are presented in Fig. 3, showing the occurrence of the new phase when Ti is added.

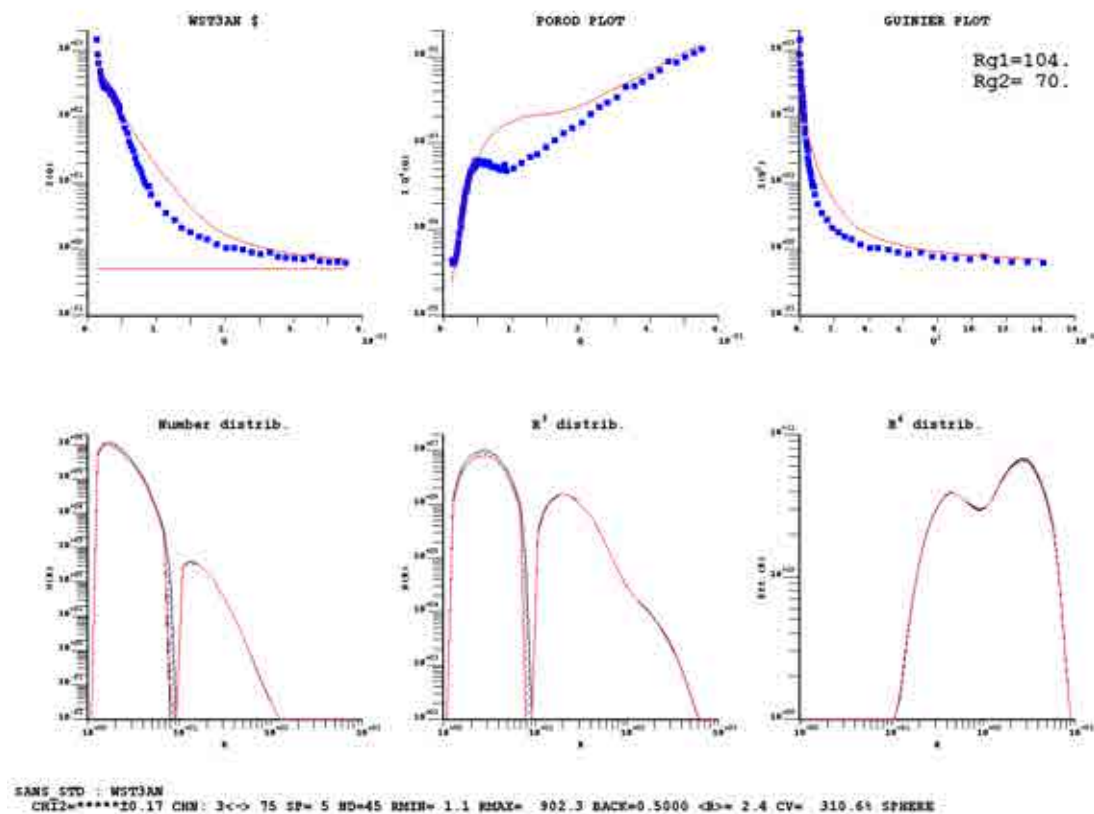
This new 14 Cr ODS heat (Ti-free reference) has been compared to 9Cr Eurofer ODS material, also previously investigated by SANS: it is clear from Fig. 4 that increasing the Cr content results in a more heterogeneous microstructure.

## 3. COLLABORATIVE EFFORTS AND RESULTS ACHIEVED

Joint work with other CRP participants has consisted in the following:

### 3.1. In collaboration with BNC-Budapest Dr. G. Torok

A series of SANS data obtained on an aged duplex steel has been analysed by the transformation method reported in ref.s [4,5] in order to contribute in assessing the reliability of the size distribution functions. The most interesting result is shown in Fig. 4, referring to the data obtained on samples showing inter-particle interference effects: even without introducing in the model the interference effect, increasing to 8-9 the number of B-spline reduces considerably the fitting problems; work is underway to eliminate the unphysical oscillations in the obtained distributions and to compare with the results obtained on the same samples by other methods.



a

## 2.1. Investigation of oxide-dispersed-strengthened steels

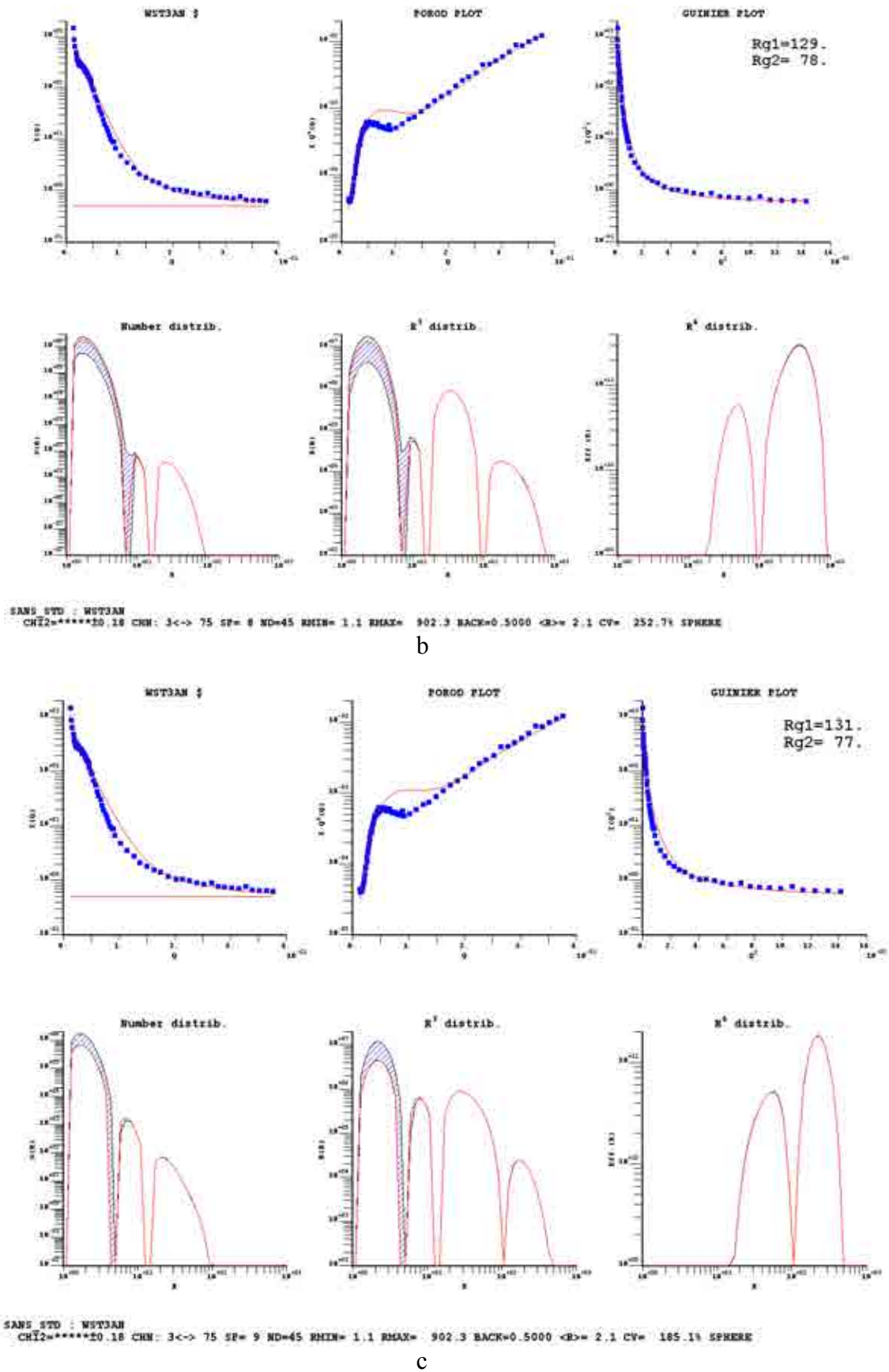


FIG. 5. Best-fits and size distributions obtained from a duplex steel aged sample increasing the number of B-splines from 5 (a) to 8 (b) and 9 (c).

## 2.1. Investigation of oxide-dispersed-strengthened steels

### 3.2. In collaboration with BNC, Dr. T. Gyula

A set of nano-structured 9 Cr Eurofer ODS, submitted to annealing at temperatures ranging between 750°C and 1150°C, [6] characterized by SANS at the ILL-Grenoble (Fig. 5) has been characterized at the at the BNC reactor. Figure 6 shows the good agreement of these two SANS measurements, carried out on the same ODS sample, at two different neutron sources. Experimental details on this “round robin” exercise will be provided in the report by Dr. T. Gyula.

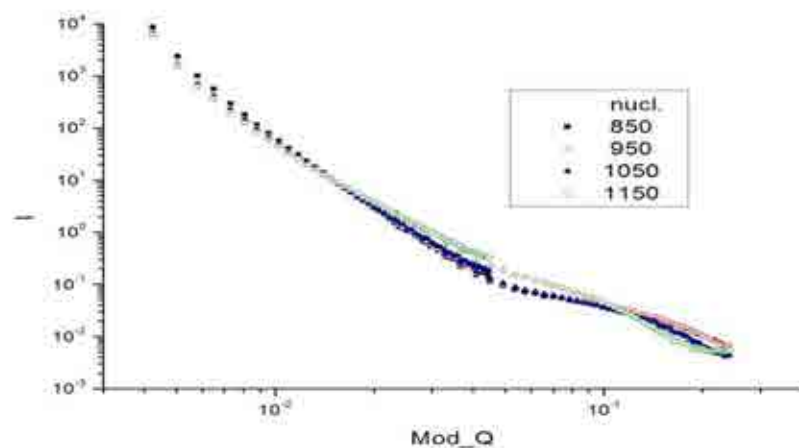


FIG. 6. Nuclear SANS cross-sections ( $\text{cm}^{-1}$  vs  $\text{\AA}^{-1}$ ) of Eurofer ODS mechanically alloyed nano-powders annealed between 850°C and 1150°C (measurements carried out at the ILL-Grenoble).

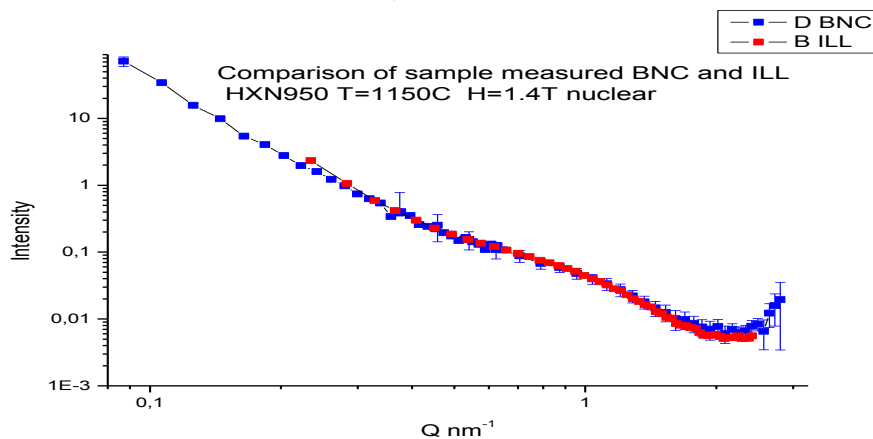


FIG. 7. Comparison of SANS nuclear cross-sections of Eurofer-ODS mechanically alloyed nano-powders submitted to 2 h annealing at 950°C measured at ILL (red) and at BNC (blue).

### 3.3. SANS measurements

SANS measurements have been carried out at the ILL-Grenoble on hydrogenated Zr specimens from KIT (preliminary results included in Dr. M. Grosse’s report) and from CNEA (Dr. J. Santisteban): highly anisotropic 2D spectra were detected but no significant differences between the samples. The tests were therefore repeated after joint discussion of sample preparation on new samples, carefully machined with homogeneous thickness and regular surfaces. The SANS measurements on these new samples were carried out at the TUM high-flux reactor thanks to the collaboration of Dr. Andre Heinemann. Sample-to-detector distances of 2 m and 11 m were utilized with neutron wavelengths of 6 Å, giving an experimental range corresponding to particle sizes ranging between 10 and 300 Å in size approximately. Figure 7 shows the comparison of the reference, H-free, and of the H-loaded sample, presenting a SANS

## 2.1. Investigation of oxide-dispersed-strengthened steels

cross-section one order of magnitude higher with a completely different high Q background. Both samples exhibit marked anisotropy (relating to the tube texture) accentuated in the H-loaded material by the growth of elongated large hydride precipitates. Figure 9 shows the size distribution obtained from the difference between h-loaded and reference sample utilizing the B-spline method for polydisperse systems: clearly, to obtain a reliable fit the system anisotropy has to be taken into account. Work is underway, as well as to try and determine the H content from integrated SANS intensity and transmission measurements.

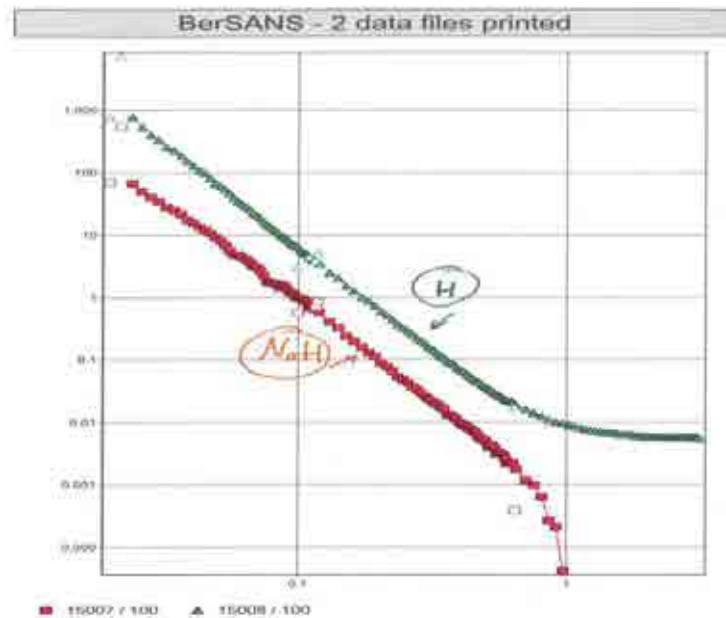


FIG. 8. Radially averaged SANS cross sections ( $\text{cm}^{-1}$  vs  $\text{\AA}^{-1}$ ) of CNEA H-loaded and H-free Zr samples (unpublished measurements carried out by Dr. Andre Heinemann, TUM).

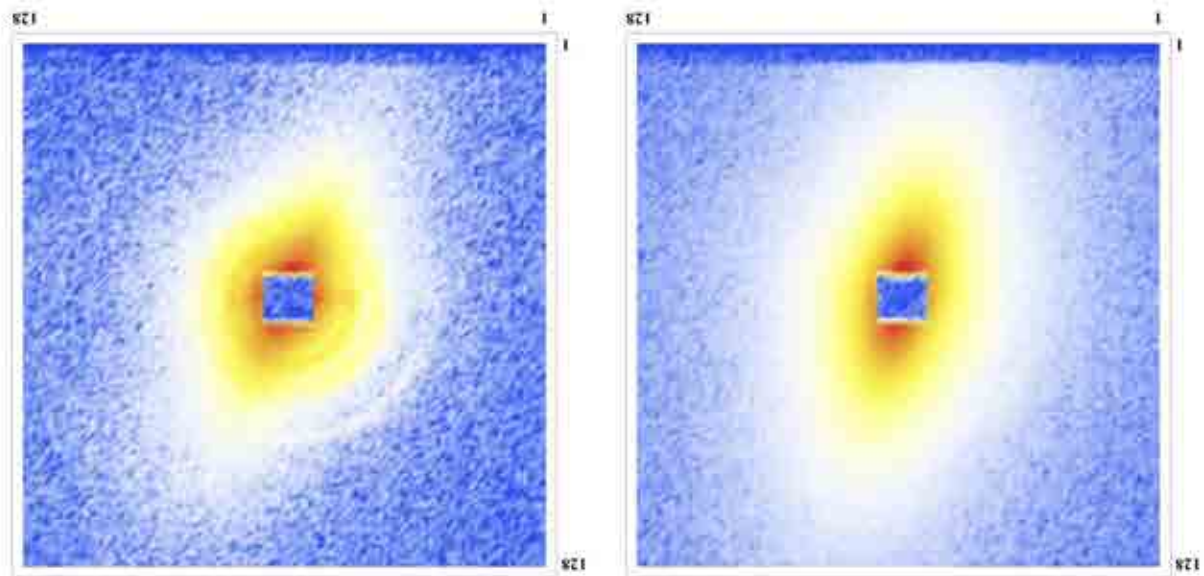


FIG. 9. 2D SANS patterns of hydrogen loaded and hydrogen free Zr<sub>2.5</sub>Nb and Zry-4 (Zr<sub>1.5</sub>Sn) alloys measured at the SANS facility at FRM2 in Garching (TU Munich) (unpublished measurements carried out by Dr. Andre Heinemann, TUM).

## 2.1. Investigation of oxide-dispersed-strengthened steels

### 4. REMAINING WORK-PLAN

#### 4.1. Individual work

As clarified in the introduction, completing the SANS and neutron diffraction data analysis of the investigated ODS materials, summarizing these findings in scientific publications.

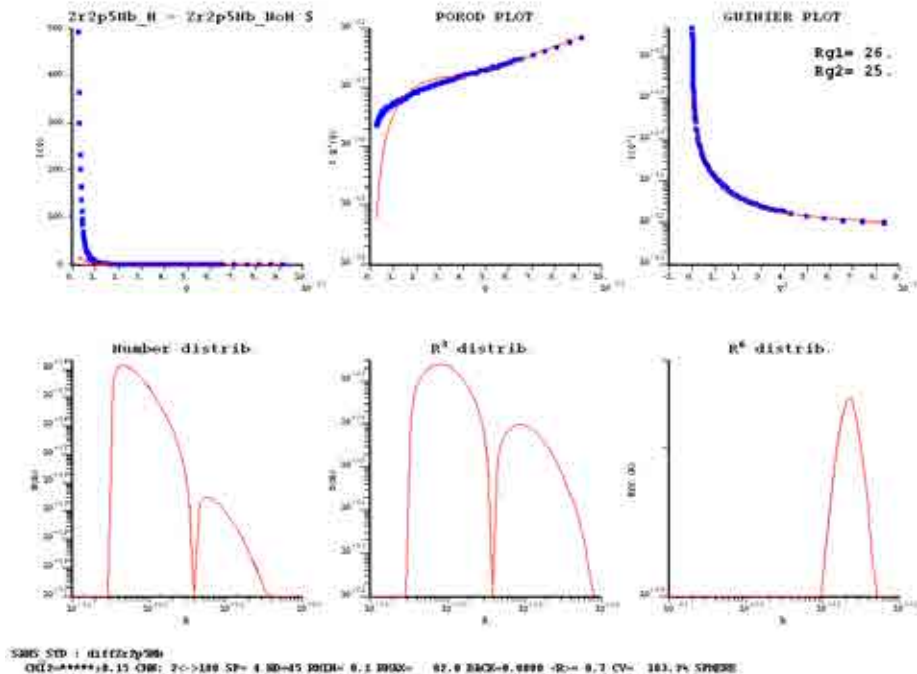


FIG. 9. Best fit and size distributions for the difference between CNEA H-loaded and H-free samples obtained by the B-spline method of Ref. (4, 5).

#### 4.2. Collaborative efforts

As a collaborative work, some completion of SANS data analysis of H-loaded Zr tubes will be done with the involved partners.

### 5. SUMMARY AND CONCLUSIONS

The activities foreseen by the agreed work plan are on schedule, they have allowed a considerable progress in the characterization of microstructural effect relating to compositional changes in ODS ferritic/martensitic steels; further progress is expected by metallurgical analysis based also on the results of other non-nuclear techniques. Additionally significant interactions have been established with other CRP participants, to be hopefully kept and further developed and in the future.

### REFERENCES

- [1] HE, P., KLIMENKOV, M., LINDAU, R., MOSLANG, A., J. of Nuclear Materials **428** (2012) 131
- [2] RHOGOZKIN, A., et al., to be published.
- [3] COPPOLA, R., RODRIGUEZ-CARVAJAL, J., WANG, M., ZHANG, G., ZHOU, Z., High-resolution neutron diffraction crystallographic investigation of oxide dispersion

## 2.1. Investigation of oxide-dispersed-strengthened steels

strengthened steels of interest for fusion technology, pres. at ICFRM16 and J. N. Mat 455 (2014) 426-430.

[4] MAGNANI, M., PULITI, P., STEFANON, M., Nucl. Inst. & Meth. **A271** (1988) 611.

[5] COPPOLA, R., KAMPMANN, R., MAGNANI, M., STARON, P., Acta Mat. **46** (1998) 5447.

[6] COPPOLA, R., LINDAU, R., MAY, R.P., MÖSLANG, A., VALLI, M., VLADIMIROV, P., WIEDENMANN, A., J. of. Ph. C **251** (2010) 012052.

## **2. RESULTS ACHIEVED**

### **2.2. RESEARCH ON ZIRCONIUM BASED MATERIALS (INCLUDING HYDROGEN UPTAKE)**

## 2.2. Research on zirconium based materials (including hydrogen uptake)

### NEUTRON SCATTERING ACTIVITY AT LOS ALAMOS NATIONAL LABORATORY

M.A.M. BOURKE

Los Alamos Neutron Science Center, MS H805, Los Alamos National Laboratory, Los Alamos, NM 87545, U.S.A.

Email: [bourke@lanl.gov](mailto:bourke@lanl.gov)

#### **Abstract.**

The nondestructive and bulk penetrating aspects of neutron scattering techniques make them well suited to the study of materials from the nuclear energy sector (particularly those which are radioactive). This report provides a summary of the facility, LANSCE, which is used at Los Alamos National laboratory for these studies. It also provides a brief description of activities related to line broadening studies of radiation damage and recent imaging and offers observations about the outlook for future activity. The work alluded to below was performed during the period of the CRP by researchers that included but were not limited to; Sven Vogel and Don Brown of Los Alamos National Laboratory; and Anton Tremsin of the University of California, Berkeley.

## 1. INTRODUCTION

Neutron scattering offers unique advantages for characterization of materials relevant to the nuclear energy sector. In contrast with electrons or (low) energy X rays, neutrons penetrate most materials to depths of several centimetres. This both allows measurements through cladding and allows concomitant use of shielding to mitigate radiation dose. Since neutron interactions with nuclei do not scale with atomic number and are isotope specific they are flexible and prove to be equally pertinent for the study of hydrogen and uranium. Although samples typically need to be larger than a cubic millimeter nevertheless a range of microstructural length scale insights are possible. To place work described below into a wider context the reader is directed to a review of neutron scattering applied to nuclear materials by Vogel [1].

Los Alamos national laboratory in collaboration with national and international partners is engaged in a range of applied and fundamental studies of radiation damage. Much of the work is applied and initiated both by the U.S. Office of nuclear energy but there is considerable complementary funding on fundamental research. The range of activities span ceramic fuels, accident tolerant cladding to metallic fuels and the use of supercomputers to connect first principles insights to engineering relevance. Industrial activity has included examination of 100 Kg structural welds that were removed from nuclear reactors. LANL routinely machines and prepares radioactive samples for electron microscopy. Hot cells are used to examine highly radioactive material removed from reactors. Thermophysical properties and fabrication processes for uranium based fuels are examined in The Fuels Research Laboratory. An Ion Beam Materials Laboratory enables simultaneous ion irradiation of surfaces in contact with molten metals to assess synergistic effects of irradiation on corrosion. A strong theoretical and simulation computational mechanics effort spans the atomistic to macroscopic regime. It is in this context that neutron scattering measurements at the LANSCE facility are employed.

## 2. LANSCE FACILITY

At the Lujan center neutrons are produced by spallation in two split tungsten targets by 800-MeV protons from the LANSCE accelerator. The accelerator operates at 100 kW, which enables a compact and efficient design. Two distinguishing features are 20-Hz operation and a

## 2.2. Research on zirconium based materials (including hydrogen uptake)

short proton pulse width. The former offers a broad bandwidth that is well suited to studies of soft condensed matter and pair distribution function analysis. The latter enables resonance imaging using epithermal neutrons for which the pulse width of the incident proton beam is critical. The Lujan Center also supports the Department of Energy's national security mission and performs programmatic and classified research in support of LANL programs.

Provided below is a brief description of activity at LANL pursued within the context of the CRP addressing studies of irradiated material and proof of principle studies of irradiated material.

At the Lujan Center several instruments have been used extensively for studies of nuclear energy related materials. HIPPO provides time-resolved studies under a variety of extreme temperature, magnetic field, and pressure conditions. NPDF provides local structure studies for amorphous, disordered, and nano materials, as well as routine high-resolution powder diffraction. SMARTS is optimized for engineering and provides *in situ* deformation, with a unique loading capability of 250 kN in conjunction with temperature from 77 K to 1800 K. Both SMARTS and HIPPO offer complementary capabilities focused on extreme conditions (temperature, stress, magnetic field and pressure), determining crystal structure, texture, and lattice strains. HIPPO provides *in situ* texture measurements at temperatures from 10 K to 2000 K, as well as at pressures to 10 GPa. Many material characteristics derive from surface and interface properties in which interactions on the atomistic, molecular, and nano scales determine higher-order morphology and properties. In work that preceded this CRP, Brown et al. utilized the engineering diffractometer SMARTS [2] to investigate the uni-axial deformation behavior of uranium at room temperature as well as 200°C and 400°C [66].

## 3. RESULTS

### 3.1. Results: diffraction studies of radiation damage

Zirconium and its alloys are used in nuclear applications due to its compromise between mechanical performance under high pressure/high temperature condition and its neutronic transparency. Thus its behavior during manufacturing, in service and under accident scenarios is a topic of interest. Pure zirconium has a hexagonal closed packed (hcp) crystal-structure up to 866°C and transforms to a body-centered cubic (bcc) crystal structure above that. For nuclear applications the main alloying elements are niobium and tin which with other minor elements form the Zircaloy 2 alloy. Neutron diffraction has been applied to zirconium and its alloys to characterize welds, characterize deformation modes to allow predictive modeling of deformation, investigate the development of texture under temperature and stress, and characterize the phase transformations including texture variant selection during the hcp/bcc phase transformation.

Understanding and predicting the evolution of the microstructure of zirconium (and of structural materials in general) at temperature and during irradiation is of importance and was a source of study during this CRP. Using neutron diffraction data from a Zr-2.5%Nb specimen removed from a pressure tube which had been in service for seven years in a CANDU reactor at a temperature of 250°C, Balogh et al utilized profile analysis techniques [4] to determine the changes in dislocation types and densities with irradiation. Concurrent deformation studies of the irradiated and non-irradiated materials showed distinct differences in dislocation types introduced by plastic deformation between the irradiated and non-irradiated materials [5].

## 2.2. Research on zirconium based materials (including hydrogen uptake)

Ferritic/martensitic steels such as T91 (9Cr1Mo) and HT-9 (12Cr1Mo) have also been used for nuclear fuel cladding. In similar work to that of the Zirconium study Hosemann et al. studied the evolution of the microstructure, i.e. phase composition, texture etc. in situ using neutron diffraction [6]. Deformation behavior was investigated by Clausen et al. [7] using in situ neutron diffraction and modeled using elasto-plastic self-consistent (EPSC) modeling. These experiments on (non-irradiated specimens) provide baseline data for future experiments on irradiated materials. Comparing the mechanical response of irradiated and non-irradiated materials will allow to understand the influence of radiation damage on the mechanical behavior of these materials and provide benchmark data for advanced deformation models that attempt to include radiation damage [8]. In complementary work Anderoglu et al. studied the microstructure and phase evolution in a fully tempered ferritic /martensitic HT-9 steel irradiated in the Fast Flux Test Reactor Facility (FFTF) up to 155 dpa at a temperature range of 380 to 504 °C [9] using small angle neutron scattering using the LQD instrument.

## 3.2. Results: proof of principle, imaging of ceramic fuels

Neutron radiography and tomography are based on the attenuation of neutron beams by the sample. Since the interaction of neutrons with matter is fundamentally different from X rays, they allow investigations that are qualitatively different. A good example is the observation of hydrogen in operating systems. Recent detector developments have allowed for spatially and time-resolved neutron detection [10] and are opening new avenues of research. Specifically the characterization of nuclear materials and nuclear fuels with isotope-sensitive imaging via neutron resonance absorption imaging [11]. A program exploring advanced non-destructive examination (NDE) capabilities using neutron and proton imaging was initiated in 2011 between Los Alamos National Laboratory and Idaho National Laboratory.

To illustrate the advantages of neutron radiography and energy-dispersive neutron radiography mock nuclear fuel rodlets were prepared using urania powder. Each consisted of five pellets and were characterized by high energy proton radiography, X ray radiography [12], energy-dispersive neutron radiography, and thermal neutron radiography [13]. To simulate cracks and voids that typically result during irradiation and burn-up, plastic wire was introduced during synthesis and which burned out during sintering leaving a range of defect features. As a proof of principle to assess the viability of the resonance technique to detecting the different fission products (that would typically form during the life cycle of a nuclear fuel) tungsten pieces of different sizes and shapes were embedded. Finally, some fuel pins were sintered with different green (pre-sintering) densities.

While both proton and X ray radiography primarily probe gravimetric density, energy-dispersive neutron radiography allows a richer range of insight albeit slower. For example in making energy dispersive measurements by viewing an image at an energy where tungsten shows an absorption resonance it proved possible to focus on the tungsten specifically (or indeed any other element with a suitable resonance). With calibrations, concentration measurements are possible. The ultimate goal of this work is characterization of irradiated fuel pins. To date the results suggest that both neutron and proton radiography have potential since for both probes the detectors are for the most part insensitive to the potential gamma dose that can be expected from irradiated nuclear fuel, while shielding can effectively be used. X ray radiography, on the other hand, employs detectors which are inherently sensitive to the gamma radiation from irradiated fuel and it is harder to conceive of a successful measurement on irradiated material. Nevertheless the combination of neutron measurements perhaps with hard X ray synchrotron diffraction could open yet another avenue of future research.

## 2.2. Research on zirconium based materials (including hydrogen uptake)

### 4. SUMMARY

Determination of the positions of light elements in the presence of heavier ones is an area of competitive advantage for neutron scattering techniques. For example the complex crystallography of urania can accommodate a large range of hyper-stoichiometric oxygen atoms and will continue to offer a rich field of research for neutron diffraction. While stoichiometric  $\text{UO}_2$  crystallizes in the  $\text{CaF}_2$  structure, concentrations up to  $\text{UO}_2:25$  are possible at elevated temperatures with the location of the excess oxygen atoms affecting lattice dynamics and therefore thermal expansion and thermal conductivity. At lower temperatures, several distinct crystallographic phases occur in the U-O phase diagram, many of which were determined and refined by neutron diffraction.

Imaging is now an integral part of the instrument suite at many neutron sources. In particular energy-dispersive neutron imaging, enabled by new detector technology, offers interesting opportunities. Further improvements in detector efficiency, for example through doping the neutron converters with specific isotopes, will further improve the potential of this technique. In the realm of data analysis further advances may also be expected. For example, when tomographic reconstruction software (that is routinely applied in medical applications) is applied to energy-dispersive neutron data. With improved sensitivity, accurate measurements of isotope concentrations will be possible, which will allow new opportunities for the study of ion migration.

Modeling of reactors depends on the precise knowledge of interaction cross-sections of thermal neutrons with reactor materials. These cross-sections are energy-dependent and in the thermal neutron energy range are convoluted with coherent and incoherent inelastic and elastic scattering properties as well as with resonant absorption. Intense pulsed spallation neutron sources offer rapid cross-section measurements in the thermal energy region for reactor materials.

The benefits of neutron diffraction for crystallographic studies of fuels, consisting of high and low Z-number elements, are obvious. Development of new fuels or advanced sample environments to study these materials at extreme conditions, will continue. Few high temperature and controlled atmosphere experiments above  $1500^\circ\text{C}$  are reported. Thus advances in sample environments at neutron sources offer potential return on investment. Combinations of diffraction with the recently developed spatially resolved neutron time-of-flight detectors for energy-dispersive neutron radiography will open up entirely new avenues of neutron scattering research.

The kinetics of reactions during annealing are relevant to optimized synthesis of fuels. Neutrons offer in situ kinetics measurements at temperature. The equilibrium state, the rate at which a reaction occurs as well as the intermediate meta-stable phases are all of importance. Whereas classical methods such as dilatometry, gravimetry, or calorimetry are sensitive probes their results are significantly augmented by crystallographic phase information that can be achieved by in situ diffraction methods. An example illustrating the power of the technique is work by Higgs et al. [14] in which a sample of hyper-stoichiometric  $\text{UO}_{2+x}$  was cycled through a phase boundary between the low-temperature two phase field and the high-temperature single phase field. Insight on the concomitant oxygen re-distribution was derived from the lattice parameters. Such experimental data contributes to e.g. the development of models for the oxidation behavior in defective fuels.

## 2.2. Research on zirconium based materials (including hydrogen uptake)

### REFERENCES

- [1] Vogel, S. “A review of neutron scattering applications to nuclear materials” in press.
- [2] M. Bourke, D. Dunand, E. Ustundag, SMARTS-a spectrometer for strain measurement in engineering materials, *Applied Physics A: Materials Science & Processing* **74** (2002) 1707–1709.
- [3] D. Brown, M. Bourke, B. Clausen, D. Korzekwa, R. Korzekwa, R. McCabe, T. Sisneros, D. Teter, Temperature and direction dependence of internal strain and texture evolution during deformation of uranium, *Materials Science and Engineering: A* **512** (2009) 67–75.
- [4] G. Ribárik, J. Gubicza, T. Ungár, Correlation between strength and microstructure of ball-milled al–mg alloys determined by X ray diffraction, *Materials Science and Engineering: A* **387** (2004) 343–347.
- [5] L. Balogh, D. W. Brown, P. Mosbrucker, F. Long, M. R. Daymond, Dislocation structure evolution induced by irradiation and plastic deformation in the zr–2.5 nb nuclear structural material determined by neutron diffraction line profile analysis, *Acta Materialia* **60** (2012) 5567–5577.
- [6] P. Hosemann, S. Kabra, E. Stergar, M. Cappillo, S. Maloy, Micro-structural characterization of laboratory heats of the Ferric/Martensitic steels HT-9 and T91, *Journal of Nuclear Materials* **403** (2010) 7–14.
- [7] B. Clausen, D. Brown, M. Bourke, T. Saleh, S. Maloy, In situ neutron diffraction and elastic–plastic self-consistent polycrystal modeling of HT-9, *Journal of Nuclear Materials* **425** (2012) 228–232.
- [8] N. R. Barton, A. Arsenlis, J. Marian, A polycrystal plasticity model of strain localization in irradiated iron, *Journal of the Mechanics and Physics of Solids* (2012).
- [9] O. Anderoglu, J. Van den Bosch, P. Hosemann, E. Stergar, B. Sencer, D. Bhattacharyya, R. Dickerson, P. Dickerson, M. Hartl, S. Maloy, Phase stability of an HT-9 duct irradiated in FFTF, *Journal of Nuclear Materials* (2012).
- [10] A. Tremsin, J. McPhate, J. Vallerger, O. Siegmund, J. Hull, W. Feller, E. Lehmann, Detection efficiency, spatial and timing resolution of thermal and cold neutron counting.

## 2.2. Research on zirconium based materials (including hydrogen uptake)

### IN-SITU NEUTRON RADIOGRAPHY INVESTIGATIONS OF THE HYDROGEN RE-DISTRIBUTION DURING DHC

M. GROSSE\*, C. RÖSSGER\*, S.VALENCE\*\*, J.BERTSCH\*\*, A. KAESTNER\*\*, J. SANTISTEBAN\*\*\*

\* Karlsruhe Institute of Technology, Institute for Applied Materials, PO Box 5640  
D-76021 Karlsruhe, Germany

\*\* Paul Scherrer Institute Villigen, CH-5232 Villigen PSI, Switzerland

\*\*\* Comision Nacional de Energia Atomica, Bariloche, Argentina

Email: [M.Grosse@KIT.edu](mailto:M.Grosse@KIT.edu)

#### Abstract.

The hydrogen uptake and re-distribution in mechanical pre-loaded Zircaloy-4 specimens were investigated by means of in-situ neutron imaging. The stress fields in the material affect the hydrogen uptake as well as its distribution in the material. The investigations confirmed the existence of an initial oxide layer formed at room temperature by contact with air. This oxide layer suppresses the hydrogen uptake until dissolution in the zirconium matrix.

## 1. INTRODUCTION

Corrosion of nuclear fuel claddings made from various zirconium alloys in water or steam results in a production of free hydrogen:



The hydrogen can be released as molecular gas into the reactor environment, as happened during the Fukushima accidents, or be absorbed by the remaining metallic zirconium:



The hydrogen uptake occurs during operation as well as under accident conditions. Partial strong local concentrations results in a degradation of the mechanical properties which may induce mechanical failure of the nuclear fuel cladding tubes at low loadings. The hydrogen absorption based reduction of strength and toughness is of high safety relevance for the reactor under service and transient conditions.

One of these failure modes, the delayed hydrides cracking (DHC), is characterized by crack propagation at macroscopic sub-critical load. It takes advantage of the interplay between stress concentrations at a stress raiser and hydrogen precipitation when the local content reaches the terminal solid solubility limit. The hydrogen diffuses in the strained region of the stress field in front the tip of a crack. It reduces the strength and toughness of this area significantly. The crack can grow in this area. The stress field shifts ahead the newly formed crack tip and the hydrogen follows. The diffusion characteristics of hydrogen in Zircaloy-4 under temperature and concentration gradients are well known [1]. Otherwise, the effect of the stress gradient is still an open issue [2]. The main blocking point pertains to the difficulty to make in-situ measurement of hydrogen content under viable testing conditions, e.g. temperature above 400 K under mechanical loading. Post-mortem investigations do not allow distinguishing between hydrogen diffusion effectively driven by the stress gradient at test temperature and by the decrease of the solubility during cooling down to room temperature. Moreover, postmortem investigations do not allow characterizing the kinetics of the hydrogen diffusion.

This paper gives an overview on the contribution of neutron imaging to study the processes connected with hydrogen in zirconium alloys and its influence on mechanical properties. The data are partially published in [3 - 5].

## 2.2. Research on zirconium based materials (including hydrogen uptake)

### 2. EXPERIMENTS

The neutron imaging investigations were performed at the ICON facility at the Swiss neutron source SINQ (Paul Scherrer Institute Villigen, Switzerland). The non-destructive character of neutron imaging allows in-situ investigations of hydrogen uptake and relocation in zirconium alloys. The strong contrast between hydrogen (very high total neutron cross section) and zirconium (very low total neutron cross section) provides the possibility to detect even small changes in the hydrogen concentrations.

For in-situ neutron radiography investigations, the INRRO (in-situ neutron radiography reaction oven) was constructed. Figure 1 shows a scheme of the furnace. It is a resistivity heated horizontal tube furnace with two windows transparent for neutrons on the front and back side. The furnace allows studying chemical reactions in a well defined flowing gas atmosphere at temperatures up to 1750 K.

The measurements were performed applying the middle imaging setup and a collimation ratio  $L/d$  of about 340. An acquisition time of 117 s results in a frame repetition time of 2 min. The spatial resolution was about 0.1 mm. For the mechanical loading during the annealing in the INRRO furnace a special sample load device was constructed.

The experiments comprise annealing at 350°C in argon/hydrogen atmosphere for hydrogen loading of the samples until complete destruction. In a second beam time, hydrogen was loaded up to a certain local hydrogen concentration followed by an annealing in inert atmosphere at the same temperature. The field of view was limited by the INRRO furnace windows with a diameter of 40 mm.

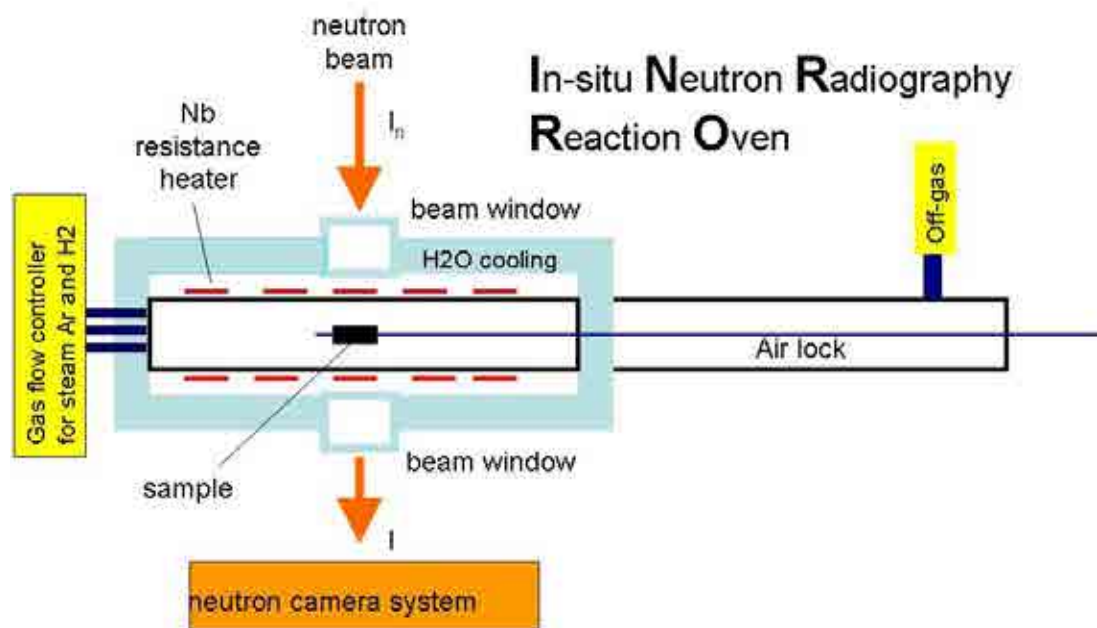


FIG. 1. Scheme of the INRRO furnace.

## 2.2. Research on zirconium based materials (including hydrogen uptake)

### 3. RESULTS

The investigations of the hydrogen uptake and redistribution in mechanical pre-stressed specimens were performed in two beam-times. At first, pre-stressed specimens were annealed at 350°C in Ar/H<sub>2</sub> atmosphere. A radiograph sequence of this experiment is given in Fig.2.

No hydrogen uptake occurred during the first 8 h. The reason may be that an initial sub-micrometer thick oxide layer formed at room temperature during manufacturing, preparation and material storage. This initial oxide layer has to be dissolved to enable hydrogen uptake. After this time, the hydrogen absorption starts at the notch position. The data do not allow deciding why the uptake starts here, if due to the stress field or to the manufacturing of the specimen. After about 10 h the hydrogen is concentrated in the specimen region with the highest tensile stress (clearly visible as darker regions e.g. in the frames taken at 37080 and 39700 s). Spallation of small hydrides from the sample starts at the same time (dark objects below the specimen).

Later, hot spots of the hydrogen uptake are formed. These dark hot spots characterized by very high hydrogen concentrations grow and result in additional breakaway of small hydrides from the sample until the specimen is completely destroyed and the mechanical stress is relieved after about 15 h.

In a second beam-time the experiment was varied. The pre-oxidation and removing of the oxide layer at both sides of the notch defined the position of the hydrogen uptake. The samples were annealed again in Ar/H<sub>2</sub> atmosphere at 350°C. In order to prevent the complete destruction of the sample, the hydrogen supply was switched off after reaching a certain gray value in the radiograph at 17000 s. Figure 3 shows a radiograph sequence of the notch and pre-crack sample region taken during the hydrogen loading phase and at the end of the experiment is given. The time needed for dissolving the initial oxide produced between the removing of the pre-oxidation at both sides of the notch and starting the annealing (several minutes) was about 4.5 h. A fast hydrogen uptake follows.

After switching off the hydrogen supply the hydrogen distribution is changed very slowly as Fig. 4 shows for various vertical distances to the crack tip. It gives a hint that the differences in the chemical potential of hydrogen do not strongly differ between the hydrogen rich stressed area ahead of the crack tip and the positions far away from the crack. Because no temperature gradient in the sample was applied, the crack growth and with it the hydrogen diffusion is low.

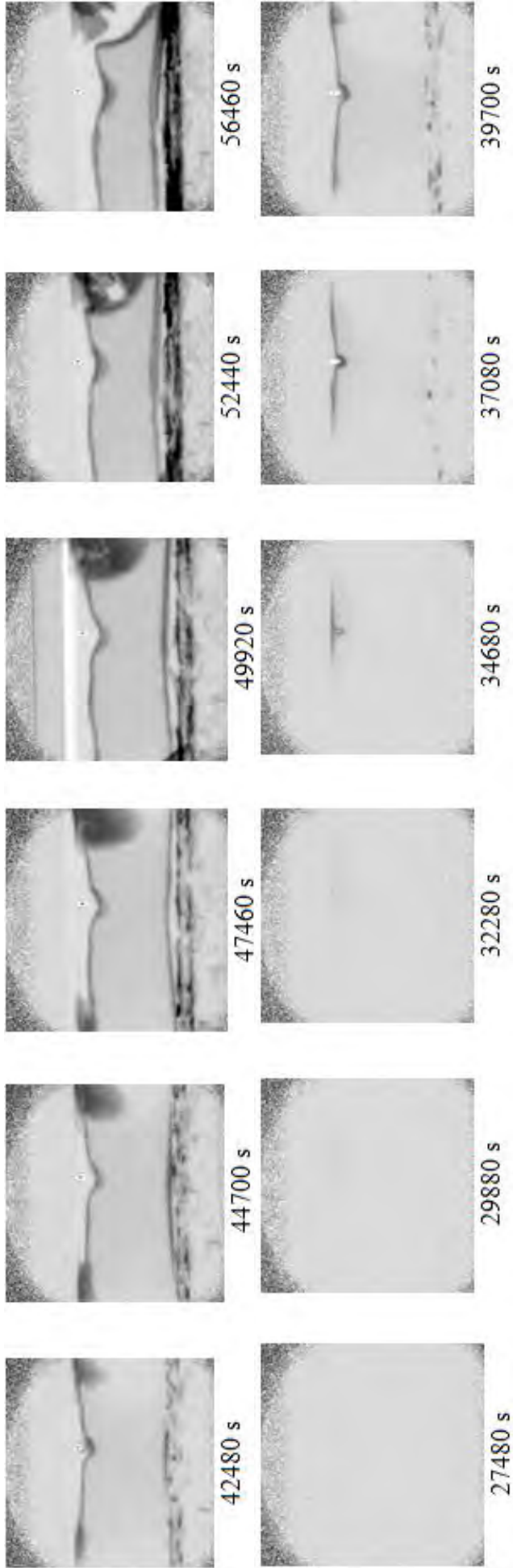


FIG. 2. Neutron radiograph sequence taken during the destruction of a mechanical stressed specimen in Ar/H<sub>2</sub> atmosphere at 350°C.



FIG. 3. Neutron radiograph sequence taken during hydrogen loading in Ar/H<sub>2</sub> atmosphere until 18000 s and inert annealing of a mechanical stressed specimen until 57000 s at 350°C.

## 2.2. Research on zirconium based materials (including hydrogen uptake)

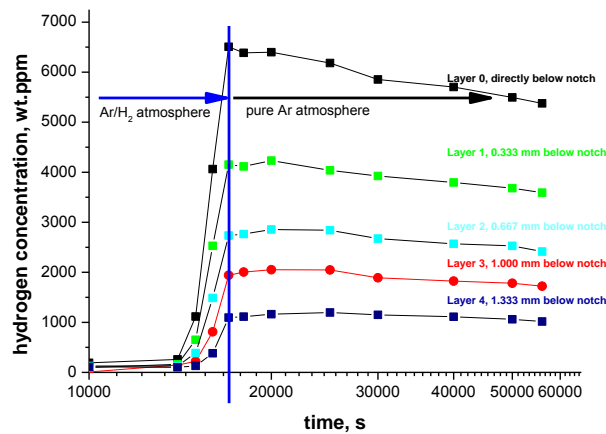


FIG. 4. Time dependence of the averaged hydrogen concentrations at various distances from the crack tip.

## 4. SUMMARY AND CONCLUSIONS

The hydrogen uptake and re-distribution in Zircaloy-4 related to delayed hydride cracking was investigated by means of in-situ neutron radiography. The stress fields in the samples influence the hydrogen uptake and distribution. Tensile stress may enhance the hydrogen uptake and results in higher hydrogen concentrations. Hydrogen uptake occurs only if an initial oxide layer is dissolved. After dissolving of the oxide layer, the absorption is fast and can result in a complete destruction after hours if enough hydrogen is available. If the hydrogen supply is stopped, only small and slowly changes in the hydrogen distribution were observed.

The investigations will be continued. The influence of the mechanical stress on the chemical potential of the hydrogen in zirconium shall be determined quantitatively. To achieve this goal the experimental setup particularly the device for mechanical loading needs further developments.

## REFERENCES

- [1] DOUGLASS, D.L., Atomic Energy Review, Supplement 1971, "The Metallurgy of Zirconium", International Atomic Energy Agency, Vienna, 1971, 7.
- [2] KAMMENZIND, B.F., Berquist, B. M., Bajaj, R., Kreyns P. H., Franklin D. G., Proc. Zirconium in Nucl. Ind., 12th Int. Symp., 196, (2000).
- [3] VALANCE, S., "Effect of stress concentration on hydrogen diffusion and ingress in Zircaloy - Experimental study using cold neutron", 17<sup>th</sup> Inten. QUENCH Workshop, Karlsruhe, Nov. 22 – 24, 2011.
- [4] GROSSE, M., "Neutron imaging investigations of the hydrogen related degradation of the mechanical properties of Zircaloy-4 cladding tubes", 18<sup>th</sup> Inten. QUENCH Workshop, Karlsruhe, Nov. 20 – 22, 2012.
- [5] GROSSE, M., VALANCE, S., STUCKERT, J., STEINBRUECK, M., WALTER, M., KAESTNER, A., HARTMANN, S., SANTISTEBAN, J., „Neutron Imaging Investigations of the Hydrogen Related Degradation of the Mechanical Properties of Zircaloy-4 Cladding Tubes”, MRS Proceedings, 1528, (2012), mrsf12-1528-vv07-05 doi:10.1557/opl.2013.364.

## 2.2. Research on zirconium based materials (including hydrogen uptake)

### POST-TEST EXAMINATION OF THE HYDROGEN DISTRIBUTION IN ZIRCONIUM CLADDINGS AFTER LOCA TESTS

M. K. GROSSE\*\*, J. STUCKERT\*, M. STEINBRUECK\*, A. J. KAESTNER\*\*, E. H. LEHMANN\*\*

\*Karlsruhe Institute of Technology, Institute for Applied Materials, PO Box 5640  
D-76021 Karlsruhe, Germany

\*\*Neutron Imaging & Activation Group, Paul Scherrer Institut, CH-5232 Villigen PSI,  
Switzerland

Email: [M.Grosse@KIT.edu](mailto:M.Grosse@KIT.edu)

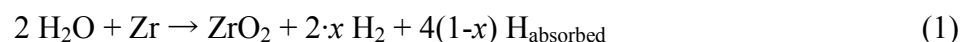
#### Abstract.

In the framework of the posttest examinations of the large scale LOCA simulation tests on fuel rod bundle scale, the hydrogen distributions in specimens prepared from the QUENCH-L0 and -L1 tests were determined by means of neutron imaging. The hydrogen distributions in samples prepared from the two tests differ significantly. Whereas clearly visible hydrogen bands were found in the inner rods of the QUENCH-L0 test; the hydrogen enrichments in no specimen prepared from the inner rods of the QUENCH-L1 test are more blurred. The reasons for these different behaviors can be the different times between reaching the temperature maxima and the quenching. In the QUENCH-L0 test the bundle was quenched immediately after reaching the maximal temperature. In QUENCH-L1 the hydrogen has about 130 s to diffuse and reach more homogeneous distributions without very pronounced contrasts between the hydrogen bands and the neighboring regions in the neutron images. In outer rods of both tests no hydrogen enrichments were found except two rods (#14 and #17) of test QUENCH-L0. The reason for it is the slightly lower temperature of the outer rods compared to the inner rods.

## 1. INTRODUCTION

Loss of coolant in nuclear power plants (NPP's) can result in ecological and economical disasters as shown in the accidents occurring after the very strong earthquake and tsunami in Japan at 11th March 2011 and thereafter. At the Karlsruhe Institute of Technology (KIT, the former research center Karlsruhe FZK) such accident scenarios were simulated experimentally on fuel rod bundle level in 18 large-scale experiments since 1997 in the framework of the QUENCH program [1]. Safe reactor behavior during loss of coolant accidents (LOCA's) is one base for licensing of a NPP. Criteria for the coolability of the reactor core are that it is ensured that the temperatures do not exceed 1200°C between loss of coolant and emergency cooling and that the oxidation level ECR (equivalent cladding reacted) of the cladding material keeps below the value of 17% [2, 3]. Various simulation experiments at single rod level have shown that in addition to the existing degradation criteria, hydrogen absorption occurring after the burst of the cladding rods has to be taken into account [4-8]. The phenomenon known as secondary hydriding results in an embrittlement of the cladding material additionally to the embrittlement caused by oxygen uptake and oxide layer formation.

During LOCA the following processes occur: At first the pressure in the reactor vessel decreases to about 3 bar and the coolant is lost. The temperature increases rapidly. Due to inner pressure resulting from initial gas filling and gaseous fission products ballooning occurs at hot spots of the cladding tube. This effect becomes strong when the temperature exceeds about 800°C at which the  $\alpha$  to  $\beta$  phase transition in zirconium starts. Simultaneously, the burst pressure of the cladding tube very strongly decreases with increasing temperature [9, 10]. When the rods burst, the fission gases are released from the fuel rods. Steam penetrates through the burst opening into the gap between fuel pellets and inner cladding surface (gap width varies due to ballooning between 0.1 and more than 2 mm). The fresh metallic inner cladding surface reacts strongly with the steam. Very simplified, the chemical reaction can be described by:



## 2.2. Research on zirconium based materials (including hydrogen uptake)

The resulting free hydrogen can be released as H<sub>2</sub> gas into the environment or can be absorbed by the remaining metallic zirconium;  $x$  is the fraction of released hydrogen. Detailed descriptions of these processes are given for instance in [11]. The release of molecular hydrogen causes the risk of a hydrogen detonation as happened in the Fukushima reactor buildings. The absorbed hydrogen changes the time scale of hydrogen release and embrittles the metallic  $\beta$ -Zr phase with the consequence of reducing the toughness of the cladding and the thermo-shock resistance, which can result in a fragmentation of the cladding tube and a re-arrangement and massive release of nuclear fuel and fission products during quenching.

The absorbed hydrogen is concentrated in axial regions close to the burst opening. The data are determined by hot extraction usually applied for quantitative measurements of hydrogen uptake by zirconium alloys. Whereas in the burst opening region no or less hydrogen is absorbed, wide hydrogen containing bands were found in some millimeters distance to the burst opening.

Because of the degradation of the mechanical properties by hydrogen uptake, the German regulation authority has extended the coolability criteria. To get and keep the license for operation of a NPP it has to be proofed that the combination of hydrogen and oxygen uptake during LOCA does not result in an embrittlement of the cladding.

In order to prove the safety of fuel rod bundles during LOCA scenarios valid for German NPP's, a series of large-scale bundle simulation experiments has been launched at KIT. In contrast to single-rod experiments already performed, the interaction between the rods is simulated, too. As a first experiment the commissioning test QUENCH-L0 [12] of this series was performed in 2010. In the test QUENCH-L1 [13] a bundle with Zircaloy-4 cladding tubes was applied. This test will be the reference for the following four tests with different cladding materials and bundle geometries.

This report is focused on the neutron imaging investigations to determine the hydrogen concentration and distribution in the cladding tubes of the two first QUENCH-LOCA test.

## 2. MATERIALS AND NEUTRON IMAGING

The cladding tubes for the QUENCH-L0 and -L1 simulation tests were made of Zircaloy-4 (Zry-4; composition: Sn-1.5, Fe-0.23, Cr-0.11 and O-0.14 wt%, Zr balance). Details of the two QUENCH-test are given in The temperature scenarios of both tests are given in Fig. 1. The QUENCH-L1 test differs from the commissioning test QUENCH-L0 mainly in a larger heating rate and a cooling phase before quenching. The QUENCH-L1 scenario corresponds with the LOCA scenarios determined for German nuclear power reactors. Detailed information about the QUENCH-LOCA tests is given in [12 - 14]. After the test the bundle was dismantled, the heaters (tungsten or tantalum) and pellets were removed from the rods and the cladding tubes were investigated separately.

The neutron imaging investigations were performed using the ICON facility at the Swiss neutron source SINQ (Paul Scherrer Institut Villigen, Switzerland) [15]. The micro-tomography setup was used as characterized by  $L/d = 343$ , a field of view 28 mm  $\times$  28 mm and a pixel pitch of 13.5  $\mu$ m. The real spatial resolution determined by measuring a Siemens star was about 25  $\mu$ m. The illumination time of the radiography measurements was 300 s. The data were analyzed using image analysis software "Image J". The tomography projections were measured using the same setup. Illumination times between 30 and 90 s per frame were applied. According to the sampling theorem, 625 radiography images detected from different

## 2.2. Research on zirconium based materials (including hydrogen uptake)

orientations were illuminated to reconstruct the 3D image without loss of information. The software MuhRec2 [16] was applied for the reconstruction.

The calibration of the correlation of the hydrogen concentrations and neutron radiography and tomography results were performed according [17-19].

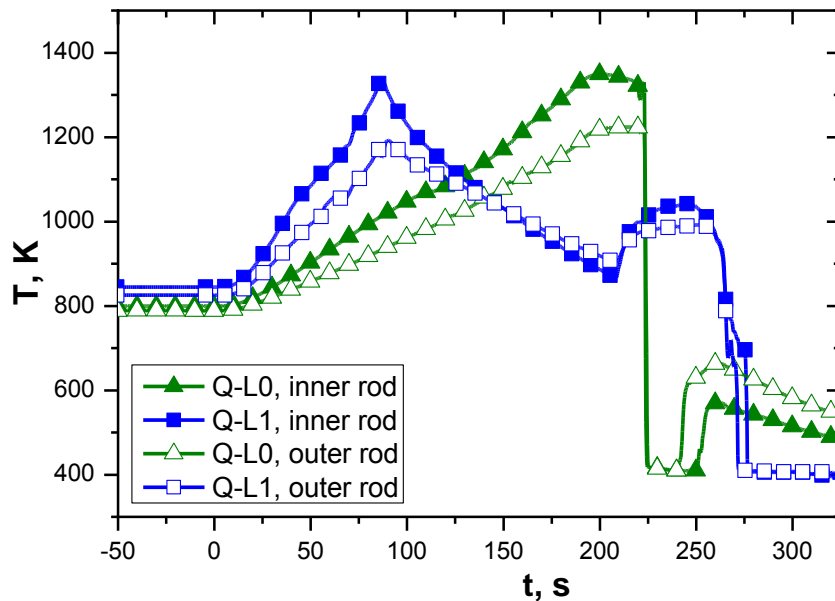


FIG. 1. Temperature scenarios for the inner and outer rods of the QUENCH-L0 and QUENCH-L1 tests, respectively.

## 3. RESULTS

Figure 2 and 3 give neutron radiographs of the claddings of the tests QUENCH-L0 and -L1, respectively. At the inner rods (rod #01 - #09) hydrogen enrichments in bands are clearly visible. These bands are bended and oriented non-perpendicular to the tube axis. In contrast, the most of the outer rods (rod #10 - #21) do not show such hydrogen enrichments.

The hydrogen enriched bands in the QUENCH-L1 specimens seems to be wider and have less contrast to the neighbored regions compared to the bands in the QUENCH-L0 samples. The rods #02, #08 and #09 show hydrogen enrichments in the burst opening region too. In the rods of the QUENCH-L0 test hydrogen enrichments at this position are not found.

Some of the rods of the QUENCH-L1 test were bended during the test. The curvatures of the rods are clearly visible for the inner rods #03 - #07, and for #17, #18, #20 and #21. Reasons for the bending are residual stresses, radial and tangential temperature gradients in the bundle, and/or inhomogeneous oxidation and hydrogenation. In contrast to the QUENCH-L0 test where the stiff tungsten heaters suppress the bending, the tantalum heaters become soft at higher temperatures and allow the deformation of the rods. The bending of the rods can result in local blockages. It can be assumed that the hydrogen enrichments in the burst opening regions of the QUENCH-L1 rods #02, #08 and #09 result from se blockage of the burst opening at these rods.

Because of the uncertainties in the remaining tube thickness and about the contribution of front and back side of the tube to the radiograph, no exact values of the hydrogen

## 2.2. Research on zirconium based materials (including hydrogen uptake)

concentrations can be determined. Therefore neutron tomography's has to be made to obtain quantitative values. Because of the long measurement times, only a limited number of samples can be investigated. Fig.4. gives three examples for the tomography results obtained for rods from the QUENCH-L0 test. At the basis of these results a maximal hydrogen concentration of 2600 wt.ppm was determined. Tomography investigations of samples from the QUENCH-L1 test are planned for June 2013.

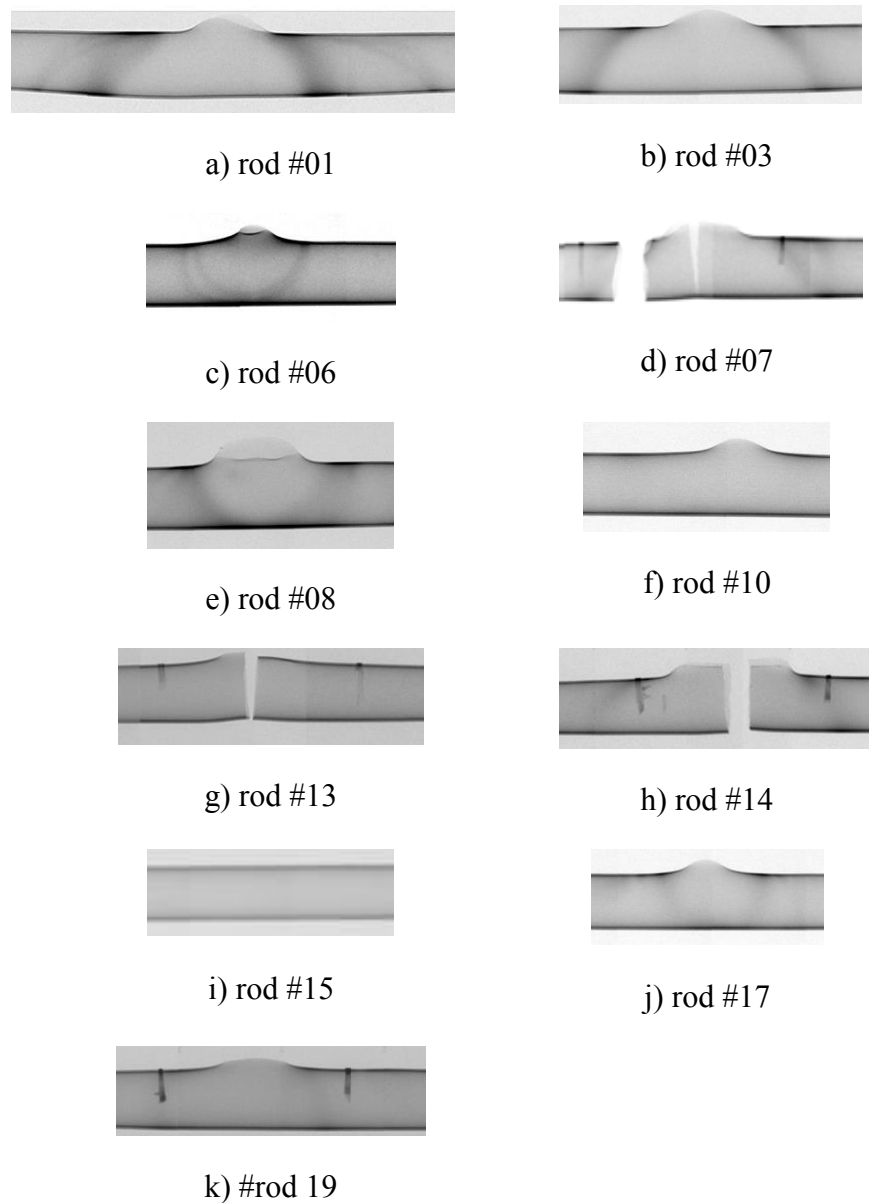


FIG. 2. Neutron radiographs of rods prepared from the QUENCH-L0 test.

The results of the radiography investigations allow understanding the fracture behaviour [12 – 14]. In order to explain the hydrogen distributions, a model is under development describing steam transport and consumption in the gap between inner cladding surface and the pellets, oxidation and hydrogen production behaviour and hydrogen transport in the gap, absorption in the remaining metallic zirconium and diffusion in zirconium [14].

## 2.2. Research on zirconium based materials (including hydrogen uptake)



a) rod #01



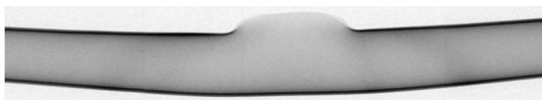
b) rod #02



c) rod #03



d) rod #04



e) rod #05



f) rod #06



g) rod #07



h) rod #08



i) rod #09



j) rod #10



k) rod #11



m) rod #12



n) rod #13



o) rod #14



p) rod #15



q) rod #16



r) rod #17



s) rod #18

## 2.2. Research on zirconium based materials (including hydrogen uptake)

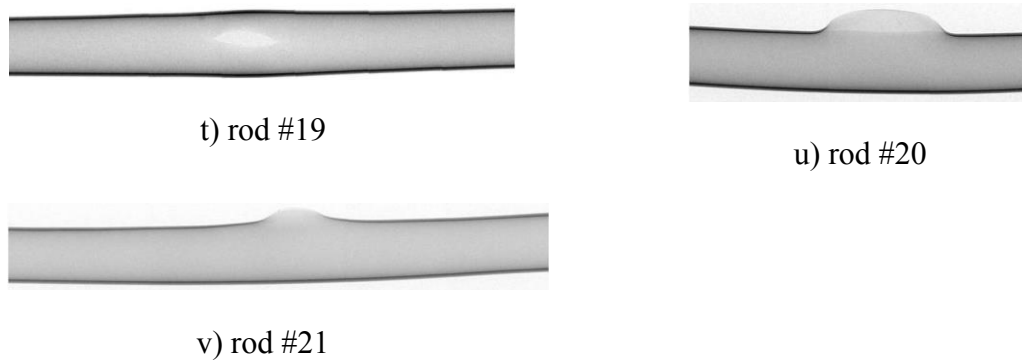


FIG. 3. Neutron radiographs of rods prepared from the QUENCH-L1 test.

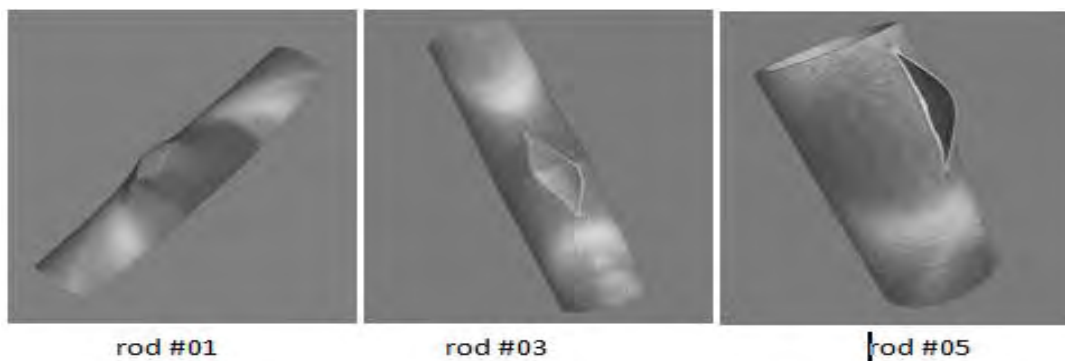


FIG. 4. 3D reconstructions of rods #01, #03 and #05 from the QUENCH-L0 test.

## 4. SUMMARY AND CONCLUSIONS

Neutron radiography and tomography were applied for the post-test examination of the hydrogen distribution in samples from the large-scale QUENCH-LOCA simulation tests. The hydrogen distributions differ significantly between both tests. Whereas in the QUENCH-L0 test for the inner rods, clearly visible hydrogen bands were found, the maxima of the hydrogen distributions in samples prepared from the QUENCH-L1 test bundle has no clear contrast with respect to neighboring tube regions. As a first hypothesis explaining these different behaviors, the differences in the temperature scenarios are proposed.

Additionally, it is proposed that the more pronounced bending of the QUENCH-L1 rods can result in:

1. closing the gap between inner cladding surface and pellets;
2. closing of some burst openings by neighbor rods and with that closure, a blockage of the steam and hydrogen transport.

The investigations will be extended to other zirconium alloys commonly used as cladding materials. Also experiments with pre-hydrided claddings simulating high burn-up are planned. Neutron imaging will keep the most important part of the posttest examinations of the fuel rod simulator bundles tested in the QUENCH-LOCA large scale experiments.

## 2.2. Research on zirconium based materials (including hydrogen uptake)

### REFERENCES

- [1] STEINBRÜCK, M., GROBE, M., SEPOLD, L., STUCKERT, J., Nucl. Engn. & Desgn **240** (2010) 1714.
- [2] “Atomic Energy Commission Rule-Making Hearing, Opinion of the Commission”, Docket RM-50-1, 28 Dec., (1973).
- [3] „RSK-Leitlinien für Druckwasserreaktoren“, Ursprungsfassung (3. Ausgabe vom 14. Oktober 1981) mit Änderungen vom 15.11.1996 (in German).
- [4] CHUNG, H. M., Nucl. Engin. & Techn., **37** (2005) 327.
- [5] UETSUKA, H., FURUTA T., KAWASAKI, S., J. Nucl. Sci. & Techn., **18** (1981) 705.
- [6] NAGASE F., FUKETA, T., J. Nucl. Sci. & Techn., **42** (2005) 209.
- [7] BILLONE, M., YAN, Y., BURTSEVA, T., DAUM, R., “Cladding Embrittlement During Postulated Loss-of-Coolant Accidents,” NUREG/CR-6967, (2008). <http://pbadupws.nrc.gov/docs/ML0821/ML082130389.pdf>.
- [8] GRANDJEAN, C., HACHE, G., “A State-of-the-Art Review of Past Programmes Devoted to Fuel Behaviour under Loss-of-Coolant Conditions. Part 3, IRSN report SEMCA 2008 093, Saint Paul lez Durance Cedex, (2008).
- [9] HOFMANN, P., RAFF, S., „Verformungsverhalten von Zircaloy-4-Hüllrohren unter Schutzgas im Temperaturbereich zwischen 600 und 1200°C“, Wissenschaftliche Berichte, KFK3168, Karlsruhe July 1981, <http://bibliothek.fzk.de/zb/kfk-berichte/KFK3168.pdf>.
- [10] HÓZER, S., GYÓRI, C., HORVÁTH, M., NOGY, I., MARÓTI, L., MATUS, L., WINDBERG, P., Nucl. Techn. **152** (2005) 273.
- [11] WAGNER, C., Ber. Bunsen-Ges. Phys. Chem. **72** (1968) 778.
- [12] GROSSE, M., STUCKERT, J., STEINBRÜCK, M., KAESTNER, A., J. Nucl. Mater. **420** (2012) 575.
- [13] Stuckert, J., Große, M., Klimenkov, M., Rössger, C., Steinbrück, M., Walter, M., “QUENCH-LOCA Program at KIT and Results of the QUENCH-L0 Bundle Tests”, Nucl. Engn. & Desgn. **255** (2013), 185.
- [14] GROSSE, M., STUCKERT, J., ROESSGER, C., STEINBRUECK, M., WALTER, M., KAESTNER, A., “Analysis of the secondary cladding hydrogenation during quench-loca tests and its influence on the cladding embrittlement”, submitted to J. AST Intern.
- [15] KAESTNER, A., HARTMANN, S., KÜHNE, G., FREI, G., GRÜNZWEIG, C., JOSIC, L., SCHMID, F., LEHMANN, E.H., Nucl. Instr. & Meths. in Phys. Res., **A659** (2011) 387.
- [16] KAESTNER, A. P., Nucl. Instr. & Meths. In Phys. Res., **A651** (2011) 156.
- [17] GROSSE, M., LEHMANN, E., VONTOBEL, P. STEINBRUECK, M., Nucl. Instr. & Methods in Phys. Res. A **566** (2006) 739.
- [18] GROSSE, M. K., STUCKERT, J., STEINBRÜCK, M., KAESTNER, A., HARTMANN, S., Physics Procedia **43** (2013), 294.
- [19] LEHMANN, E. H., KAESTNER, A., VONTOBEL, P., HOVIND, J., GROSSE, M., “Progress report about activities at PSI (Switzerland) 2011-2012“, IAEA CRP F1.20.23, Id 1575 Development, Characterization and Testing of Materials of Relevance to Nuclear Energy Sector Using Neutron Beams.

## 2.2. Research on zirconium based materials (including hydrogen uptake)

### SMALL ANGLE NEUTRON SCATTERING INVESTIGATION OF HYDRIDE PRECIPITATIONS IN ZIRCALOY-4

M. GROSSE\*\*\*, R. COPPOLA\*\*, M. H. MATHON\*\*\*

\*Karlsruhe Institute of Technology, PO Box 3640, D-76021 Karlsruhe, Germany

\*\*ENEA-Casaccia, Via Anguillarese 301, 00123 Roma, Italy

\*\*\*CEA Centre de Saclay, Laboratoire Leon Brillouin, F-91191 Gif sur Yvette, France

Email: [Mirco.Grosse@KIT.edu](mailto:Mirco.Grosse@KIT.edu)

#### Abstract.

The precipitation and annealing behavior of hydrogen in Zircaloy-4 was investigated by means of small angle neutron scattering. The results show that already during cool down in the air lock of the applied furnace zirconium hydride precipitates are formed. The size of the hydrides seems to be greater than the upper detection limit of the SANS experiments performed. These hydrides seem to be stable during various annealing at temperatures between 573 and 773 K for 1 to 16 days in inert atmosphere.

## 1. INTRODUCTION

During design basis loss of coolant accidents (LOCAs) hydrogen is picked up [1-3]. It is enriched in banded bands oriented non-perpendicular to the tube axis. Those hydrogen enriched bands results in a degradation of the mechanical properties [4]. In the framework of the post-test examinations of the samples prepared from the QUENCH-LOCA simulation experiments, neutron imaging and X ray diffraction (XRD) investigations were performed. The analysis of the neutron images gives hydrogen concentrations in the enrichment zones up to 2600 wt.ppm. No zirconium hydrides were found by XRD investigations even in the hydrogen enriched bands [5]. On the other hand, shifts of the zirconium peaks gave hints that the hydrogen is not precipitated but in a sub-cooled solution in the hexagonal (hcp) zirconium lattice. These results initiate systematic investigations of the precipitation process of hydrogen in Zircaloy-4 (Zry-4) in the framework of a bachelor thesis [6]. Small angle neutron scattering (SANS) investigations were an important part of this research. Due to the negative value of the hydrogen neutron scattering length, neutron scattering techniques are unique tools for investigating hydrogen problems in nuclear materials. More specifically SANS is utilized since long time to investigate hydride precipitates in Zr alloys in a non-destructive way [7]. The measurements were performed in cooperation between KIT, ENEA and CEA.

## 2. MATERIALS AND SANS MEASUREMENTS

Segments of a length of 20 mm were prepared from original Zry-4 cladding tubes. These segments were annealed at 1273 K in Ar/H<sub>2</sub> atmosphere with a hydrogen partial pressure of 4 kPa. According to Sieverts' law a hydrogen equilibrium concentration of 13.4 at% (~1480 wt.ppm) was established by this annealing. The samples were cooled down to nearly room temperature during about 300 s in flowing argon. After this treatment the samples were isothermally annealed in argon atmosphere at temperatures between 573 and 773 K for varying times between one and 16 days. Additionally, samples were annealed for 6 h at 673 K and further cooled down with cooling rates between 0.1 and 5 K/s.

The specimens were cut axially for the SANS investigations.

The SANS investigations were performed at the PAXY facility at LLB Saclay by KIT/CEA and at the D22 facility at ILL Grenoble by ENEA. Table 1 gives the parameters of the measurements.

## 2.2. Research on zirconium based materials (including hydrogen uptake)

TABLE 1. PARAMETERS OF THE SANS MEASUREMENTS

Instrument	Institution	Wavelength, nm	Sample – Detector - Distances, m
PAXY	LLB Saclay	0.6	1.5
		0.6	6.0
D22	ILL Grenoble	0.6	1.6
		0.6	5.6
		1.15	17.6

## 3. RESULTS

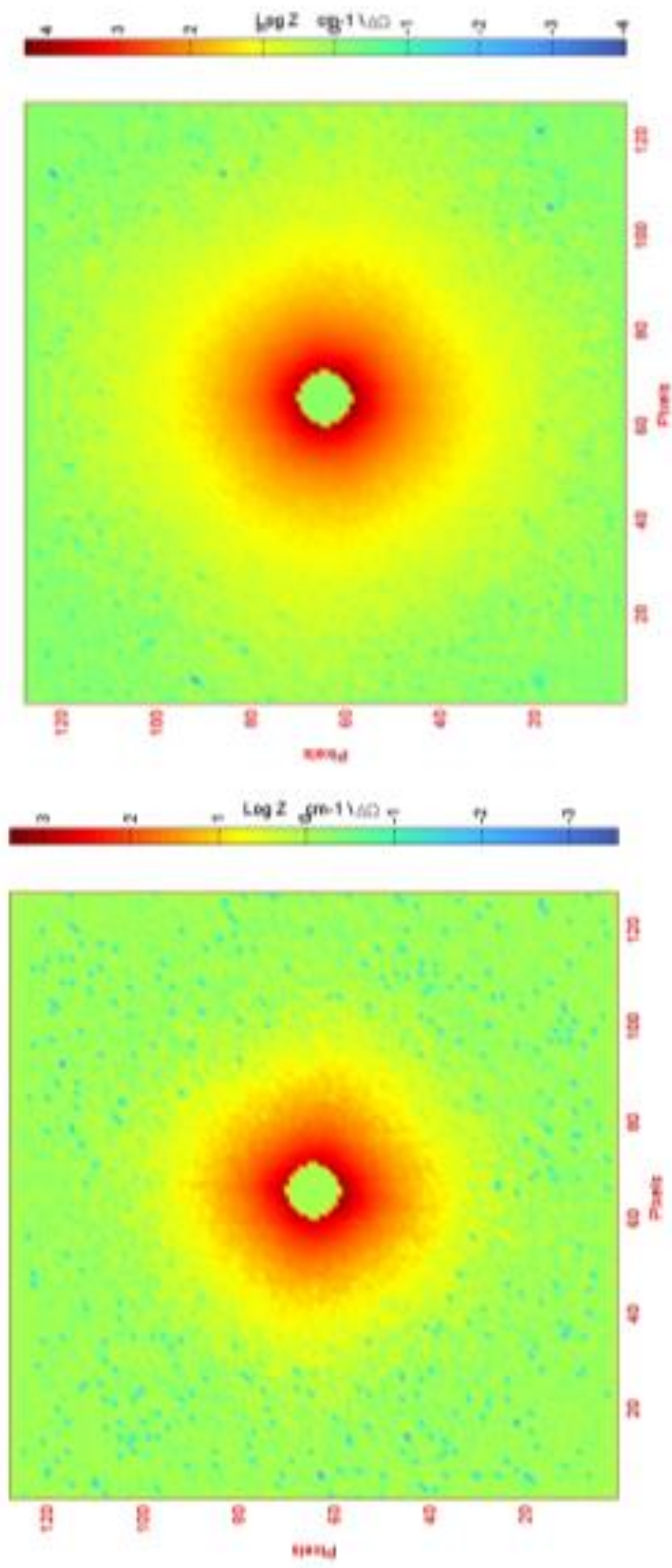
Figure 1 compares the 2D SANS cross-sections measured at 17.6 m sample-to-detector distance for the as-received and the hydrogen loaded specimens. A strong increase in the SANS intensity at small  $Q$  values is clearly visible. The 2D patterns are more or less radially symmetrical which allows a radial averaging for quantitative analysis.

Figure 2 plots the  $Q$  dependence of the radial averaged intensities of the two material states. The following information can be obtained from the curves:

The absorbed hydrogen results in an increase of the constant intensity caused by the strong incoherent scattering of hydrogen. An analysis of the constant scattering contribution in the Porod-Plot allows to separate this intensity contribution from the SANS itself. Figure 3 gives examples for the corrected scattering. The small angle scattering of the as-received state is not zero. It is caused mainly by the iron and chromium containing so called second phase particles (SPP). The  $Q$  dependence of the scattering intensity is close to the power law.

It means that the Porod range of the scattering is detected which gives no information about the size distribution of the hydrides. However, it gives a hint that the mean size of the SPP is larger than the size range detectable by small angle scattering. It agrees with the result of other methods like TEM.

In Fig. 4, the difference intensity between the as received and the hydrogen loaded state is plotted. On the basis that the only change in the sample structure is the formation of the zirconium hydrides, this difference is the scattering of the hydrides. The  $Q$  dependence of the SANS intensity is close to the power law with an exponent close to 4 at most of the  $Q$  as the solid line in Fig. 4 shows only at  $Q < 5 \times 10^{-3} \text{ nm}^{-1}$  the SANS pattern differs significantly from the power law. It shows that the hydrides are large and detectable only at the low  $Q$  end of the measurements.



a) 2D SANS pattern of the as-received state

b) 2D SANS pattern of the hydrogen loaded sample

FIG. 1. Comparison of the 2D SANS pattern of an as-received and a hydrogen loaded sample (measurements carried out by ENEA at ILL D22).

## 2.2. Research on zirconium based materials (including hydrogen uptake)

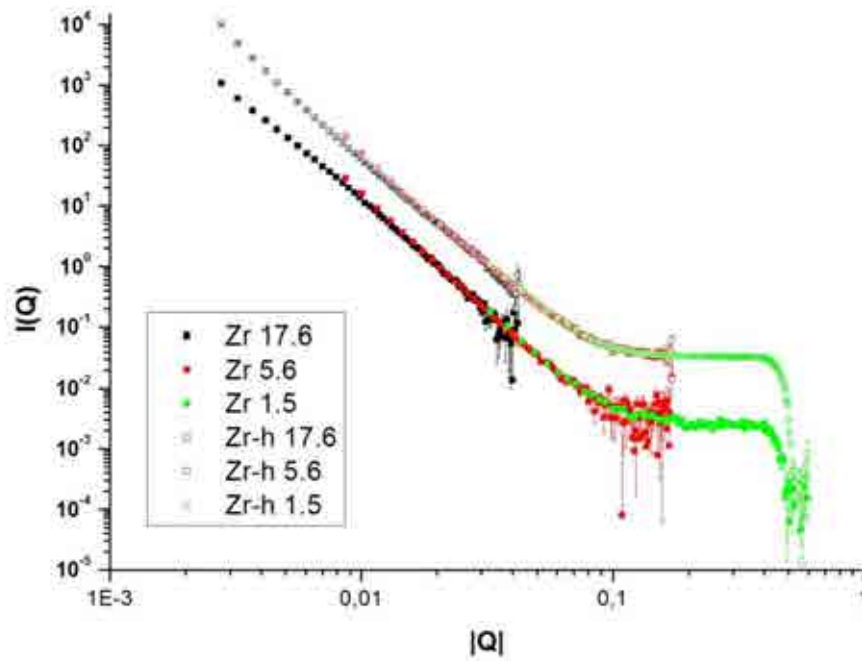


FIG. 2. Radially averaged SANS cross-sections for hydrogen free (“Zr”) and hydrogen loaded (“Zr-H”) zircalloy samples measured at the D22 instrument, ILL-Grenoble.

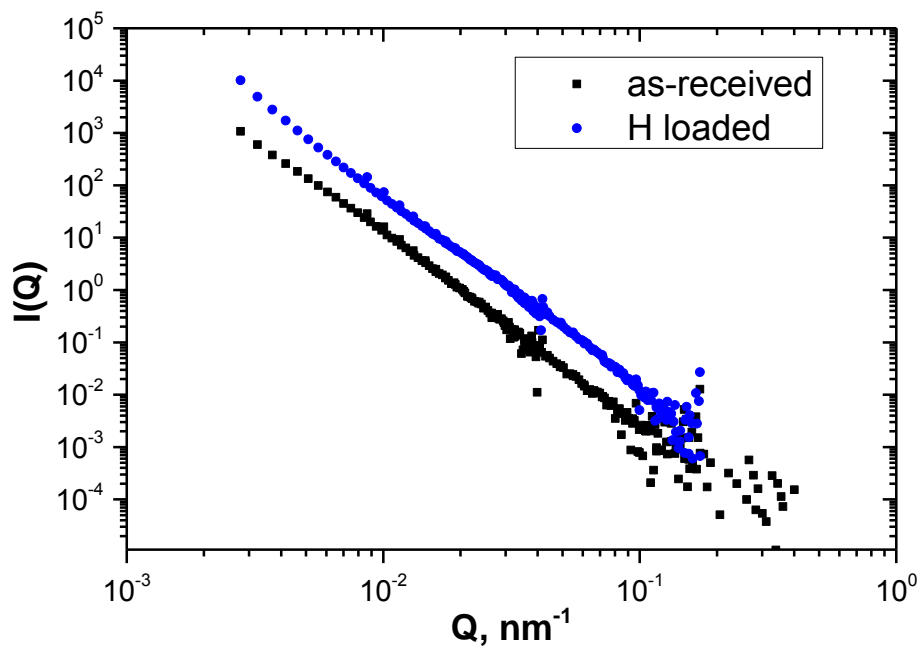


FIG. 3. SANS pattern of an as-received and a hydrogen loaded sample corrected for constant scattering contributions.

## 2.2. Research on zirconium based materials (including hydrogen uptake)

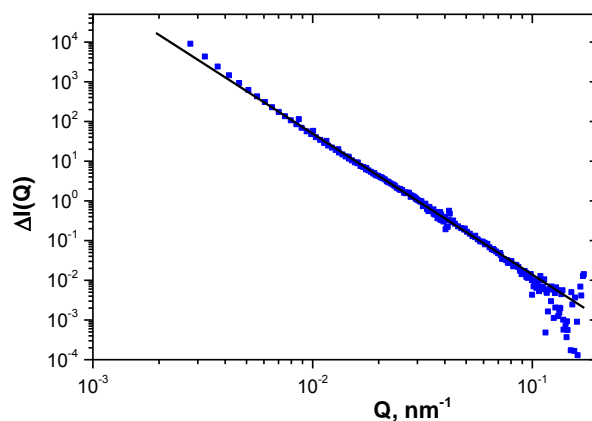


FIG. 4. Difference SANS intensity caused by the hydrides.

On the other hand, metallographic and scanning electron microscopy investigations show objects of a length of about 15  $\mu\text{m}$  and a width of 1-2  $\mu\text{m}$ . The hypothesis discussed at the CRP meeting in Beijing that these hydrides consist of smaller precipitates could not be confirmed by the SANS investigations. Changes in the size range between 0.1 and 1  $\mu\text{m}$  cannot be detected neither by SANS nor by light optical and scanning electron microscopy.

A large number of specimens annealed at various temperatures and times after identical hydrogen loading were measured at the LLB (Saclay, France). As an example, Fig. 5. compares the SANS pattern of the as-received state, the hydrogen loaded state and the hydrogen loaded + transient annealed state and Fig. 6. the SANS pattern of samples which were hydrogen loaded and annealed at 400°C for 1, 4, 9 and 16 days.

The results of these investigations can be summarized as follows:

The comparison given in Fig. 5. shows the effect of absorbed hydrogen on the incoherent background which is not dependent on the scattering vector  $Q$ . The differences in the constant intensity at high  $Q$  between the hydrogen loaded and hydrogen loaded and transient annealed specimen show that some hydrogen is released during the thermal treatment.

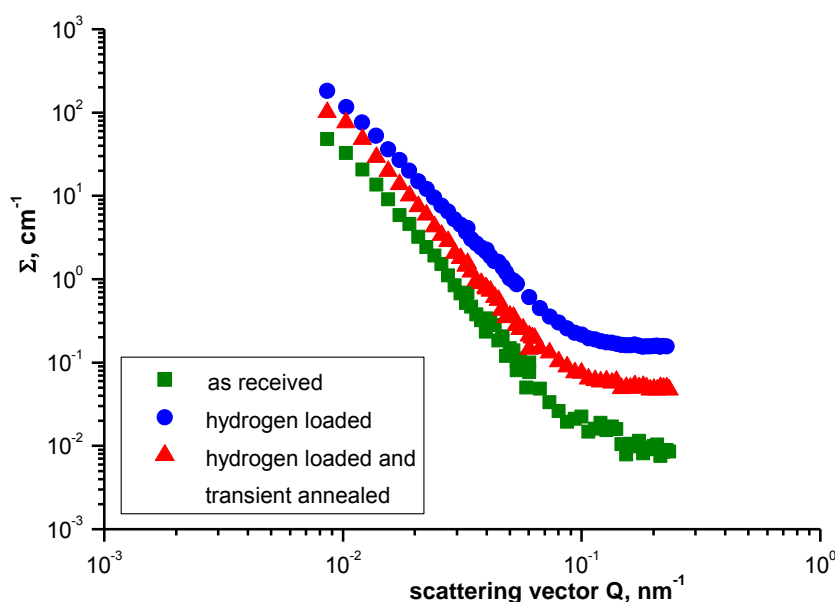


FIG. 5. Comparison between SANS of the as-received, hydrogen loaded and hydrogen loaded and transient annealed specimen.

## 2.2. Research on zirconium based materials (including hydrogen uptake)

Figure 6 shows that the annealing applied does not change the hydrogen precipitates at least in the size range significant for the SANS measurements.

This confirms that during the rapid cooling after hydrogen loading (from 1273 K to room temperature in about 300 s) stable hydride precipitates with dimensions above the detectable range ( $\sim 0.1 \mu\text{m}$ ) are formed.

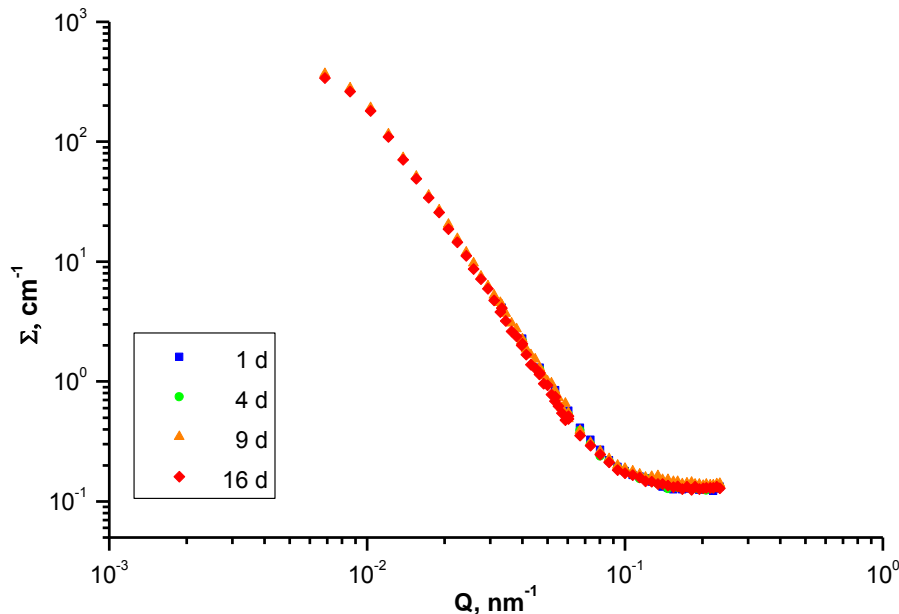


FIG. 6. Comparison between the SANS of samples annealed at  $400^\circ\text{C}$  for 1, 4, 9 and 16 days.

## 4. SUMMARY AND CONCLUSIONS

The precipitation behavior of hydrides in Zry-4 was investigated by means of SANS in the framework of the IAEA CRP.

The results show that:

- Hydride precipitations are already formed during relative fast cool down after annealing in Ar/H<sub>2</sub>.
- The  $Q$  dependence of the SANS intensity respects the power law. It gives a hint that the size of the hydrides is larger than detectable by the SANS measurements.
- The hypothesis that the microscopic hydrides consist of sub-microscopic precipitates was disproved at least under the applied loading and cooling conditions.
- Significant hydrogen release was only observed after 16 d annealing at 773 K.
- The hydrides are very stable. No coarsening during all annealing treatments was detected by the applied methods.

It is planned to continue the cooperation on this topic even the CRP is finished. Actually a new basis for the cooperation has to be defined. To obtain smaller hydrides precipitates or subcooled hydrogen solution in the zirconium lattice another high temperature facility has to be applied which allows water quenching from the temperature of hydrogen loading.

## 2.2. Research on zirconium based materials (including hydrogen uptake)

### REFERENCES

- [1] NAGASE, F., FUKETA, T., J. Nucl. Sci. & Techn., **42** (2005) 209.
- [2] BILLONE, M., YAN, Y., BURTSEVA, T., DAUM, R., “Cladding Embrittlement During Postulated Loss-of-Coolant Accidents,” NUREG/CR-6967, (2008). <http://pbadupws.nrc.gov/docs/ML0821/ML082130389.pdf>.
- [3] GRANDJEAN, C., HACHE, G., “A State-of-the-Art Review of Past Programmes Devoted to Fuel Behaviour under Loss-of-Coolant Conditions. Part 3, IRSN report SEMCA 2008 093, Saint Paul lez Durance Cedex, (2008).
- [4] GROSSE, M., STUCKERT, J., STEINBRÜCK, M., KAESTNER, A., J. Nucl. Mater. **420** (2012) 575.
- [5] GROSSE, M., STUCKERT, J., ROESSGER, C., STEINBRUECK, M., WALTER, M., Kaestner, A., “Analysis of the secondary cladding hydrogenation during the quench-loca bundle tests with ZIRCALOY-4 claddings and its influence on the cladding embrittlement”, submitted to J. ASTM Intern.
- [6] PRESTEL. S., Bildung von Hydridausscheidungen in Zircaloy-4“, final report No 12/23, KIT and Hochschule Karlsruhe (2013).
- [7] FONG, R., and SPOONER, S. Scripta Met. Mat., **30** (1994) 649.

## 2.2. Research on zirconium based materials (including hydrogen uptake)

### FINAL REPORT ABOUT ACTIVITIES AT PSI (SWITZERLAND) 2011-2013

E. H. LEHMANN\*, A. J. KAESTNER\*, P. VONTOBEL\*, J. HOVIND\*, M. GROSSE\*\*

\*Neutron Imaging & Activation Group, Paul Scherrer Institut, CH-5232 Villigen PSI, Switzerland

\*\*Karlsruhe Institut for Technology (KIT), Institute for Applied Materials, Germany

Email: [eberhard.lehmann@psi.ch](mailto:eberhard.lehmann@psi.ch)

#### Abstract.

In order to bring tomography with neutrons more and more towards a routine method and to develop it into a quantitative three-dimensional technique we developed a set of tomography test specimen in a sense of a round robin procedure for several interested and involved partners in the CRP. This initiative has been started by producing and delivery of the specimen to 10 countries until now. The progress in the evaluation and several problems will be reported. In respect to materials for the nuclear energy we investigated in collaboration between KIT and PSI the hydrogen ingress into fuel rod cladding under accidental (simulated) conditions by using quantitative neutron imaging methods. It was shown by calibration test measurements that the sensitivity for the hydrogen detection can be further increased when the beam line BOA with a much higher contribution of cold neutrons (compared to the commonly exploited facility ICON) is used. Over the range of hydrogen concentration (H/Zr ratio up to 2) a linear attenuation behavior was found for all three neutron imaging facilities at PSI.

We continued the investigations of highly activated samples from our previous spallation target with success. The particular method with Dy doped imaging plates was applied with success and delivered many new insights about the problems of spallation source targets operated at high dose levels of proton exposure. Our experiences and technical solutions can be transferred on demand to other partners within the CRP.

## 1. INTRODUCTION

The national site for research with neutrons in Switzerland is the spallation neutron source SINQ, operational with success since 1997. It has the capability to provide thermal and cold neutrons via beam ports and neutron guides to the presently 20 separate facilities. Among them, the majority of installations belong to the field of neutron scattering. But there are two beam lines in use for neutron imaging (NEUTRA, ICON), one beam port for a test beam line (BOA) and four channels for test irradiations in high flux environment.

This report is focused to the field of neutron imaging because the involved parties in this CRP have their background in this area and the direct access to the neutron imaging facilities at PSI.

## 2. WORK PLAN AS DISCUSSED AND AGREED WITH PARTNERS WITHIN THE CRP

The three main topics are given here:

- Neutron beams (techniques) utilized for tomography can be compared on the basis of test phantom samples (sensitivity, resolution).
- Hydrogen test samples from KIT will be investigated at the three imaging beam lines at PSI (NEUTRA, ICON; BOA).
- The method for imaging of highly activated samples will be communicated for interested partner of the CRP. The PSI facility NEURAP stays available for dedicated studies by the CRP members.

In particular, the following details were discussed and agreed among the collaborators:

- 2.1. Establishing the layout of test samples for inter-calibration for sensitivity and spatial resolution in neutron tomography (now agreed after discussion); manufacturing process of the sensitivity test device individually done until now – 5 copies to be produced at

## **2.2. Research on zirconium based materials (including hydrogen uptake)**

- PSI with the support by IAEA. Further, we will contribute to the non-invasive determination of hydrogen in Zr alloy by using well defined specimen from KIT.
- 2.2. Definition and preparation of test specimen suitable for tomography validation based on the design of Dr. Sim (Korea), rejection of the resolution phantom from Korea, Brazil and South Africa. Definition of a new design with flexible structure (drawing attached).
  - 2.3. Hydrated Zircaloy specimens are delivered from KIT to PSI for sensitivity tests at the three beam lines NEUTRA, ICON, BOA. After the end of the measurements, these samples (or equivalent) will be made available for further tests and calibrations at other participating facilities in this CRP.
  - 2.4. It is still intend to transfer the know how in the inspection of highly activated samples to other CRP members (in particular China). The offer stands that activated samples can be investigated at our facilities on demand.
  - 2.5. Collaborative efforts: there is a tight contact established among the participating partners interested in neutron imaging (South Africa, Germany, Switzerland, South Korea, Indonesia and also China). This connection will be intensified in the framework of the CRP collaboration. At least two students will be involved into the evaluation procedure of the tomography phantom studies at the participating facilities.

## **3. INDIVIDUAL PROGRESS REPORT ON THE WORK**

### **Test objects for neutron tomography evaluation and quantification**

Neutron tomography (nCT) on routine basis is a relatively young method compared to X ray tomography. Until now, there has been little done in terms of comparing the performance of different instruments and instrument configurations. For X ray tomography, driven by medical imaging, there are quality assessment methods developed and available to certify the quality of the delivered images.

The approach reported here is a first step into the direction of creating a quality assessment (QA) routine for nCT. Once the routine is stable and all involved partners in the project agree on the procedure this could be defined as a standard for evaluating performance of neutron tomography configurations. The currently described methods aim at quantifying the ability to detect materials with different contrasts and to give a measure on the resolution of an nCT configuration. Furthermore, the degree of precision will be estimated for the different involved materials.

Currently, there are five boxes with three QA phantoms each. The samples are prepared by the Neutron Imaging and Activation group (NIAG) at Paul Scherrer Institut (PSI), Switzerland, in the name of IAEA. The sample boxes have been sent to different neutron imaging sites in the world. The sample distribution and data collection of the results was managed by NIAG. It was decided to use a test routine where the sample boxes always are returned to PSI to assure that the condition of the boxes always is as intended before they are sent to the next user.

### **3.1. Contrast sample**

The purpose of the contrast sample is to show the variation in reconstructed neutron attenuation coefficients for different materials. The original sample design contains the following materials: Sample body, Al, and insets rods of Pb, PE, Fe, Ni, Al, and Cu. From these insets the PE is difficult to handle since the transmission is so low that starvation artifacts are introduced in the reconstructed images. The Al inset on the other hand has the

## 2.2. Research on zirconium based materials (including hydrogen uptake)

same attenuation as the sample body. The purpose of this inset was to investigate if edge effects will appear at the interface between two well-fitted objects. The sample dimensions are 30mm diameter of the sample body and the insets have a diameter of 6mm and are placed equidistantly on a 18mm ring. The sample outline is illustrated in Fig. 1 below.

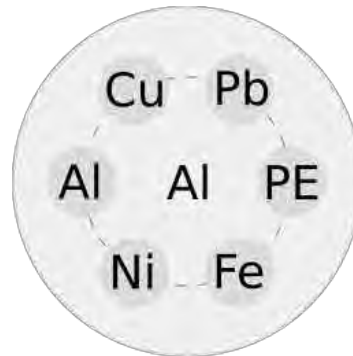


FIG. 1. Top view / horizontal slice of the “contrast sample” with 6 individual inserts of pure metals.

## 3.2. Resolution sample

The purpose of the resolution sample is to determine the thinnest feature that can be detected with the resolution provided by the current imaging configuration. In the currently used sample a single foil or a compressed stack of foils is used to create the contrast feature. With this configuration the feature may be detected even though the foil is thinner than the spatial resolution of the imaging system. In the case of sub-resolution foils a partial volume effect will be observed this means that the feature will appear to be thicker than it actually is and the value of the attenuation coefficient will be a mix of the feature and the sample body.

The resolution sample consists of two blocks that are assembled with two screws. The gap between the two blocks is used to insert a thin contrast feature. There are two different configurations of the resolution sample included in the round robin experiment performed during 2012. One with positive feature contrast, i.e. the foil has a higher attenuation coefficient than the sample body. In this sample the body was made of Al and the foils of Cu. The second sample has a complementary configuration providing a negative feature contrast with a sample body of Fe and the foils of Al.

## 2.2. Research on zirconium based materials (including hydrogen uptake)

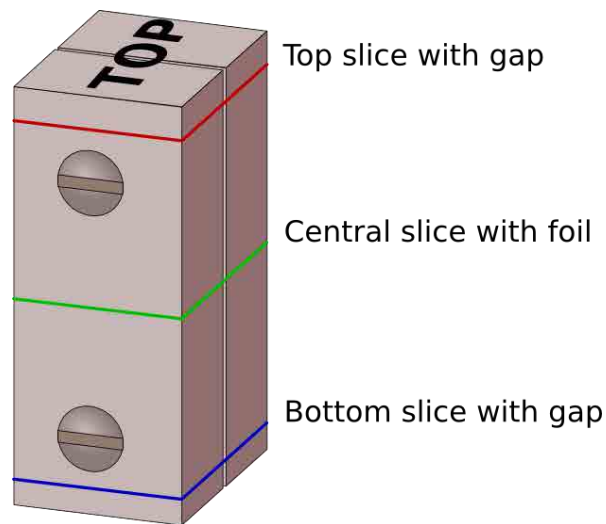


FIG. 2. Perspective view on the “resolution sample” which was made in two versions by Al and Fe.

The evaluation procedure as it is practiced for the moment is described in [1, 2]. There is still demand and potential for methodical improvements, according to the findings and problems in the course of the international exercise.

### 3.2.1. Quantification of the hydrogen content in Zr fuel cladding materials

Test rod pieces of fuel cladding which were hydrated artificially in gas flows were delivered to PSI and investigated with neutron imaging methods at three individual beam lines: NEUTRA [3] (thermal neutrons), ICON [4] (cold neutrons), BOA [5] (higher content of cold neutrons). The raw image data were related to the “open beam” after removal of the “dark current” signal according to the exponential attenuation law. The derived linear attenuation coefficients are compared to the well known hydrogen contents of the 6 test samples (including the pure reference sample).

In Fig. 3, the image data are compared for the 6 test specimen showing the increased hydrogen content qualitatively as darker areas. Using the well-known hydrogen content of the samples (as given in Table 1), the diagram in Fig. 4 is obtained.

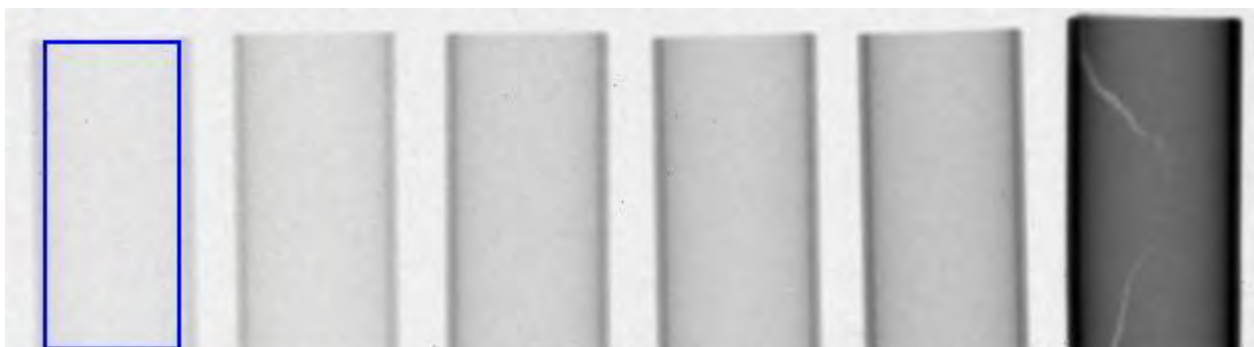


FIG. 3. Image data from the 6 investigated test specimen: Zr fuel cladding rods with well defined hydrogen content (see Table 1) – the increasing amount of absorbed hydrogen is clearly visible by the darkness of the images.

## 2.2. Research on zirconium based materials (including hydrogen uptake)

TABLE 1. HYDROGEN CONTENT OF THE INVESTIGATED ZR CLADDING TEST SPECIMEN

Probe	H/Zr ratio
8	0
9	0.127
10	0.268
11	0.312
12	0.418
13	1.924

The results of this study indicate that there is a linear attenuation behavior over a wide range of hydrogen concentration which enables to apply neutron imaging techniques for a non-invasive determination of the H/Zr ratio with high precision. However, due to spectral differences among different imaging facilities, a transpose of data without internal calibration is not easily possible. The highest sensitivity for hydrogen is obtained at the facility with the softest spectral conditions (BOA) enabling to observe smallest amounts of hydrogen. The accuracy for the hydrogen detection might be approximately the same in the interim range for all three facilities.

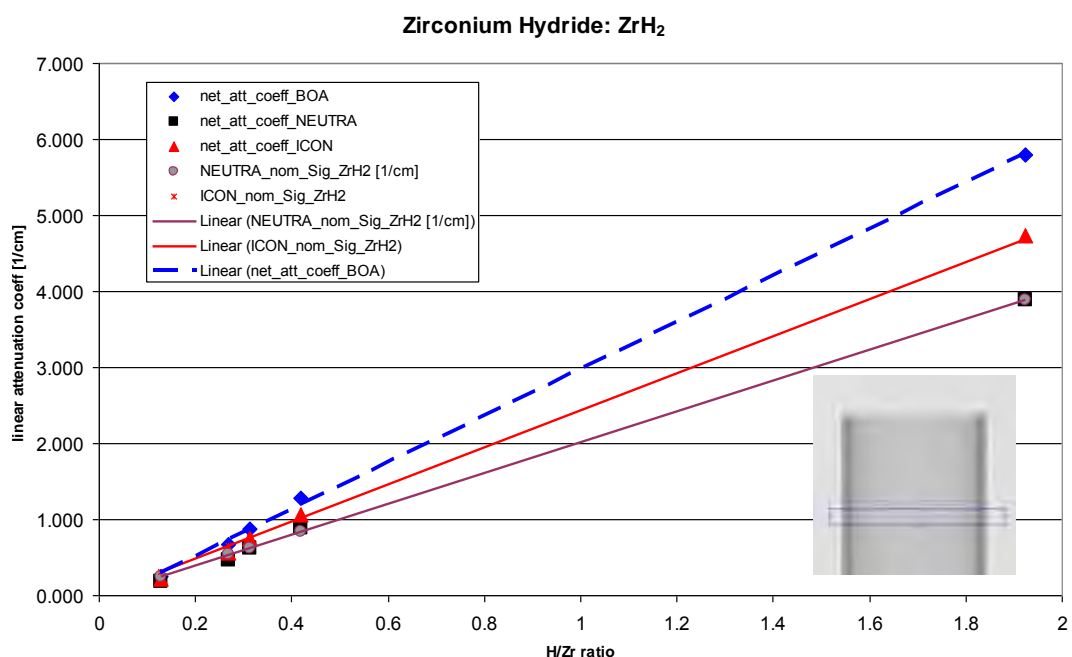


FIG. 4. Evaluation of the hydrogen content of Zr fuel cladding samples with neutron imaging: results obtained at three individual imaging facilities at PSI.

### 3.2.2. Inspection of SINQ target rods

The 1 MW spallation source has been running since 1997 with high success and with high availability until now. Compared to the “day 1” target, consisting of solid Zircaloy rods in a hexagonal bundle arrangement, the neutron yield has been increased by a factor 2.2 by using lead rods in a Zircaloy cladding. Outside the heat affected area (where lead inside the

## 2.2. Research on zirconium based materials (including hydrogen uptake)

rods melts regularly under exposure) a Pb blanket has been installed for higher neutron output too.

There are two cycles for target rod inspections.

1. Material tests for quality assurance of the initial target rods prior to the operation; in particular, the distribution of the molten lead is checked inside the cladding. Neutrons are most useful because of the good penetration, in particular for lead.
2. Post-irradiation tests using the NEURAP [6] facility; the change of the material under long term irradiation (for more than 6 Ah protons) is visualized and even quantified in some relevant cases on the basis of the image data.

While the first cycle can be done under normal conditions without any shielding requirements, the study of the highly activated samples requires much more percussion. The NEURAP setup is a well shielded environment where up to 5 single target rods are delivered from a hot cell and handled remotely controlled in the iron shielding block.

In addition to the shielding demands, there is a special technique for obtaining the neutron images: Dy doped imaging plates operated in a special procedure [7]. The resulting good image quality is demonstrated in Fig. 6.

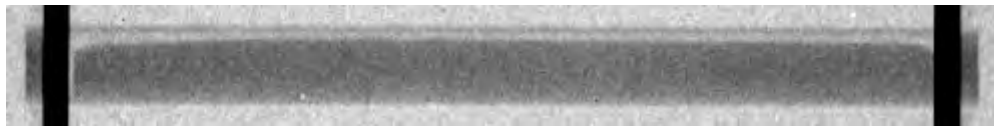


*FIG. 5. Pb target rod of SINQ before the exposure with the proton beam; the molten inner part can be distinguished from the void and the Zircaloy cladding.*

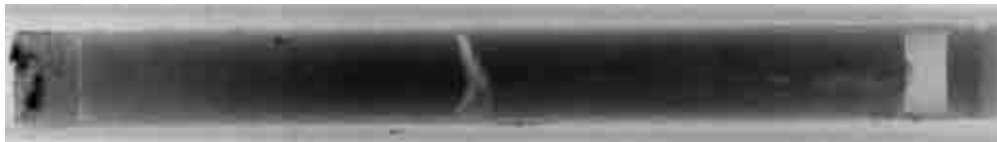


*FIG. 6. Pb target rod after long-term exposure; the accumulation of spallation products follows the proton beam profile in the centre of the rod; some material changes and the interaction with cladding become visible.*

## 4. COLLABORATIVE EFFORTS AND RESULTS ACHIEVED

There is a tight contact established among the participating partners interested in neutron imaging (South Africa, Germany, Switzerland, South Korea, Indonesia and also China). This connection will be intensified in the framework of the CRP collaboration. At least two students will be involved into the evaluation procedure of the tomography phantom studies at the participating facilities.

## 2.2. Research on zirconium based materials (including hydrogen uptake)

TABLE 2. INSTITUTES PARTICIPATING IN ROUND ROBIN EVALUATION OF THE QA SAMPLES

Country	Institute
Algeria	Centre de Recherche Nucleaire de Birine
Argentina	Centro Atomico Bariloche
Brazil	Centro do Reator de Pesquisas - CRPq
Germany	Helmholtz-Zentrum Berlin
Hungary	Nuclear Analysis and Radiography Laboratory
Indonesia	National Nuclear Energy Agency (BATAN)
Israel	Soreq Nuclear Research Center
Malaysia	Agensi Nuklear Malaysia
Poland	National Centre for Nuclear Research
Portugal	Instituto Tecnologico e Nuclear
Slovenia	Jozef Stefan Institute
South Africa	Nuclear Energy Corp. of South Africa
Switzerland	Paul Scherrer Institut

## 5. REMAINING WORK-PLAN

The next period has to be used to evaluate the Round-Robin exercise data carefully. It is expected that a methodical update in the layout of the sample structure will be needed. Furthermore, some simplification and generalisation of the evaluation procedure is required and will be performed within the actions period.

The reader is also advised to consult other related references e.g. [8-12], for additional information regarding applications of neutron imaging.

## 6. SUMMARY AND CONCLUSIONS

It was shown that PSI provides modern methods for the non-invasive study of nuclear materials like fuel cladding and spallation target materials. The neutron imaging methods are established at the beam lines NEUTRA, ICON and BOA which can be booked via the proposal scheme (see <https://duo.psi.ch/duo/>).

Furthermore, the process for neutron tomography validation was started by providing 3 individual test samples for the determination of the inherent contrast and the spatial resolution (and defect analysis). The results from the 13 participating institutions and their evaluation will be a first step in the standardization process in neutron tomography.

## 2.2. Research on zirconium based materials (including hydrogen uptake)

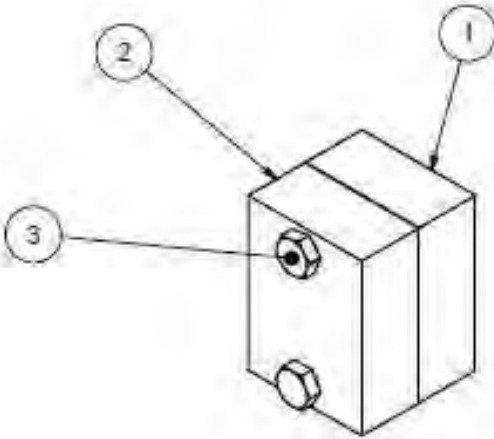
### REFERENCES

- [1] RADEBE, M.J., et al. "Evaluation Procedures for Spatial Resolution and Contrast Standards for Neutron Tomography", Physics Procedia - Proceedings of the ITMNR7, Kingston, Canada, (2012).
- [2] KAESTNER, A.P., et al. "Verifying neutron tomography performance using test objects", Physics Procedia - Proceedings of the ITMNR7, Kingston, Canada, (2012).
- [3] LEHMANN, E., PLEINERT, H., The new neutron radiography station at the spallation source SINQ, INSIGHT Vol.40, No. 3, March (1998).
- [4] KAESTNER, A.P., HARTMANN, S., KÜHNE, G., FREI, G., GRÜNZWEIG, C., JOSIC, L., SCHMID, F., LEHMANN, E.H., The ICON beamline – A facility for cold neutron imaging at SINQ, Nuclear Instruments and Methods in Physics Research Section A: Accelerators, Spectrometers, Detectors and Associated Equipment, **659**, 1, (2011), 387-393.
- [5] FILGES, U., First experiments on the new BOA instrument at SINQ, Swiss Neutron News 40, Aug. (2012) [http://sgn.web.psi.ch/sgn/snn/snn\\_40.pdf](http://sgn.web.psi.ch/sgn/snn/snn_40.pdf)
- [6] NEURAP facility at the NEUTRA beam line of SINQ, report in preparation.
- [7] VONTOBEL P., TAMAKI M., MORI N., ASHIDA T., ZANINI L., LEHMANN E.H., JAGGI M., Post-irradiation analysis of SINQ target rods by thermal neutron radiography J. of Nuc. Mater. **356** (1-3): 162 – 167, (2006), <http://dx.doi.org/10.1016/j.jnucmat.2006.05.033>
- [8] D. L. Chichester, J.W. Sterbentz, Neutron Resonance Transmission Analysis (NRTA): Initial Studies of a Method for Assaying Plutonium in Spent Fuel, Technical Report, Idaho National Laboratory (INL), (2011).
- [9] C. Morris, M. Bourke, D. Byler, C. Chen, G. Hogan, J. Hunter, K. Kwiatkowski, F. Mariam, K. McClellan, F. Merrill, et al., Qualitative comparison of bremsstrahlung X rays and 800 MeV protons for tomography of uranium fuel pellets, Review of Scientific Instruments 84 (2013) 023902–023902.
- [10] A. Tremsin, S. Vogel, M. Mocko, M. Bourke, V. Yuan, R. Nelson, D. Brown, B. Feller, Non-destructive studies of fuel pellets by neutron resonance absorption radiography and thermal neutron radiography, in print, Journal of Nuclear Materials (2013).
- [11] J. Higgs, W. Thompson, B. Lewis, S. Vogel, Kinetics of precipitation of U<sub>4</sub>O<sub>9</sub> from hyperstoichiometric UO<sub>2+x</sub>, Journal of Nuclear Materials 366 (2007) 297–305.
- [12] MCP detectors, Nuclear Instruments and Methods in Physics Research Section A: Accelerators, Spectrometers, Detectors and Associated Equipment 604 (2009), 140–143.

## 2.2. Research on zirconium based materials (including hydrogen uptake)

### Appendix

#### CONSTRUCTION DRAWINGS OF THE TEST SAMPLE



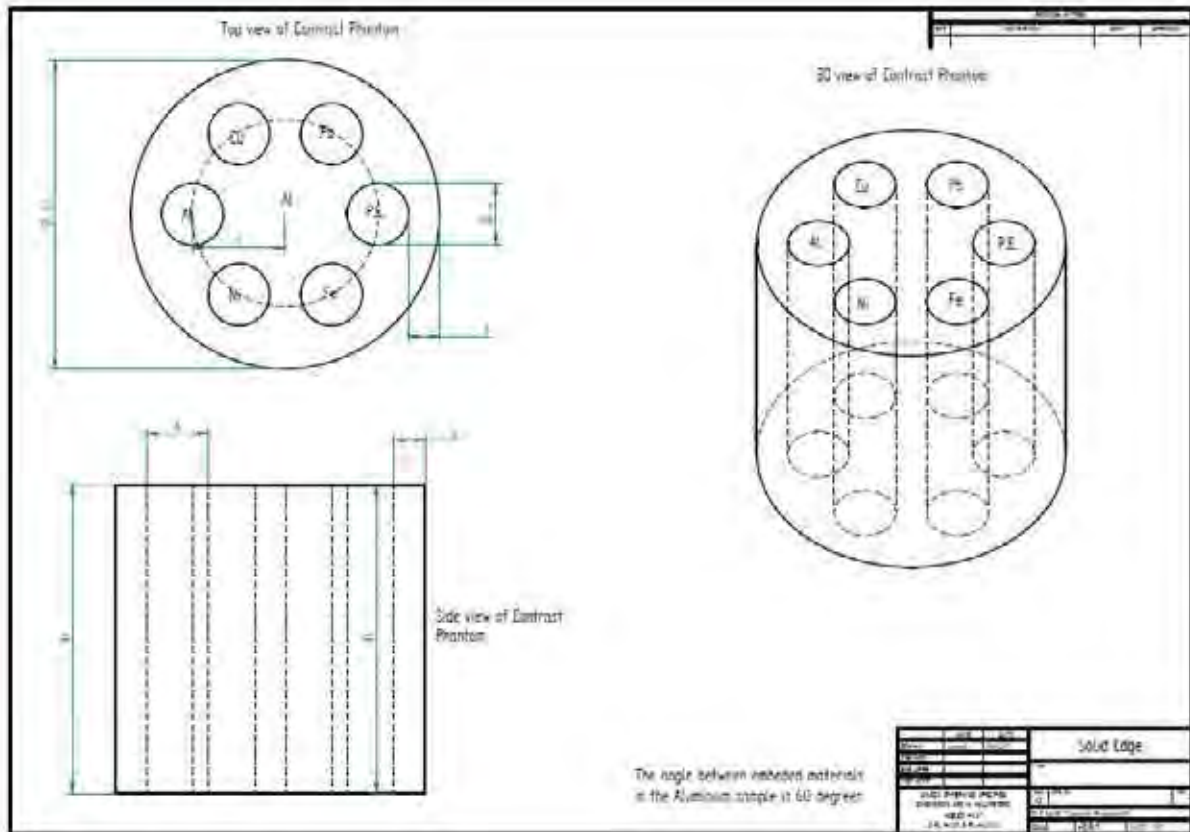
Please note:  
The screws must be made out of aluminium!

3	2		(DIN 933/ISO 4017)	Sechskantschraube M5x30 Aluminium			
2	1		300911-4	Pressstück_unten 2			
1	1		300911-5	Pressstück_oben 2			
Pos.	Menge	Einheit	Sachnummer	Benennung / Merkmale			
Anlage	a		d	Gezeichnet	30.09.2011	Jan Hovind	Massst. 1:1
	b		e	Geprüft			
	c		f	Archiviert			
Anlage				Ersetzt durch			
Baugruppe				Ersetzt fuer			
Pressdummie B				Stueckl. Nr.			
				Zusammenst.Nr.			
		Titel <b>Zusam_Pressdummie B</b>		Zeichnungs-Nr. <b>300911-3</b>			

Nachdruck und Verbreitung ohne schriftliche Genehmigung der Paul-Henning-Werke ist untersagt.  
 Nachdruck und Verbreitung ohne schriftliche Genehmigung der Paul-Henning-Werke ist untersagt.



## 2.2. Research on zirconium based materials (including hydrogen uptake)



## 2.2. Research on zirconium based materials (including hydrogen uptake)

### PRELIMINARY ROUND ROBIN ON THE DETERMINATION OF CRYSTALLOGRAPHIC TEXTURE OF ZR COMPONENTS BY NEUTRON DIFFRACTION

J.R. SANTISTEBAN<sup>\*</sup>, F. MALAMUD<sup>\*</sup>, P. VIZCAINO<sup>\*\*</sup>, M. J. LI<sup>\*\*\*</sup>, S.C. VOGEL<sup>+</sup>, P. LIAW<sup>++</sup>, D. G. CARR<sup>++</sup>, V. I. SUMIN<sup>+++</sup>, R. VASIN<sup>+++</sup>

<sup>\*</sup> Centro Atómico Bariloche, CNEA, Bariloche 8400, Argentina

<sup>\*\*</sup> Centro Atómico Ezeiza, CNEA, Argentina

<sup>\*\*\*</sup> China Advanced Research Reactor, CIAE, Beijing 102413, China

<sup>+</sup> Los Alamos Neutron Science Center, LANL, Los Alamos, NM 87545, USA

<sup>++</sup> ANSTO, Kirrawee, NSW 2232, Australia

<sup>+++</sup> IBR-2, JINR, Dubna 141980, Russian Federation

#### Abstract.

A preliminary round-robin study on the determination of the texture of Zr-based components by neutron diffraction experiments has been conducted, with the participation of both texture diffractometers and residual stress diffractometers from five international laboratories. Both constant-wavelength and polychromatic neutron beams have been used to define the texture of specimens from a warm-rolled and annealed Zircaloy-4 plate, and from a Zr2.5%Nb pressure tube. Results are consistent and reproducible, both qualitatively in terms of pole figures, and quantitatively by means of Kearns factors and texture index.

## 1. INTRODUCTION

Due to its good mechanical strength, high corrosion and creep resistance, combined with excellent neutronic properties, Zr-based alloys have been selected as the material of choice for fuel cladding worldwide (Zircaloy-4 and 2), and for pressure tubes in CANDU and RBMK reactors (Zr2.5%Nb and Zr1%Nb). Because of the anisotropy of physical properties, the crystallographic texture of tubing is a parameter carefully specified by designers, due to its impact on in-reactor performance. Texture is specified through Kearns factors [1] which are parameters assessing the proportion unit cells with their hexagonal *c*-axes that are projected along the three principal axes of specimen. For tubing these would be ( $f_H, f_R, f_A$ ), for *Hoop*, *Radial* and *Axial*, respectively. Kearns factors are normally calculated from experimental pole figures measured by laboratory X rays [2]. Due to its high penetration, neutron beams offer non-destructive characterization of bulk textures with minimal sample preparation required [3], an important advantage for the investigation of highly radioactive irradiated specimens after long times in service [4]. Besides this, materials science neutron diffractometers are usually furnished with stress rigs and furnaces, which allow following the texture changes that occur during thermo-mechanical treatments, as a result of phase transformations or large microstructural changes [5-7].

Finally, the spatial resolution available at residual stress diffractometers is an attractive option for non-destructive studies of texture variation across specimens [8]. Texture is precisely quantified in terms of the orientation distribution function of crystallites (ODF), usually obtained from least-squares fits to experimental pole figures or multi-histogram Rietveld refinements [9]. Different instruments using either monochromatic or pulsed white neutron beams, with a variety of detector and collimator arrangements are currently available for this task. The main aim of this *preliminary* round robin exercise is to validate the measurement strategies for texture determination in the laboratories participating in the present CRP. This is a preliminary exercise in the sense that there are only a reduced number of participants. Besides this we are also interested in assessing the quality of the information obtained from incomplete measurements of pole figures. A secondary, more-specific aim of

## 2.2. Research on zirconium based materials (including hydrogen uptake)

this round robin is to determine the standard uncertainty to be expected for the Kearns factors obtained by different neutron diffraction techniques.

### 2. SAMPLES

#### 2.1. Zr-2.5%Nb pressure tubes

Small specimens with dimensions of  $\sim 10 \times 20 \text{ mm}^2$  along the axial and rolling directions, respectively, were machined out from an experimental Zr-2.5%Nb pressure tube produced at CNEA, Argentina [10]. Starting from Zr2.5%Nb billets forged at  $\sim 800^\circ\text{C}$ , the fabrication route of these pressure tubes included extrusion at  $\sim 800^\circ\text{C}$ , followed by *cold rolling* to  $\sim 28\%$  strain, and autoclaving at  $400^\circ\text{C}$  for 24 h.. The microstructure of the pressure tube consists of  $\alpha$ -grains up to about  $10 \mu\text{m}$  long,  $1 \mu\text{m}$  wide and  $0.5 \mu\text{m}$  thick which have an *hcp* crystal structure containing between 0.6-1 wt% Nb, surrounded by a grain boundary network of Nb stabilized  $\beta$ -Zr, with a *bcc* crystal structure, containing about 18-20 wt% Nb (Fig. 1-a). The texture of Zr2.5%Nb pressure tubes is very strong and is mainly defined at the extrusion stage [11]. The ODF of the material is dominated by crystals having their (10-10) axes along the tube axial direction and their *c*-axes along the tube hoop direction. This produces a very intense axial (10-10) pole density maximum, and a less sharper (0002) pole density maximum along the hoop direction, which extends towards the radial direction (Fig. 3).

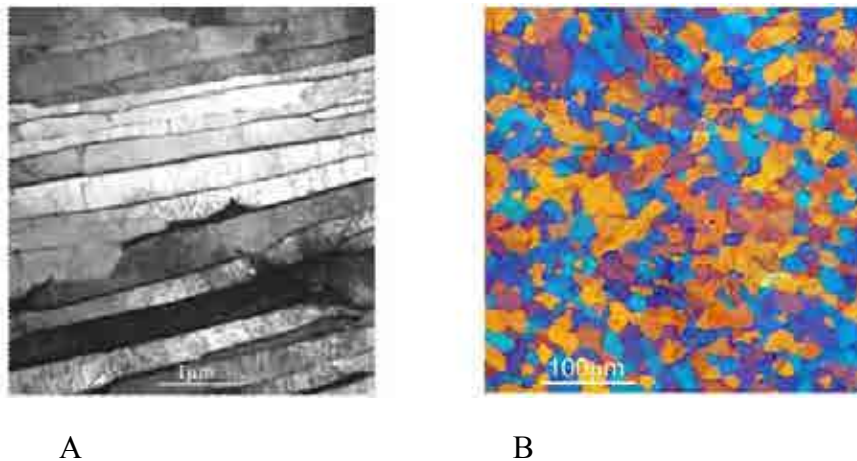


FIG. 1. A) TEM image of specimen from Zr2.5%Nb pressure tube (radial-hoop plane). B) Polarized light image of warm-rolled Zircaloy-4 plate (normal-transverse plane).

#### 2.2. Zircaloy-4 plates

The second set of samples consisted of small coupons machined from a warm-rolled Zircaloy-4 plate of 6.25 mm thickness, produced by Wah Chang, USA (ASTM B352, Grade R60804). Coupons had dimensions of 10 mm along the transverse direction (TD) and 7mm along the rolling direction (RD). This material was used in the manufacture of the reflector vessel for OPAL, a research reactor at ANSTO, Australia [8]. Figure 1-b shows the microstructure of the material across the ND-TD plane, as observed in the microscope under polarized light, after polishing and etching of the samples following the procedures described in Ref [12]. Different colours correspond to different grain orientations. This Zircaloy-4 plate has the typical equiaxed grain structure of annealed rolled plates, with diameters ranging from 10-20  $\mu\text{m}$ , very similar to that of the Zircaloys used for fuel cladding. A thorough characterization of this material has been presented in Ref [13]. The rolled plate presents a

## 2.2. Research on zirconium based materials (including hydrogen uptake)

typical rolling texture, which can be idealized as being composed by two Zr grains having their *c*-axes lying on the ND-TD plane, at angles of  $\pm 33^\circ$  to the ND. For comparison with other techniques, the texture of both specimens was also characterized by X ray diffraction.

## 3. INSTRUMENTS

Three specifically designed texture diffractometers (SKAT, HIPPO, CARR-TD), and two residual stress diffractometers (Kowari, ENGIN-X) were used for this exercise. Two of them are constant-wavelength instruments (Kowari, CARR-TD), and three are polychromatic instruments using the time-of-flight (TOF) technique (SKAT, HIPPO, ENGIN-X). Brief descriptions of each of them are given below. It is worth noting that constant-wavelength diffractometers rely on well-resolved peaks for individual pole figure measurements, while TOF diffractometers typically utilize the information contained within the full pattern, typically by Rietveld-type least-squares refinement.

HIPPO (LANSCE, LANL, USA): This instrument is a general purpose TOF diffractometer located at a  $\sim 9$ m long flight path optimized to perform fast quantitative texture analysis. It has a three-dimensional arrangement of detector banks with 1240  $^3\text{He}$  tubes, on five conical rings with scattering angles ranging from  $2\theta = 60^\circ$  to  $150^\circ$ . A large sample chamber can accommodate ancillary equipment such as an automatic sample changer, furnaces, cryo-equipment, a load-frame, high pressure cells or a magnet. Flux at sample is  $\sim 10^7 \text{ n}\cdot\text{cm}^{-2}\cdot\text{s}^{-1}$  with a 10 mm beam diameter [14].

SKAT (IBR-2, JINR, Russia): This is a TOF diffractometer located at a  $\sim 100$ m long flight path, specially designed for measurement of texture in large-grained geological specimens. SKAT has an axisymmetrical arrangement of detector modules on a single Debye-Scherrer cone at a scattering angle of  $2\theta = 90^\circ$ . This results in identical positions of the diffraction peaks for all detectors, so all  $\lambda$ - and  $\theta$ - dependent corrections (except for sample shape related ones) are avoided, and only the detector efficiency needs to be considered. [15]

Texture Diffractometer (CARR, CIAE, China): This recently commissioned constant-wavelength diffractometer is located at a thermal neutron beam and it has been specifically designed to measure texture. A Cu(111) monochromator directs a  $25 \times 25 \text{ mm}^2$  neutron beam of  $1.43 \text{ \AA}$  into a sample located at 180 cm, fit into an Eulerian cradle of 25 cm diameter. Pole figures are produced using a single  $^3\text{He}$  detector tube.

Kowari (OPAL, ANSTO, Australia): This is a constant-wavelength diffractometer located at a thermal neutron guide specifically designed for measuring residual stresses. The incident wavelength between can be varied between  $1 \text{ \AA}$  and  $2.4 \text{ \AA}$  due to a variable take-off angle from a double-focusing bent-perfect crystal silicon monochromator. Flux at sample is  $\sim 2 \times 10^7 \text{ n}\cdot\text{cm}^{-2}\cdot\text{s}^{-1}$  (depending on incident wavelength). For texture measurements, the radial collimator in front of the detector is removed [16].

ENGIN-X (Isis, STFC, UK): This is a TOF residual stress diffractometer located at a  $\sim 50$ m flight path at the end of a curved ( $m = 3$ ) guide seeing a methane moderator. It is optimized to measure high-resolution diffraction patterns at precise locations deep in the interior of bulk samples. Two diffraction banks centered at Bragg angles  $2\theta = \pm 90^\circ$  measures full diffraction patterns along two perpendicular directions simultaneously [17]. Details of the strategy used for texture measurements and associated data-analysis can be found in Ref [18].

## 2.2. Research on zirconium based materials (including hydrogen uptake)

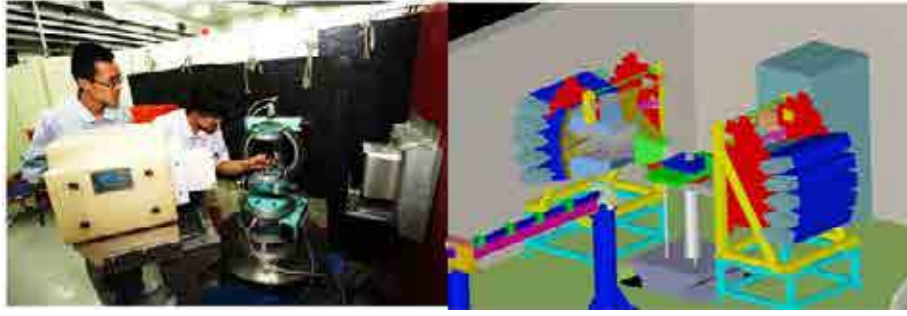


FIG. 2. a) Texture diffractometer at CARR, China. b) Schematic diagram of ENGIN-X.

## 4. ODF ANALYSIS AND DERIVED PARAMETERS

Specimens were distributed among participants for the determination of direct pole figures. A reduced number of complete pole figures were produced in the two constant-wavelength diffractometers. The  $\{(10-10), (0002), (10-11), (11-20)\}$  were measured at Kowari, and the  $\{(10-10), (0002)\}$  were measured at CARR-TD. These experimental pole figures were used to produce the ODF's using the Matlab Toolbox MTEX [19]. On the other hand, a larger number of inverse pole figures were measured at the TOF diffractometers, because in these instruments several reflections are measured simultaneously. In all three TOF instruments, a partial coverage of the pole figures was provided by the detector suite, which was completed by performing a limited number of specimen rotations. Three rotations were used at HIPPO and 18 rotations at SKAT for complete coverage of the pole figures. Four rotations were used at ENGIN-X, yet in this case pole figure coverage was incomplete and focused on the most relevant areas of the  $Zr_{2.5}\%Nb$  pole figures. This was used as an exercise for texture determination at TOF residual stress diffractometers, where a limited number of specimen orientation is usually explored, due to limitations in the beam time available to users.

Due to the complexity of the detector arrangement and incident beam corrections, pole figure extraction and ODF texture analysis at TOF diffractometers is simultaneously done by Rietveld-type full pattern software. At HIPPO the ODF was described in terms of a generalized spherical harmonics model using the code GSAS [20]. At SKAT, the ODF was described by the E-WIMV method using the code MAUD [21]. For presentation and calculation of derived parameters, recalculated pole figures produced by those programs were used as input to define the ODF within the MTEX Toolbox.

In quantitative texture analysis, the most frequently used measure to quantify the texture strength, i.e. the extent of preferred orientation, on which most of the macroscopic properties of anisotropic materials depend, is the texture index  $t$  [22],

$$t = - \int f(g)^2 dg \quad (1)$$

where  $g$  represents any orientation within the three dimensional orientation space, and  $f(g)$  is the ODF. The texture index aids in comparing the overall texture evolution of sample series, provided texture components of the same type are present in the polycrystalline aggregate.

In hexagonal materials, the Kearns texture factor [1] is another widely used method for quantifying texture information. This factor is a quantification of the volume fractions of crystallites with (typically) basal poles aligned along any single sample direction,

## 2.2. Research on zirconium based materials (including hydrogen uptake)

$$f_z = \int_0^{\pi} I_{(0002)}(\varphi) \sin \varphi \cos^2 \varphi d\varphi, \quad (2)$$

where  $z$  is the direction of interest, and  $I_{(0002)}(\varphi) \sin \varphi$  is the fraction of crystals having their  $c$ -axis at an angle  $\varphi$  from that direction. In particular, for three mutually orthogonal sample directions (e.g., hoop, radial or axial), the Kearns texture factors necessarily sum to one. In principle this parameter represents the effective value of a physical property along the (0001) crystal direction, projected into the specimen direction of interest; hence it includes the projection from all constituent crystallites.

All Kearns factors and texture indices were calculated from the refined ODF's using the MTEX Toolbox.

## 5. RESULTS

### 5.1. Zr-2.5%Nb pressure tubes

Experiments on the Zr2.5%Nb specimens have been performed on the SKAT, Kowari and ENGIN-X. Figure 3 shows the pole figures recalculated from the ODFs and Table 2 the derived Kearns factors and texture indices. Good agreement is found both qualitatively and quantitatively between the different instruments.

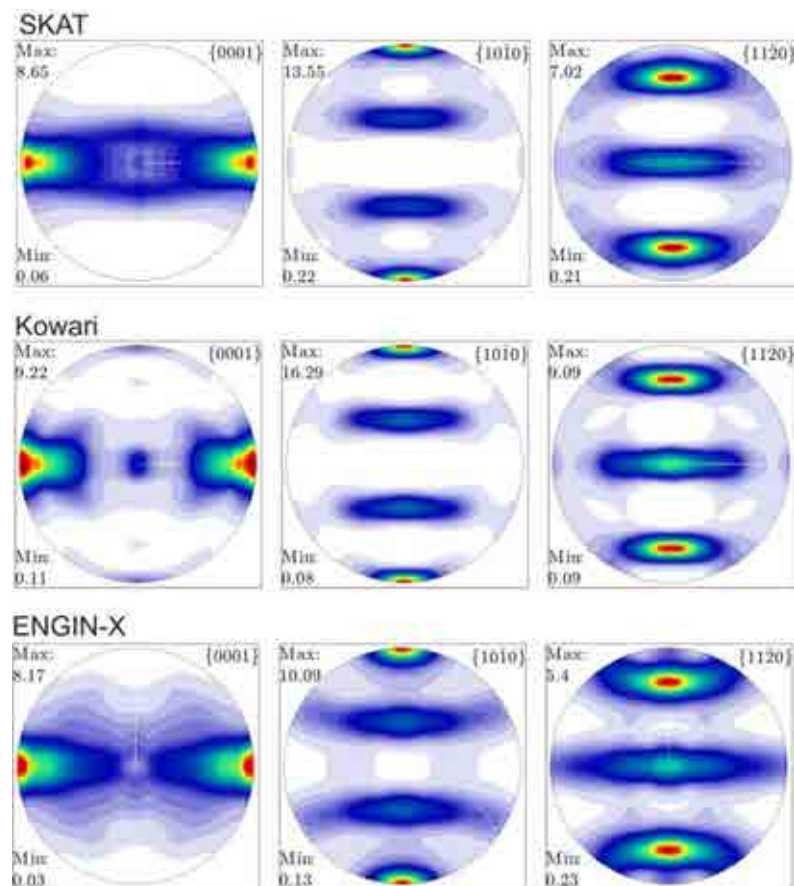


FIG.3. Recalculated pole figures for the Zr2.5%Nb specimens.

## 2.2. Research on zirconium based materials (including hydrogen uptake)

TABLE 1. KEARNS FACTORS AND TEXTURE INDEX FOR THE ZR2.5%NB SPECIMENS. TYPICAL UNCERTAINTY IS 0.02

	Hoop	Radial	Axial	Sum	Text index
SKAT	0.564	0.344	0.090	0.998	6.6
Kowari	0.546	0.356	0.094	0.996	6.9
ENGIN-X	0.566	0.326	0.105	0.997	4.9

## 5.2. Zircaloy-4 plates

Experiments on the Zircaloy-4 specimens have been performed on the CARR, HIPPO and Kowari. Figure 4 shows the pole figures recalculated from the ODFs and Table 3 the derived Kearns factors and texture indices. Good agreement is found both qualitatively and quantitatively between the different instruments.

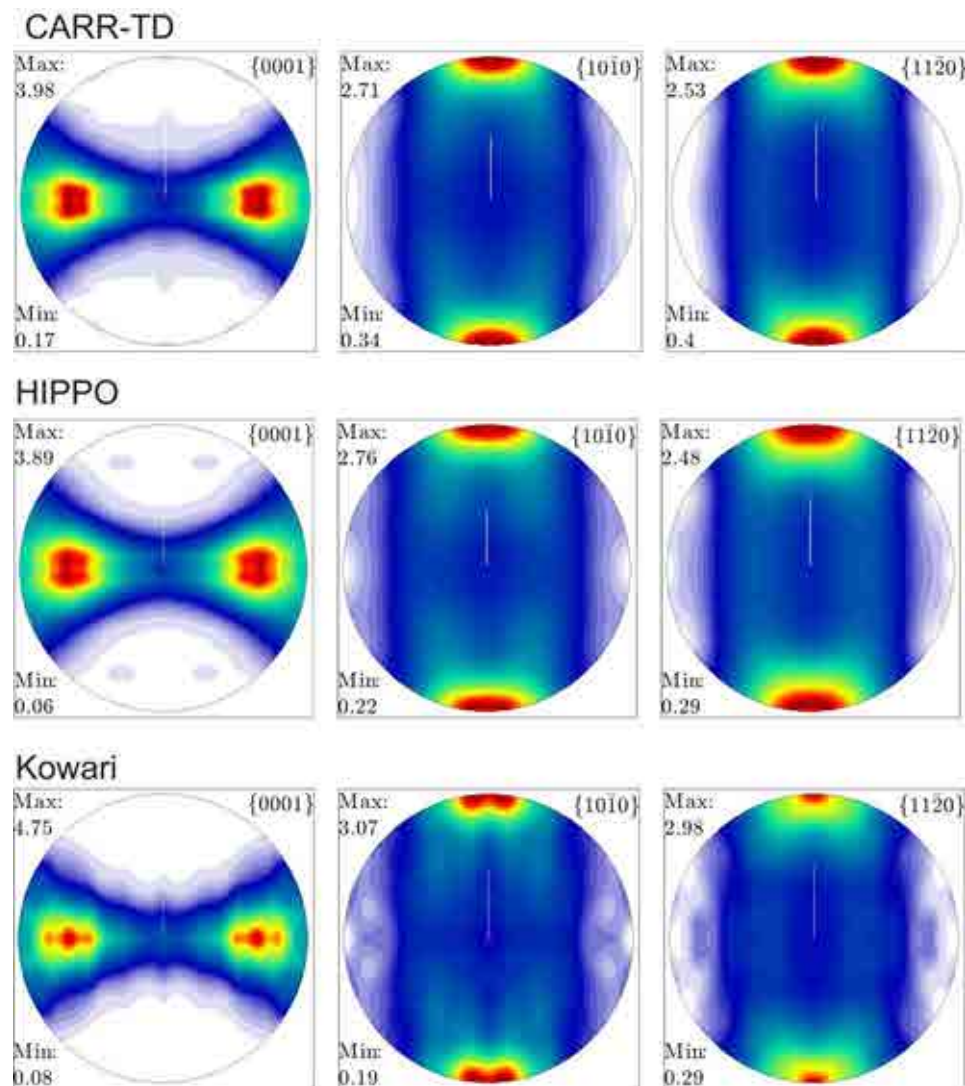


FIG. 4. Recalculated pole figures for the Zircaloy-4 specimens.

## 2.2. Research on zirconium based materials (including hydrogen uptake)

TABLE 2. KEARNS FACTORS AND TEXTURE INDEX FOR THE ZIRCALOY-4 SPECIMENS. TYPICAL UNCERTAINTY IS 0.02

	Transverse	Normal	Rolling	Sum	Text index
CARR-TD	0.352	0.527	0.118	0.997	2.02
HIPPO	0.359	0.543	0.096	0.998	2.15
Kowari	0.357	0.551	0.090	0.998	2.32

## 6. DISCUSSION

Overall, good agreement is found both qualitatively and quantitatively among the pole figures obtained for the two materials at the different neutron diffractometers. All Kearns factors are within an uncertainty of 0.02, which is lower than typical differences usually found between different batches, or between the start and end of pressure tubes [23]. This is deemed very satisfactory, and can be compared with a variation of  $\sim 0.06$  reported in a 14-participants round robin Zircaloy-4 texture measured by X ray diffraction [2]. The reliability of neutron diffraction for texture measurements was also documented previously [24]. The Kearns factors measured for the transverse, normal and rolling directions of the Zircaloy-4 plate are comparable to the values reported in that work for stress-relieved Zircaloy-4 fuel cladding of 0.635 mm wall thickness,  $f_H = 0.30-0.36$ ,  $f_R = 0.54-0.66$ ,  $f_A = 0.03-0.09$ , respectively. On the other hand, the Kearns factors measured for the pressure tube compare well with values obtained by X ray diffraction,  $f_H = 0.53-0.56$ ,  $f_R = 0.34-0.39$ ,  $f_A = 0.06-0.10$  [23]. So, the 0.02 uncertainty found between laboratories is small compared to conventional X ray diffraction. This is very likely because of the much larger volume of material gauged by neutron instruments. Variations in texture indices were larger than for Kearns factors, particularly for the Zr2.5%Nb pressure tubes. This is because the sharpness of this texture makes the ODF determination much more sensitive to the exact gridding used in the experiments and angular range of crystallite orientations that is ‘seen’ by each detector.

It is interesting to mention that satisfactory results were obtained from the residual stress diffractometers (ENGIN-X, Kowari), although these instruments are not optimized for this purpose. This opens the possibility of exploiting the spatial resolution provided by such instruments to precisely quantify the characteristic texture variation found in Zr-alloys welds [8].

## 7. CONCLUSIONS

The crystallographic texture of specimens made of Zr alloys can be precisely quantified in a variety of neutrons instruments worldwide with little sample preparation required. A preliminary round robin on specimens made of Zr2.5%Nb and Zircaloy-4 was successful, and demonstrated that operational parameters such as Kearns factors are defined with a typical uncertainty of  $\pm 0.02$ .

## 2.2. Research on zirconium based materials (including hydrogen uptake)

### REFERENCES

- [1] KEARNS, J., *J. Nuclear Materials* **299** (2001) 171-174.
- [2] LEWIS, J et al, *Proc. 5<sup>th</sup> Conf. Zr in Nuclear Industry*, ASTM STP **754** (1982) 39-62.
- [3] SUMIN, V., et al., *J. Nuclear Materials* **421** (2012) 64–72.
- [4] BALOGH, L., et al, *Acta Materialia* **60** (2012) 5567-5577.
- [5] XU, F., et al., *J. Nuclear Materials* **394** (2009) 9-19.
- [6] CAI, S., *Acta Materialia* **60** (2012) 3355-3369.
- [7] WENK, H., *Acta Materialia* **52** (2004) 1899-1907.
- [8] CARR, D., et al, *J. Nuclear Materials* **359** (2006) 202-207.
- [9] KOCKS, U., TOME, C.N., WENK, H.-R., *Texture and Anisotropy*, Cambridge Univ. Press (2000).
- [10] BANCHIK, AD., et al, *CNEA Technical Report CNEA DD-ATN40MF-001* (2009).
- [11] HOLT R., ALDRIDGE, S., *J. Nuclear Materials* **135** (1985) 246-259.
- [12] KAUFMANN, P., *ASTM STP* **551** (1974) 52.
- [13] ZANELATO, O., *Ph D Thesis, The Open University, United Kingdom* (2009).
- [14] WENK, H., *Nuclear Instr. Methods A* **515** (2003) 575–588.
- [15] ULLEMEYER, K., et al, *Nuclear Instr. Methods A* **412** (1998) 80-88.
- [16] BRULE, A., KIRSTEIN, O., *Physica B* **385,386** (2006) 1040–1042.
- [17] SANTISTEBAN, J.R., et al, *J. Applied Crystallography* **39** (2006) 812–825.
- [18] MALAMUD, F, SANTISTEBAN, J.R., submitted to *J. Applied Crystallography*.
- [19] HIELSCHER, R., SCHAE BEN, H., *Journal Applied Crystallography* **41** (2008) 1024-1037.
- [20] VON DREELE, R., et al., *Applied Crystallography* **15** (1982) 581–589.
- [21] WENK, H., et al., *Mater. Sci. Forum* **157,162** (1994) 473-480.
- [22] BUNGE, H., *Texture analysis in materials science: mathematical methods*. Butterworths (1982).
- [23] BUIOLI, C., et al, *Proc 39<sup>th</sup> Meeting of Argentina Nuclear Tech. Association-AATN*, (2012).
- [24] WENK, H., *J. Appl. Cryst.* **24** (1991) 920-927.

## 2.2. Research on zirconium based materials (including hydrogen uptake)

### CRYSTALLOGRAPHIC PHASES, TEXTURE AND DISLOCATION DENSITIES OF Zr2.5%Nb PRESSURE TUBES AT DIFFERENT STAGES OF MANUFACTURING

J. R. SANTISTEBAN\*\*, P. VIZCAÍNO\*\*, M. A. VICENTE-ALVAREZ\*, F MALAMUD\*, A TARTAGLIONE\*

\*CONICET and Instituto Balseiro, Centro Atómico Bariloche, Bariloche, Argentina

\*\*Centro Atómico Ezeiza, Comisión Nacional de Energía Atómica, Buenos Aires, Argentina

#### Abstract.

Neutron diffraction experiments have been performed on specimens produced from Zr2.5%Nb pressure tubes, in order to characterize the crystallographic phases, texture and dislocation densities at different stages of a new manufacturing schedule developed in Argentina. Experiments were performed on ENGIN-X a time-of-flight neutron strain scanner at the Isis Facility, UK, using an optimized measurement strategy that exploits the well-known crystallographic texture of the pressure tubes.

## 1. INTRODUCTION

Due to its good mechanical strength, high corrosion resistance and strong creep resistance, combined with excellent neutronic properties, Zr2.5%Nb has been selected as the pressure tube material for CANDU reactors. In order to assess the operating life of pressure tubes, properties such as hydride cracking, creep and irradiation growth have been thoroughly investigated in the past. It has been found that the irradiation response of Zr2.5%Nb pressure tubes is strongly dependent on the texture, microstructure and intergranular residual stresses, which are controlled by the manufacturing schedule [1]. Starting from Zr2.5%Nb billets forged at  $\sim 800^{\circ}\text{C}$ , the general fabrication route of CANDU pressure tubes consists of:

- i) extrusion at  $\sim 800^{\circ}\text{C}$ , followed by air cooling;
- ii) cold draw to  $\sim 20\text{--}30\%$  strain;
- iii) autoclaving at  $400^{\circ}\text{C}$  for 24 h.

After extrusion, the material consists of  $\sim 90\%$  hcp  $\alpha\text{-Zr}$ , which has Nb content  $< 1\%$ , and  $\sim 10\%$  metastable bcc  $\beta\text{-Zr}$ , which contains approximately 20% Nb. During autoclaving,  $\beta\text{-Zr}$  partially transforms to  $\beta\text{-Nb}$  ( $\sim 95\%$  Nb) and contains a metastable  $\omega$ -phase and an enriched  $\beta\text{-Zr}$  ( $\sim 50\%$  Nb). The texture and the density of dislocations of the finished tube are important variables that are carefully specified by the designer, due to their impact on in-reactor performance. Texture is specified through the Kearns factors ( $f_H$ ,  $f_R$ ,  $f_A$ ) [2], parameters assessing the proportion of c-axes that are projected along the tube three principal axes; i.e., *Hoop*, *Radial* and *Axial*, respectively. The Kearns factor is normally calculated from experimental (0002) or (0004) pole figures measured by laboratory X rays [3]. Regarding dislocation densities, designers specify maximum numbers for *a*-type and *c*-type dislocations, as they evolve differently upon irradiation. Dislocations densities are also commonly defined by X ray diffraction, from the observed broadening of the peaks [4].

In Argentina, CNEA has developed a slightly different processing schedule which starts from the extruded tubes and replaces the cold-draw stage by a cold pilgering stage [5]. Although the tube deformation introduced by cold drawing and cold rolling are equivalent ( $\sim 20\text{--}30\%$  strain), differences in starting material and deformation processes suggest that dislocation densities, residual stresses and texture profiles of finished tubes would not be identical. In order to characterize this processing schedule, in this work we have determined the texture and dislocations densities of experimental pressure tubes at different stages of manufacturing by TOF neutron diffraction experiments performed at the ENGIN-X neutron strain scanner, Isis Facility, UK [6]. The present results open interesting perspectives for the

## 2.2. Research on zirconium based materials (including hydrogen uptake)

characterization of Zr tubing at neutron strain scanners. The use of neutrons allows the non-destructive characterization of bulk specimens with minimal sample preparation required, an important advantage for the investigation of irradiated specimens after long times in service [7]. Moreover, the spatial resolution available at neutron strain scanners allows the non-destructive investigation of the variation of texture and dislocation densities across specimens [8]. Finally, it is also possible to follow the changes in such properties during thermo-mechanical treatments, as these instruments are usually furnished stress rigs and furnaces available while recording diffraction data.

## 2. SAMPLES

Small sections having dimensions of  $\sim 10 \times 20$  mm along the axial and rolling directions, respectively, were machined out of experimental Zr-2.5%Nb pressure tubes, corresponding to different stages of the manufacturing route being developed at CNEA. The first specimen is from a extruded tube, the starting material for the process. The second specimen corresponds to the same material after 28% cold rolling. The third specimen is from a finished tube, obtained after a 24 hours heat treatment at 400°C of the cold-rolled material.

Texture of the cold-rolled and heat-treated tube was also measured by conventional techniques. Pole figures were measured by constant wavelength neutron diffraction experiments performed at the Kowari beamline, OPAL, Australia, and at the SKAT beamline, IBR-2, Russia [9]. Besides this, several pole figures of specimens taken from the front and back of three finished tubes were determined by X ray diffraction experiments in Argentina [10]. The Kearns factors derived from those measurements are listed in Table 1.

TABLE 1. KEARNS FACTORS OF (COLD-ROLLED + HEAT-TREATED) SPECIMENS OBTAINED BY CONVENTIONAL TECHNIQUES: NEUTRON DIFFRACTION (KOWARI, SKAT) AND X RAYS. TYPICAL UNCERTAINTY IS 0.02

	Hoop	Radial	Axial	Sum
Kowari	0.546	0.356	0.094	0.996
SKAT	0.564	0.344	0.09	0.998
X rays	0.532	0.376	0.076	0.984

## 3. EXPERIMENTS

Neutron diffraction experiments were performed on the ENGIN-X beamline, at the ISIS Facility, UK. ENGIN-X is a TOF strain scanner [6], i.e., an energy-dispersive neutron diffractometer with precise and flexible definition of the gauge volume, capable of measuring diffraction patterns deep in the interior of bulk samples. A schematic description of the instrument is presented in Figure 1. Two diffraction banks centered at Bragg angles  $2\theta = \pm 90^\circ$  allow measuring full diffraction patterns along two perpendicular directions simultaneously, i.e., the hoop and radial direction of the tube displayed in the figure. The pressure tube samples were fitted into a goniometer in order to record diffractograms for three more orientations of the specimen. Two orientations corresponded to  $15^\circ$  and  $30^\circ$  rotations around the vertical (axial) axis respectively, and the third one to a  $90^\circ$  rotation around the horizontal (radial) axis. These four sample orientations were carefully chosen in order to cover the most relevant parts of the pressure tube pole figures. Strain scanning experiments

## 2.2. Research on zirconium based materials (including hydrogen uptake)

require a narrow divergence of the incident beam, but in the present experiments this was relaxed in order to reduce counting times. Measurement were performed using a gauge volume of  $\sim 6 \times 4 \times 4 \text{ mm}^3$  and a counting time of 6.5 minutes per orientation, making a total time of  $\sim 1/2$  hour per sample and  $\sim 2$  hours to complete the experiment.

Two different data analysis strategies were adopted. For the study of crystallographic phases all diffractograms recorded for each specimen were summed up together, in order to obtain a single *bulk* diffractogram representative of the bulk of the material, i.e., independent of sample orientation. On the other hand, for the study of texture and intergranular stresses the diffractograms recorded along the different specimen directions were analyzed separately. Moreover, for the texture analysis the angular resolution of the instrument was increased *a posteriori*, by splitting the relatively large solid angle covered by the detection banks into smaller sub-units. Each diffraction bank actually consists of 1200 individual detectors, 3 mm wide and 196 mm high, arranged in a grid of  $240 \times 5$ , covering  $\pm 16^\circ$  in the horizontal plane and  $\pm 21^\circ$  in the vertical plane. Here, we divided each bank into  $(8 \times 5 =)$  40 smaller units, each one containing 30 detectors and covering  $\sim 2^\circ \times 4^\circ$ , in order to explore 80 points of the pole figure from a single orientation of the specimen. The inset in Fig. 3 shows the actual directions in the specimen explored by the present experiments with the four sample orientations explained above.

All diffraction spectra were normalized by the spectra recorded for a VNb specimen, which represents a good approximation to an elastic-incoherent scatterer. Diffractions peaks from a  $\text{CeO}_2$  calibration powder were nearly symmetrical, due to the large broadening resulting from the increased incident divergence. The position, integrated area, and width of all diffraction peaks were obtained by using least-squares Gaussian fit to the normalized peaks.

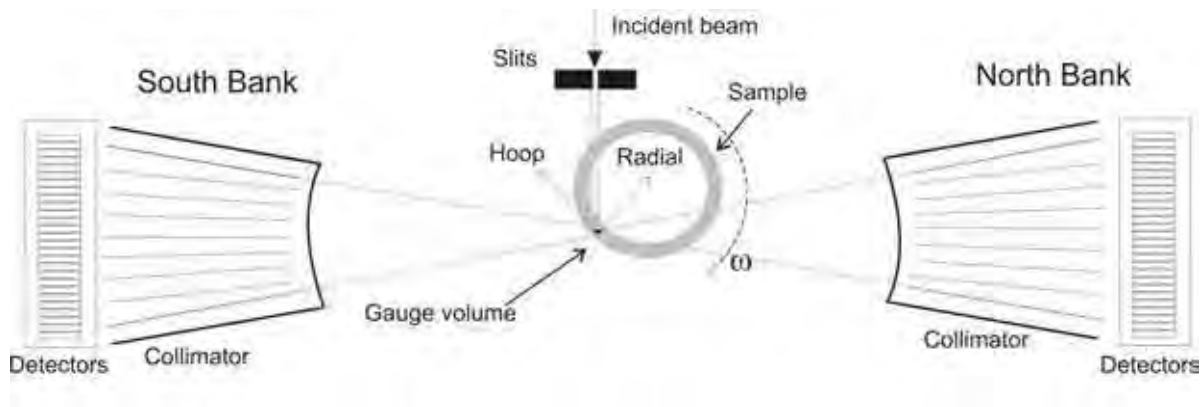


FIG. 1. Schematic diagram of experimental arrangement showing the sample directions (hoop, radial) respectively explored by the two diffraction banks (south, north) for this sample orientation.

## 4. RESULTS

### 4.1. Crystallographic phases

Figure 2 shows a detail of the bulk diffractograms obtained for the different manufacturing stages, where the main crystallographic phases have been indexed. As expected, all diffractograms look very similar with the hexagonal  $\alpha$ -Zr phase dominating the pattern, yet with broader peaks observed for the cold worked material. The main differences in microstructure reveal through changes in the minority phases. The extruded material displays sharp (200), (211), (110) peaks from the  $\beta$ -Zr phase of a composition of  $\sim 23\%$  Nb

## 2.2. Research on zirconium based materials (including hydrogen uptake)

( $\beta_{23\%}$  phase). The composition is calculated from Vegard's law for the ZrNb system given in Ref. [11],  $a_{\beta-Zr} = 3.5878 - 0.00288 \times \text{at\% (Nb)}$ , with  $a_{\beta-Zr}$  the lattice parameter of the cubic  $\beta$  phase in Å. The  $\beta_{23\%}(200)$  peaks displays a small left shoulder which could be due to some segregation of localized regions enriched in Nb. The  $\beta_{23\%}$  phase is also observed in the cold worked material, with the peaks substantially broader due to the 28% cold deformation. Besides this, the  $\alpha(0002)$  peaks shifts towards shorter  $d$ -spacings, and a shoulder appears on the left side of this peak.

After the heat treatment, the  $\beta_{23\%}$  phase decomposes into a  $\beta$ -Zr phase with a composition of  $\sim 40\%$  Nb and the  $\omega$ -Zr phase. The  $\beta_{40\%}(200)$  peak appears much broader than the  $\alpha(20-21)$  peak. On the other hand, the  $\alpha$ -Zr peaks become sharper, but they are still slightly broader and less intense than those of the extruded material. Besides this, the background level between diffraction peaks is clearly lower for the extruded specimen than for the other two specimens. These two observations indicate that the very high short-range strains responsible for the increase in background and the decrease in peak intensity are more stable than the small long-range strains responsible for the increase in line breadths [12].

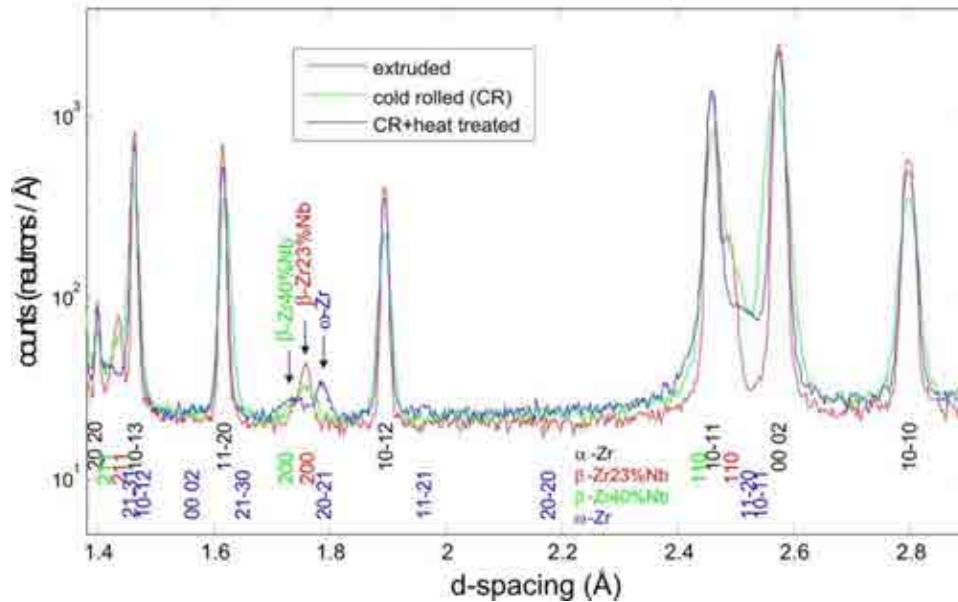


FIG. 2. Bulk diffractograms for specimens from the different manufacturing stages.

## 4.2. Texture and Kearns factor

The texture of Zr2.5%Nb pressure tubes is very strong and is mainly defined at the extrusion stage [13]. The orientation distribution function of the material is dominated by crystals having their (10-10) axes along the tube axial direction and their  $c$ -axes along the tube hoop direction. This produces a very intense axial (10-10) pole, and a less sharper (0002) pole along the hoop direction, that extends towards the radial direction (Figure 4). The aim of the present study is to reveal the differences that may exist between the different manufacturing stages, and to quantify such differences in terms of the Kearns factor [2],

$$f_z = \int_0^{\pi} I_{(0002)}(\varphi) \sin \varphi \cos^2 \varphi d\varphi, \quad (1)$$

## 2.2. Research on zirconium based materials (including hydrogen uptake)

where  $z$  is the direction of interest (hoop, radial or axial), and  $I_{(0002)}(\varphi) \sin \varphi$  is the fraction of crystals having their  $c$ -axis at an angle  $\varphi$  from that direction. To do this, the experimental exploration of the pole figures was concentrated along the hoop-radial line and around the axial direction, as observed in the experimental (0002) pole figure shown in the inset of Fig. 3. Details of the hoop-radial line of such pole figure (indicated by the pink line) for the three specimens are displayed by the solid symbols in the plot. Cold rolling produces a drop of  $\sim 30\%$  in the number of crystals with  $c$ -axes along the hoop direction ( $\varphi = 90^\circ$ ), and an increase in those with  $c$ -axis at angles  $\varphi < 60^\circ$ . The heat treatment partially reverses this effect.

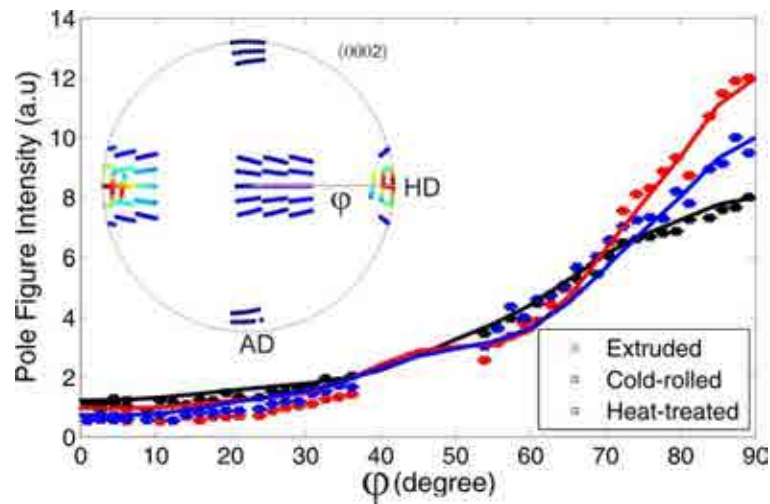


FIG. 3. Experimental pole figures along the hoop-radial direction recorded for the three specimens. Angular resolution in  $\varphi$  is  $1^\circ$ . Solid lines are calculated values from the refined ODF's.

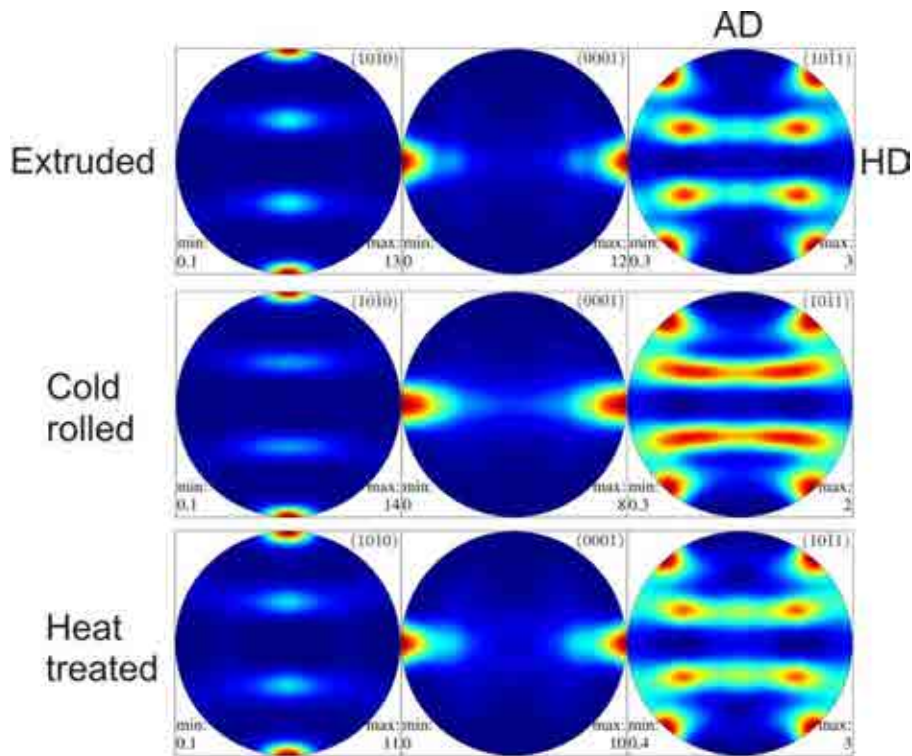


FIG. 4. Recalculated pole figures the specimens from the different manufacturing stages.

## 2.2. Research on zirconium based materials (including hydrogen uptake)

The ODF of each sample was determined using the Matlab MTEX toolbox [14] from four experimental pole figures  $\{(10-10), (0002), (10-11) \text{ and } (10-12)\}$ , following the procedure described in Ref. [8]. The MTEX algorithm is optimized for sharp textures and high-resolution pole figures measured with respect to arbitrarily scattered specimen directions. Figure 4 displays recalculated pole figures. Please, note that the different pole figures have different maximum intensities. In addition to the referred intensity changes of the (0002) pole figure along the hoop direction, cold rolling produces a  $\sim 10\%$  increase in the sharp axial (10-10) pole, followed by a  $\sim 20\%$  decrease after heat treatment. Recalculated pole figures for the radial-hoop line are given by the solid lines in Fig. 3, which show that the refined ODF's effectively capture the small differences between specimens. The Kearns factor obtained from the recalculated (0002) pole figures are listed in Table 1. The results for the CRHT (cold-rolled+heat-treated) specimen compare well with those obtained by the traditional techniques presented in Table 1. Cold rolling produces an increase in the hoop Kearns factor from 0.56 to 0.62. This reflects the increase in the number of crystals having  $c$ -axes at intermediate angles between the hoop and radial directions, as these contribute more due to the  $(\sin \varphi \cos^2 \varphi)$  factor in the integral. The heat-treatment results in a hoop Kearns factor very close to that of the original extruded tube, despite the clear differences between specimens observed in Fig. 3. These results highlight that rough estimations of Kearns factors based solely on intensities registered at principal directions may be misleading.

## 2.2. Research on zirconium based materials (including hydrogen uptake)

TABLE 2. RESULTS OF THE ANALYSIS PERFORMED ON THE THREE SAMPLES. NOTE:  $\sigma_c$ : STANDARD DEVIATION OF LATTICE PARAMETER  $c$ ,  $\langle \varepsilon^2 \rangle^{1/2}$ : MEAN-SQUARE STRAIN,  $\Delta K_0$ : INTERCEPT OF W-H PLOT (FIG. 5)

Sample	Kearns factor ( $\pm 0.02$ )			$\sigma_c$ [ $\mu\varepsilon$ ]	$\langle \varepsilon^2 \rangle^{1/2}$ [ $\mu\varepsilon$ ]	$\Delta K_0$ [ $10^{-4} \text{Å}^{-1}$ ]	Dislocation density [ $\times 10^{14} \text{m}^{-2}$ ]		
	Hoop	Radial	Axial				$\rho_a$	$\rho_c$	$\rho_a + \rho_c$
	Extruded	0.564	0.361	0.073	100	330	3.2	0.1	0.04
cold-rolled (CR)	0.618	0.288	0.091	900	1200	2.2	9.2	1.8	11.0
CR+heat-treated	0.556	0.335	0.108	500	640	2.4	1.3	0.36	1.66

## 4.3. DISLOCATION DENSITIES

The microscopic deformation of the lattice manifests through broadening of the diffraction peaks. The most simple analysis of peak broadening is that of Williamson and Hall [12], in which the *physical* broadening is analyzed in the reciprocal space using the variable  $K=1/d$ , where  $d$  is the interplanar distance corresponding to each peak. Figure 5 shows the Williamson-Hall plots obtained for the three specimens. Only reflections whose width could be properly defined for all three specimens were included in the plot. Other reflections were considerably affected by neighboring peaks (either from  $\alpha$ -Zr or from secondary phases). Diffraction peaks in  $d$ -scale were well-described by Gaussian profiles, so the physical broadening (in  $d$ ) was calculated from the observed broadening as  $\sigma_{phys} = (\sigma_{obs}^2 - \sigma_{instr}^2)^{1/2}$ , with  $\sigma_{instr}$  the (interpolated) Gaussian width measured for a CeO<sub>2</sub> reference powder. The extruded and CRHT specimens display reasonably linear behavior, yet the deviations from a straight line are much higher than the uncertainty of the measured points. For the cold-rolled specimen such deviations are  $\sim 20\%$  and a linear dependence is not evident. The slope ( $m$ ) obtained by a least-squares fit gives a measure of the mean-square strain in the material,  $\langle \varepsilon^2 \rangle^{1/2} = m/\sqrt{2\pi}$ . The values obtained for the three specimens are listed in Tab. 2. These strains are comparable to the standard deviation observed of the lattice parameter  $c$  ( $\sigma_c$ ), measured along directions between the hoop and radial directions, and obtained from the position of the 0002 and 0004 peaks. The intersection of the  $\Delta K$  curves with the origin ( $\Delta K_0$ ) is defined by the average grain size of the material. In the present case, the intercept of all three least-squares lines are  $\Delta K_0 \sim 0.0002 \text{ Å}^{-1}$ , indicating rather large grain sizes that will be difficult to define by these technique. This conclusion is valid even considering that for the Gaussian peak shapes observed here the DK curves should flatten near the origin.

An estimation of the density of dislocations within the material can be obtained by considering that the observed slopes are exclusively due to dislocations. For an isotropic distribution of dislocations, the dislocation density can be calculated from the mean-square strain,  $\rho = K \langle \varepsilon^2 \rangle^{1/2} / b^2$ , with  $b$  the Burgers vector and  $K$  a constant that includes details of the dislocation type [15]. For the anisotropic distribution of dislocations in hexagonal close-packed Zr, this equation can be modified to calculate the type- $a$  and type- $c$  component dislocations. In the present analysis we have followed the assumptions in Ref [4], which gives

$$\rho_c = \langle \varepsilon^2 \rangle_c 10^{20} \text{ m}^{-2}, \quad \rho_a = 5 \langle \varepsilon^2 \rangle_a 10^{20} \text{ m}^{-2}, \quad (2)$$

## 2.2. Research on zirconium based materials (including hydrogen uptake)

with  $\langle \varepsilon^2 \rangle_c$  and  $\langle \varepsilon^2 \rangle_a$  the mean-square strains obtained for the basal (0001) and prism (10-10 and 11-20) planes of the hexagon respectively. The dislocations densities obtained for the three specimens studied here are listed in Table 2. We have used the basal (0002) and (0004) peaks to define  $\langle \varepsilon^2 \rangle_c$ , and the (10-10) and (20-20) prism peaks of type I to define  $\langle \varepsilon^2 \rangle_a$ , as indicated in Figure 5 for the cold-rolled specimen. The reported dislocation densities are within the values expected for this material for these microstructural conditions [4]. The values of the CRHT lie within the specifications for the final product.

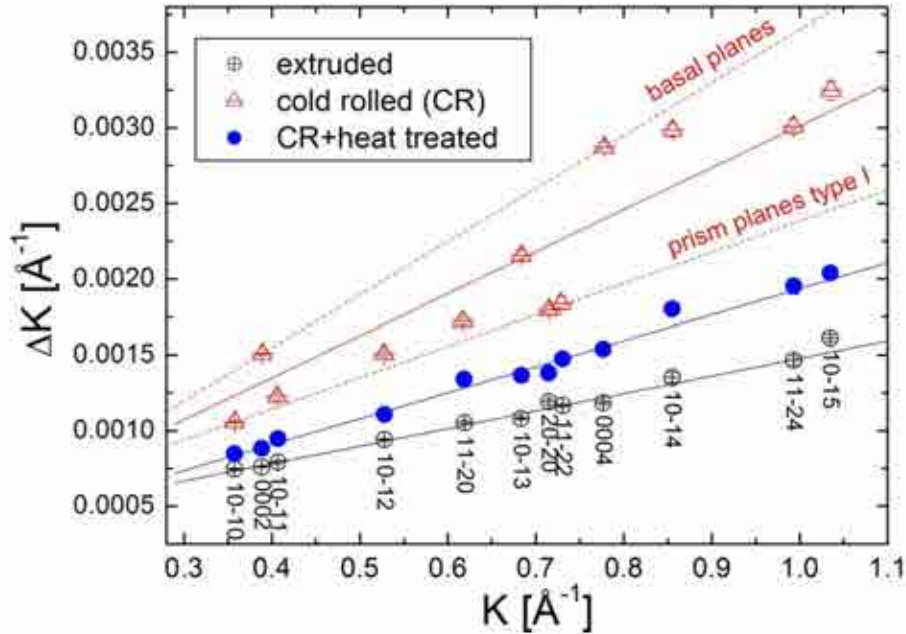


FIG. 5. Williamson-Hall plot of the physical peak broadening measured for the three samples.

A more sophisticated analysis of peak widths based on a modified Warren-Averbach method [16] was also applied, but the details of this analysis procedure are beyond the scope of this work. The analysis provided a value of  $\rho_{\text{tot}} = (1.4 \pm 0.6) \times 10^{14} \text{ m}^{-2}$  for the CRHT specimen, composed by  $\rho_a = 0.84 \times 10^{14} \text{ m}^{-2}$ ,  $\rho_c = 0.18 \times 10^{14} \text{ m}^{-2}$  and  $\rho_{a+c} = 0.36 \times 10^{14} \text{ m}^{-2}$ . Both the total and discriminated values agree well with the data reported in Table 2, when the  $a+c$  dislocation density is evenly distributed between type- $a$  and type- $c$  dislocations.

So far, attempts of such analysis have been unsuccessful for the extruded and cold-rolled specimens. In the first case it was because the observed broadening was too close to the instrument resolution, severely affecting the deconvolution procedure used to evaluate the physical broadening. In the second case it was not possible to find a combination of working slip systems responsible for the observed peak broadenings. This suggests that the analysis should include other deformation modes such as stacking faults or twinning.

## 5. CONCLUSIONS

Subtle microstructural changes occur during the manufacturing of Zr2.5%Nb pressure tubes, which must be properly controlled in order to satisfy design specifications. Diffraction experiments using a collimated polychromatic beam of neutrons have allowed a very detailed characterization of such changes in specimens produced at three stages of the manufacturing process: after extrusion, after 28% cold-rolling and after an autoclaving heat treatment. Due to

## 2.2. Research on zirconium based materials (including hydrogen uptake)

an optimized measurement strategy, a relatively short time of ~30 minutes was required to characterize each sample.

Microstructural changes manifested through small changes in the intensity and broadening of diffraction peaks from the main  $\alpha$ -Zr phase, and by substantial changes in the composition and crystal structure of the secondary phases ( $\beta$ -Zr and  $\omega$ -Zr). Subtle changes in the number of crystals having  $c$ -axis lying in the hoop-radial plane of the tubes were resolved by the experiments. Such variations were quantified in terms of the orientation distribution of crystallites (ODF), and by Kearns factors, the operational variable used in manufacturing. A Williamson-Hall analysis of the relatively large variations observed in peak width provided the mean-square strain for each condition, which correlated well with angular variations observed in interplanar distances. An interpretation of such strain in terms of dislocations allowed the quantification of the dislocation densities of type- $a$  and type- $c$ , which were well within the ranges expected for the material after the different thermo-mechanical treatments.

The present work can be used as a guideline for the precise characterization of Zr2.5%Nb pressure tubes using time-of-flight neutron strain scanners.

## 2.2. Research on zirconium based materials (including hydrogen uptake)

### REFERENCES

- [1] HOLT, R.A., J. Nuclear Materials **372** (2008) 182-214.
- [2] KEARNS, J.J., J. Nuclear Materials **299** (2001) 171-174.
- [3] LEWIS, J.E., et al, Proc. 5<sup>th</sup> Conf. Zr in Nuclear Industry, ASTM STP **754** (1982) 39-62.
- [4] WINEGAR, J.E., AECL Technical Report CRNL-4098 (1987).
- [5] BANCHIK, A.D., et al, CNEA Technical Report CNEA DD-ATN40MF-001 (2009).
- [6] SANTISTEBAN, J.R., et al, J. Applied Crystallography **39** (2006) 812-825.
- [7] BALOGH, L., et al, Acta Materialia **60** (2012) 5567-5577.
- [8] MALAMUD, F., SANTISTEBAN, J.R., submitted to J. Applied Crystallography.
- [9] SANTISTEBAN J.R., et al, Preliminary Round Robin on the determination of crystallographic texture of Zr components by neutron diffraction, this report.
- [10] BUIOLI, C., et al, Proc 39<sup>th</sup> Meeting of Argentina Nuclear Technology Association-AATN, (2012).
- [11] AURELIO, G., et al, Metall. Materials Transactions **A32** (2001) 1903-1910.
- [12] WILLIAMSON, G.K., HALL, W.H., Acta Metallurgica **1** (1953) 22-31.
- [13] HOLT, R.A., ALDRIDGE, S.A., J. Nuclear Materials **135** (1985) 246-259.
- [14] HIELSCHER, R., SCHAEBEN, H., J. Applied Crystallography **41** (2008) 1024-1037.
- [15] WILLIAMSON, G. K., SMALLMAN, R.E., Philos. Mag. **1** (1956) 34.
- [16] UNGAR, T., et al, J. Applied Crystallography **34** (2001) 298-310.

**2. RESULTS ACHIEVED**  
**2.4. RESULTS WITH IRRADIATED**  
**MATERIALS**

## 2.4. Results with irradiated materials

### EXAMINATION OF AUSTENITIC STEELS MICROSTRUCTURE CHANGE INDUCED NEUTRON IRRADIATION BY USING OF NEUTRON SCATTERING METHODS

A. KOZLOV\*, M. EVSEEV\*, I. PORNYKH\*, N. GLUSHKOVA\*, A. PIROGOV\*\*, S. BOGDANOV\*\*, V. VORONIN\*\*, I. BERGER\*\*

\* Institute of Nuclear Materials, 624250 Zarechny,  
Sverdlovsk Region,  
Russian Federation

\*\* Institute of Physics Metals, Yekaterinburg,  
S. Kovalevsky street, 18,  
Russian Federation  
Email: [alexim@e-sky.ru](mailto:alexim@e-sky.ru) ; [irm@irmatom.ru](mailto:irm@irmatom.ru)

#### Abstract.

Two cladding pin austenitic steels ChS68 and EK164 irradiated in the BN-600 reactor up to maximum dose ~80 dpa were examined by methods: neutron diffraction; small angle neutron scattering; X ray and electron microscopy. The formation and growth of both dislocation loops and radiation voids, as well as formation of segregation profiles, second phase precipitates, and chemical composition changes in a crystalline matrix were revealed in the steels after irradiation. All these resulted in growth of micro deformations in the crystalline matrix and changes of texture of the cladding pin steels, which were fixed by neutron diffraction and X ray methods. Texture decreasing more clearly occurred after low irradiation temperature (370°C) then after higher temperature irradiation (520°C). Observing of small angle neutron scattering increasing with dose growth is probably caused in He-v voids nucleus and segregations formed along dislocations and grain boundaries. At the present time the nature of scattering centers were not uniquely established. It is connected with an insufficiently adequate calculation model of small angle neutron scattering. Therefore solving of this problem requires additional development of calculation models. On the whole the examination shows that neutron scattering methods are very effective for research radiation induced structure changes.

## 1. INTRODUCTION

Austenitic steels are used as internal materials in the vessel of fast reactors. The steels operate under neutron irradiation at temperatures of 370-600°C and damage rate about  $10^{-6}$  dpa/s. The formation and growth of both dislocation loops and radiation voids [1], as well as formation of segregation profiles, second phase precipitates, and chemical composition changes in the crystalline matrix [2] were occur. In particular, helium and hydrogen playing important pole in swelling are generated in the steels under transmutation processes [3]. All these factors lead to changes in structure dimensions of vessel internal elements, loose of strength, and embrittlement of the materials, so it limits life-time of constructions [4]. An actual task is to examine the radiation-induced structural changes in the materials.

At present such methods as X ray analysis and electron microscopy are used for examination of structural changes occurred under irradiation. These procedures together with incontestable advantages have a common disadvantage. Data are obtained only from a local surface area or a thin near-surface layer (2-3  $\mu\text{m}$ ). Moreover, high induced activity increases radiation background under X ray examinations. The methods of small angle neutron scattering and neutron diffraction have no disadvantages mentioned above. Data are obtained from the whole transmission volume of a specimen. There is no excess noise produced by induced activity.

The procedures of small angle neutron scattering (SANS) and neutron diffraction (ND) have no disadvantages mentioned above. Data are obtained from the whole transmission volume of a specimen. There is no excess noise produced by induced activity.

A possibility of using of the procedures is limited by two circumstances:

## 2.4. Results with irradiated materials

- most of examination laboratories have no license for works with high radioactive specimens;
- due to the small thickness (0.4 mm) of a fuel pin cladding an effect of the low angle neutron scattering method is little.

The purpose of the work was to examine the austenitic steels microstructure changes of austenitic steels after their irradiation in the BN-600 reactor by the neutron scattering methods and to compare the results obtained by neutron scattering methods with data of electron microscopy and X ray examinations.

## 2. THE MATERIALS AND METHODS OF EXAMINATION

Specimens are fragments of a tube  $\varnothing 6.9 \times 0.4 \text{ mm}^2$ , manufactured of the austenitic steels *ChS68* (16Cr15Ni2Mo1Mn) and *EK164* (16Cr19Ni2Mo2Mn) in pre- and post irradiation exposure in the BN-600 reactor up to the maximum dose  $\sim 80$  dpa.

Fragments sizes were:

- a tube of 16 mm length for X ray;
- a tube of 30 mm length for neutron diffraction;
- plates of  $3 \times 3 \times 0.4 \text{ mm}^3$  for TEM;
- segments of  $18 \times 2.2 \times 0.4 \text{ mm}^3$  for SANS were prepared, as shown in Fig.1.

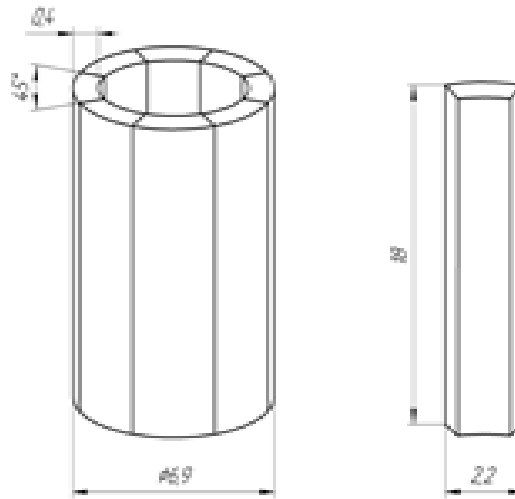
For examination we used specimens after two types of irradiation conditions: “low dose” specimens irradiated from 0.5 to 14.5 dpa at temperatures of 370-389°C and “high dose” specimens irradiated from 68-81 dpa at temperatures of 490-528°C. At once unirradiated specimens were examined as well as irradiated one. Table 1 exhibits irradiation characteristics of the examined specimens.

Neutron diffraction, small angle neutron scattering, the X ray, and transmission electron microscopy methods were used for steels examinations. The characteristics of each procedures and current technique are presented below.

### 2.1. The neutron diffraction method

Neutrons having different energies with wavelengths of ( $10^{-4}$ - $10^{-5}$ ) nm to  $\sim 1$  nm are born under nuclear reactions. The monochromators reflect neutrons and select the definite neutron wavelength. In the diffractometer D7a, which was used for examination, a monochromic beam of 0.1805 nm wavelength comes up to the specimen and it's reflected from atomic planes of the specimen. During operation the detector registers both natural and scattering radiation displaced with the angle increment of  $0.1^\circ$  thus the whole available angular interval covers approximately of 5-120°. Obtained data are recorded by a computer and processed with the certain software.

## 2.4. Results with irradiated materials



*a – a tube sample cutting on 8 segment specimens; b – a single segment.*

*FIG. 1. The schema of the specimens manufacturing.*

TABLE 1. THE EXAMINATION IRRADIATION CHARACTERISTICS OF SPECIMENS

Material	Conditions	Dose, dpa	Dose rate, dpa/s	Irradiation temperature, °C
ChS68	Unirradiated	0	0	
	High dose	77-81	$(1.6-1.7) \cdot 10^{-6}$	490-520
	Low dose	0.5-1.5	$(1.1-3.1) \cdot 10^{-8}$	370
EK164	Unirradiated	0	0	
	High dose	68-72	$1.5 \cdot 10^{-6}$	490-528
	Low dose	0.5-14.5	$3.0 \cdot 10^{-7}$	370-389

## 2.2. Small angle neutron scattering

A small angle here is the angle which complies with the limit of scattering vectors  $q < 1-10 \text{ nm}^{-1}$ . The effect of small angle scattering is appeared when there are heterogeneities of  $\sim 1$  to  $100 \text{ nm}$  sizes, which have sufficient contrast. The contrast  $\rho$  - is the neutron scattering amplitude difference between matrix ( $\rho_0$ ) and particles (heterogeneities -  $\rho_1$ ):  $\rho = \rho_0 - \rho_1$ . Intensity of small angle scattering depends on square of the contrast:  $I \sim \rho^2$ .

It is possible to obtain the data of subatomic structure such as: size and form of particles, their concentration, specific surface of voids from the angular dependence of intensity of scattering in small angles. A neutron beam created by the diffractometer D6 has average wavelength  $\lambda = 0.478 \text{ nm}$  and resolution  $\Delta\lambda / \lambda = 30\%$ . Beam polarization is equal to  $P_0 = 0.95$ . The cantilever turns on the angle  $2\theta \pm 5^\circ$  from the direct beam.

## 2.4. Results with irradiated materials

Slit geometry is used with the incident beam of  $1 \times 30 \text{ mm}^2$ . Accuracy of neutron flux determination is less than 0.6%. Additionally the neutron diffractometer D3 was used for increasing of information values in region heterogeneities size with  $q = 0.6\text{-}1.0 \text{ nm}^{-1}$ . It used the neutron beam of wave length  $\lambda = 0.243 \text{ nm}$ .

## 2.3. X ray method

X ray analysis was used for measuring a lattice parameter, half-wide of reflexes and microstress. A lattice parameter was determined by the extrapolation method using the Nelson-Reilly function. The reflexes (111), (200), (220), (311) and (331) were used for the calculation. The accuracy of determination was  $\pm 0.00005 \text{ nm}$ . The errors of half-wide determination were less than 10%. Microstress was calculated using the half-wide of the  $K_{\alpha 1}$  component (331) of the reflex by the formula:

$$\sigma = \frac{E \cdot (B - b + \sqrt{B \cdot (B - b)})}{8 \cdot \text{tg} \theta} \quad (1)$$

where  $E$  – Young's modulus, GPa;

$B$  and  $b$  – values of linear half-width of the line (331) on cladding specimens of the examined fuel pin element and a standard sample;

$\theta$  - the Bragg angle of scattering.

## 2.4. Transmission electron microstructure examination

TEM examination was carried out by the electron microscope JEM-2000 EX using accelerate voltage 120 kV. 3 mm segments were cut from ring specimens by the special in-hot cell cutting machine. Then they were thinned by a grinding paper up to 0.12 mm. The foils were prepared by TENUPOL equipment with the help of the electro polishing method. Magnification during photographing was within 3000 to 100000. The calculation program SIAMS Photolab was used for quantitative handling of TEM photos.

## 3. RESULTS

### 3.1. The neutron diffraction results

According to the ND data the specimens of both steels have bright marked texture. It is connected with cold deformation treatment during tube manufacturing. The relations of the intensity of the reflexes (111)/(200), (111)/(220), and (111)/(311) were calculated to trace the texture changes. The textures of the materials remain even after irradiation up to 81 dpa, but become less than original one. Maximum decreasing is observed after irradiation at temperatures of 370-390°C and low doses. The effect is weaker after irradiation at temperatures of 520-528°C even at high doses. Table 2 demonstrates the observation results. The table shows that the texture of the *EK164* steel is more stable under irradiation, than in case of the *ChS68* steel. For example, the relative change characteristics of specimens irradiated up to high doses in comparison with unirradiated specimens of the steel *ChS68* are equal to 1.38 and 1.19 (for different reflexes). In the case of the *EK164* steel this relations are 1.19 and 1.04 correspondently.

## 2.4. Results with irradiated materials

TABLE 2. THE RELATIONS OF THE INTENSITY OF THE REFLEXES (111)/(200), (111)/(220), AND (111)/(311) FOR THE *ChS68* AND *EK164* STEELS

Steel	Dose, dpa	(111)/(200)	(111)/(220)	(111)/(311)
<i>ChS68</i>	0	0.33	0.13	0.37
	1.5	0.33	0.20	0.48
	81	0.30	0.18	0.44
<i>EK164</i>	0	0.35	0.21	0.51
	14.5	0.37	0.27	0.55
	72	0.39	0.25	0.53

Microdeformations ( $\Delta d/d$ ) and size of coherent scattering areas ( $L_{CSA}$ ) were calculated by different reflexes characteristics of ND. They are exhibited in Tables 3 (for *ChS68* steel) and Table 4 (for *EK164* steel). The microdeformation changes are different for steels. They increase with dose growth for the *ChS68* steel. These changes are non monotonic for the *EK164* steel. The dose dependences on size of coherent scattering areas are different too. It increases with dose growth for the *ChS68* steel and decrease for the *EK164* steel respectively.

Obtained results have shown anisotropy microdeformations in the irradiated and unirradiated specimens of both steels. Table 5 exhibits relations of microdeformations in the directions (100) / (111) and (110) / (111). Here the data were taken from the work [5].

The relations for both steels are equal for unirradiated as well as for irradiated specimens. Thus, micro deformation anisotropy is inherent in the austenitic steel cladding tubes and it is remained under irradiation.

## 3.2. The SANS results

The dose growth leads to low angle scattering increasing for both *ChS68* and *EK164* steels. The dependences of the SANS section  $d\Sigma/d\Omega$  on the wave vector  $q$  for the *ChS68* and *EK164* steels are shown in Fig. 2. The comparison shows that the changing effect of the *EK164* steel is greater than of the *ChS68* steel.

The base property determined by SANS is the contrast. An amplitude density of coherent scattering depends on compound and structure of the steel. The calculation shows that  $\rho_0 = 7.1 \cdot 10^{14} \text{ m}^{-2}$  for both steels. We suggested that scattering centers in initial state are particles of carbide phase  $\text{TiC}_x$ . Its contrast is  $(\rho_0 - \rho_{\text{TiC}}) = 6.3 \cdot 10^{14} \text{ m}^{-2}$ . Other carbides have small contrast for the possibility to be a reason of the scattering observation.

## 2.4. Results with irradiated materials

TABLE 3. THE VALUES OF MICRODEFORMATION AND THE SIZE OF CSA OF SPECIMENS OF THE CHS68 STEEL CALCULATED BY NEUTRON – DIFFRACTION DIAGRAMS

Characteristic	Dose, dpa	0	1.5	81
	Temperature, °C	-	370	520
Indexes(hkl)				
Micro deformation $\Delta d / d \cdot 10^{-4}$	111	9.8	11.9	13.4
	200	29.5	35.9	40.3
	220	14.8	17.9	20.1
	311	24.2	29.4	33.0
	222	9.8	11.9	13.4
	400	29.5	35.9	40.3
	average	18	24	27
	$L_{CSA}$ , nm	64	68	105

TABLE 4. THE VALUES OF MICRODEFORMATION AND THE SIZE OF CSA OF SPECIMENS OF EK164 STEEL CALCULATED BY NEUTRON – DIFFRACTION DIAGRAMS

Characteristic	Dose, dpa	0	14.5	72
	Temperature, °C	-	390	528
Indexes(hkl)				
Micro deformation $\Delta d / d \cdot 10^{-4}$	111	10.7	15.2	11.4
	200	32.2	45.7	34.1
	220	16.1	22.8	17.1
	311	26.4	37.4	27.9
	222	10.7	15.2	11.4
	400	32.2	45.7	34.9
	average	21	30	23
	$L_{CSA}$ , nm	74	54	46

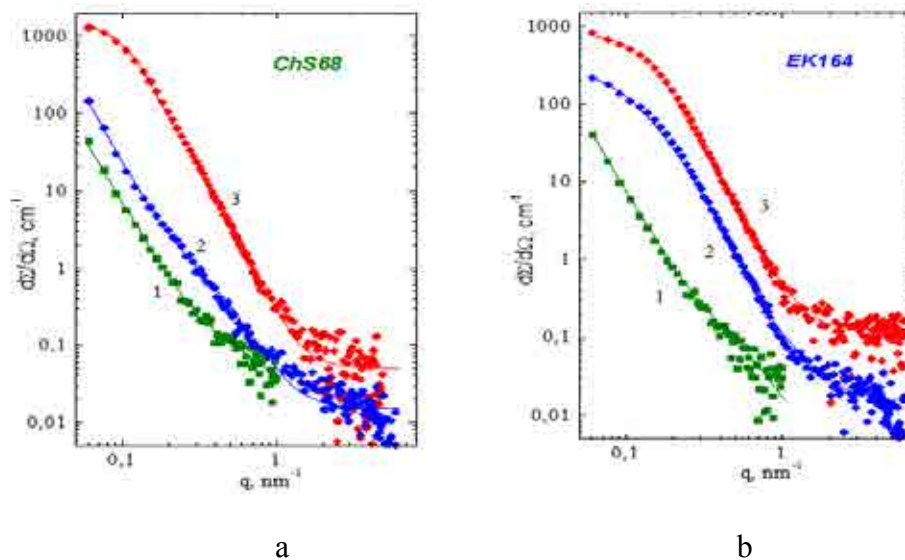
## 2.4. Results with irradiated materials

TABLE 5. THE ANISOTROPY OF MICRO DEFORMATIONS OBSERVED IN BOTH STEELS. THE RELATIONS OF MICRO DEFORMATIONS IN THE DIRECTIONS (111)/(200) AND (111)/(220)

Steel	Dose, dpa	(111)/(200)	(111)/(220)
ChS68	0	0.33	0.67
	1.5	0.33	0.66
	81	0.33	0.67
EK164	0	0.33	0.66
	14.5	0.33	0.67
	72	0.33	0.67
Date of Schmatz W. for steel 316, [5]		0.36	0.69

We used the two-modes model for the calculation of scattering of irradiated specimens. The Mode1 is based on stochastic phase particles distribution; here we used the Debye-Pored formula [6]. The Mode 1 parameters are the particle size –  $r$ , their volume part –  $C$  and Pored parameter  $D_s$ .

The Mode 2 is described by power distribution on particles size:  $N(R) \sim R^{-(3+\Delta)}$  within the interval from  $R_{\min}$  to  $R_{\max}$  [7]. We used  $1 \mu\text{m}$  as an upper limit. Parameters:  $R_{\min}$ ,  $R$ ,  $\Delta$ ,  $N$ ,  $C$  were fitted to improve the correspondence calculation results with experimental date.



1 – the unirradiated specimen; 2 – the specimen irradiated up to low dose; 3 – the specimen irradiated up to high dose; points – experimental date; lines – modeling calculation

FIG. 2. The dependences of the SANS section  $d\Sigma/d\Omega$  on the wave vector  $q$  for the ChS68 (a) and EK164 (b) steels.

## 2.4. Results with irradiated materials

The suggestion about two kinds scattering particles of different size gives best description of the results, obtained on low dose specimens. The results, obtained on high dose specimens are more correctly described in the Mode 2. The calculation results are shown in table 6.

TABLE 6. PARAMETERS OF SUBATOMIC STRUCTURE OF SPECIMENS OF CHS68 AND EK164 STEELS

Specimen and type of conditions	Moda 1		Moda 2					
	$2r$ , nm	C	$D_s$	$N$ , $\times 10^{21} \text{ m}^{-3}$	$2R_{\min}$ , nm	$\Delta$	C	$2R$ , nm
ChS68 <sub>unir</sub>	1.6	0.0024	2	0.27	4	0.5	0.0003	6.6
ChS68 <sub>low dose</sub>	4.0	0.0008	2	0.32	4	0.2	0.0005	7.2
ChS68 <sub>high dose</sub>	–	–	–	28	4	0.1	0.005	5.7
EK164 <sub>unir</sub>	2.4	0.0008	2	0.29	4	0.5	0.0003	6.6
EK164 <sub>low dose</sub>	1.0	0.002	2	–	$2R = 17$	$D_s = \frac{2}{2}$	0.005	–
EK164 <sub>high dose</sub>	–	–	–	45	4	0.1	0.006	5.2

## 3.3. The X ray results

The results of X ray analysis are exhibited in Table 7.

TABLE 7. THE RESULTS OF X RAY ANALYSIS OF SPECIMENS OF THE CHS68 AND EK164 STEELS IRRADIATED IN THE BN-600 REACTOR

Specimens and irradiation conditions	Lattice parameter , nm	Half wide, angle min.		micro stress, GPa
		(220)	(331)	
EK164 D=0.6 dpa, T=370°C	0.35912	25	78	0.35
EK 164 D=68 dpa, T=490°C	0.35955	30	78	0.32
ChS68 D=0.5 dpa, T=370°C	0.35944	17	52	0.28
ChS68 D=81 dpa, T=513°C	0.35959	22	75	0.21

## 2.4. Results with irradiated materials

The *ChS68* steel lattice parameter is bigger than it is of the *EK164* steel after irradiation up to low dose.

Dose growth leads to increasing of the lattice parameter for both steels. Half wide of the (220) reflex is increased for both steels after irradiation up to high dose. While the (331) reflex becomes wider only for the *ChS68* steel.

Two kinds of processes lead to lattice parameter changes:

- the dislocation loops formation (increase value);
- interstitial impurity (C, N) going out of crystalline matrix (decrease value).

## 3.4. Transmission electron microscopy results

Electron-microscopic examinations have showed that microstructure of both steels is qualitatively identical in initial state, Fig. 3.

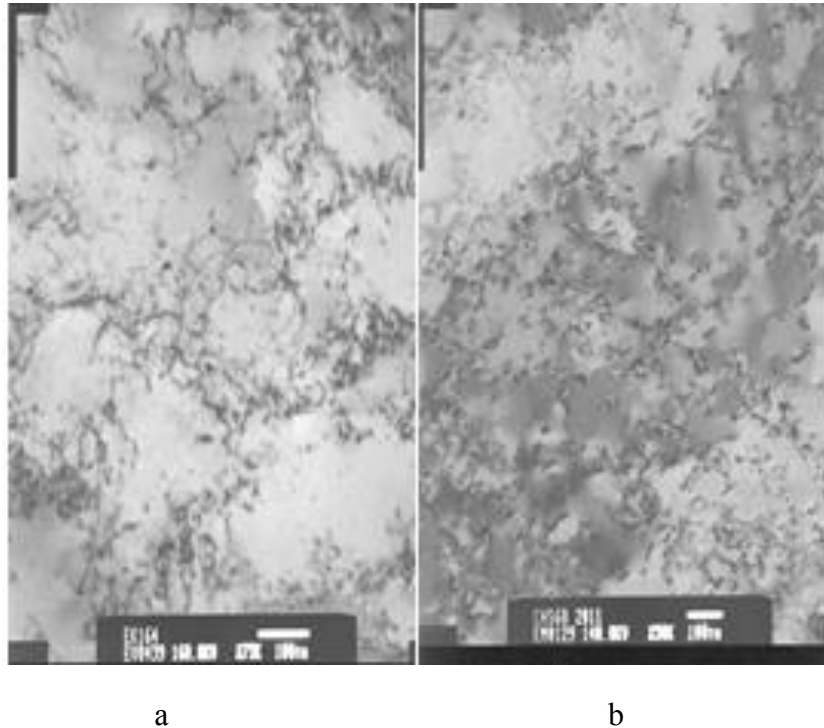


FIG. 3. Initial microstructure of *EK164* (a) and *ChS68* (b) steels.

They have dislocation cell structure. There are small precipitates of the carbide *MeC* in both steels.

There are only single elements of dislocation cell structure in both steels after low dose irradiation. Radiation voids have sizes of 2-5 nm and their concentration is  $(2-3) \cdot 10^{20} \text{ m}^{-3}$  in the *ChS68* steel. The void concentration of similar size in the *EK164* steel is less than  $1 \cdot 10^{19} \text{ m}^{-3}$ . Microstructure of both steels after irradiation up to low dose at the temperature 370°C is shown in Fig.4.

## 2.4. Results with irradiated materials

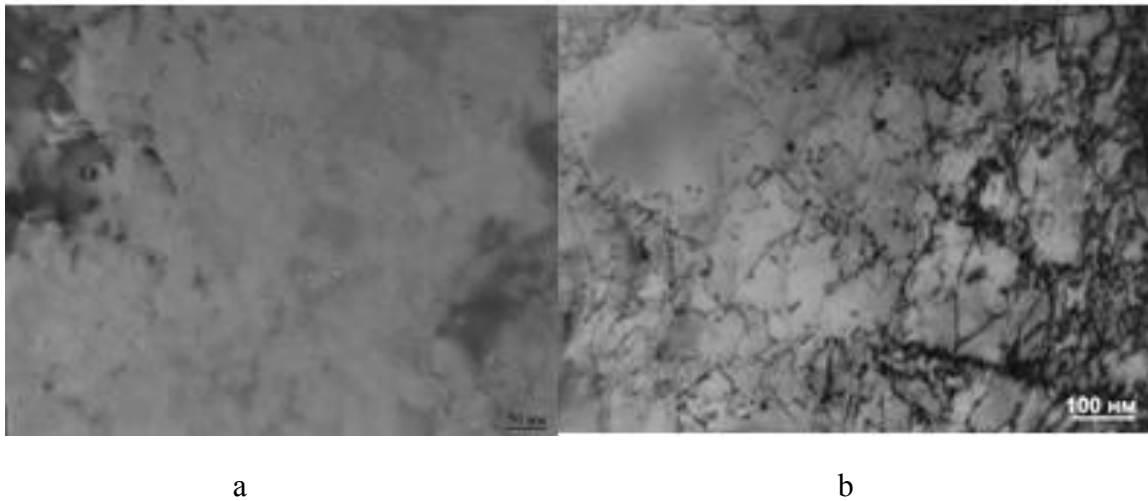
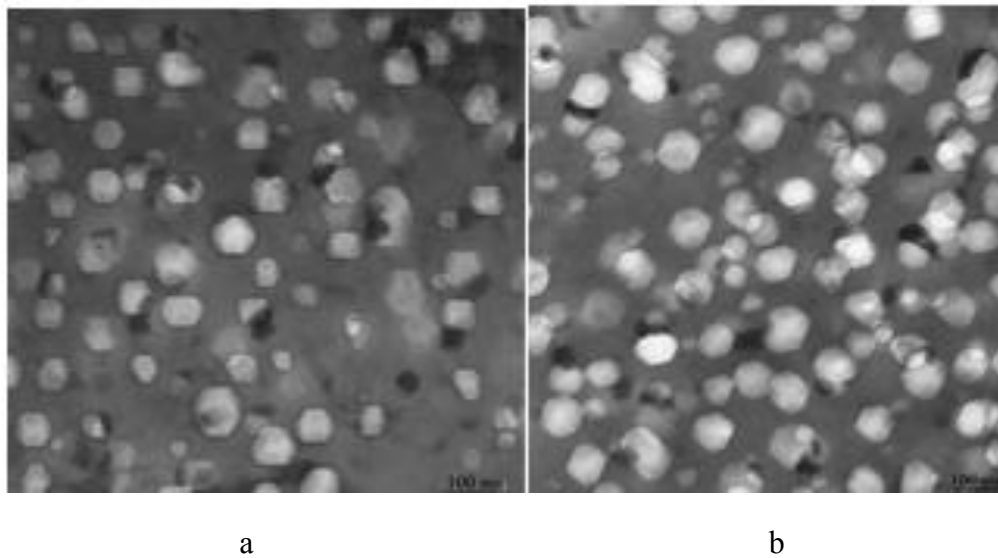


FIG. 4. Microstructure of the specimens of the ChS68 (a) and EK 164 (b) steels irradiated to  $\sim 0.5$  dpa at  $370^\circ\text{C}$ .

Voids mainly connected with precipitates of high-nickel intermetallic compound (*G*-phases) are observed in the specimens of the ChS68 steel irradiated to 79 dpa at  $\sim 490^\circ\text{C}$  and 81 dpa at  $515^\circ\text{C}$ , Fig. 5. Besides, void characteristics are different for various specimens irradiated at identical temperature to the same doses. It testifies about material heterogeneity. Histograms of void distribution on size illustrating this distinction are given in Fig. 6.



*a* –  $D=79$  dpa,  $T=490^\circ\text{C}$ ; *b* -  $D=81$ dpa,  $T=515^\circ\text{C}$

FIG. 5. Microstructure of ChS68 steel after high dose irradiation.

## 2.4. Results with irradiated materials

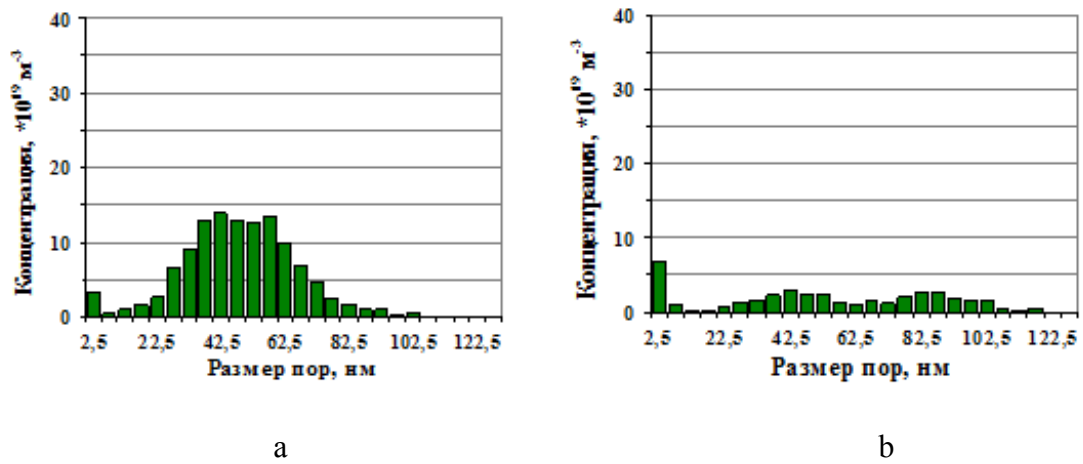


FIG. 6. Histograms of void distribution on sizes of two specimens of the ChS68 steel, irradiated to 81 dpa at  $\sim 515^\circ\text{C}$ .

The voids in the EK164 steel are less than in ChS68 steel, Fig.7. Size distributions of voids on sizes in specimens of the EK164 steel irradiated at close condition are differed as well as in the ChS68 steel, Fig.8.

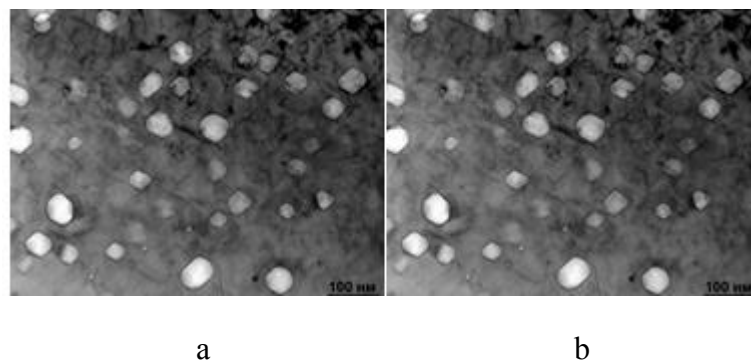


FIG. 7. Voids and precipitates of G-phase in the specimens of the EK164 steel, irradiated to 70 dpa (a) and to 72 dpa (b) at  $T=515^\circ\text{C}$ .

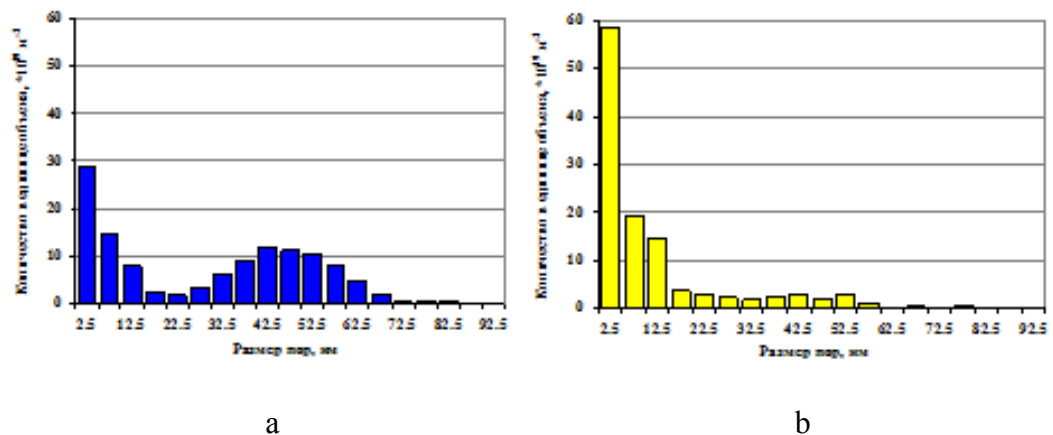


FIG. 8. Histograms of void distribution on sizes in the specimens of the EK164 steel irradiated to 72 dpa (a) and 70 dpa (b) at  $T=515^\circ\text{C}$ .

## 2.4. Results with irradiated materials

### 4. SUMMARY

The irradiation leads to increasing of the lattice parameter in both steels. It was fixed by the X ray method. The accuracy of the neutron diffraction method is insufficiently for establishing the effect, Fig. 9.

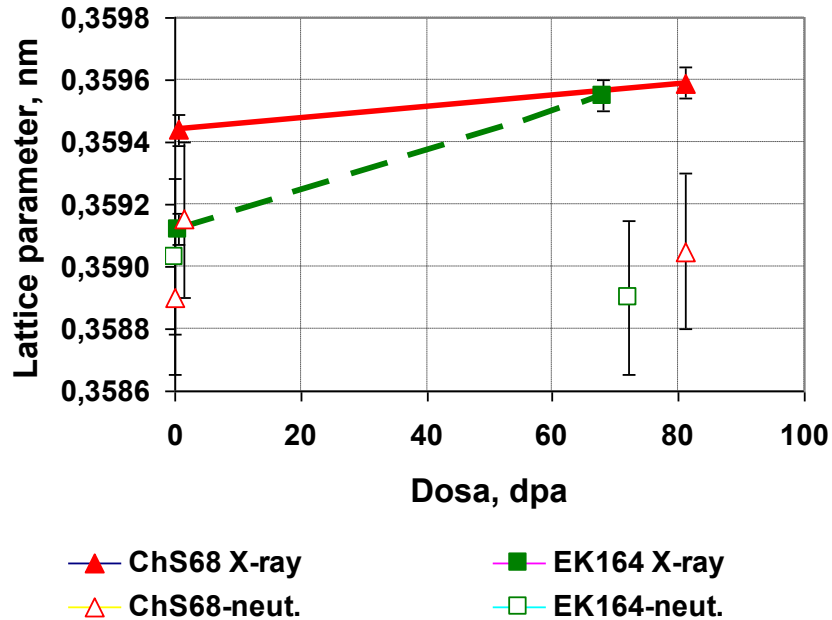


FIG. 9. Parameters of crystalline parameters of the specimens of ChS68 and EK164 steels before and after neutron irradiation.

Temperature dependence of micro deformation values was obtained by the ND method which display more preference than by X ray one. The micro deformation in both irradiated steels is larger in comparison with their initial state. The date of the ChS68 steel are exhibited in Fig.10.

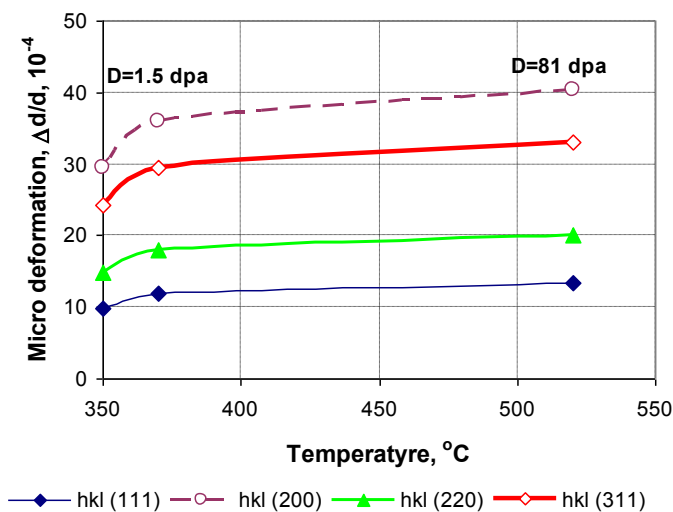


FIG. 10. Dependence of microdeformations on neutron irradiation temperature of the ChS68 steel.

## 2.4. Results with irradiated materials

Micro deformation increasing is connected with dislocation loops formation and small voids creation. Their quantity is much more in the *EK164* specimen irradiated up to 14.5 dpa, than it is in the ChS68 specimen irradiated to 1.5 dpa. Hence, micro deformation in this case is higher (Fig. 11).

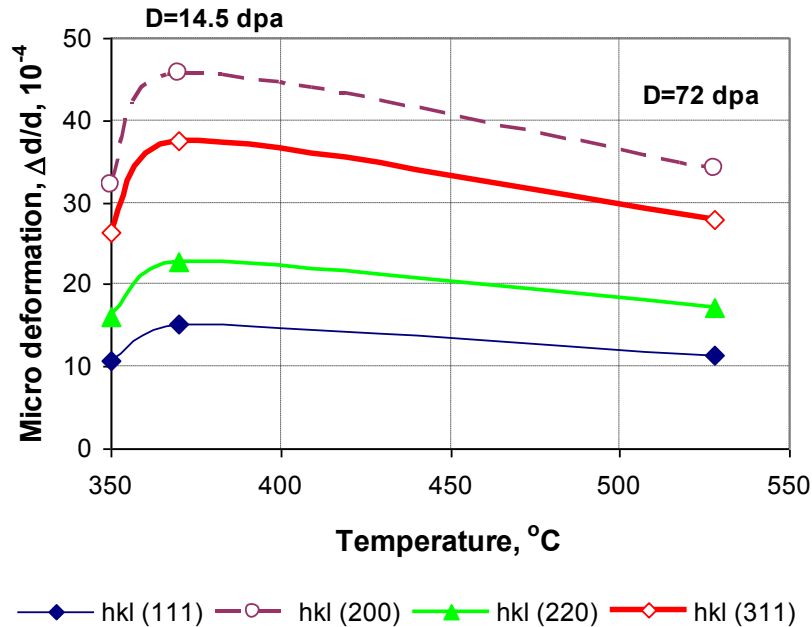


FIG. 11. Dependence of microdeformations on neutron irradiation temperature of the *EK164* steel.

Comparison of the SANS results with electron microscopy data shows that amplitude density of coherent scattering is close in order of magnitude to dislocation density. SANS diagram changes induced by irradiation at 370°C give the size of scatter particles of ~4 nm. It is close to small void size. However, voids concentration is less than the particles one in order of magnitude. The difference is more considerable in specimens irradiated to high dose (~520°C). Other fine-dispersed objects caused SANS can be small He-v bubbles – void nuclei. They are formed on dislocations and have sizes between 1.5 nm (at 370°C) and 4 nm (at 520°C) [8]. It is difficult to observe them by the electron microscopy method because they don't give elastic contrast.

Precipitates capable to cause the recorded change of SANS are absent in irradiated steel specimens. Other scattering objects can be segregations formed along dislocations and grain boundaries.

SANS description by real defects and chemical heterogeneities requires development of calculation models that imitates real microstructure more adequately. Particularly the model of scattering by longitude scatter agglomeration and plate scatter agglomeration would be useful.

## 2.4. Results with irradiated materials

## 5. CONCLUSION

Both steels in initial state and after irradiation have preference texture (111) along axial tube direction.

Irradiation leads to texture decreasing. It appears more brightly at low irradiation temperature (370°C) than at higher irradiation temperature (520°C).

Micro deformations in the tube specimens of both steels are anisotropic. They increase under irradiation but meanwhile anisotropy power is saved.

Lattice parameters increase with dose growth. It is greater in the *EK164* steel in comparison with that one in the *ChS68* steel.

SANS is increased with dose growth in both steels.

Comparison of SANS centre characteristics calculated by the globular particles model with electron microscopy data does not make it possible to surely establish the nature of scattering centers.

It is reasonable to develop the SANS calculation models more adequately corresponding to real radiation-induced microstructure changes.

## REFERENCES

- [1] GARNER, F.A. "Irradiation Performance of Cladding and Structural Steels in Liquid Metal Reactors" Material Science and Technology: A Comprehensive Treatment. 1994. V. **10**. Ch. 6., 419-543.
- [2] PECHENKIN, V.A., EPOV, G.A., The influence of radiation induced segregation on precipitate stability in austenitic steel, J. Nucl. Mater. **199**, 3207, 303-312.
- [3] KOZLOV, A.V., GLUSHKOVA, N.V., PORTNYKH, I.A., Mechanism of the effect of transmutation helium produced in fuel claddings made from austenitic steel ChS-68 under neutron irradiation on the formation of pores, Metal Physics and Metal Science, **108**, 3, (2009), 276-282.
- [4] KOZLOV, A.V., SKRYABIN, A.V., PORTNYKH, I.A., TSCHERBAKOV, E.N., ASIPTZOV, J.I., Formation and evolution of cascade regions and their electron microscopic examination, Problems of Atomic Science and Technology (VANT, in Russian) series "Material science and new materials", (2004) B.1(62), 299-309.
- [5] VANDERMEULEN, W. SCIBETTA, M. LEENAERS, A.J. "Schuurmans, R. Gerrard, "Measurement of the Young modulus anisotropy of a reactor pressure vessel cladding" Journal of Nuclear Materials **372** (2008) 249–255.
- [6] SVERGUN, D.I., FEYGIN, L.A. "X ray and Neutron Small-Angle Scattering" M. Science, (1986) 34.
- [7] SCHMATZ, W. "Proceedings of the Conference on Neutron Scattering. Gatlinburg" Tennessee, USA, June 6-10, (1976) V. **2**. 1037.
- [8] KOZLOV, A.V., PORTNYKH, I.A., BLOKHIN, A.I., BLOKHIN, N.A., DEMIN, N.A. "The dependence of the critical pore diameter in the austenitic steel ChS-68 from the temperature of neutron irradiation in the model of helium-vacancy formation of bubbles", Physics and chemistry of materials processing, (2012) №1, 16-22.

## 2.4. Results with irradiated materials

# DEVELOPMENT, CHARACTERIZATION AND TESTING OF MATERIALS OF RELEVANCE TO NUCLEAR ENERGY SECTOR USING NEUTRON BEAMS IN CHINA

Y. LIU, D. CHEN, J. GAO

China Institute of Atomic Energy (CIAE)  
Beijing PO Box 275(30)  
Beijing, China  
Email: [ytliu@ciae.ac.cn](mailto:ytliu@ciae.ac.cn)

### Abstract.

A 60 MW research reactor, so called China Advanced Research Reactor (CARR,) was built in CIAE, neutron scattering and neutron imaging are one of the main research and application fields based on it. With the support of members in the CRP initiated by IAEA five instruments related to applications on materials of relevance to nuclear energy sector, have been designed/improved and constructed. Since August 21st, 2012 instruments started to do commissioning with neutrons and some scientific research related to nuclear materials were also carried out at CARR and abroad.

## 1. INTRODUCTION

A 60 MW research reactor, so called CARR, was built in CIAE, and at the first phase ten instruments were planned to be built by neutron scattering laboratory (NSL), which were a Neutron Residual Stress Diffractometer (RSD), a texture diffractometer (TD), a four circle diffractometer, a powder diffractometer, two triple axis spectrometers, a reflectometer, a small angle neutron scattering diffractometer (SANS) and two neutron imaging instruments (cold and thermal) (CNI and TNI).

Recent years the neutron scattering instruments are to be used for characterization, testing and qualification of nuclear fuels, advanced structural materials and components produced and/or under development for applications in fission and fusion, and now are playing more and more important role. With the support of members in the CRP initiated by IAEA five instruments, RSD, TD, SANS, CNI and TNI, have been designed/improved and constructed. Since August 21st, 2012 instruments got some chances (5 MW 8 hours, 10 MW 8 hours, 53 MW 20 minutes) to do commissioning with neutrons and some scientific research related to nuclear materials were also carried out at CARR and abroad, which showed that it was quite promising to do the research related to the materials in nuclear energy sector using the facilities at CARR in the future. Detail information is reported as follows.

## 2. PROGRESS REPORT ON THE WORK CARRIED OUT AND RESULTS OBTAINED

### 2.1. Neutron residual stress diffractometer

Components of RSD were constructed and installed before 2012 (Fig.1). The instrument specifications are as follows.

Monochromator:	Si(311), Cu(220)
Take-off angle:	41° ~ 109°
Neutron wavelength:	0.895 Å ~ 2.666Å
Detector:	ORDELA 1128N
M-S distance:	190 cm ~ 220 cm
S-D distance:	60 cm ~ 110 cm
Sample table Load capacity:	200 kg
Best Resolution:	2%

## 2.4. Results with irradiated materials

The designed shielding drum of the monochromator can change its take-off angle from  $41^\circ$  to  $109^\circ$  continuously, so that the incident neutron wavelength can be changed continuously within a certain range, which will be very helpful for neutron diffraction residual stress measurement to get a cubic gauge volume for different materials. The rotating part of shielding is driven by motors with the angle error less than  $0.05^\circ$ . The neutron monochromator goniometer is one of the mechanical components, which is designed to install two monochromators, Si(311) and Cu(220). Si(311) is a double focusing monochromator. A commercial one was purchased from a company in Switzerland and just arrived at CIAE. At the same time a Si(311) double focusing monochromator is developed to understand know-how. During the reactor operation two slabs, each with 3 pieces, are tested and the procedure to fix silicon pieces together was improved.

ORDELA 1128N neutron is a gas-filled, multi-anode proportional neutron counter, ordered by IAEA through a TC program. On August 21<sup>st</sup>, 2012 Residual Stress Diffractometer got the first diffraction peak of Fe(211) at CARR when the reactor power reached 3MW. The experimental setup and result are shown in Fig. 2. After the reactor reached the 5 MW the attitude of monochromator was optimized, and then the flux at sample position gain factor of 13. The residual strain of a high strength steel sample was measured. The experimental setup and result of full width at half maximum of diffraction peak and residual strain at different position of the sample are shown in Fig. 3.

In order to simulate working conditions of materials related to nuclear energy sector in-situ 10 kN, 50 kN stress rigs and a fatigue testing machine are equipped, shown as Fig. 4, a furnace (from room temperature to  $1000^\circ\text{C} \pm 1^\circ\text{C}$ ) are developed and fabricated successfully, which is shown in Fig. 5.

## 2.2. Neutron texture diffractometer

TD is modified from a four circle diffractometer which was relocated from Juelich institute in Germany, and the monochromator shielding was designed and fabricated in China. The installation of TD was finished in 2011 (Fig. 6). The instrument specification is as follows.

Monochromator:	Cu(111)
Take-off angle:	$40^\circ$
Neutron wavelength:	1.43 Å
Detector:	3He tube
M-S distance:	180 cm
S-D distance:	42 cm
Eulerian Cradle:	25 cm diameter

2.4. Results with irradiated materials



FIG. 1. Neutron residual stress diffractometer installation.

## 2.4. Results with irradiated materials

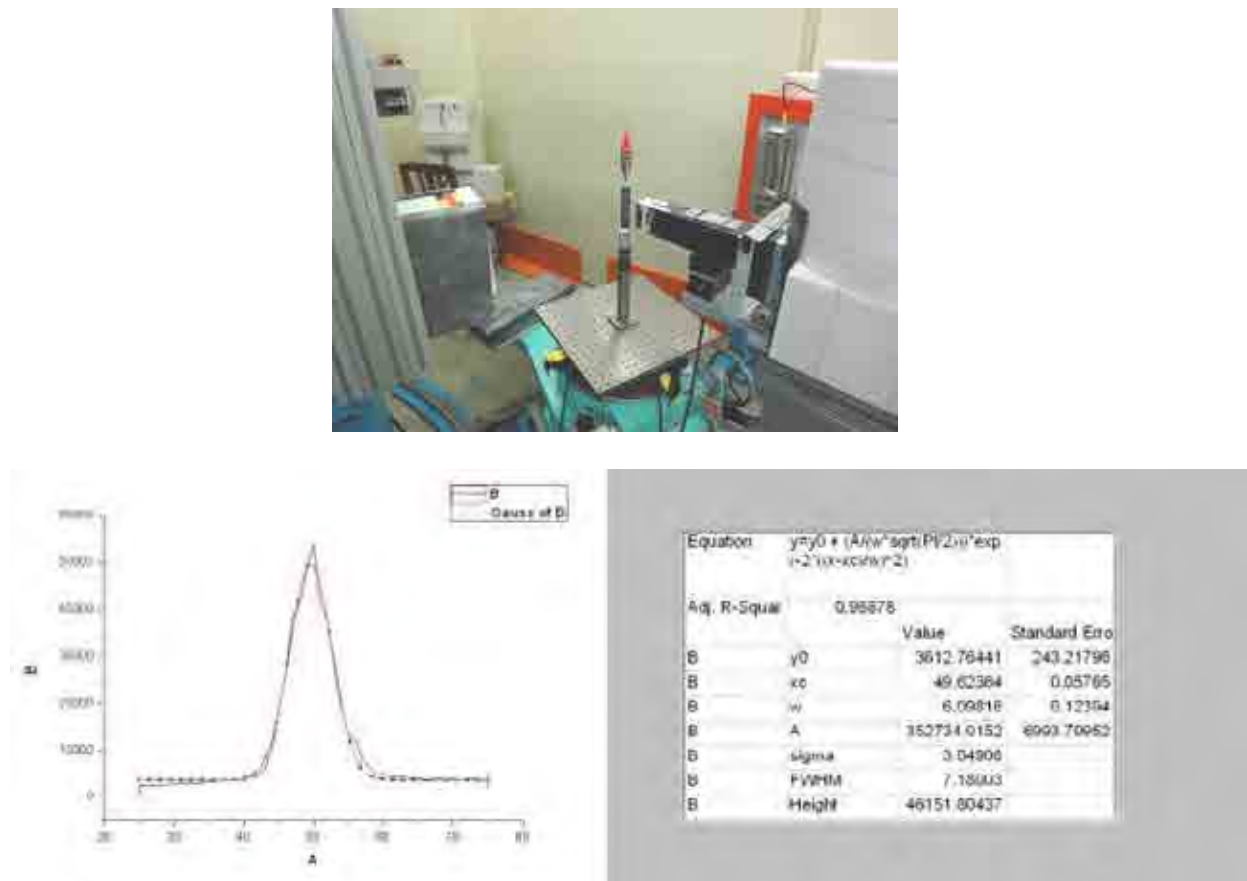


FIG. 2. The experimental setup and the result of the first peak obtained by Neutron Residual Stress Diffractometer at CARR in China Institute of Atomic Energy.

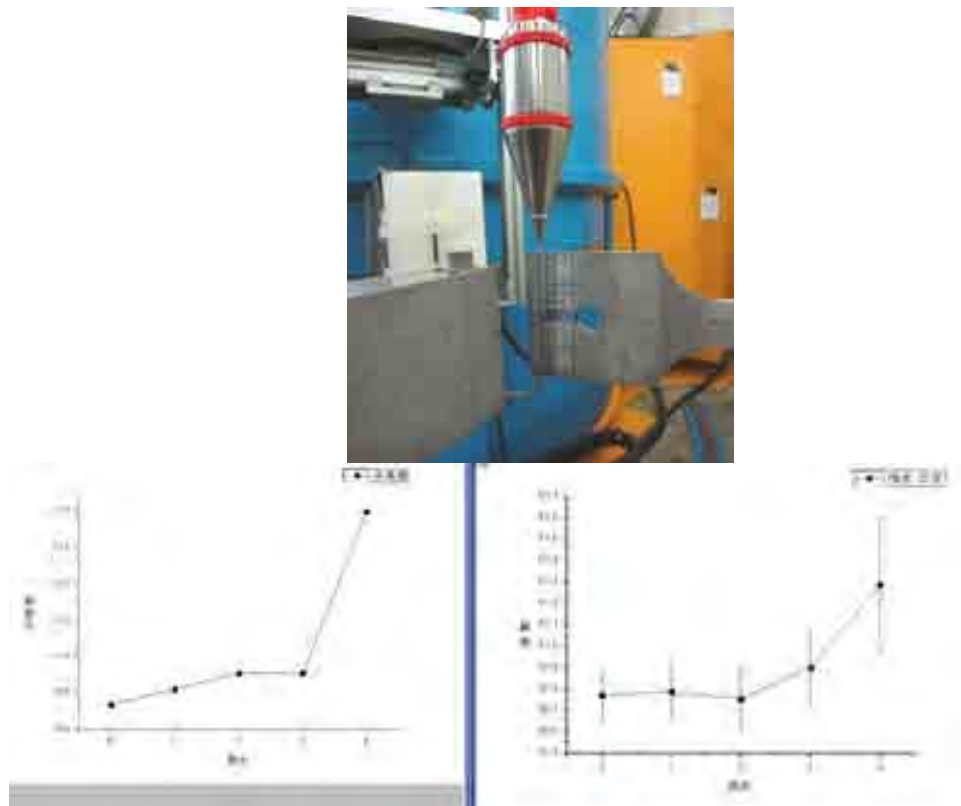


FIG. 3. The experimental setup and result of full width at half maximum and residual strain at different position of the high strength steel sample.

2.4. Results with irradiated materials



(a) (b)  
FIG. 4. (a) 50 kN stress rig, (b) Fatigue testing machine.

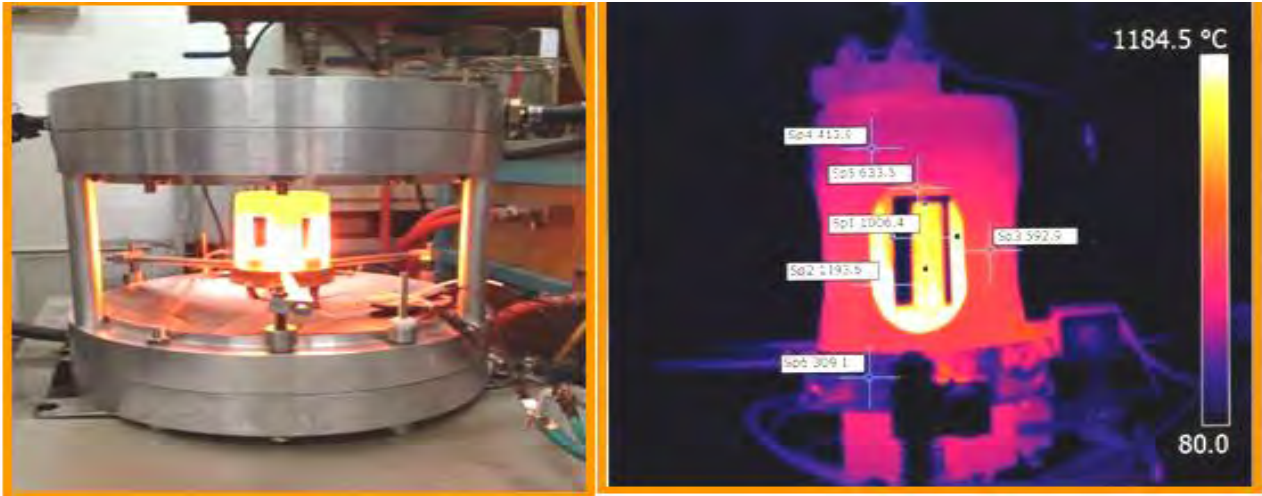


FIG. 5. The furnace developed and fabricated at CARR.

## 2.4. Results with irradiated materials



FIG. 6. Neutron texture diffractometer installation.

On August 21<sup>st</sup>, 2012, a standard  $\text{TiO}_2$  powder sample was measured to get a diffraction pattern in order to calibrate and optimize the TD instrument, and the motion control system and the data processing and acquiring system were optimized at the same time. Through the diffraction pattern of  $\text{TiO}_2$  (Fig.7) the actual wavelength and zero shift of diffraction angle was obtained.

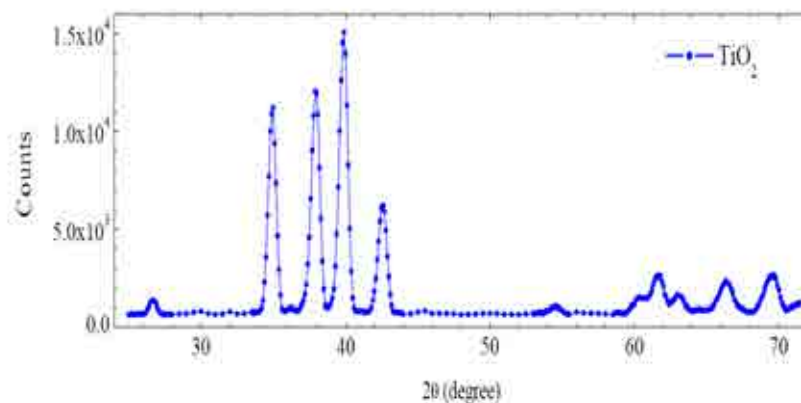


FIG. 7. The first diffraction spectrum obtained from NTD at CARR.

To qualify this Neutron Texture Diffractometer, a round-robin sample of warm-rolled Zircaloy-4 plate offered by Dr. Javier Santisteban, a member of this CRP project, was measured. Due to the limited beam time (10 MW, 8 hours), just three pole figures  $\{10\cdot10\}$ ,  $\{0002\}$  and  $\{1100\}$  were obtained, which is quite comparable with results obtained at LANSCE using a similar sample.

## 2.4. Results with irradiated materials

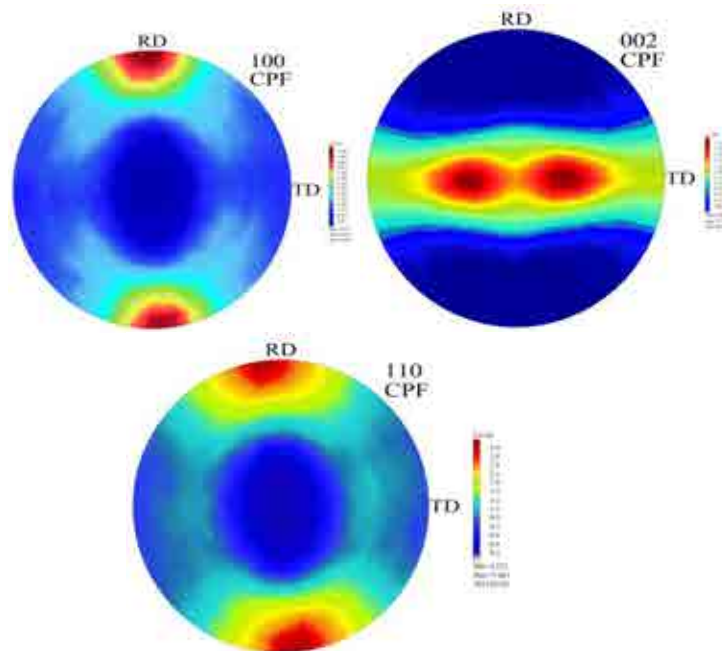


FIG. 8. The first pole figures obtained from NTD at CARR.

## 2.3. Small angle neutron spectrometer

SANS finished its installation before the end of 2012 (Fig. 9), neutrons were transferred from the reactor through neutron guides and detected at the two dimensional position sensitive detector in September. The instrument specification is as follows.

Source	Curve neutron guide (CNGD) 50 mm × 50 mm
Wavelength range	4.0 Å ~ 20.0 Å
Wavelength resolution	$\Delta\lambda/\lambda(\text{FWHM}) = 10\% \sim 22\%$
collimation	pinhole, multi-pinhole and focusing lens
Sample size	5 mm ~ 25 mm
Q-range	$0.0008 \text{ \AA}^{-1} \sim 0.5 \text{ \AA}^{-1}$
Detector	64 mm × 645 mm He3 PSD, 5 mm × 5 mm



FIG. 9. Small Angle Neutron Spectrometer.

## 2.4. Results with irradiated materials

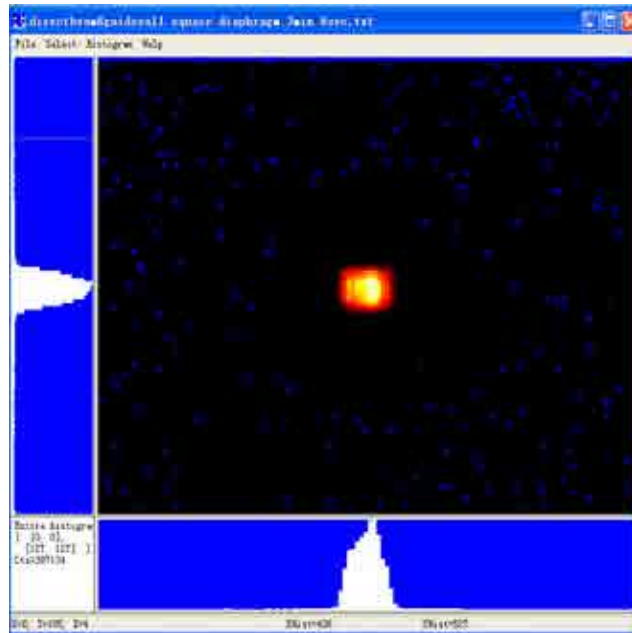


FIG. 10. The first neutron beam image on the detector.

Supported by Dr. Jose Teixeira, a member of the CRP project, ODS samples (Fig. 11) were measured in LLB by SANS instrument scientist from CIAE, Dr. Li ZHANG (Fig. 12). The samples offered from the scientist of university of science and technology Beijing through collaboration and data analysis is still on the way.

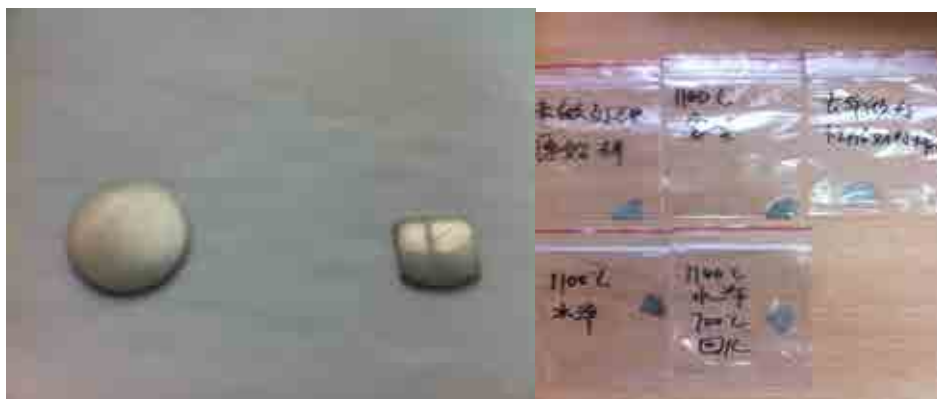


FIG. 11. Some ODS sample photo.

## 2.4. Results with irradiated materials

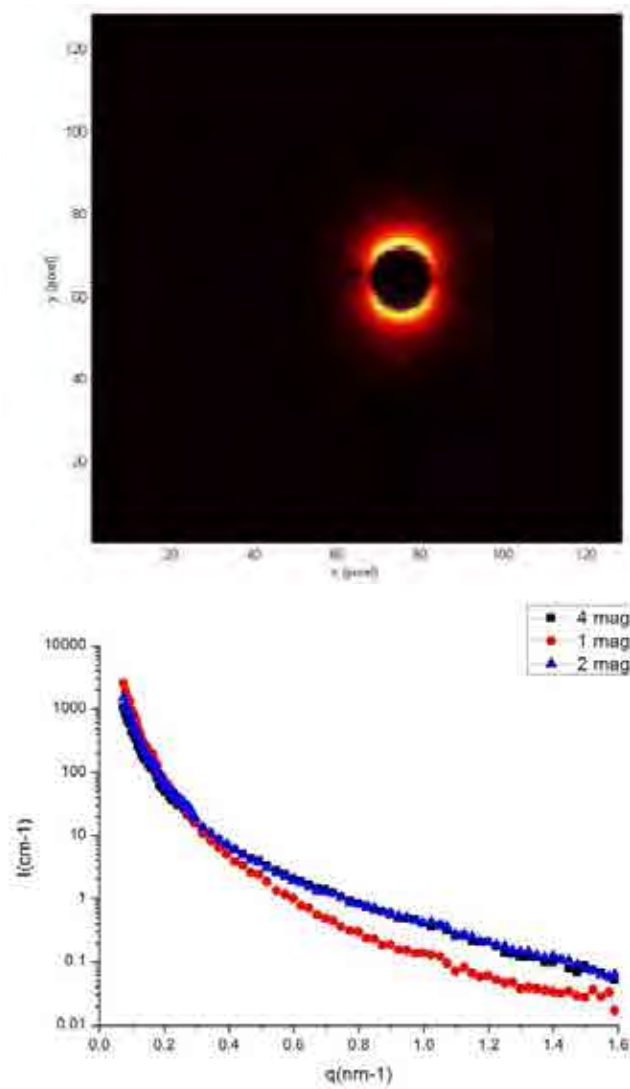


FIG. 12. The data image and the first result got from SANS at LLB.

## 2.4. Neutron image instrument

Two neutron imaging instruments TNI and CNI are planned to be built, and the financial support is also confirmed by the government. In 2011 2<sup>nd</sup> RCM related to this CRP was organized in Beijing. During the meeting neutron imaging instrument scientists at CARR presented their designs and experts attending this meeting review their design and gave very useful suggestions and comments. Those suggestions and comments were considered and the physical designs of NI instruments were improved (Fig. 13 and Fig. 14), whose parameters are shown in Table 1.

According to characters of nuclear fuel rod and neutron imaging technology, experimental methods of non-destructive inspection of nuclear fuel rod by means of neutron imaging technology have been developed. The experimental platform used for carrying out the experiment to inspect nuclear fuel rod and other radioactive materials by indirect neutron imaging has been finished (Fig. 15). The simulated nuclear fuel rod with length of 20cm and the box for transferring the radiated neutron converter screen have been fabricated. The scintillator used for thermal neutron radiography was developed by using  $\text{H}_3^{10}\text{BO}_3$  as neutron absorbing material and  $\text{ZnS}(\text{Ag})$  as fluorescent material. The  $\text{ZnS}(\text{Ag})/\text{H}_3^{10}\text{BO}_3$  scintillators were fabricated successfully by spraying method. In order to improve the performance of the

## 2.4. Results with irradiated materials

scintillators, the particles' sizes of the neutron converter and phosphor materials were optimized to be  $2\mu\text{m}$  and  $2.5\mu\text{m}$  in radius respectively by using simulation method. The mass ratio between the  $\text{ZnS(Ag)}$  and  $\text{H}_3^{10}\text{BO}_3$  were optimized to be 6.5:1 by experimental method. The spatial resolution of the scintillators with the thickness of 0.40 mm and 0.35 mm are 1.11 lp/mm (MTF=0.1) and 1.33 lp/mm (MTF=0.1) respectively, which are close to the commercial  $\text{ZnS(Ag)/}^6\text{LiF}$  scintillators (Fig. 16). It indicated that  $\text{H}_3^{10}\text{BO}_3/\text{ZnS(Ag)}$  Scintillator have potential application for thermal neutron radiography. Furthermore,  $\text{ZnS(Ag)/}^{10}\text{BN}$  scintillators with polyurethane is also being developed and quite promising, the experimental results will come soon.

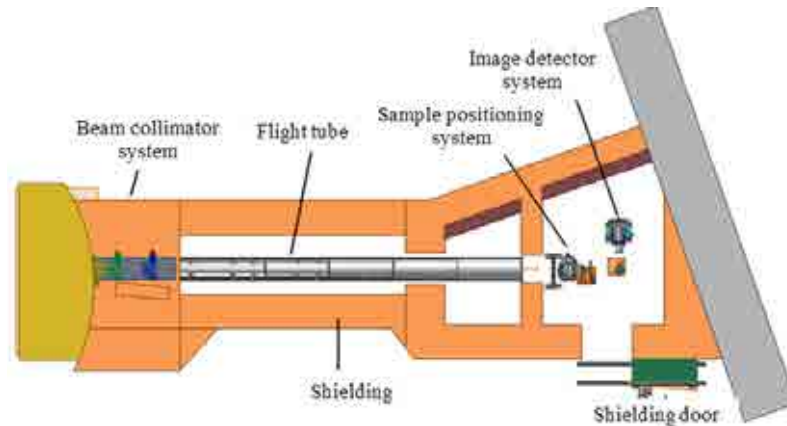


FIG. 13. Setup of the thermal neutron imaging facility.

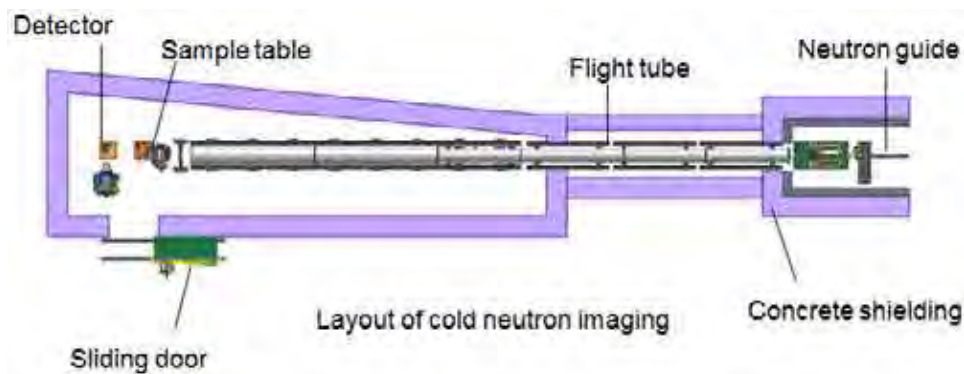


FIG. 14. Setup of the cold neutron imaging facility.

TABLE 1. DESIGNED PARAMETERS OF THERMAL AND COLD NEUTRON IMAGING FACILITIES

Parameter	Thermal	Cold
Aperture D (cm)	4, 2, 1, 0.5	5, 4, 2 and 1
Experimental position(cm)	850 and 1140	8 and 16
L/D	212-2280	160~1600
Beam size ( $\text{cm}^2$ ) (2 <sup>nd</sup> position)	22 cm × 40.6 cm	30 x 30
$n/\gamma$ (n $\text{cm}^{-2}\cdot\text{mR}^{-1}$ )	$>1.0\times 10^6$	$>1.0\times 10^6$
Cd-ratio	$>100$	$>100$
Desired resolution(mm)	0.15	0.12

## 2.4. Results with irradiated materials

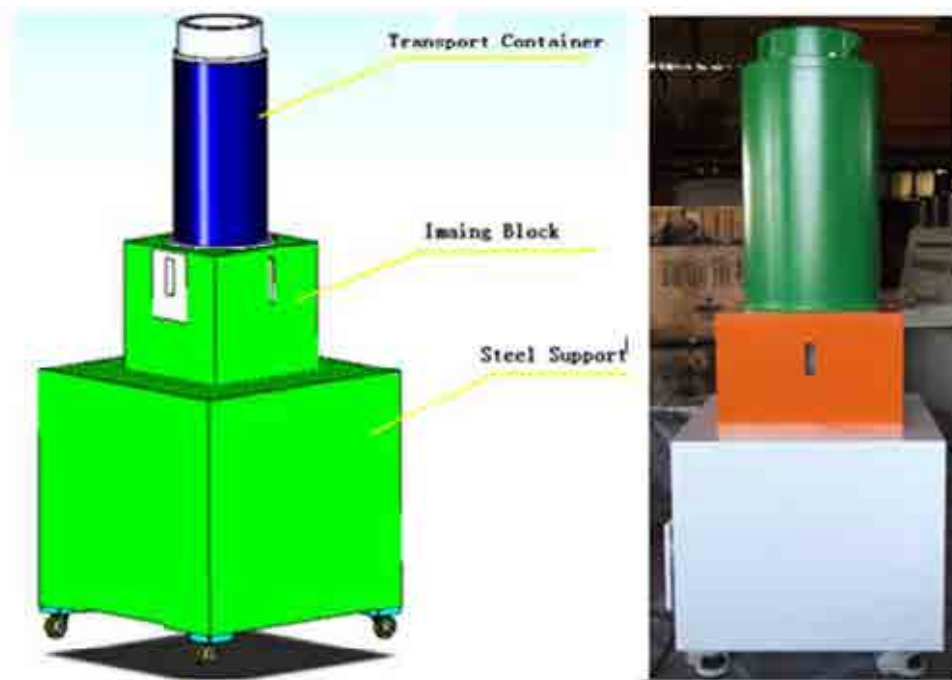


FIG. 15. The design and photo of fabricated transportation container for radioactive materials.

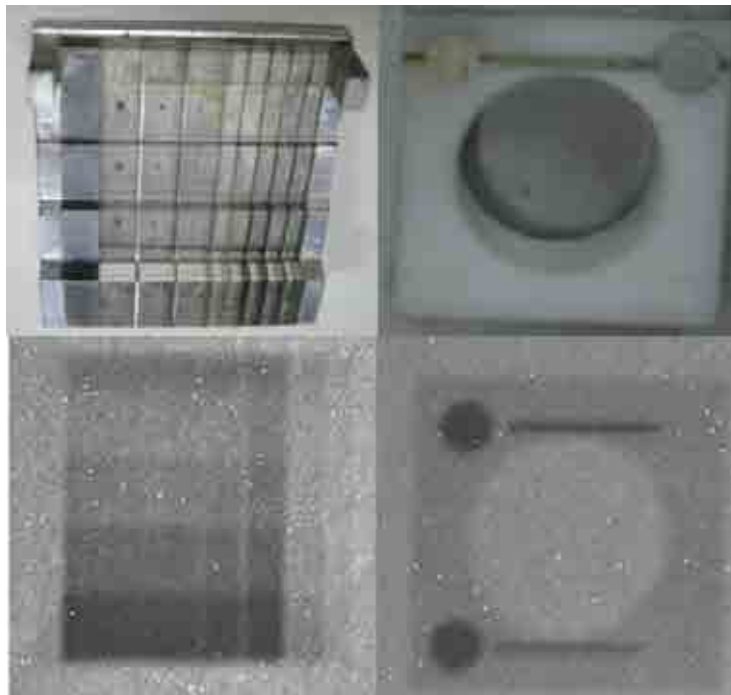


FIG. 16. Setup of the cold neutron imaging facility.

With the rapid growth of nuclear power industry, more and more attention has been paid to nuclear safety in China. The fuel rods with high standard of quality assurance are crucial to prevent nuclear leakage accident. The simulated nuclear fuel rod by neutron radiography was carried out at CARR using very limited neutron beam time. The work described above provides possibility and primary guideline for investigating the real irradiated fuel rod by neutron radiography at CARR in the future. The displacement and gap, different

## 2.4. Results with irradiated materials

fuel enrichment, hydrogen concentration and impurity content of simulated nuclear fuel elements have been studied by neutron images (Fig. 17 and Fig. 18).

Real-time Neutron image device was finished at CARR. Using this device a real-time neutron image of flashlight experiment was carried out on May 1<sup>st</sup>, 2013. The image is showing as below with 200 pictures accumulated. The neutron flux is about  $10^6 \text{ n}\cdot\text{cm}^{-2}\cdot\text{s}^{-1}$ . Space resolution from MTF method is 0.5 mm. Pixel size is 0.136 mm. Exposure time is 2 seconds (Fig. 19 and Fig. 20).

Furthermore a  $\gamma$  ray remote monitoring system (Fig. 21) was also developed and equipped at CARR in order to get irradiation information at some place where a radioactive sample is stored.



*FIG. 17. Simulated Nuclear fuel elements made from Pb and Al.*



*FIG. 18. The photo (upper), X ray image (middle) and neutron image (lower) of simulated Nuclear fuel elements.*

## 2.4. Results with irradiated materials

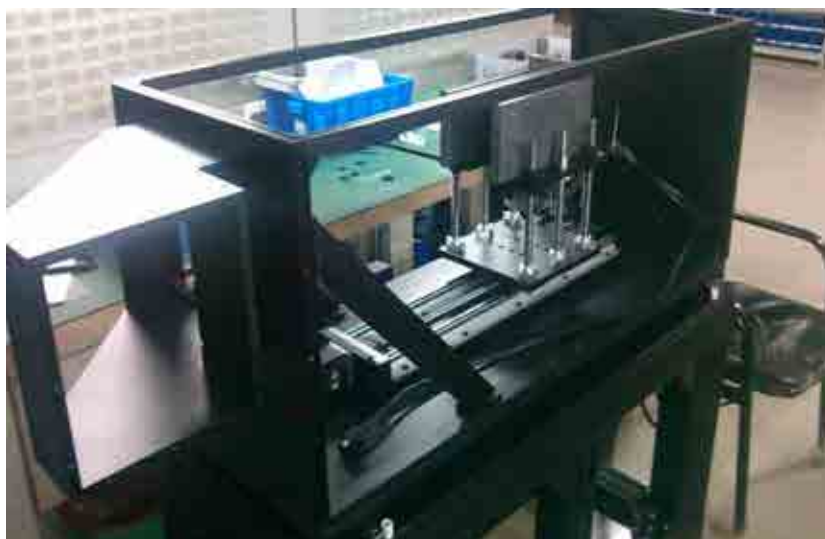


FIG. 19. Real-time Neutron image device was finished at CARR.



FIG. 20. Real-time Neutron image of flashlight. The neutron flux is about  $10^6 \text{ n}\cdot\text{cm}^{-2}\cdot\text{s}^{-1}$ . Resolution from MTF method is 0.5 mm. Pixel size is 0.136 mm. Exposure time is 2 seconds. 200 pictures accumulated.

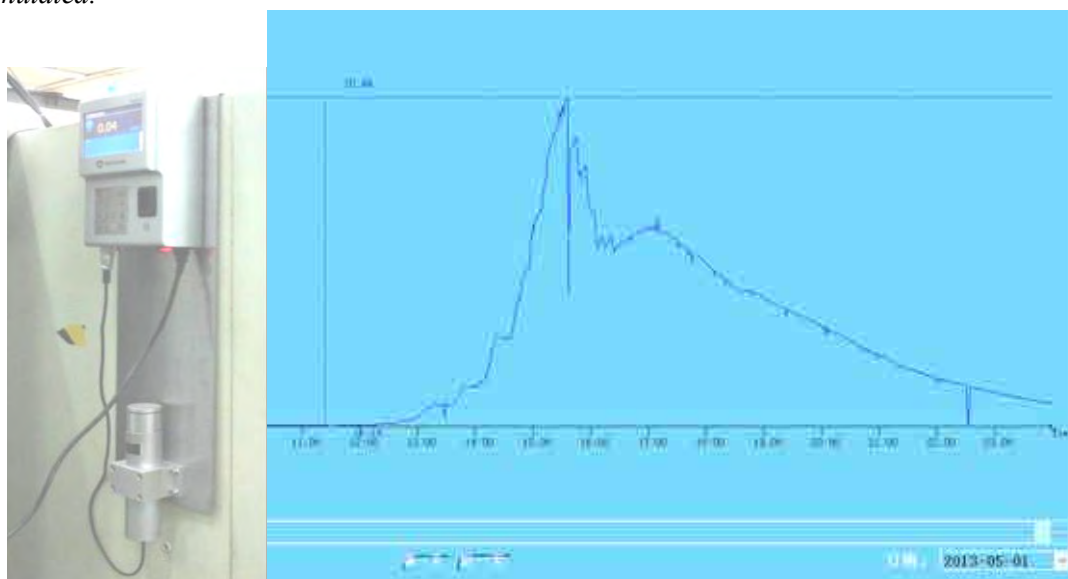


FIG. 21. Remote  $\gamma$  ray monitor.

## **2.4. Results with irradiated materials**

### **3. CONCLUSIONS**

Recent years the neutron scattering instruments are to be used for characterization, testing and qualification of nuclear fuels, advanced structural materials and components produced and/or under development for applications in fission and fusion, and now are playing more and more important role. CIAE has strong intention to study the materials related to nuclear energy sector and a 60 MW research reactor was built in CIAE, With the support of members in the CRP initiated by IAEA five instruments related to applications on materials of relevance to nuclear energy sector, have been designed/improved and constructed, and some scientific research on it were also carried out with the members of this CRP. It is a very good starting point for researches on nuclear materials at CARR, CIAE will further strengthen the cooperation with experts of this CRP in the future.

## 2.4. Results with irradiated materials

# NEUTRON BEAM ANALYSIS ON MATERIALS FOR NUCLEAR APPLICATIONS, BEING IRRADIATED IN FISSION REACTORS AND HAVING RADIOACTIVITY

T. SHIKAMA\*, A.NISHIMURA\*\*

\*Institute for Materials Research, Tohoku University,  
2-1-1 Katahira, Aobaku, Sendai, 980-8577  
Japan

\*\*National Institute for Fusion Science, 322-6 Oroshi, Toki, Gifu,  
509-5292 Japan

Present address: ITER Organization, Cadarache,  
France

Email: [shikama@imr.tohoku.ac.jp](mailto:shikama@imr.tohoku.ac.jp); [nishi-a@nifs.ac.jp](mailto:nishi-a@nifs.ac.jp)

### Abstract.

Extensive supports are given from the public sectors to the neutron beam analysis on advanced materials developed mainly in the framework of fundamental solid state physics, through the Japan Atomic Energy Agency and the Institute for Solid State physics in University of Tokyo. However, the related activities are mainly on non-radioactive materials with some limited exceptions, though the facilities for the neutron beam analysis are installed in the radiation controlled areas. Research activities in the field of nuclear related materials have concentrated their efforts for nano structural analysis into the other techniques of the post irradiation examinations, such as the high resolution transmission microscopy, the three dimensional atom probe tomography, and the positron annihilation techniques, than the neutron beam analysis. In the meantime, more detailed analysis on the radiation induced nanostructures are becoming more and more essential for the further understanding of the radiation effects in the materials which will be used in the advanced nuclear systems, such as the nuclear fusion reactors and the generation-IV nuclear fission reactors. Utilizing of the cutting edge techniques for the nanostructural analysis on materials irradiated by neutrons, all of which cannot be installed in the limited area of available hot laboratories, is urgently demanded, of course, satisfying the related legal restrictions and the safety demands. The present study was focused on as the realization of the neutron beam analysis on the nanostructural evolutions of the superconductive materials, which will be used in the ITER, the international thermonuclear experimental reactor, being under construction in Cadarache, France, and the glassy metals, which have some unique and advantageous features for the nuclear applications.

## 1. INTRODUCTION

Japan has an extensive program for utilizing neutron beams for materials development, characterization and testing. For materials analysis utilizing neutron beams (the diffraction, the small angle scattering, the radiography, the activation analysis, etc.; hereafter referred as the analysis by the neutron beam (ANB)) are under coordination of the Japan Atomic Energy Agency (JAEA) and Institute for Solid State physics in University of Tokyo. Related facilities are equipped mainly in JRR-3 and J-PARC in the JAEA-Tokai. In the meantime, hot laboratories are mainly sited in the JAEA-Oarai area, including JAEA's large-scale facilities as well as Tohoku University's and Nuclear Fuel Development Co. Ltd. (NFD)'s facilities. Until about 20 years ago, a major scope for the ANB was for the advanced materials characterization for solid state physics, however, the ANB on materials for industrial application tends to have more and more utilization share in these years, especially through the collaboration between industries and academia, with the promoting program of the JAEA.

The major ANB facilities are inside of the RI-control area, however, analysis of radioactive materials are limited due to several reasons. There will be three major factors which is restricting the ANB techniques for application to radioactive materials;

1. Hardware issues; radiation shieldings and other facilities needed for handling radioactive materials.
2. Regulatory issues.
3. Not-tolerant attitude of related researchers and workers in the ANB and related divisions facilities for handling radioactive materials.

## 2.4. Results with irradiated materials

At present, only very limited and specially designed ANBs are carried out with radioactive materials only by the JAEA researchers. (few of the collaborators out of the JAEA).

Improvement of the research environments mentioned above will be strongly needed for the further deployment of the ANB for materials study in the nuclear sectors especially with radioactive materials irradiated heavily in fission reactors, however, an remarkable improvement in a short time-span will not be a realistic scenario and some compromised approaches will be mandatory in Japan. There will be two realistic ways for overcoming these issues;

1. Handling radioactive materials as low-level sealed radio isotopes (RIs) in the RI control area of the same RI establishment.

2. Handling radioactivity whose quantity is smaller than the lowest quantity limit of a specific RI in the regulation in the designated and permitted area in the same RI using establishment.

The first scenario is only possible in the JAEA, who takes care of the ANB facilities. Up to now, very limited numbers of the neutron beam diffraction analysis on some uranium and actinide compounds were carried out in the JAEA and under the collaboration between the JAEA and Tohoku University. The second scenario will be more and more realistic under the present sociological situation in Japan after the Fukushima accident. In that case, the materials which could be handled will be very limited, namely, materials that would not have high radioactivity after the reactor radiation. Examples will be graphite (C) (highly pure carbon materials, including single crystal, diamond, and composites), silicon (Si) and silicon carbide (SiC) (including highly pure SiC composites), aluminum (Al) and magnesium (Mg), and their alloys (including highly pure ceramics such as alumina (sapphire;  $\text{Al}_2\text{O}_3$ ) and  $\text{MgO}$ ), and highly pure vanadium (V). Some of the nuclear functional materials and components, typically superconductive materials which need less neutron fluence, namely, less than  $10^{22} \text{ n}\cdot\text{m}^{-2}$  could be also handled occasionally.

## 2. EXAMPLES OF RESEARCH ACTIVITIES, TRYING TO IMPROVE THE PRESENT SITUATION

K. Kikuchi of Ibaraki Univ. is planning to carry out the ANBs in the J-PARC, the accelerator based neutron beam facilities in Tokai, who is extensively working as a liaison between universities and the JAEA J-PARC, including irradiated materials. He is proposing the encapsulation of irradiated materials in a vanadium subcapsule, as the vanadium is nearly transparent to the neutron beam. His scheme is depicted in Fig. 1, and the outlook of the vanadium encapsulation is shown in Fig. 2.

## 2.4. Results with irradiated materials

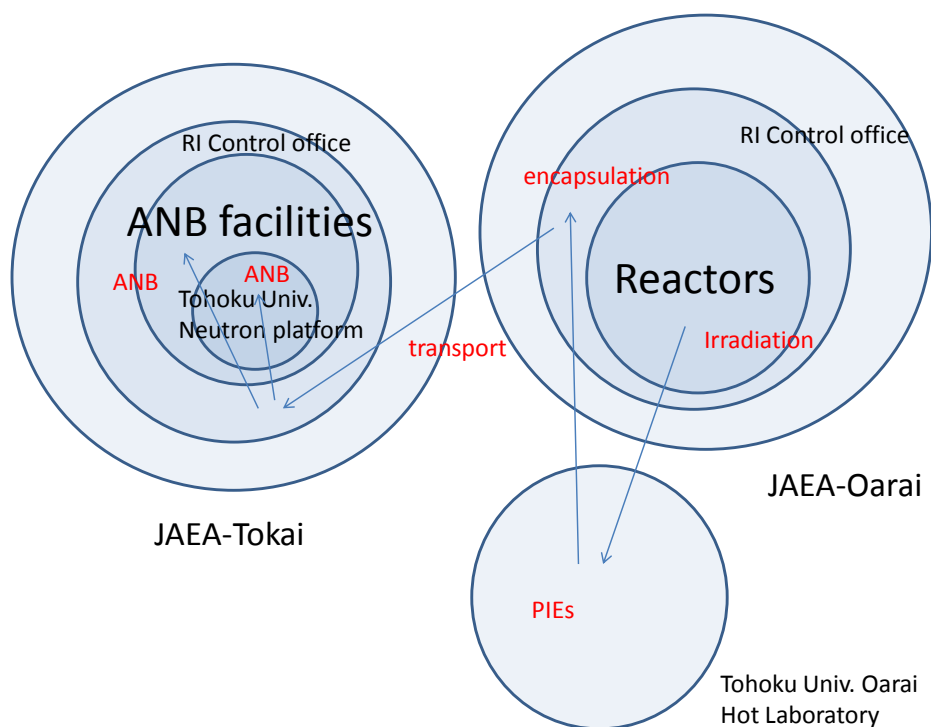


FIG. 1. Flows of irradiated materials for the ABNs, under collaboration between the JAEA and the Oarai Branch of Institute for Materials Research of Tohoku University. The plan under consideration.



FIG. 2. Outlook of the vanadium encapsulation developed by K. Kikuchi.

Also, the KEK (High Energy Physics Laboratory) and Tohoku University had a financial support from the Japanese Government to develop the new ANB facilities for materials characterizations in J-PARC. K. Ohoyama of the IMR, Tohoku University is now responsible for this project. The general scheme of the project is shown in Fig.3. The newly installed facility is mainly for non-radioactive materials, however, the Oyama's group for the ABN of the IMR and the Oarai Branch of the IMR plan to establish a more interactive relationship between the ABN activities in the JAEA-Tokai area and the hot laboratory activities in the JAEA-Oarai area.

## 2.4. Results with irradiated materials



FIG. 3. The new facilities of the ABN to be installed in the J-PARC for advanced materials.

In the meantime, A. Nishimura of National Institute for Fusion science is studying radiation effects in the superconductive materials for the nuclear application. There, irradiated materials should be examined in a high magnetic field and behaviors of the radiation induced nano-to-micro size defects should be clarified by the ANBs. He is carrying out his experiment as shown in Fig. 4, utilizing PIE facilities in the Oarai Branch of Institute for Materials Research (IMR) of Tohoku University. Once, the scheme shown in Fig. 1 mentioned above is established, minute defects in the irradiated superconductive materials could be analyzed by the ANBs in the JAEA-Tokai. However, the superconductive systems are composed of many materials, conductors and insulators, etc., and their induced radioactivity will be substantial. International collaborations are taken into consideration for the ANBs of the medium-radioactive materials. In 2013, Prof. Nishimura changed his position to the ITER organization. Now, he is in the position to organize wider researchers-network to develop large-scale magnetic coils for the ITER, which will be one of the most challenging scientific enterprises. In the design, the superconductive magnetic coil would be well shielded from the radiation from the nuclear burning plasma in the ITER. However, the radiation shielding is a very difficult technology and it would be inevitable for the superconducting magnet to have some radiation exposure, especially by high energy neutrons. Figure 6 shows the 15.5 Tesla liquid-helium free superconducting magnet installed in the hot laboratory in the Oarai Branch of the IMR, which is expected to play an important role to evaluate radiation effects in the ITER super conductive magnetic coils.

## 2.4. Results with irradiated materials

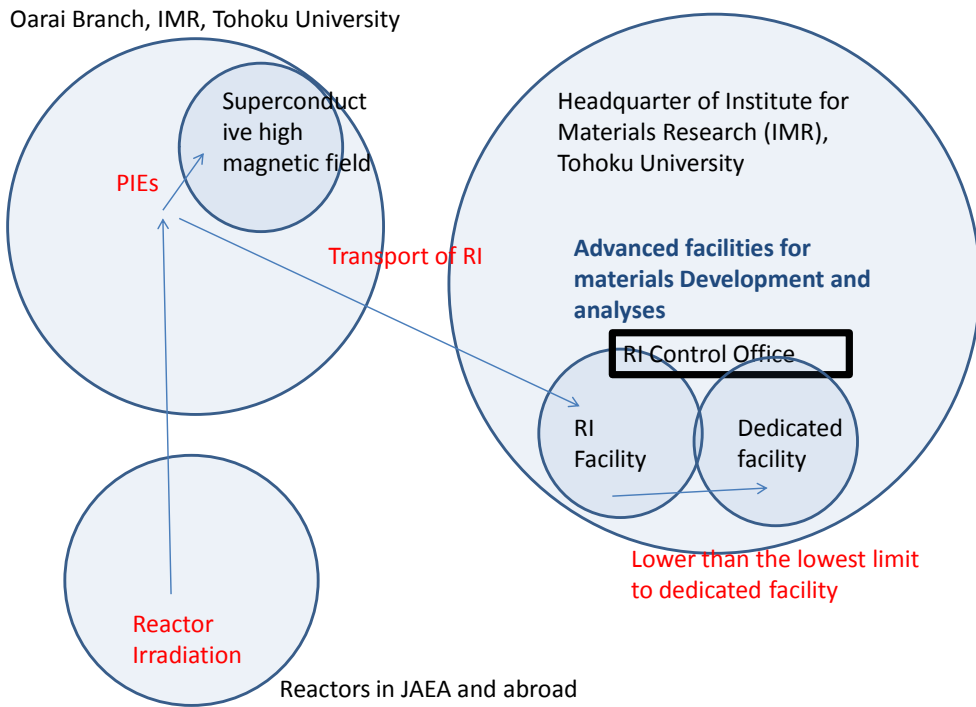


FIG. 4. Present scheme of PIEs for the irradiated superconductive materials.

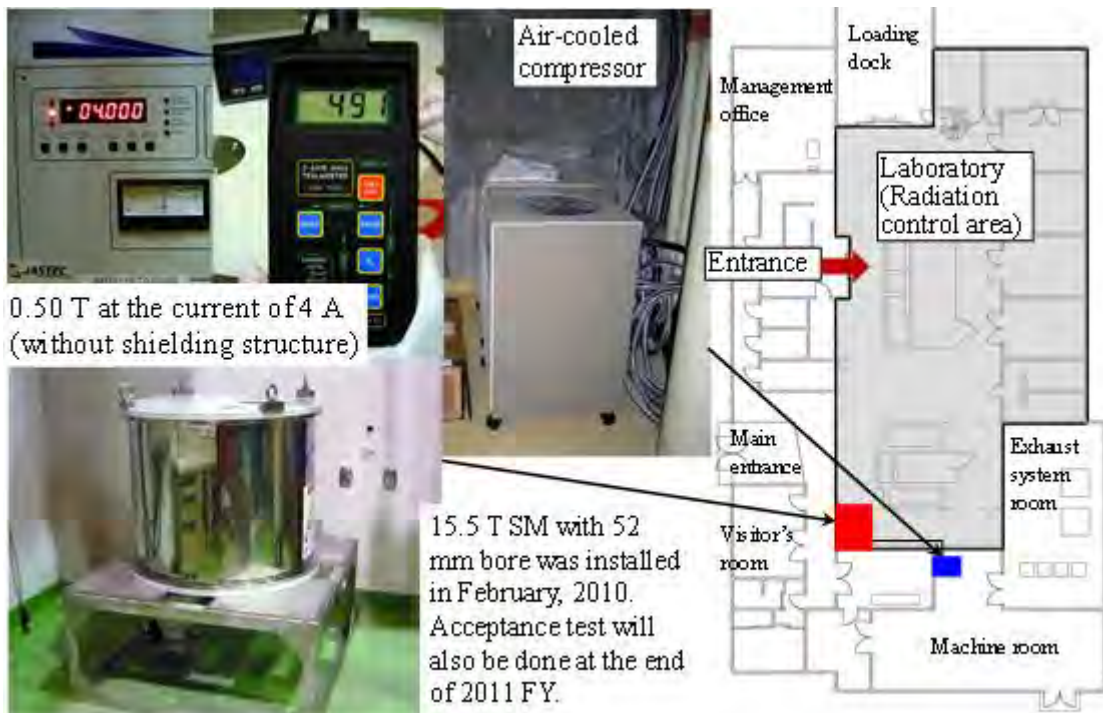


FIG. 5. Location of superconducting magnet in hot lab at Oarai branch.

## 2.4. Results with irradiated materials



FIG. 6. Superconducting 15.5 Tesla magnet installed in the hot cell of the Oarai Branch of the IMR.

The superconducting behaviors of irradiated materials were studied with the above mentioned facility. Figure 7 shows the critical temperature vs. the outer magnetic field of the niobium-tin superconductive material ( $\text{Nb}_3\text{Sn}$ ). The irradiation by  $1 \times 10^{22} \text{ n}\cdot\text{m}^{-2}$  fast neutrons ( $E > 0.1\text{MeV}$ ) looked to improve the the superconductive properties. However, the results are rather controversial and the experimental conditions should be examined much more precisely. The experiment is still under way, and the irradiated  $\text{Nb}_3\text{Sn}$  would be examined by the ABN, when the experimental framework discussed above is well settled.

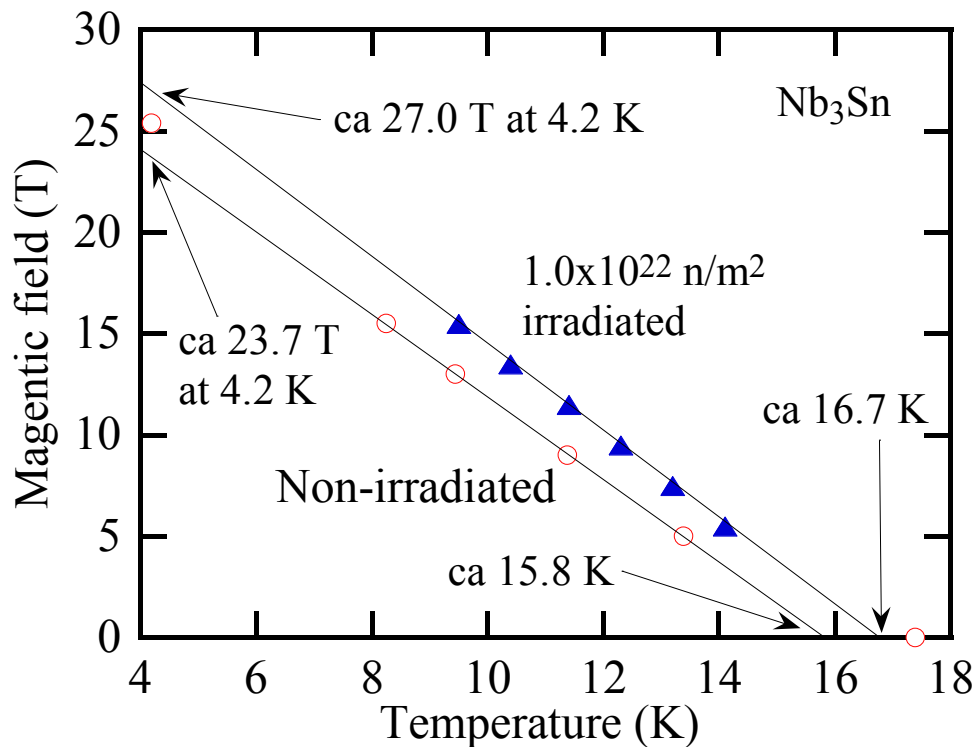


FIG. 7. Critical magnetic field as a function of temperature, comparing non-irradiated and irradiated  $\text{Nb}_3\text{Sn}$ .

The other programs are under consideration for the ANBs with irradiated materials, such as hydrogen in the zirconium hydride for a neutron reflector in an advanced nuclear power system by K. Konashi of Tohoku University under the collaboration with the JAEA,

## 2.4. Results with irradiated materials

detailed analysis of nano-scale structures of glassy metals H. Kimura of Tohoku University. Also, the hydrogen and its isotopes in the neutron irradiated plasma facing materials in the framework of bidirectional collaboration between National Institute for Fusion Science and Institute for Materials Research of Tohoku University, with wider collaborations among Nagoya University, Kyushu University, Tsukuba University, etc. N. Ohno of Nagoya University and H. Kurishita of Tohoku University are developing the small simulator machine for the plasma materials interactions shown in Fig. 8. The machine can handle heavily neutron irradiated materials. The study could be much more fruitful, when the nano-structures of the irradiated materials and the hydrogen (deuterium) in the irradiated materials could be analyzed by the ANB in parallel. The radiation effects, namely, the modification of nano to micro structures of materials will affect and change the plasma materials interactions, which may cause serious technological setbacks in the burning plasma machines such as the ITER and its beyond.

Design of compact divertor plasma simulator equipped with Thermal Desorption Spectroscopy (TDS) Device

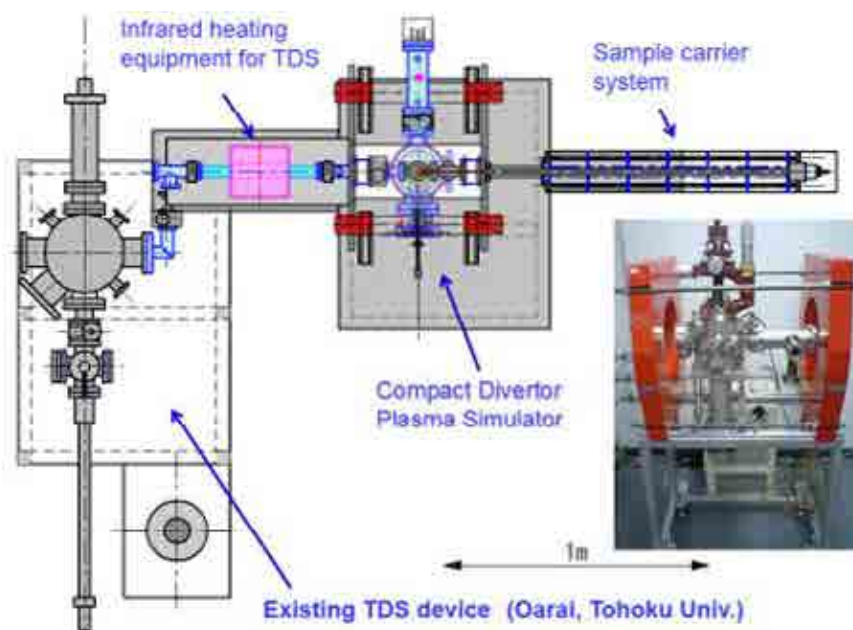


FIG. 8. Plasma simulator connected to Thermal Desorption Spectroscopy (TDS), to be installed in the hot laboratory in the Oarai Branch of the IMR.

## 3. SUMMING UPS

After the Fukushima accident, all of the research reactors were shut down except for the Kyoto University Research Reactor (KUR) and the small critical assembly. The ABN activity in the JRR-3, which is the major activity of the ABN in Japan, is completely stopped. The Japanese academia is trying to persuade the related organization to restart the research reactors as soon as possible, especially for supporting fundamental researches utilizing research reactors, such as the neutron therapy and the ABN. However, it would need much more time for the research reactors to restart. Under these circumstances, the followings are the summaries of the activities for this CRP in Japan.

## **2.4. Results with irradiated materials**

### **4. MATERIAL PREPARATION**

#### **4.1. Materials preparation is done in Japan. (glassy metals)**

Some irradiation was done in JRR-3 but all the domestic activity is now stopped after the Fukushima accident. Under several international collaborations, with such as Belgium (SCK/CEN) and the USA (ORNL), the irradiation is continued.

Major parts of the conventional PIEs (meaning PIEs except for Neutron Beam Analysis) were done in Japan.

1. Neutron Bean Analysis will be done in partners' facilities. (not done yet.)
2. Correlation between the Neutron Beam Analysis results and the other PIEs' will be analyzed with the radiation effects models established up to now. The outputs will be fed back to the radiation effects model.

#### **4.2. Regulatory improvement**

Improvements of the regulatory situations for experiments with radioactive materials are under way. Examples will be;

- IMR of Tohoku University had done and will do commissioning procedures for improve the situations for handling radioactive materials in concerned experimental facilities.
- Ibaraki University and IMR, Tohoku University are doing some preparation for handling irradiated and radioactive materials in neutron beam analysis systems in J-PARC and in JRR-3. The scheme in the J-PARC will be hopefully realized in 2013.
- Kyushu University got registration of  $^{92m}\text{Nb}$  to observe magnetic vortex by a scanning SQUID microscope.

#### **4.3. Hardware improvements**

- Installation of 15.5T superconductive magnet for heavily irradiated materials was just finished in Oarai of IMR, Tohoku University. The control and the data acquisition systems have been completed. The improvement of accuracy for controlling the irradiation conditions was completed.
- Installation of high resolution TEM and SEM is completed.
- Collaboration with Oak Ridge National Laboratory (ORNL) on the neutron irradiation of concerned materials is established, along with the continuing collaboration with the SCK/CEN (Belgium Nuclear Research Center). The eccentric materials, which include glassy metals and some compounds and will have a potential radiation resistance, are now under irradiation in the HFIR.
- Possibility of strengthened collaborations with the CEN(Grenoble, France) and the ORNL on the neutron beam analysis on eccentric materials are under survey.

#### **4.4. Collaborative efforts**

- Continuation of collaborations with the SCK and the ORNL is confirmed.
- The new venture on the heavy neutron effects on eccentric materials (high-enthalpy materials, glassy materials, etc.) is just launched with the ORNL.
- Possibility of collaborations on the neutron beam analysis is surveyed, with the CEN, Grenoble, France, and the ORNL, the USA. Especially, the possibility of

## **2.4. Results with irradiated materials**

the neutron beam analysis on the irradiated superconductive materials is sought with the AEKI, Hungary. After official framework, specimens will be sent to AEKI from Japan, hopefully in 2013.

- Nishimura changed his position to that in the ITER organization. He is now in the leading position to fabricate the large-scale magnetic coils in the ITER, and the present program will be helpful for him for establishing desirable quality control of the magnetic coils.
- Tohoku University and the concerned division of the ORNL implemented a new program on the irradiation effects in eccentric materials, including glassy metals, which would have a potential highly radiation resistance.

## **4.5. Future actions**

It is now expected that the Japan Nuclear regulatory board will show the guide line for the restart of the research reactors in Japan, by the end of the year of 2013. For a moment, the restart of the research reactors in Japan will be in the year of 2014 at the earliest chance.

For neutron beam analysis in Japan, its prospect is very pessimistic after the Fukushima accident and the international collaboration will be essential. Understanding this severe condition, expansion of international collaborations is extensively sought. Examples will be with the SCK/CEN, the ORNL, the CEA, the Halden Reactor Project (HRP) and the AEKI, Hungary.

## 2.4. Results with irradiated materials

### INVESTIGATION OF IRRADIATED RPV AND ODS STEELS BY SANS AND RESIDUAL STRESS (HUNGARY)

G. TÖRÖK\*, Á. HORVÁTH\*\*, A. ULBRICHT\*\*\*, L. TATÁR\*\*, Z. SZÁRAZ<sup>+</sup>, F. GILLEMOT\*\*, C. OHMS<sup>+</sup>, I. IONITA<sup>++</sup>, R. COPPOLA<sup>+++</sup>

\* Wigner Research Centre for Physics of the Hungarian Academy of Sciences, Budapest, Hungary

\*\* Centre for Energy Research of the Hungarian Academy of Sciences, Budapest, Hungary

\*\*\* Helmholtz-Zentrum Dresden-Rossendorf e.V., Dresden, Germany

<sup>+</sup> Joint Research Centre, Petten, The Netherlands

<sup>++</sup> Institute for Nuclear Research, Pitesti, Romania

<sup>+++</sup> ENEA-Casaccia Roma, Italy

#### Abstract.

We have investigated a RPV steel 15H2MFA type irradiated by different fluency by SANS and reactor pipe weld and cladding by residual stress. In cooperation were investigated the aging of other reactor materials as Incoloy 800 and 304L treated at different temperature. Using the SANS technique, the phase separation in the oxide dispersion strengthened (ODS) ferritic steels (PM2000 and MA956) were investigated.

### 1. INVESTIGATION OF RPV CLADDING STEEL BY NEUTRON DIFFRACTION IN ORDER TO OBTAIN STRESS VALUES

The base materials of the PWRs are low-alloyed Cr-Mo Cr-Mo-V or Cr-Mo-Ni steels.

In the case of the WWR-s the first layer is over-alloyed using Sv-07Ch25N13 electrode (containing 25% Cr and 13% Ni) weld by one pass, the second is made with Sv-08Ch19N10G2B electrode usually at least by three passes. Typical chemical composition of the cladding of these two groups of RPV is in the Table 1.

TABLE 1. CHEMICAL COMPOSITION OF DIFFERENT CLADDING LAYERS

Type	Layer	Composition									
WWR 440		C%	Si%	Mn%	P%	S%	Cr%	Mo%	Ni%	Cu%	Nb%
	1	0,056	0,86	1,16	0,015	0,004	22,8	-	13,3	0,06	-
	2	0,034	0,60	1,46	0,013	0,004	18,2	0,015	9,3	0,07	0,88

The whole thickness of the cladding is made from at least two layers, and several welding passes, consequently it is inhomogeneous. We have carried out stress measurement both in perpendicular (CLAD4, Fig.2.) and parallel (CLAD6, Fig.3.) to surface

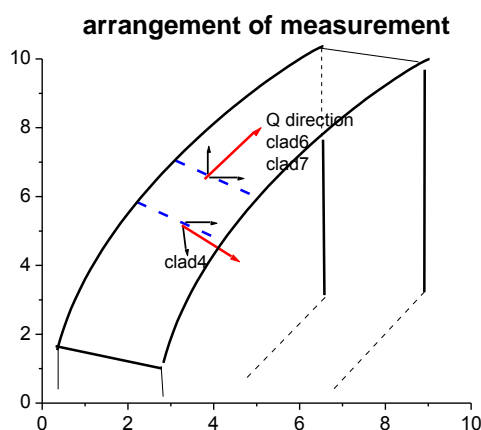


FIG. 1. The arrangement of residual stress measurements in the cladded sample. The gauge volume is 2x2x10mm step between points is 2mm.

## 2.4. Results with irradiated materials

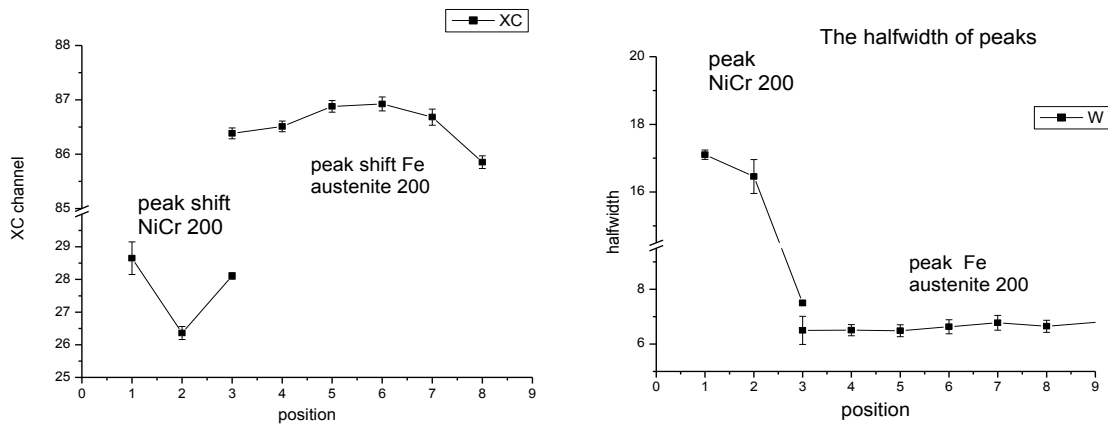


FIG. 2. The peak position and microstrain in austenite and cladding material, measurement on perpendicular to surface.

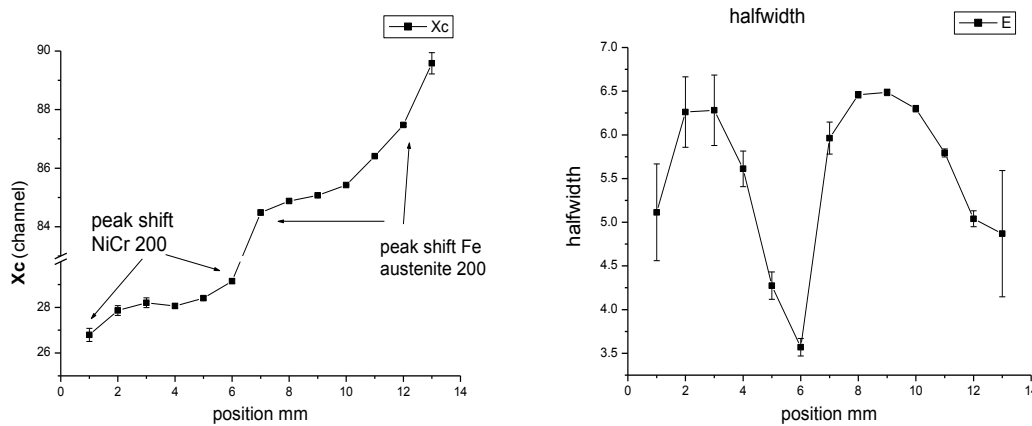


FIG. 3. The peak position and microstrain in austenite and cladding material. Residual stress measurement (parallel to surface) clad6 arrangement.

### 1.1. Conclusion

On pattern's well seen the phase of austenite and ferrite at boundaries and the cladding material. The peak shift in cladding material is less then in base one, showing that less mechanical stress are inside. That confirms the results of other type of measurements about internal stress. From diffraction patterns is clearly seen a strong preferred orientation of crystallites. i.e. especcally at the surface the cladding layer, the diffraction peak is some cases are very weak nearly absent, while in perpendicular arrangement the diffraction is well detected. The half-width of peaks near by the boundary is dropping down, showing a less microstress in the region. The stress result is further analyzed using a  $d_0$  samples for getting absolute values.

### 1.2. Installation of new irradiation rig, start of high temperature irradiation programme

The irradiation rig is installed and irradiations are in process, SANS and residual stress measurement are foreseen.

The rig capacity is (appr. 1200 gr steel). The specimen sizes and shape can be varied according to the requirements. The maximum fluence rate is  $1-5 \times 10^{13} \text{ n}\cdot\text{cm}^{-2}$  with  $E > 1 \text{ MeV}$ . The irradiation rig is shielded with boron carbide, filtering thermal neutrons, reducing the activity of the irradiated specimens and the nuclear heating. For the controlling the irradiation temperature at each of the six zones, the electric heating can be separately controlled, to keep the required temperature within  $\pm 5^\circ\text{C}$ . Irradiation temperature can be

## 2.4. Results with irradiated materials

controlled between 150°-650°C with gamma and electric heating and helium-nitrogen gas mix cooling.

The new target pick up and eject system allows the quick target change, and use an active target also (e.g. irradiated and annealed material can be reirradiated). The target rotation during irradiation assures the same irradiation of the specimens.

The equipment is ready and the control software is tested several hundred hours. Twelve different safety tests performed successfully, and the Hungarian National Safety Authority permitted the installation into the reactor. The rig operates from January 2013 in several research projects.

The ODS samples were already characterized by SANS method at the Budapest Neutron Centre (BNC), and the experimental work will continue with irradiated samples. In order to be able to handle activated material a strengthened shielding is used.

## 2. SANS MEASUREMENT OF IRRADIATED RPV STEEL 15KH2MFA (IN COOPERATION WITH HELMHOLTZ-ZENTRUM DRESDEN-ROSSENDORF)

A 15H2MFA type VVER440 rpv forging material in the unirradiated reference condition and three different irradiation conditions (samples: A, B and C) up to neutron fluences of  $2.94 \times 10^{20}$ ,  $9.52 \times 10^{20}$  and  $14.5 \times 10^{20} \text{ cm}^{-2}$  ( $E > 0.5 \text{ MeV}$ ), respectively, were investigated by SANS at the Budapest Research Reactor. A new measurement was carried out with extended q range and statistical accuracy. (Fig. 4A, B).

TABLE 2. COMPOSITION OF THE 15H2MFA TYPE FORGING VALUES IN WT%

C	Si	Mn	S	P	Cr	Ni	Mo	V	As	Co	Cu
0.17	0.26	0.54	0.019	0.01	2.66	0.05	0.66	0.28	0.001	0.005	0.09

## 2.1. Experimental

### 2.1.1. The Irradiation

The fluencies were evaluated from the dosimetry foils over 0.5 MeV, and the fast fluence over 1MeV given in Table 2 are estimated values. Beside the foil dosimetry (Cu, Nb, Fe, Al-Co foils used) reactor physics calculation is used to evaluate the fluencies. The average difference between the measurement and calculation are within 10%, of which is a very good agreement at long term irradiation. The small size capsules used are ensured the stable specimen temperature. The irradiation temperatures for all specimens were in the range 275-280°C.

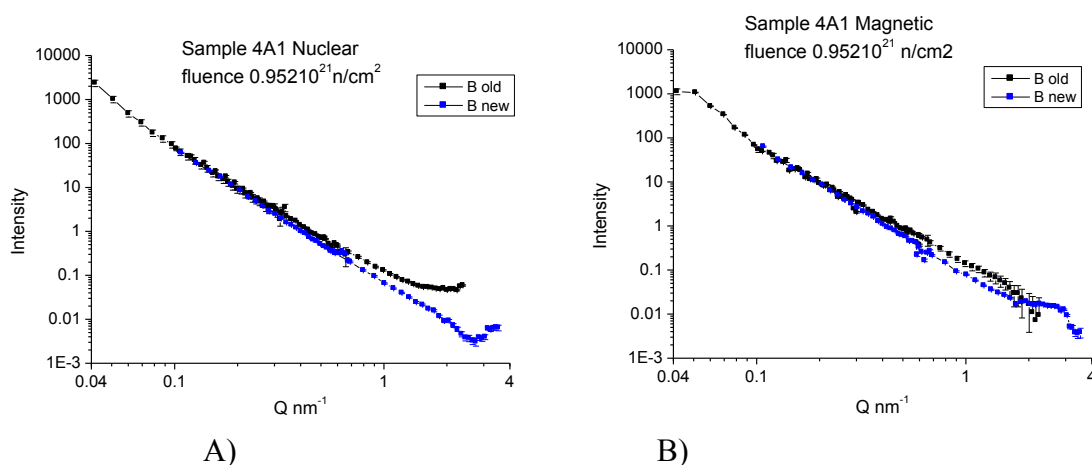


FIG. 4. A) The nuclear scattering at new and old measurement at irradiated material. B) The magnetic scattering at new and old measurement at irradiated material.

## 2.4. Results with irradiated materials

### 2.1.2. SANS measurement

The SANS measurements were performed at the instrument 'Yellow Submarine' with a two dimensional position sensitive at neutron wavelength of 0.57 nm, two sample-detector distances of 1.03 m and 5.6 m. This allows a range of scattering vectors from about 0.2-3.3 nm<sup>-1</sup> to be covered.

TABLE 3. CHARACTERISTICS OF THE IRRADIATION-INDUCED DEFECT CLUSTERS, VOLUME FRACTION, C, N, MEAN RADIUS,  $\bar{R}$  AND A-RATIO

sample	Fluence in cm <sup>-2</sup> ( $E > 0.5$ MeV)	$c$ in vol%	$\bar{R}$ nm	averaged A-ratio
Z	0	0	0	
A	$0.294 \times 10^{21}$	$0.120 \pm 0.01$	0.75	$1.7 \pm 0.1$
B	$0.952 \times 10^{21}$	$0.252 \pm 0.01$	1.01	$2.2 \pm 0.1$
C	$1.45 \times 10^{21}$	$0.437 \pm 0.02$	1.03	$2.1 \pm 0.1$

The samples were placed in a magnetic field of 1.4 T. Absolute data calibration was done using a reference sample of well-known scattering cross-section. Data reduction was carried out using the 'BerSANS program. The SANS intensities of the unirradiated reference sample were subtracted from the measured intensities of the irradiated conditions in order to get the scattering contribution of the irradiation-induced defect/solute atom clusters. The corresponding intensities are plotted in Fig. 4.

The size distributions of the clusters were calculated using the indirect Fourier transform method. The size distributions are shown in Fig.6. The absolute value of volume fraction of clusters is estimated under the assumption that the clusters are non-magnetic scatterers, whereas in Fig. 6B the volume fraction is weighted with the currently unknown nuclear scattering contrast. Differences in scaling of both magnetic and nuclear size distributions give a hint of different cluster composition. Information about the cluster composition is included in the  $A$ -ratio. Primary, the  $A$ -ratio was defined by the ratio of the SANS intensities perpendicular and parallel to the magnetic field direction. In practice, we observe a  $Q$ -dependence of the  $A$ -ratio. Therefore, we calculated an averaged  $A$ -ratio

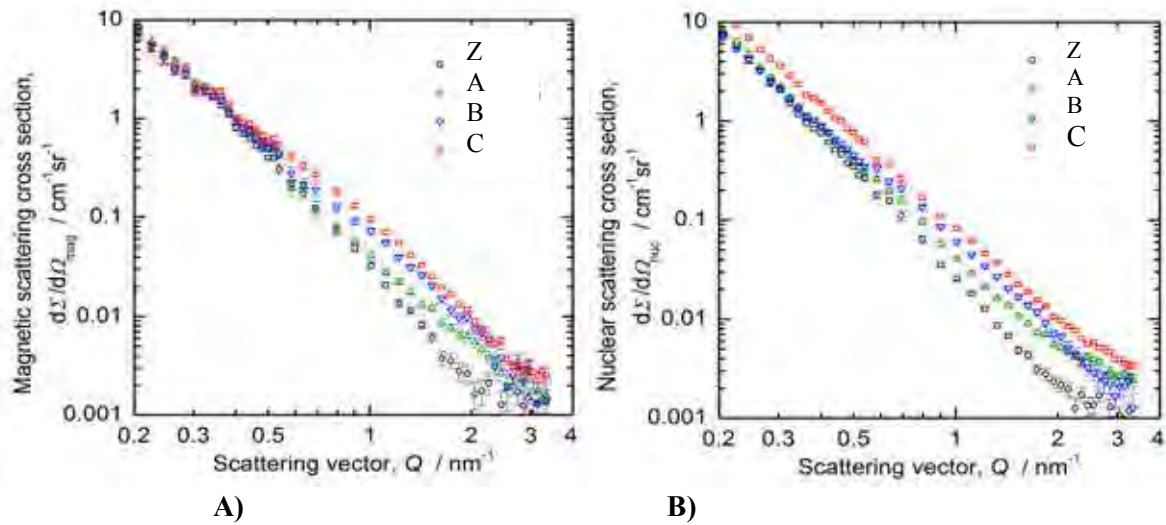


FIG. 5. A) Measured nuclear scattering cross-sections, B) Measured magnetic scattering cross-sections of different fluency of 15H2MFA

## 2.4. Results with irradiated materials

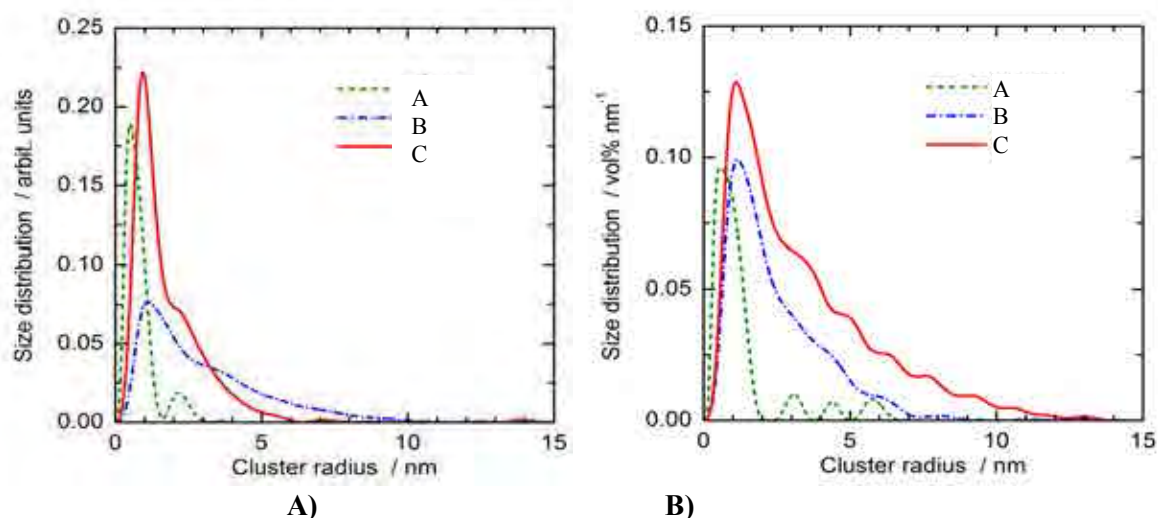


FIG. 6. A) Size distributions of irradiation-induced defect atom clusters calculated from the nuclear scattering contributions (Fig. 5. A). B) Size distributions of atom clusters calculated from the magnetic scattering contributions (Fig. 5. B).

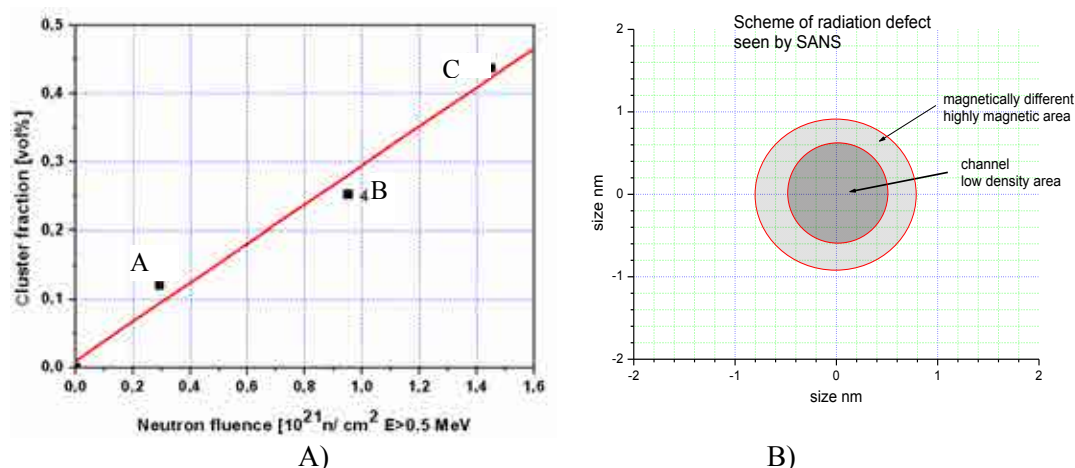


FIG. 7. A) The volume of the clusters is nearly linearly growth with the neutron fluence. B) The structure of radiation defect as SANS can “see”.

### 2.1.3. Conclusions

Similarities in the figures 6A and 6B shown, that very small clusters are at the first irradiation level (A) and somewhat larger clusters at the second and third irradiation level (samples B, C). Differences are in the scaling of the magnetic and nuclear size distributions. Therefore, a different mean cluster composition seems the reason. The mean cluster size increases slightly from 0.75 nm at the lowest fluence to about 1 nm at the higher fluences. The A-ratio also slightly increases with fluence. The result verified the earlier statement of the size of magnetic damage bigger than the nuclear one. The size of nuclear damage is between 1-2 nm while the magnetic one is more.

## 3. COOPERATIVE MEASUREMENT OXIDE DISPERSION STRENGTHENED STEEL INVESTIGATIONS WITH SANS FOR CHROMIUM CONTENT

At BNC a series of experiments using SANS technique were performed with ODS steel samples of different chemical compositions and after various heat treatments for the investigation of irradiation effects (in collaboration with JRC, The Netherlands). We have

## 2.4. Results with irradiated materials

continued investigation the phase separation in two oxide dispersion strengthened (ODS) ferritic steels, PM2000 and MA956, during isothermal ageing at 475°C. The samples used for the measurements were cut from the bars in the shape of plates of 1 mm thickness. The covering scattering vector range was from  $4 \cdot 10^{-2} \text{ nm}^{-1}$  to  $2.5 \text{ nm}^{-1}$ . The samples were placed into an external saturating magnetic field ( $\sim 1.4 \text{ T}$ ) perpendicular to the incident neutron beam direction in order to separate the nuclear and magnetic intensity. The ratio of these two contributions was used to gain information on the chemical composition of the scatterers.

The ferritic matrix of the investigated materials separates into Fe-rich  $\alpha$  and Cr-rich  $\alpha'$  phases during ageing at this temperature. The size distribution and the volume fraction of the precipitates were evaluated from the scattering data. The A-ratios of the aged MA956 samples ( $A = 1.90 \pm 0.2$ ) are in good agreement with  $\alpha - \alpha'$  phase separation of the ferritic matrix. Higher A-ratios ( $A = 2.3 \pm 0.4$ ) for PM2000 sample aged 100 h indicates the presence of other processes besides  $\alpha'$  formation during the early stages of the ageing.

Figure 9 shows the nuclear coherent scattering cross-sections of the as received and the three aged states of both investigated materials. A pronounced ageing-induced increase is found on the magnetic and nuclear scattering at scattering vectors  $q > 0.35 \text{ nm}^{-1}$  and  $0.40 \text{ nm}^{-1}$  for PM2000 and MA956, respectively. Compared to the as-received material, additional small scatterers (with sizes below  $\sim 6-8 \text{ nm}$ ) are present in the aged samples.

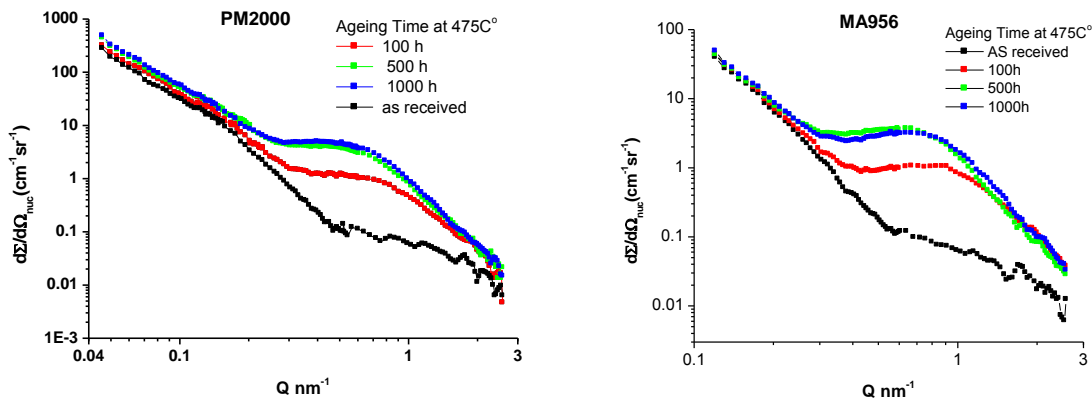


FIG. 8. Nuclear SANS scattering cross-sections for PM2000 and MA956 in as-received and three aged conditions.

It was concluded that the SANS measurements revealed the formation and subsequent growth of Cr-rich precipitates on the nanometer scale. The size distribution and the volume fraction of the precipitates were evaluated from the scattering data (Fig. 9).

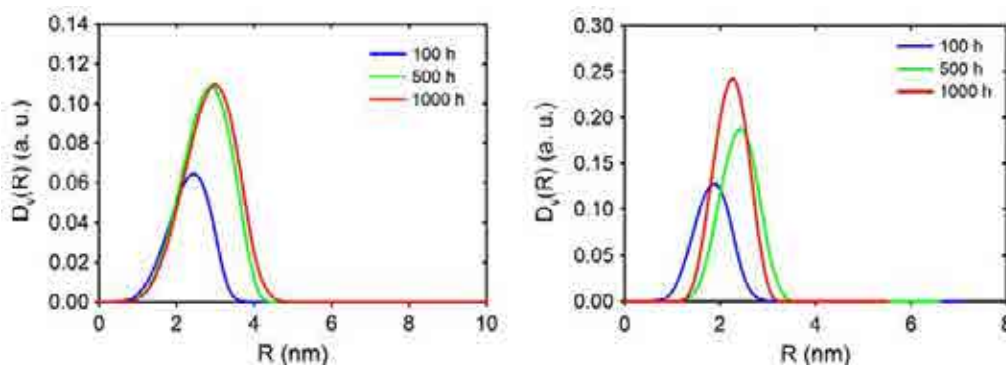


FIG. 9. Particle size distribution at three aged conditions in PM2000 (left) and MA956 (right).

## 2.4. Results with irradiated materials

For PM2000 sample aged 100 h indications were found of the presence of other processes besides  $\alpha'$  formation during the early stages of the ageing. Microhardness was found to significantly increase as a function of ageing time for both materials. The hardening is related mainly to the formation of a Cr-rich  $\alpha'$  phase.

## 4. COOPERATIVE MEASUREMENT WITH INSTITUTE FOR NUCLEAR RESEARCH PITESTI

We have investigated the stainless steel 304L and Incoloy 800HT steels used in reactor technique treated at different temperatures. We analyzed the results of SANS measurement has been carried out in BNC SANS at  $\lambda = 0.571$  nm applying magnetic field of 1.4 T, and at  $q$  range  $0.08 \text{ nm}^{-1} - 2.5 \text{ nm}^{-1}$

### 4.1. SANS investigation of heat treated incoloy 800 HT steel

Samples:

No1	No2	No3	No4
treated at 450°C for 60 day	treated at 500°C for 60day	treated at 550°C for 60 day	treated at 600°C for 60 day

#### 4.1.1. Magnetic scattering

We had a very weak magnetic scattering in stainless steel samples. The presence of magnetic component is due to martensitic phase is assumed [3] As the scattering shows the intensity of scattering from martensitic part of steel is growing as a result of applied heat treatment, nearly two order of magnitude. The characteristic size of scatterers is practically remained the same order, around 15 nm.

#### 4.1.2. Nuclear scattering

The scattering intensity of nuclear part is fitted by a sum of Guinier function and a fractal part.

$$I(q) = I_1 \exp\left(\frac{-q^2 R^2}{3}\right) + F \times q^C \quad (1)$$

Where the first part is a simplest approximation of scatterers and the second term represents the density fluctuations at the border of precipitates. (Usually that is formed by diffusion processes) From data is seen that the characteristic size of precipitates remains the same till 550°C while at 600°C a decreasing takes place. That well agrees with the growing of magnetic scattering, i.e. the growing of martensitic phase.

The surface of the precipitate border has a volume fractal feature with dimension 2.9-2.6 except at sample treated at 600°C what has surface fractal structure with dimension 2.6 (very hairy structure).

## 2.4. Results with irradiated materials

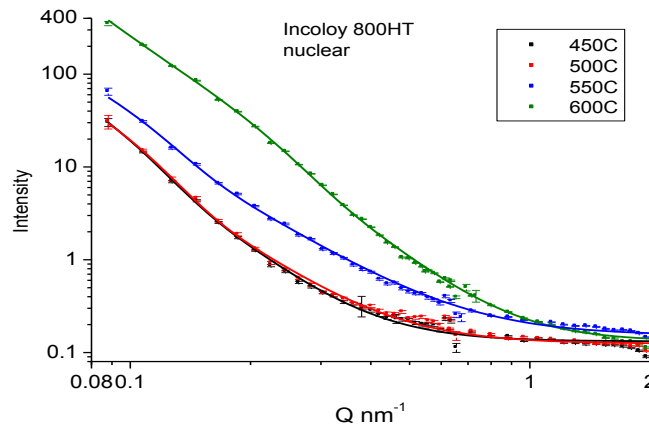


FIG. 10. Nuclear scattering at Incoloy 800 HT steel at 450°C, 500°C, 550°C and 600°C respectively. Solid lines are the fits by formulae (1).

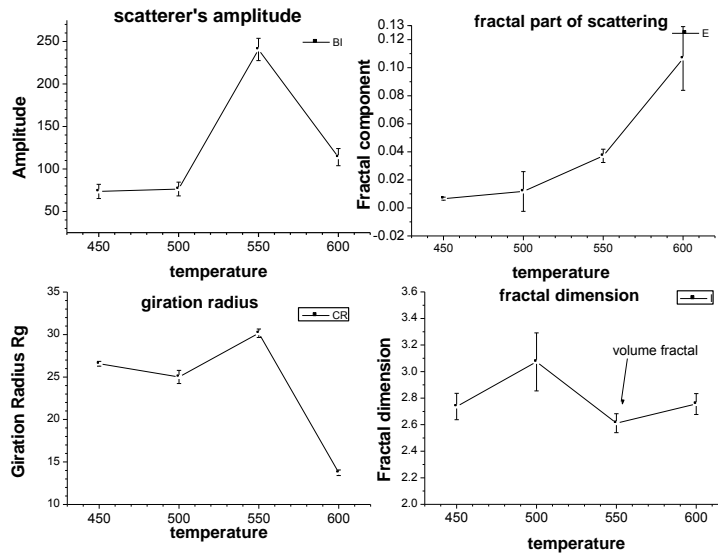


FIG. 11. Parameters of fit of scattering at Incoloy 800 HT steel at temperatures. 450°C, 500°C, 550°C, 600°C respectively, according to Eq. (1).

The scattering intensity of nuclear part is fitted by a sum of Guinier function and a fractal part. The parameters of applied models showed a structural change of samples showing the limit of useful temperature regime

Well seen that the phase transition begins at 500°C with decreasing gyration radius and increasing roughness (fractal surface dimension) of scatterers what transforms at 550°C growth of scatterer size with volume fractal structure and a fall of gyration radius at 600°C with surface fractal precipitate borders.

From data is seen that the characteristic size of precipitates remains the same till 550°C while at 600°C a decreasing takes place and the inner fractal surface is growing.

### 4.2. SANS measurement on 304L steel

Samples:

No1	No2	No3	No4
treated at 450°C	treated at 500°C	treated at 550°C	treated at 600°C
for 60 days	for 60 days	for 60 days	for 60 days

#### 4.2.1. Magnetic scattering

## 2.4. Results with irradiated materials

At steel 304L originally the magnetic scattering is weak. Only the presence and some correlation can be detected, but the measured curve not available for model fit.

At heat treatment 500°C and 550°C we observe a rising of size of magnetic scatterer. At 600°C the magnetic scattering drops so we can conclude that the martensitic phase is disappears.

### 4.2.2. Nuclear scattering

The scattering intensity of nuclear part is fitted by a sum of two Guinier function and a fractal one.

$$I(q) = I_1 \exp\left(\frac{-q^2 R_1^2}{3}\right) + I_2 \exp\left(\frac{-q^2 R_2^2}{3}\right) + F \times q^C \quad (2)$$

So we can follow the evolution of two components and a precipitate border feature.

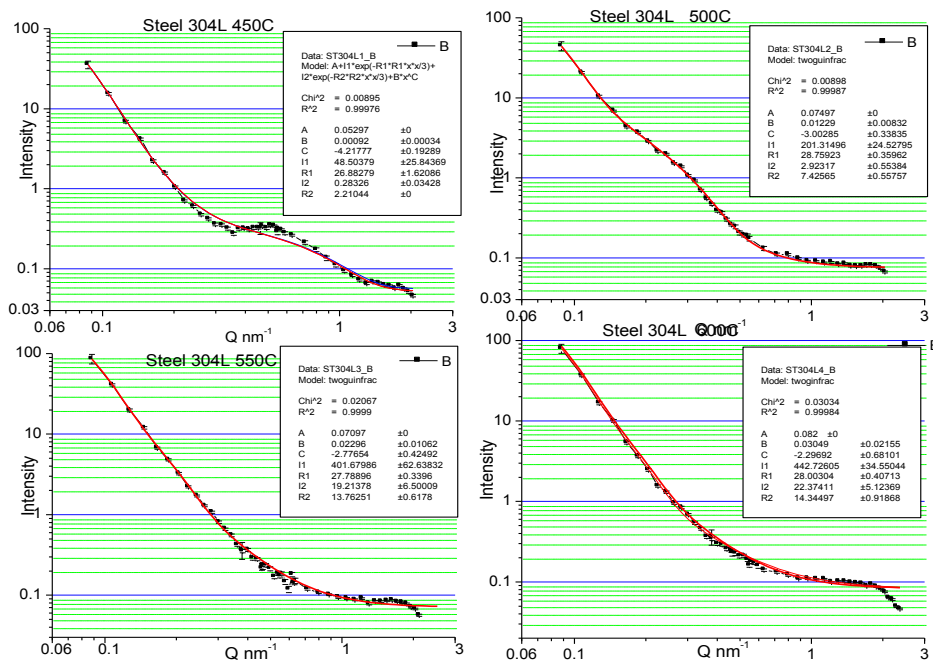


FIG. 12. Nuclear scattering at 304L steel 450°C, 500°C, 550°C, and 600°C. Solid lines are the fits according to formulae (2).

Displaying parameter changes of Eq. (2) vs. temperature we can conclude that the bigger precipitate has a characteristic size ~25 nm and no substantial changes while the smaller precipitate size's changes from 2-8 nm. The precipitate's border has a volume fractal feature with dimension 2.3-2.8 except at sample treated at 600°C where the border has surface fractal structure with dimension 2.7 (very hairy structure).

## 2.4. Results with irradiated materials

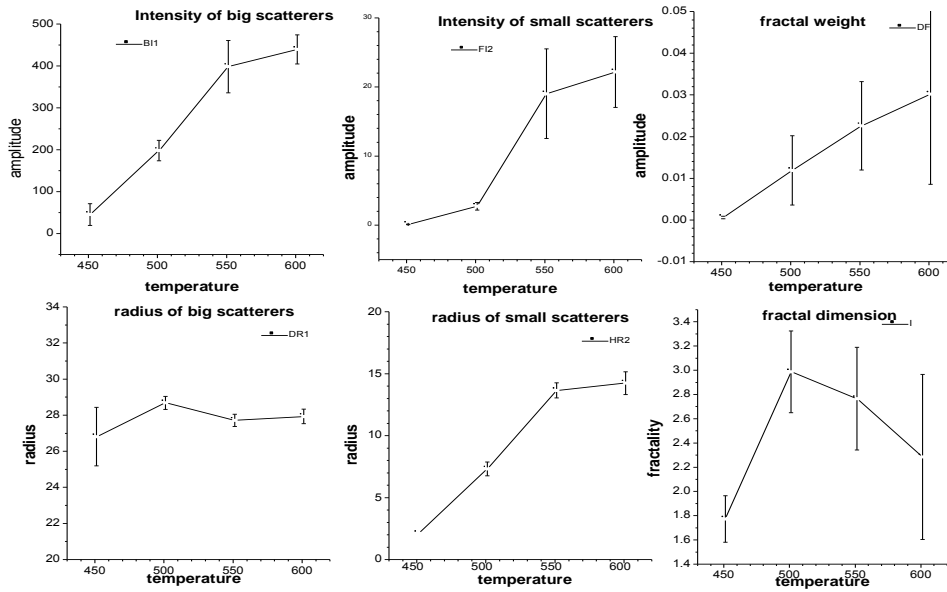


FIG. 13. Parameters of fit of scattering at 304L steel at temperatures 450°C, 500°C, 550°C and 600°C respectively.

Also seen (Fig.13) that the phase transition begins at 500°C with constant (big) gyration radius and increasing scattering intensity showing the growth the volume fraction Also the small precipitates has increasing character both the intensity and size. The surface roughness (fractal surface dimension) of scatterers is also growing monotonically.

## 5. COOPERATION WORKS WITH ENEA

We compared the SANS results of ILL and BNC measured on the same ODS steel HXN850 sample and found a good agreement in data. A further common work on analyse and interpretation of received results is in process (Fig. 14).

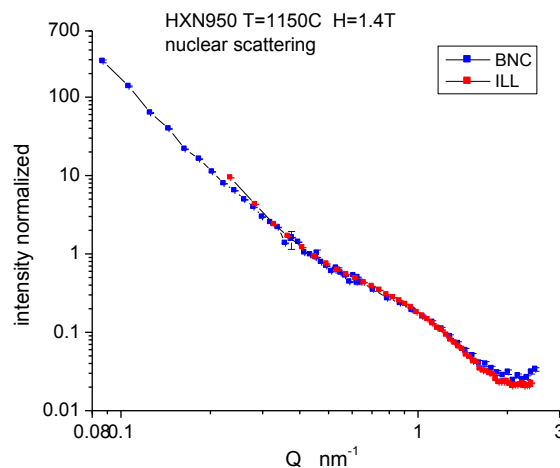


FIG. 14. SANS results of ILL and BNC



## 2.4. Results with irradiated materials

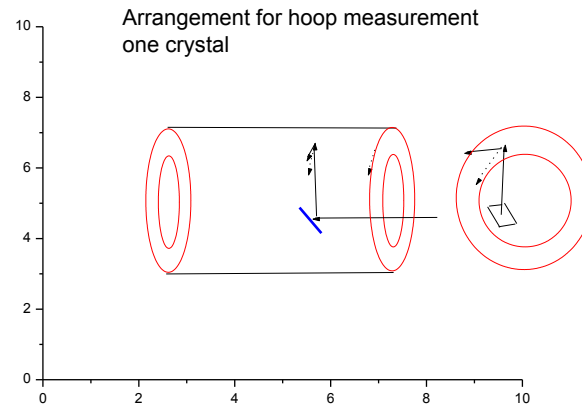


FIG. 17. Arrangement with one crystal reflection.

### 6.1. Results

Test measurement using PG crystal was carried out with periscope arrangement (Fig. 17). We had some technical stability problem and the angular spread of beam became much higher than desirable in double reflection, arrangement. The intensity gain was not enough high to carry out the measurement on the full sample. Using improved mechanics and better crystals hopefully will get better results, because this arrangement is more comfortable than the one crystal arrangement.

In case of measurement with one reflecting crystal for the perpendicular arrangement we need to use wavelength 0.286 nm. Then the incoming beam is vertical and the outgoing is horizontal that can be fulfilled approximately with Cu(111) or Ni(111) reflector crystal. For PG crystal such arrangement exists only for 0.26 nm, so we had a 10 deg. inclination of reflected beam. Due to technical reasons we have carried out the measurement with PG crystal. After the necessary mathematical transformations we get the necessary results for hoop arrangement in big sample. An example of resulted serial of measured stresses is in Fig. 18.

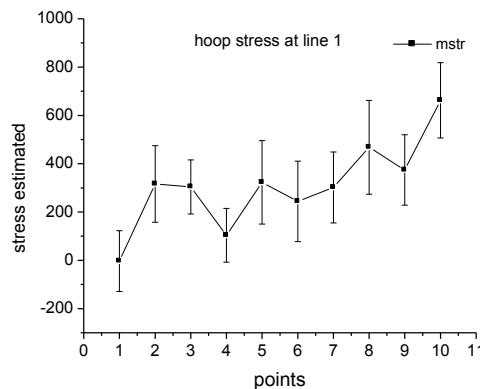


FIG. 18. The hoop stress near by the inner surface of nozzle. Points are started at conical part with distances 4.5 mm between them. Clearly seen that the compressive stress is growing with sample thickness.

### REFERENCES

- [1] KEIDERLING, U., Applied Physics A **74** (2002) S1455–S14571
- [2] HEINTZE, C., J. Nucl. Mater. **409** (2009) 106-111].
- [3] S.S.M. Tavares, M.R. da Silva, J.M. Neto, S. Miraglia, D. Fruchart

## 2.4. Results with irradiated materials

Ferromagnetic properties of cold rolled AISI 304L steel *Journal of Magnetism and Magnetic Materials* **242–245** (2002) pp.1391–1394

### Publications has been done during the CRP

[A] Z. Száraz, G. Török, V. Krsjak, P. Hähner, C. Ohms Microstructure evolution of high Cr-content ODS steels during thermal ageing DIANA I: 1st International Workshop on Dispersion Strengthened Steels for Advanced Nuclear Applications, Aussois, France, April 4-8 (2011).

[B] Z. Száraz, Gy. Török, C. Ohms, P. Hähner

SANS investigation of microstructure evolution in high Cr-content oxide ECNS2011 Prague

[C] F. Gillemot, N. Kresz, F. Oszwald, A. Ulbricht, M. Hernández Mayoral, Gy. Török, B. Radiguet, S. C., Ákos Horváth, M. Horváth, A. Kovács Paper Title: Microstructural changes in highly irradiated 15H2MFA steel Symposium: 26th Symposium on the Effects of Radiation on Nuclear Materials

[D] Gy. Török, R. Székely, F. Gillemot, Á. Horváth SANS and residual stress investigations in BNCR IAEA-meeting RER/4/032/9017-01 Regional Workshop on Concerted Actions in Research and Applications with Neutron Beams in Europe, Budapest, Hungary, 1-3 June (2011).

[E] Gy. Török, H. Ákos, R. Székely, F. Gillemot Investigation of Reactor Materials Using Neutron Beam IAEA Technical Meeting on Catalogue of Products and Services of Research Reactors: Applications of Neutron Beams /5 – 9 September (2011) IAEA, Vienna, Austria.

[F] Z. Száraz, Gy. Török, V. Kršjak, P. Hähner SANS investigation of microstructure evolution in high chromium ODS steels after thermal ageing *Journal of Nuclear Materials*, Volume **435**, Issues 1–3, April (2013) 56-62

[G] L. Tatár, Gy. Török, D. J Smith, Son Do, C. Ohms, L. Kovács

Manufacture, Residual Stress Measurement and Analysis of a VVER-440 Nozzle Mockup Proceedings of the ASME 2013 Pressure Vessels & Piping Conference, PVP, July 14-18, (2013) Paris, France



## **2. RESULTS ACHIEVED**

### **2.5. OPTIMIZATION OF INSTRUMENTS FOR RESIDUAL STRAIN/STRESS MEASUREMENTS**

## 2.5. Optimization of instruments for residual strain/stress measurements

### FINAL REPORT ON EVALUATING RESIDUAL STRESSES AND INTERNAL DEFECTS IN NUCLEAR MATERIALS AT THE OPAL REACTOR AT ANSTO, AUSTRALIA

M. LAW, D. CARR

ANSTO, Locked bag 2001, Kirrawee DC  
NSW, 2232  
Australia  
Email: mlx@ansto.gov.au

#### **Abstract.**

This project is concerned with developing capabilities in characterizing materials of relevance to the nuclear energy sector with neutron beams. A number of measurements were; residual stress measurements on a fusion first wall candidate composite material and a Zircaloy vessel which contains the cold neutron source. Texture measurements were made on 3 Zircaloy samples from reactor components. Planned SANS measurements were not possible as the instrument was not available. The neutron imaging instrument Dingo was constructed, commissioned, and is now operating.

## 1. INTRODUCTION

The Opal reactor in Sydney, Australia has been successfully commissioned and has run for 6 years. It has beamlines for thermal and cold neutrons, although the cold source was not operating during the period of this project. This project was focussed on using neutron beam methods to investigate materials of interest to the nuclear energy sector. The techniques of interest available at the Opal reactor are diffraction (including residual stress), texture measurement, Small Angle Neutron Scattering (SANS), and radiography.

## 2. WORK PLAN

- 2.1. Design, construct and commission neutron radiography facility DINGO.
- 2.2. Design flasks for moving radioactive samples and for measurement.
- 2.3. Assess shielding requirements.
- 2.4. Investigate the experience of other facilities in the examination of radioactive samples.
- 2.5. Manufacture transfer flask and additional shielding for KOWARI.
- 2.6. Undertake texture measurements on KOWARI on Zircaloy samples.
- 2.7. Undertake residual stress measurements on irradiated samples from OPAL.
- 2.8. Undertake neutron radiography/tomography measurements on samples of hydrided zirconium that have been irradiated.
- 2.9. Undertake SANS measurements of irradiation damage over a range of fluences.

## 3. COOPERATIVE ACTIVITIES AS DISCUSSED AND AGREED WITH PARTNERS WITHIN THE CRP

- 3.1. Evolution of Phases, Inter-granular Stresses and Texture in Cold Rolled Zr Pressure Tubes; coordinated and specimens provided by J. Santisteban, (CNEA).
- 3.2. SANS measurements on VVR 440 vessel material: coordinated and specimens are provided by G. Török (SZFKI).
- 3.3. Neutron diffraction measurements on thermo-mechanical loaded ODS steel rods: Coordinated by M. Bourke (LANL) with specimens from M.-H. Mathon (CEA).
- 3.4. SANS measurements on ODS steels: Coordinated and specimens provided by M.-H. Mathon/J.Teixeira (CEA).

## 2.5. Optimization of instruments for residual strain/stress measurements

3.5. Residual stress investigations by neutron diffraction in ODS friction weld: Coordinated by R. Martins (IE) with specimens provided by M.-H. Mathon (CEA).

### *Year 1 work plan and progress*

DINGO was completed in March and commissioned in May 2013. First measurements were made in mid-2013 (Fig. 1). (Task 2.1 Design neutron radiography facility DINGO).



*FIG. 1. First image from DINGO neutron radiography instrument.*

### *Handling and shielding for active samples*

ANSTO is constructing hot-cells for nuclear materials research and a metallography laboratory dedicated to handling active materials with the emphasis on specimen preparation (cutting, grinding, and etching) and characterization (microscopy). We have sourced transport flasks for moving samples between the hot-cells, active metallography labs, and the beam-lines. We have not designed instrument-specific shielding due to the lack of information on activity for the Round-robin samples. We have requested information from Chalk River on shielding used during residual stress measurements made on active samples.

### *Tasks*

- 2.2. Design flasks for moving radioactive samples and for measurement.
- 2.3. Assess shielding requirements.
- 2.4. Investigate the experience of other facilities in the examination of radioactive samples.
- 2.5. Manufacture transfer flask and additional shielding for KOWARI.

### *Additional activities year 1*

- Received 2 samples of reactor pressure vessel steel from SZFKI for SANS analysis.

## 2.5. Optimization of instruments for residual strain/stress measurements

- Submitted a beam-time proposal for the Round-robin “SANS of reactor materials”.
- Received a texture measurement protocol from CNEA.
- Submitted a beam-time proposal for the Round-robin “Texture of Zircaloy tubes”.

### *Texture measurements*

Texture measurements were made of Zircaloy samples from J. Santisteban, (CNEA), on the Kowari instrument at ANSTO.

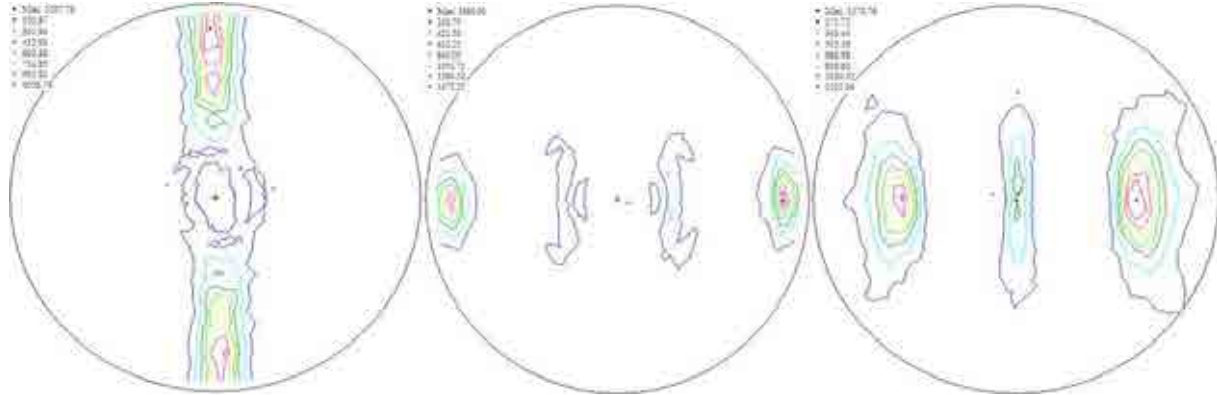


FIG. 2. Pole figures of Zr 2.5 tubing supplied by J. Santisteban, (CNEA), the texture measurements were made on Kowari at ANSTO.

### *Tasks*

2.6 Undertake texture measurements on KOWARI on Zircaloy samples.

3.1 Evolution of Phases, Inter-granular Stresses and Texture in Cold Rolled Zr Pressure Tubes; coordinated and specimens provided by J. Santisteban, (CNEA).

### *Residual stress measurements in a fusion first wall candidate material*

Residual stresses in a fusion first wall candidate material (diffusion bonded W/Cu composites produced by Professor Zhangjian Zhou from the Beijing Technical University) were measured on Kowari (Fig. 3).

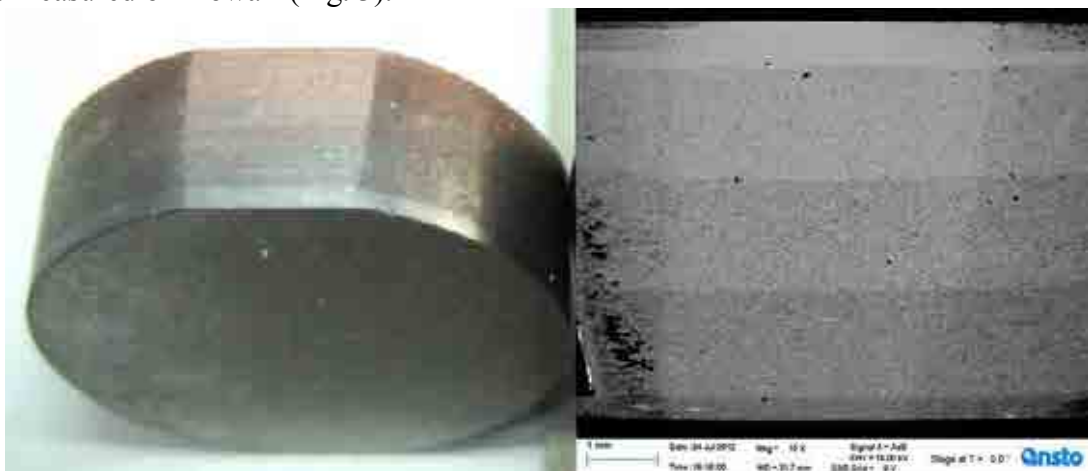


FIG. 3. L) Five layer composite W (base) and Cu (top). R) SEM image of polished flat area in same orientation (W dark, at base) showing composition changes.

## 2.5. Optimization of instruments for residual strain/stress measurements

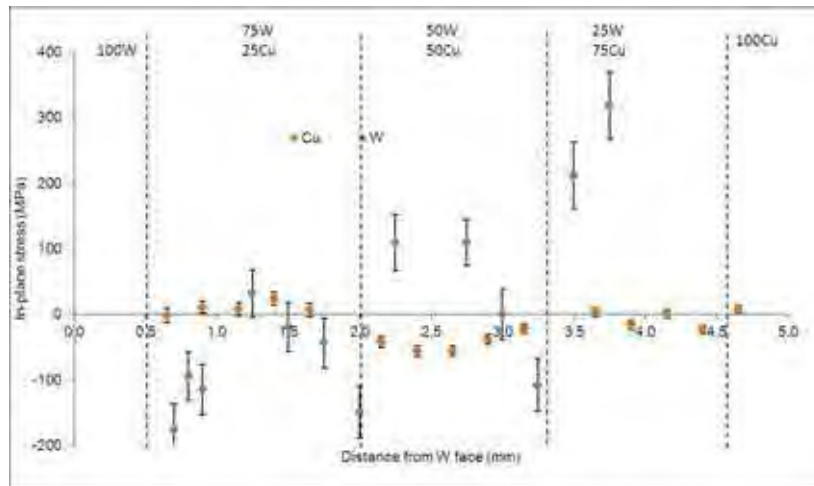


FIG. 4. Residual stress measurements across compositional gradient.

Residual stress measurements were made on a weld in a Zircaloy containment vessel, this vessel contains the cold neutron source at the Opal reactor (Fig. 5).



FIG. 5. Section of Cold neutron source containment vessel (left) and weld in cross section (left).

The weld was a qualifying weld made during manufacture. As the weld had received post-weld heat treatment the stresses were low (Fig. 6).

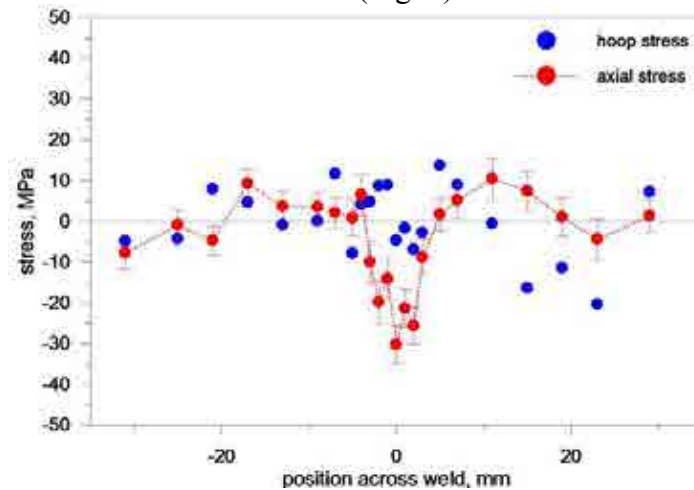


FIG. 6. Stresses across weld in Zircaloy containment vessel.

## 2.5. Optimization of instruments for residual strain/stress measurements

### *Additional work*

- In-progress: Writing a book chapter “Characterization of materials for the nuclear energy sector” for the *Neutron Scattering Applications and Techniques* book series with Mark Bourke, Don Brown, and Sven Vogel, from Los Alamos National Laboratories.

### *Uncompleted tasks*

For operational reasons several instruments were unavailable during the time of this project. The SANS instrument (Quokka) was not running for entire period of the project. The following experiments were not possible:

- Tasks 2.9 Undertake SANS measurements of irradiation damage over a range of fluences.
- Task 3.2 SANS measurements on VVR 440 vessel material from G. Török (SZFKI)
- 316 stainless steel based ODS steel samples for SANS analysis from Professor Zhangjian Zhou from the Beijing Technical University.

As Dingo has only begun commissioning task 2.8 (radiography on samples of hydrided zirconium) has not been started.

Neutron diffraction measurements on thermo-mechanical loaded ODS steel rods:  
Coordinated by M. Bourke (LANL) with specimens from M.-H. Mathon (CEA).

- No protocol or samples received.  
SANS measurements on ODS steels: Coordinated and specimens will be provided by M.-H. Mathon/J.Teixeira (CEA).
- No protocol or samples received.  
Residual stress investigations by neutron diffraction in ODS friction weld: coordinated by R. Martins (IE) with specimens provided by M.-H. Mathon (CEA).
- No protocol or samples received.

### *Remaining work-plan, both individual activities and joint activities*

- SANS measurements will be made on ODS samples from G. Török (SZFKI) and from Z. Zhou (Beijing Technical University) when the SANS instrument (Quokka) is available.
- Further residual stress measurements will be made on W/Cu composite samples from Z. Zhou (Beijing Technical University) when new (larger) samples are manufactured.
- Book chapter will be published.

## 4. SUMMARY AND CONCLUSIONS

Valuable collaborations have been initiated; we have made neutron measurements of materials developed for the nuclear energy sector and have collaborated on a book chapter on the precise topic of this CRP. The expertise of the group has allowed us to gain knowledge quickly, and draw upon member’s experience.

## 2.5. Optimization of instruments for residual strain/stress measurements

### REFERENCES

In production: book chapter “Characterization of materials for the nuclear energy sector” for the *Neutron Scattering Applications and Techniques* Springer book series.

## 2.5. Optimization of instruments for residual strain/stress measurements

### DEVELOPMENT AND OPTIMIZATION OF HIGH-RESOLUTION NEUTRON SCATTERING INSTRUMENTS DEDICATED TO CHARACTERIZATION AND TESTING OF MATERIALS OF RELEVANCE TO NUCLEAR ENERGY SECTOR AND RELATED EXPERIMENTS IN SANS, RESIDUAL STRAIN/STRESS AND TEXTURE STUDIES

M. VRANA, P. MIKULA  
Nuclear Physics Institute ASCR,  
250 68 Rez,  
Czech Republic  
Email: [vrana@ujf.cas.cz](mailto:vrana@ujf.cas.cz)

#### **Abstract.**

In this report we present the results we have received in the frame of participation in the CRP project. According to the plan of the project several experiments related namely to characterisation and testing of materials of relevance to nuclear sector were carried out. In this way two experimental methods were used: residual strain/stress measurements by neutron diffraction and small angle neutron scattering (SANS). A special attention has been paid to the following samples: Austenitic stainless steel plates with a longitudinal weld joint, Charpy-V notched specimen of low-alloy ferritic steel, 50 mm thick welds in ferritic steel, austenitic single pass fillet steel welds, Ni-based CMSX4 superalloy.

## 1. INTRODUCTION

The following working plan was accepted:

1. Participation on TECDOC in the field of neutron diffraction a high resolution SANS
2. Ex-situ and in-situ structure change studies by powder diffraction.
3. Microstructure measurements and studies of precipitates in superalloys and porosity by high-resolution SANS.
4. Strain/stress measurements of metallic polycrystalline samples around the welds.
5. Instrumentation development, software.

In detail the following main experimental work has been done:

- Residual strain/stress measurements in the vicinity of electron beam welds of Charpy-V notched specimen. Specimen with welds on one side as well as with welds on two opposite sides was prepared by reconstitution method. The samples are then subject of mechanical tests for determination of irradiation influence on parameters of reactor vessel steels.
- HAZ microstructure of irradiated specimens of A347 austenite stainless steel around the core shroud weld.
- investigation of an optimum composition of the additive material in order to decrease residual stresses in the vicinity of the foot of the welding joint on high strength steels.
- Residual strain/stress instrument development permitting effectively to measure residual strains in the depth of 50 mm.
- Creep studies in Ni-based CMSX4 superalloy by SANS.

## 2.5. Optimization of instruments for residual strain/stress measurements

### 2. RESIDUAL STRAIN/STRESS MEASUREMENTS IN THE VICINITY OF WELDS

#### 2.1. Principles of the neutron diffraction method of residual strain/stress measurements

The principle of the neutron diffraction method is well known. It consists in the precise determination of the  $d_{hkl}$ -spacing of particularly oriented crystal planes. Knowing the stress-free lattice spacing  $d_{0,hkl}$ , the lattice strain  $\varepsilon_{hkl}$  can be calculated according to the equation

$$\varepsilon_{hkl} = \frac{d_{hkl} - d_{0,hkl}}{d_{0,hkl}} = \frac{\Delta d_{hkl}}{d_{0,hkl}} \quad (1)$$

In general, the measured quantity in the diffraction experiment is the lattice strain component. For determination of the stress tensor components, Hooke's law can be used. For diffraction experiments, this formula for  $\sigma_x$  stress component can be written in the form

$$\sigma_x = \frac{E_{hkl}'}{(1 - 2\nu_{hkl}')(1 + \nu_{hkl}')}] [(1 - \nu_{hkl}')\varepsilon_x^{hkl} + \nu_{hkl}'(\varepsilon_y^{hkl} + \varepsilon_z^{hkl})] \quad (2)$$

where  $\varepsilon_{x,y,z}^{hkl}$  is the  $x,y,z$ -component of the lattice strain measured at the  $hkl$  crystal lattice plane,  $E_{hkl}'$  and  $\nu_{hkl}'$  are the diffraction elastic Young modulus and diffraction Poisson ratio, respectively. The  $\varepsilon_{x,y,z}^{hkl}$  lattice strain components are determined in the neutron diffraction experiment. Corresponding relations for other  $y$  and  $z$  stress components are obtained by simple permutations of  $x$ ,  $z$  and  $y$  indexes.



FIG. 1. Photograph of the 2HG21 welded plate and chosen system of coordinates (compatible with Fig. 2).

#### 2.2. Neutron diffraction mapping of internal residual stresses around weld joint of austenitic stainless steel plates

Three austenitic stainless steel plates with a longitudinal weld joint were examined. The material is used for reactor vessel construction. The plates were marked as B3282, B32182 and 2HG21. The photograph of one specimen and introduction of the system of coordinates is shown in Fig. 1. For the neutron diffraction experiment we used the austenitic reflection (111) and two neutron wavelengths. Because of the rather large thickness of the plates varying from

## 2.5. Optimization of instruments for residual strain/stress measurements

24-29 mm, the measurement of the strain components  $x$  and  $y$  had to be performed with a lower diffraction angle ( $2\theta = 44^\circ$ ). In the case of measured  $x,y$ -strain components, the neutron beam carrying the desired information is passing through the plate thickness (see Fig. 2). In the case of the recommended diffraction angles  $2\theta = 90^\circ$ , the neutron beam path through the plate is too long and the transmitted neutron intensity is attenuated due to absorption. In this case, the diffraction arrangement with  $2\theta = 44^\circ$  and corresponding neutron wavelength of  $\lambda = 1.5 \text{ \AA}$  was used to overcome the above mentioned problem. The  $z$ -strain components was measured with the diffraction angle of  $2\theta = 69^\circ$  and the neutron wavelength of  $\lambda = 2.3 \text{ \AA}$ .

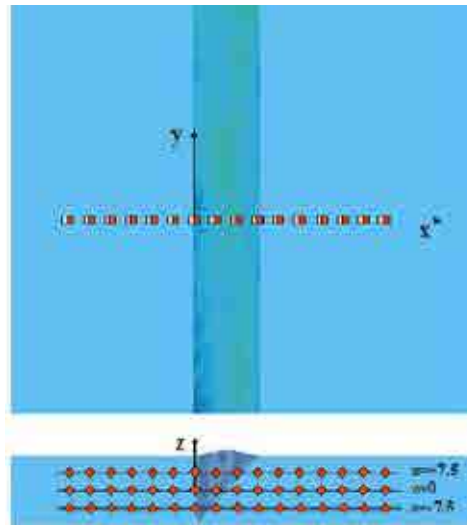


FIG. 2. Introduction of the system of coordinates for experimental measurement of internal stresses around the weld joint in different depths. Red squares show the inspected gauge volume.

Two Cd-slits of  $3 \times 3 \text{ mm}^2$  and  $3 \times 40 \text{ mm}^2$  in incident and diffracted beam, respectively, were used for definition of the gauge volume, resulting information on internal stresses is thus averaged over the volume of  $27 \text{ mm}^3$ . In the case of the present tested welded materials, the chemical composition of the used weld material is different from the base austenitic steel and, consequently, the stress-free lattice parameter of the weld material is different than base material of welded parts. To avoid the misinterpretation of the observed different lattice parameter in base and weld material, respectively, as a lattice strain, we have to perform a calibration and correction measurement. For this purpose, the special correction specimen was produced from each welded plate. The thin slices of 2.5-4 mm thickness were cut from the end face of the welded plates. These slices were further cut to release the internal residual stresses. For calculation of the stress tensors the values of diffraction elastic constants for austenitic steel were found in literature ( $E_{111} = 248 \text{ GPa}$ ,  $\nu_{111} = 0.24$ ). The resulting  $x$ ,  $y$ ,  $z$  stress components are plotted in Figs 3-5.

All examined plates exhibit similar distribution of residual stresses around the weld joint. The maximum stress level has been found in the case of the  $\sigma_y$  stress component; the tensile stresses of the maximum amplitude from 300 MPa (plate B3282 and B32182) to 500 MPa (plate 2HG21) were detected. On the other hand,  $\sigma_z$  stress component remain practically negligible in all cases. Surprisingly, observed stress distribution behaves in an opposite way – higher stress level ( $\sigma_z = \sim 500 \text{ MPa}$ ) and larger relaxation length of stresses in heat-affected zone ( $\sim 30 \text{ mm}$ ) are detected in the 2HG21 plate. More favorable values were observed in B3282 and B32182 plates; amplitude of  $\sigma_z = \sim 300 \text{ MPa}$  and relaxation length of about 20 mm).

2.5. Optimization of instruments for residual strain/stress measurements

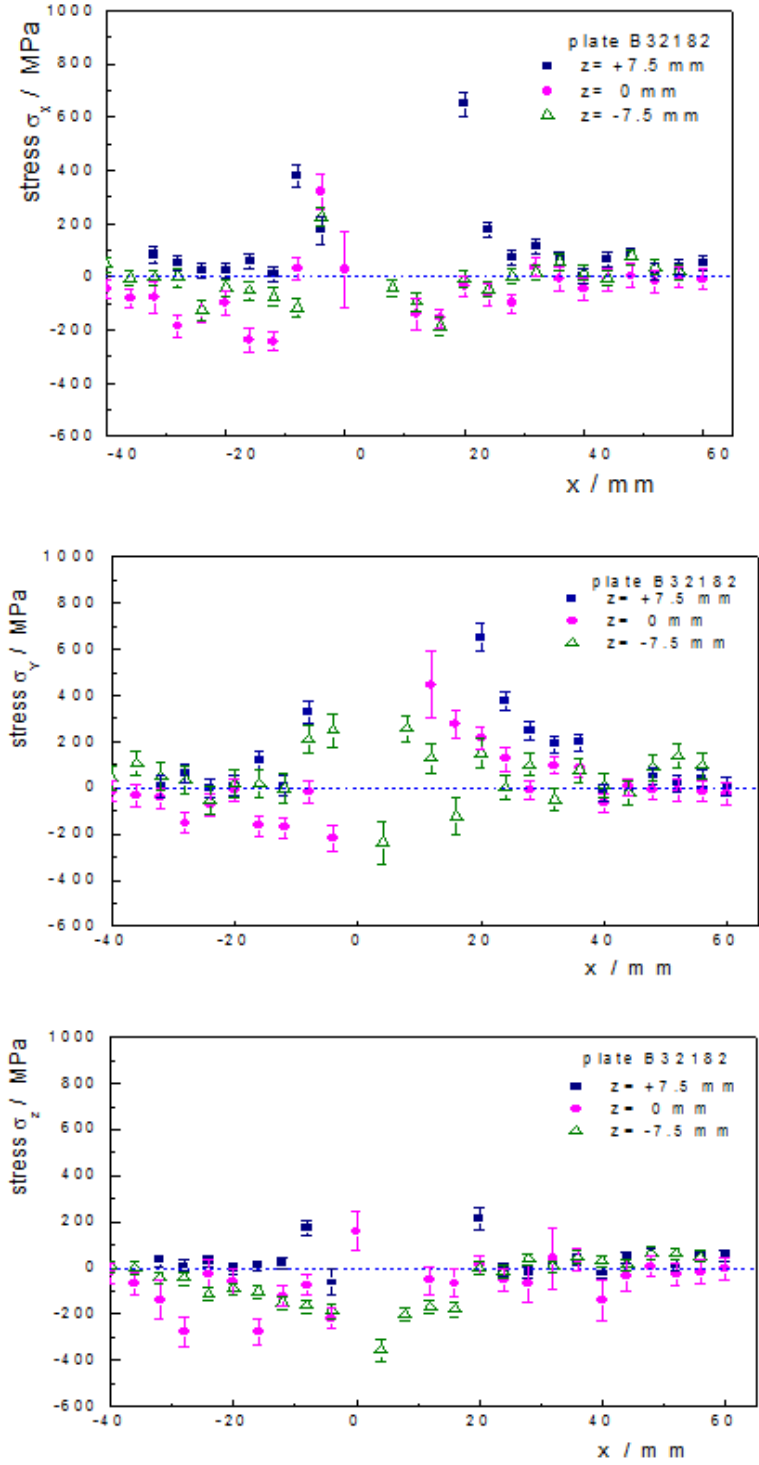


FIG. 3 a,b,c. Scans of individual stress components measured at a different depths in the plate B32182 (x-component (a), y-component (b) and z-component (c)).

2.5. Optimization of instruments for residual strain/stress measurements

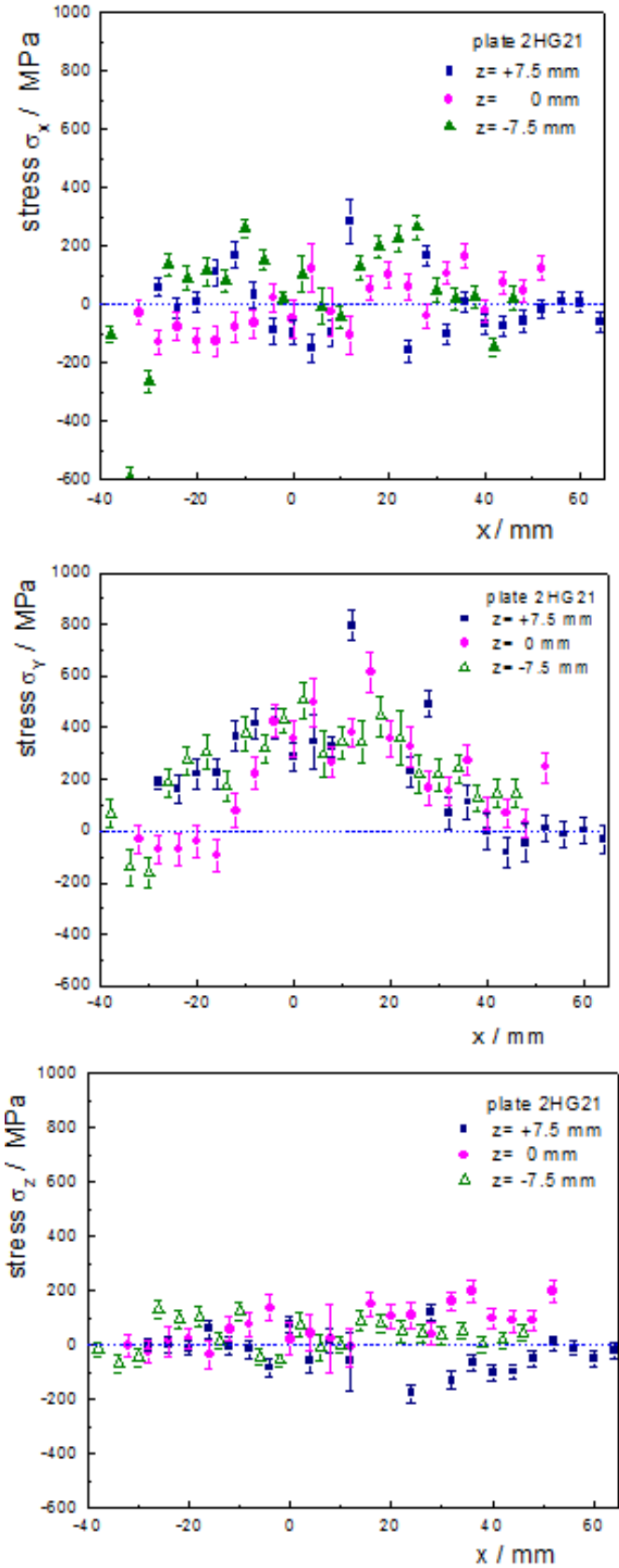


FIG. 4 a,b,c. Scans of individual stress components measured at a different depths in the plate 2HG21 (x-component (a), y-component (b) and z-component (c)).

2.5. Optimization of instruments for residual strain/stress measurements

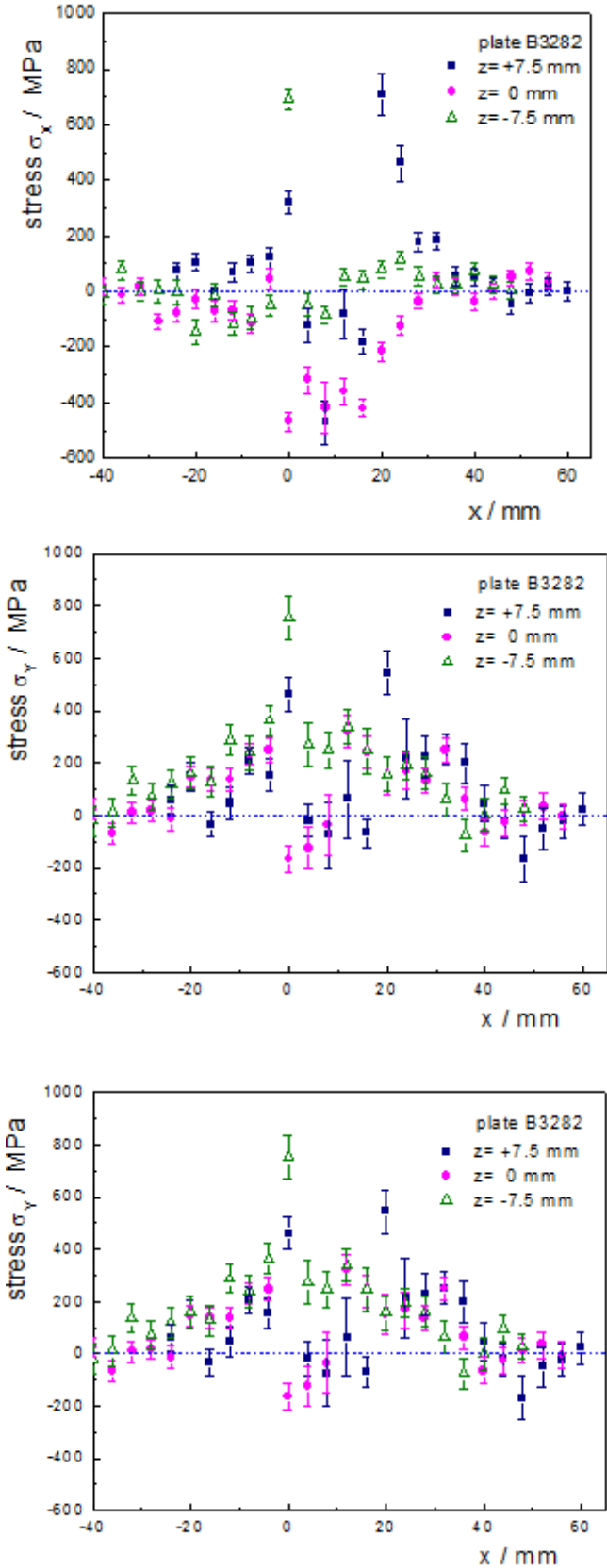


FIG. 5 a,b,c. Scans of individual stress components measured at a different depths in the plate B3282 (x-component (a), y-component (b) and z-component (c)).

## 2.5. Optimization of instruments for residual strain/stress measurements

The width of stress relaxation region in heat-affected zone of the 2HG21 is practically identical in all examined depths (see Fig. 4). On the other hand, the width of stress relaxation region in plates B3282 and B32182 follows the width of the weld joint insight the plate and becomes narrower in  $z = 0$  mm and  $z = -7.5$ mm (see Fig. 3b).

In the case of the B32182 plate, it was practically impossible to measure reliable values of the strains within the weld joint, because the diffracted neutron intensities were strongly attenuated in this region, especially in strain components measured in transmission geometry. The possible interpretation of this effect is a slight contamination of the weld metal by an element strongly absorbing thermal neutrons, such as cadmium or boron.

## 2.3. Neutron diffraction mapping of residual stresses in the vicinity of electron beam welds of Charpy-V-notch specimen

In this case, the specimens with welds on one side as well as with welds on two opposite sides were prepared by reconstitution method. Welding was performed with electron beam in a vacuum and proceeded in accordance with the ASTM E 1253 standard. The reconstitution technique of constructing specimens from small pieces of material is usually called reconstitution. Such miniaturized specimen technology permits the characterization of mechanical behaviour while using a minimum volume of material. The compound specimen is achieved by attaching an additional material (A) around a material of interest (the insert material - B) which results in a test specimen of standard dimensions. The incorporation of a small piece from a previously tested specimen into a compound one, allows e.g. to multiply the number of tests. This can be especially important if the amount of the available material is restricted and mechanical parameters have to be determined. Very often one can meet with such necessity in the nuclear power plant industry e.g. nuclear pressure vessel surveillance, failure analysis, and post irradiation testing.

The interface between the stud and the insert is created by using welding techniques. However, before testing the mechanical properties the microstructure after welding has to be examined to ensure that the material in the vicinity of the notch is essentially unchanged after the welding process. For example, it is well known that the residual stresses resulting from the welding process can be nonnegligible even at the distance up to several millimetres from the notch and thus significantly influence the mechanical properties of the material and in this case on the insert material.

In our case electron-beam welding (EBW) was used. Welded pieces were of low-alloy ferritic steel material. The central part of the samples was made from reactor pressure vessel steel (surveillance material). Welding was performed with electron beam in a vacuum and proceeded in accordance with the ASTM E 1253 standard. After the residual strain/stress measurements, the Ch-V specimens were used for performing the impact tests in accordance with the standards ČSN ISO 148-1 and ASTM E 23. In the present case the strain/stress measurements had to map the internal stresses after welding, especially in the middle part of the testing sample B, which is the subject of the followed mechanical tests. The main notch is located in the center of the specimen.

## 2.5. Optimization of instruments for residual strain/stress measurements



*FIG. 6. Photo of the specimen with the weld on one side as installed on the neutron beam defined by slits.*

Figures 7 and 8 document that residual stresses are present in the vicinity of electron beam weld. Their maximum achieves the value 400-500 MPa. They are, of course, not present at the depth of 7.5 mm of the sample with the weld only on one side where the heat affected zone is missing (see Fig. 7c). Taking into account stress distribution along the scan-axis in the material (along the longest edge of the sample) it can be seen that significant stresses are extended in the area of the length of about 5 mm and in the case of the welding on both sides, the stresses reach the middle area of the insert, where mechanical tests should be carried out.

2.5. Optimization of instruments for residual strain/stress measurements

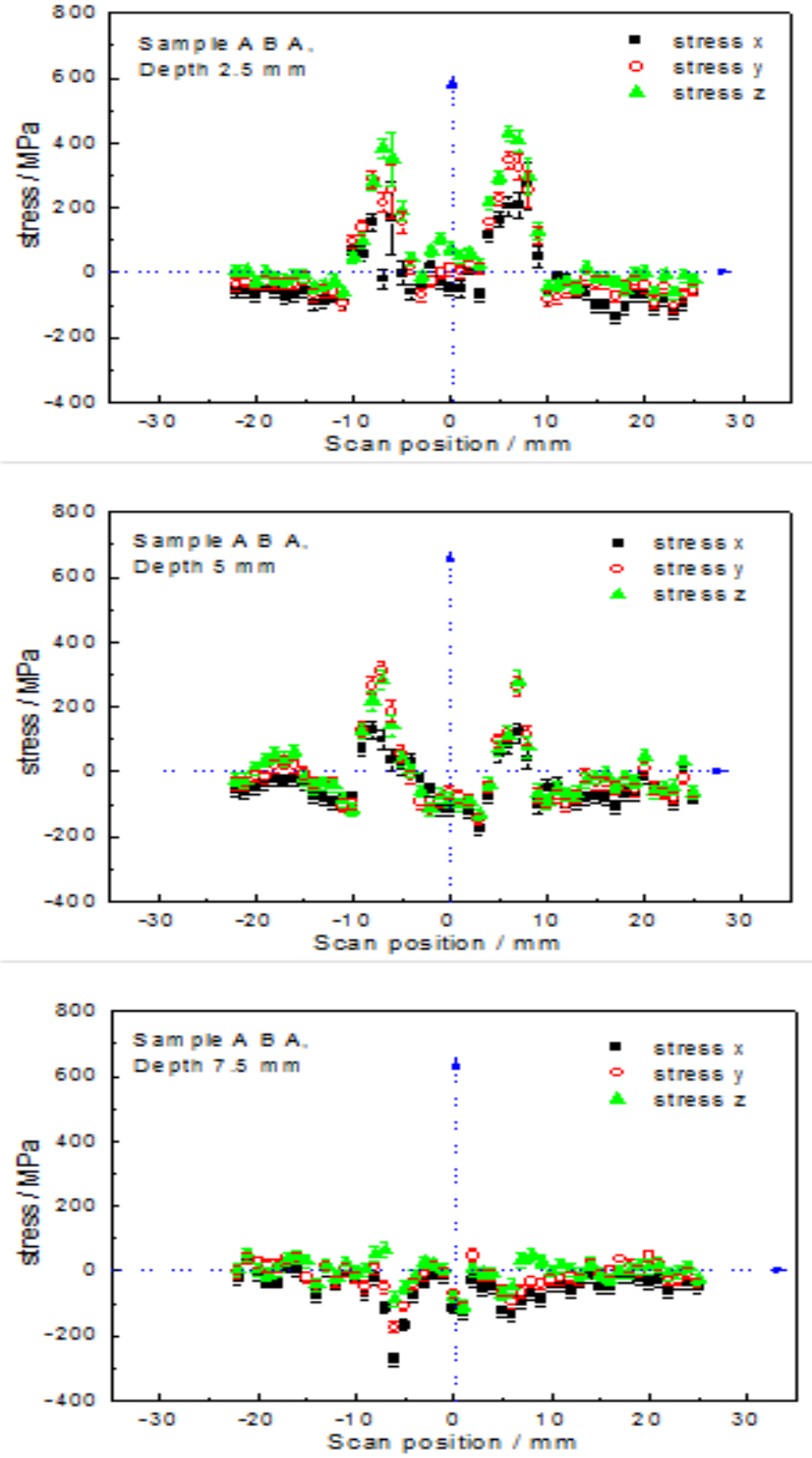


FIG. 7. Residual stress scans performed at different depths in the material for the sample with the weld on one side.

2.5. Optimization of instruments for residual strain/stress measurements

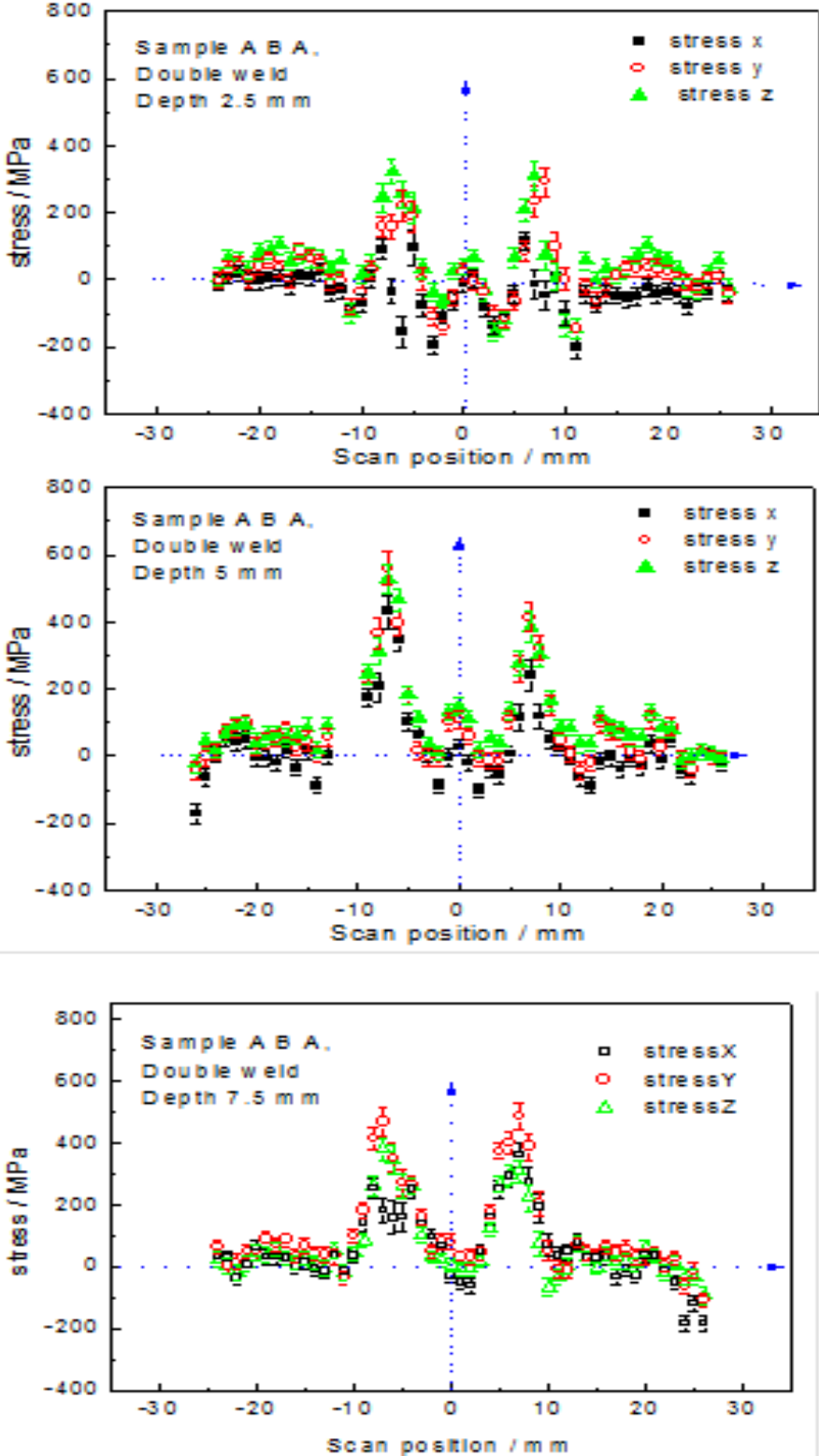


FIG. 8. Residual stress scans performed at different depths in the material for the sample with the weld on both sides.

## 2.5. Optimization of instruments for residual strain/stress measurements

### 2.4. Residual stress distribution measurement by neutron diffraction of the feritic single pass fillet steel welds

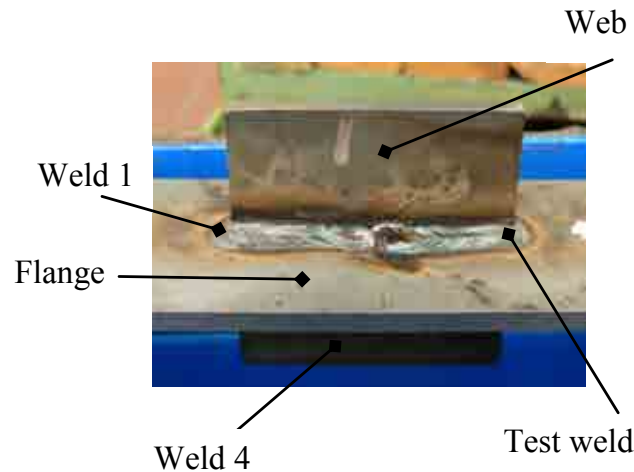


FIG. 9. Photo of one of the samples.

TABLE 1. COMBINTATIONS OF PARENT AND FILLER MATERIALS

Specimen designation	Parent material	Filler material
A11	WELDOX 700	LTT-M6
B10	WELDOX 700	B-M3
C11	WELDOX 700	D4-647
E12	WELDOX 700	OK Tubrod 14.03
J11	DOMEX 650	D3-5724
K12	X2CrNi12	D3-6547
L12	X2CrNi12	OK Tubrod 15.30

The aim of these studies was to find an optimum composition of the additive material in order to decrease residual stresses in the vicinity of the foot of the welding joint and consequently to increase the fatigue strength [1,2]. It is based on the conception of so called LTT (low transformation temperature) metal used for electrodes which (according to a theory) de-creases the level of residual stresses and increases the fatigue strength. WELDOX 700 and DOMEX 650 – refined high strength steels having the yield strength 700 MPa (in reality up to 817 MPa resp. 650 MPa) were used as a base material. Three parent materials and seven different filler materials were used for the test specimen preparation. Altogether seven test specimens were used for the residual stress distribution measured by neutron diffraction. The photo of one of the samples is shown in Fig. 9. Combintations of parent and filler materials are shown in Table 1. Shielding gas Ar + 2%CO<sub>2</sub> was used for welding.

2.5. Optimization of instruments for residual strain/stress measurements

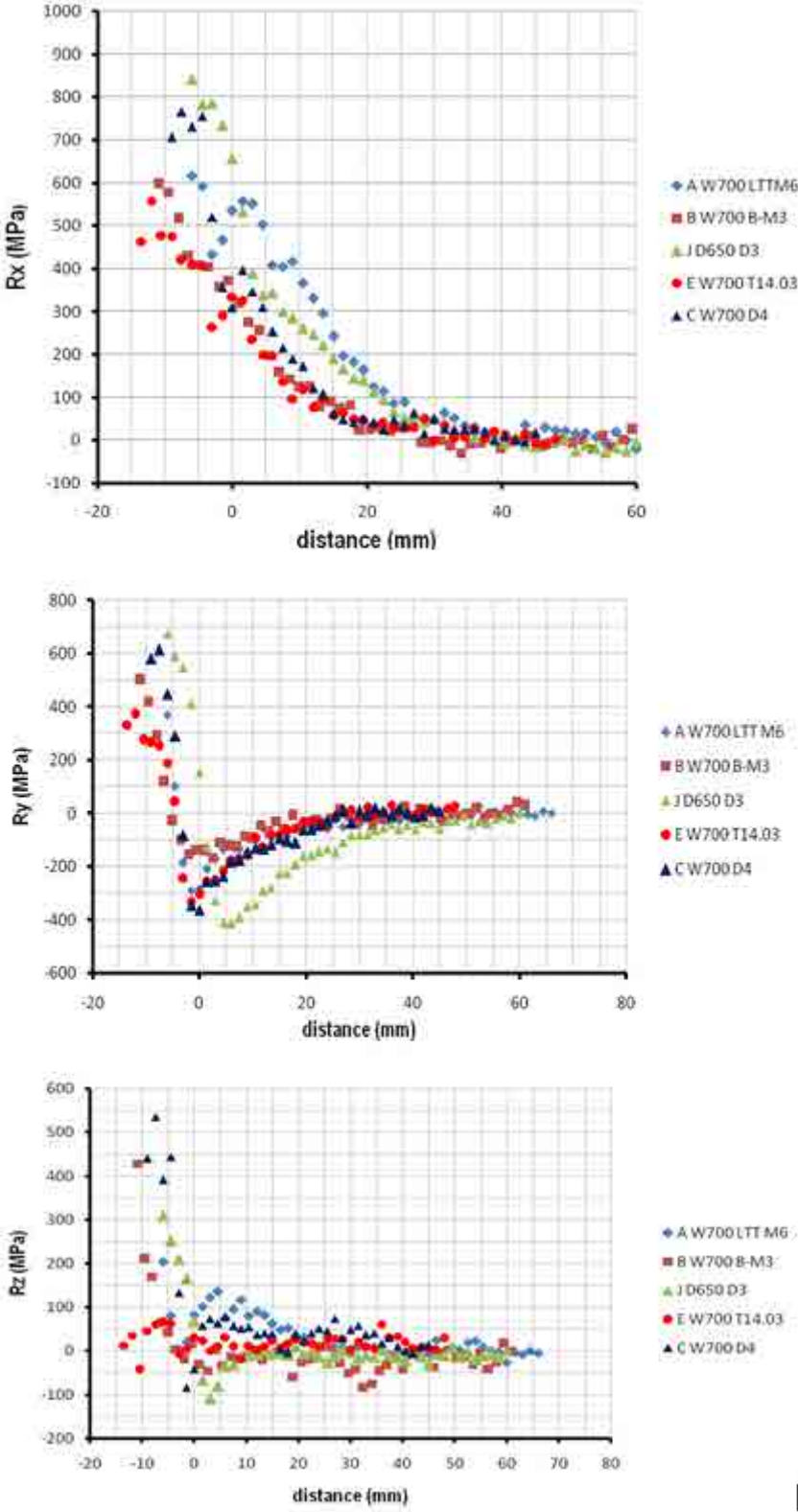


FIG. 10. Components of residual stresses in the vicinity of the weld for the WELDOX 700/690QL parent material and several different fillers.

As an example of variety of the obtained experimental results, the following figures demonstrate the effect of using different filler materials (A - LTT-M6, B - B-M3, C – D4-

## 2.5. Optimization of instruments for residual strain/stress measurements

6547, E - Tubrod 14.03, J - D3-5724) on individual components of residual stress distribution in the vicinity of the weld with the parent material WELDOX 700/690QL.

The following possible phenomena were studied:

The effect of filler material LTT-M6(A), B-M3(B), D4-6547(C), Tubrod 14.03(E) welded on high strength steel WELDOX 700 on residual stress distribution; the effect of filler materials D4-6547 and Tubrod 15.30 welded on high alloyed steel\_X2CrNi12 (1.4003) parent material on Rx, Ry and Rz residual stress components distribution; the effect of parent material high strength WELDOX 700/690QL and Domex 650MCD steels welded by D4-6547 and D3-5724 respectively, on Rx, Rz and Ry stress components; the effect of parent materials high strength Weldox 700/S690QL and high alloyed X2CrNi12 (1.4003) steels welded by D4-6547 filler material on Rx, Rz and Ry stress components; the effect of parent materials high strength Weldox 700/S690QL and high alloyed X2CrNi12 (1.4003) steels welded by Tubrod 14.03 and Tubrod 15.30 respectively, on Rx, Rz and Ry stress components; the effect of weld location\_of the no. 1 and no. 4 test fillet welds prepared on high strength steel Weldox 700/S690QL welded by D4-6547 filler material on Rx, Rz and Ry stress components.

## 3. CREEP STUDIES IN NI-BASED CMSX4 SUPERALLOY BY SMALL ANGLE NEUTRON SCATTERING

Ni-based superalloys exhibit a two-phase microstructure consisting of  $\gamma'$  precipitates growing in the gamma phase matrix. It is the basic feature which determines e.g. a high creep-resistance of nickel-base superalloys. Outstanding high-temperature mechanical properties of these materials strongly depend on the morphology of the precipitates and thus also on the applied heat treatment. During the creep load on CMSX4 superalloy, rafting of originally cuboidal precipitates takes place. The degradation procedure can be investigated by the analysis of the geometrical parameters of  $\gamma'$  precipitates in  $\gamma$  matrix. A new conical form of the sample which was exposed at 1100°C for 100 h was used (see Fig. 11). It permitted to test the stress level continuously in one sample and to obtain variation of the microstructural changes (see Fig. 12). The development of the morphology of rafts on the value of deformation could be obtained by SANS - average thickness of the channels between the rafts in different crystallographic directions of the single crystal, development of the dimensions of  $\gamma'$  precipitations and their distance and the development of specific surface of the precipitates (see Fig. 13) [3,4].

## 2.5. Optimization of instruments for residual strain/stress measurements

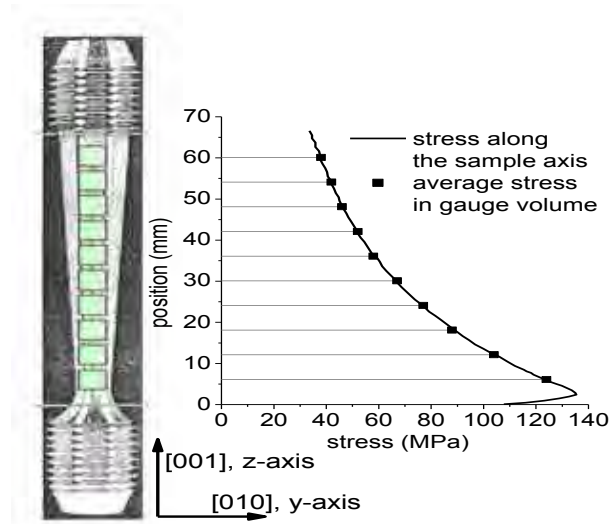


FIG. 11. The picture of the tested specimen (left). Ten points scanned during the SANS experiment are marked. Stress dependence ( $\sigma_{min} = 35$  MPa,  $\sigma_{max} = 135$  MPa) on the position along the sample axis and average stress in the measured gauge volumes (right).

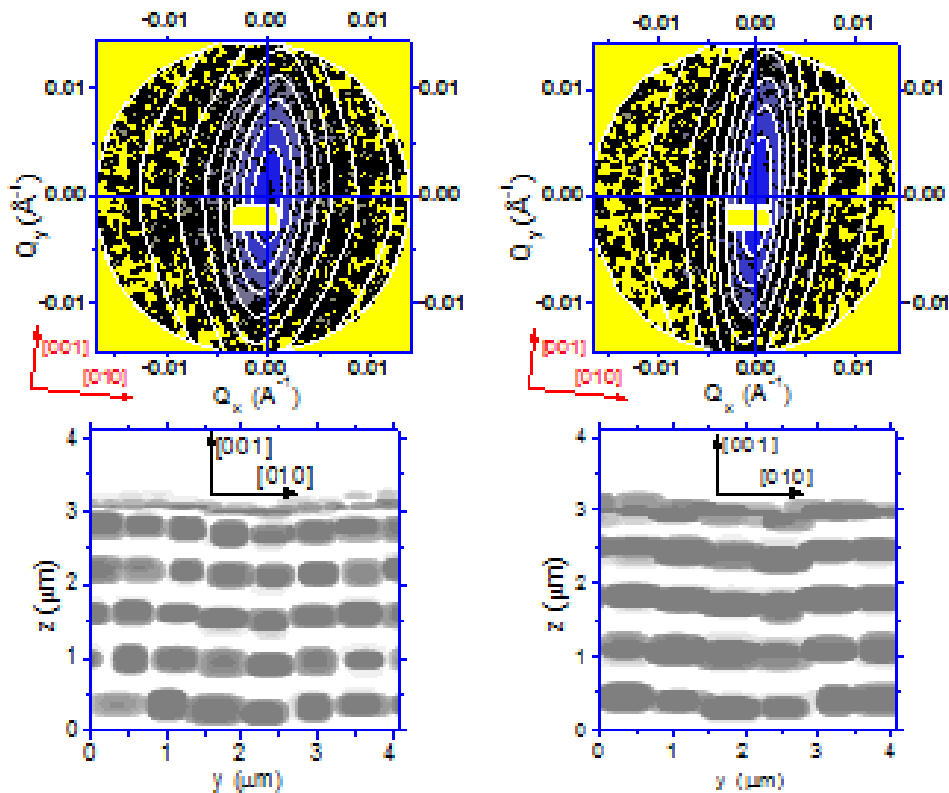


FIG. 12. Scattering curves at two of the scanned points: (a) minimum and (b) maximum stress, respectively. Orientation:  $[100]$  parallel to the beam,  $[001]$  nearly vertical. Measured data are shown as the colour-scale maps whereas the optimum 2D fits are depicted by the white equiintensity lines. (c), (d): sections through the optimum 3D models (gray:  $\gamma'$  rafts; white: matrix) for the (a) and (b) fits, respectively.

## 2.5. Optimization of instruments for residual strain/stress measurements

### 4. NEUTRON DIFFRACTION ANALYSIS AT RT OF INCOLOY 800HT AND 304L STEEL SAMPLES WITH DIFFERENT HEAT TREATMENT

This experiment was carried out in cooperation with the CRP partner - Institute for Nuclear Research Pitesti, Romania, where the samples were prepared. In total 8 samples of two groups were analysed by neutron diffraction on the powder diffractometer MEREDIT at room temperature. First group, referenced here as ig800 was Incoloy 800 HT steel, was consisting of four samples which passed heat treatment at 450°C, 500°C, 550°C and 600°C for 60 days. The second group, referenced here as ol304L was 304-L steel, was consisting also from four samples which passed the same heat treatment at 450°C, 500°C, 550°C and 600°C for 60 days. Samples were all of the form of sheets with the rectangular shape of  $15 \times 25 \text{ mm}^2$  of the thickness of 2 mm with a small hole in the top part. The hole was used for fixing the samples by Cd-wire to the carousel and placed perpendicularly into the neutron beam. The diffraction pattern was collected from whole volume of the sample. Mosaic copper monochromator (reflection 220) providing the wavelength  $1.46 \text{ \AA}$  was used for this measurement in the range of scattering angles between  $4^\circ$  and  $144^\circ$ . Refinement was performed using FullProf software. First refinements were performed using the full pattern refinement with the structural model just to see and identify the phases in the samples. Next refinement strategy was selected to refine the individual reflections without any structural model to see "movement" of the angular reflection position as a function of temperature of the thermal treatment. During the calculation global parameters of background and for individual reflection parameters of intensity, position and value of FWHM were refined.

For the full pattern refinement we used the IRF (Instrumentation Resolution File) which describes the profile parameters coming from the instrument and were obtained by refinement of the  $\text{SiO}_2$  standard sample at the similar conditions. The apparent reflections in the diffraction pattern were analysed and identify as coming from the austenite phase with space group  $\text{Fm}\bar{3}\text{m}$  and cell parameter  $a \approx 3.59 \text{ \AA}$  for all 8 samples. So, there were no phase changes brought about by changing the temperature of the thermal treatment. Small reflections observed on the background at different angles were identified as  $(\lambda/2)$ -reflections because of very high (over 8000 counts) intensity of main reflections. The contamination of the  $(\lambda/2)$  - reflections denoted by the ratio of  $I(\lambda/2)/I(\lambda)$  was about 0.44%. Observed and calculated diffraction patterns for the sample ig800-450 are shown on the Fig. 14. As all the samples seemed to be a monophase, we analysed the relative peak position and peak broadening by the fitting of the individual reflections. For the refinement, all 8 reflections of austenite structure visible in the diffraction pattern in the measured  $2\theta$  region, namely 111, 200, 220, 311, 222, 400, 331 and 420 reflections, were selected. We omitted  $(\lambda/2)$ -reflections. The profile parameters were taken from the IRF2 file. The refined parameters of each reflection were: angular position, shift of FWHM and integrated intensity. From the refined position we calculated sample strain parameter  $\varepsilon$  by using of Eq. (1). Then from the angular shift of the peak position the resolution  $\Delta d/d$  was obtained from the Bragg equation. The evolution of these parameters ( $\varepsilon = \Delta d/d$ ) as a function of the temperature of the thermal treatment is shown in the Figs. 15 and 16 for both groups of the samples. The temperature of 450°C of thermal treatment was taken as reference (for  $d_{0,\text{hkl}}$ ) for  $\varepsilon$  calculation.

## 2.5. Optimization of instruments for residual strain/stress measurements

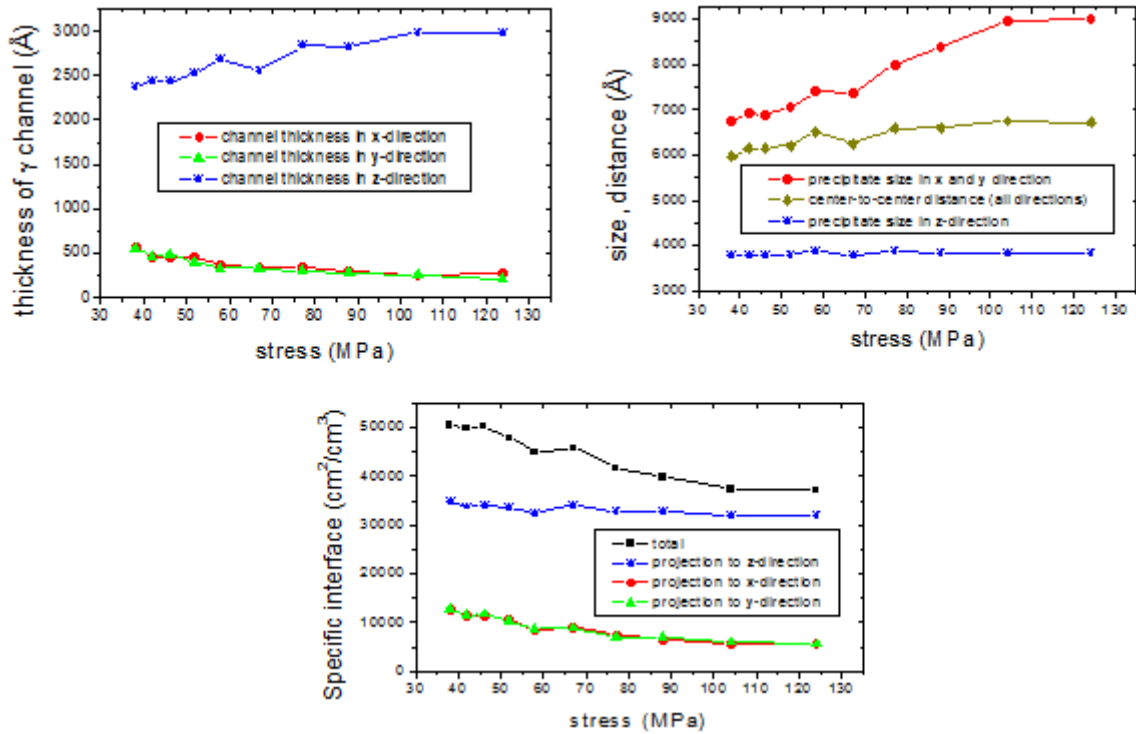


FIG. 13. Resulting evolution of parameters. (a) the mean thickness of the  $g'$  channel in the respective directions ( $x$ -direction is  $[100]$ ,  $y$ -direction is  $[010]$  and  $z$ -direction is  $[001]$ ), (b) the relative evolution of the average precipitate size and distance, (c) the relative evolution of the specific interface - total and projection to the respective directions.

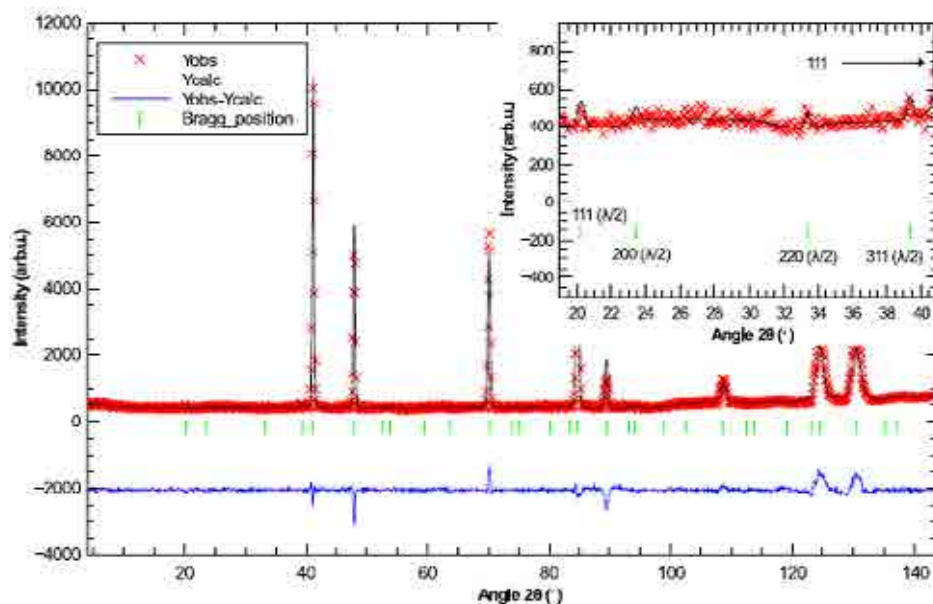


FIG. 14. Observed and calculated diffraction pattern for the sample ig800-450. Inlet shows the small reflections attributed to the second contributions of the main reflections.

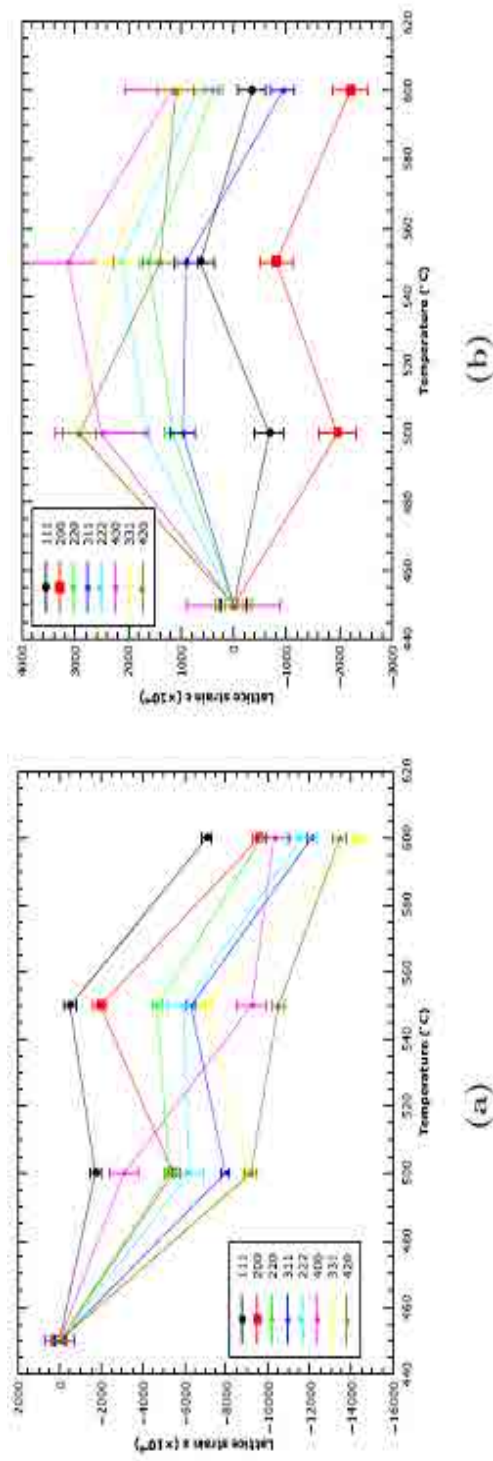


FIG. 15. Sample strain  $\epsilon$  calculated for the individual reflections as a function of temperature for samples ig800 (a) and ol304L (b).

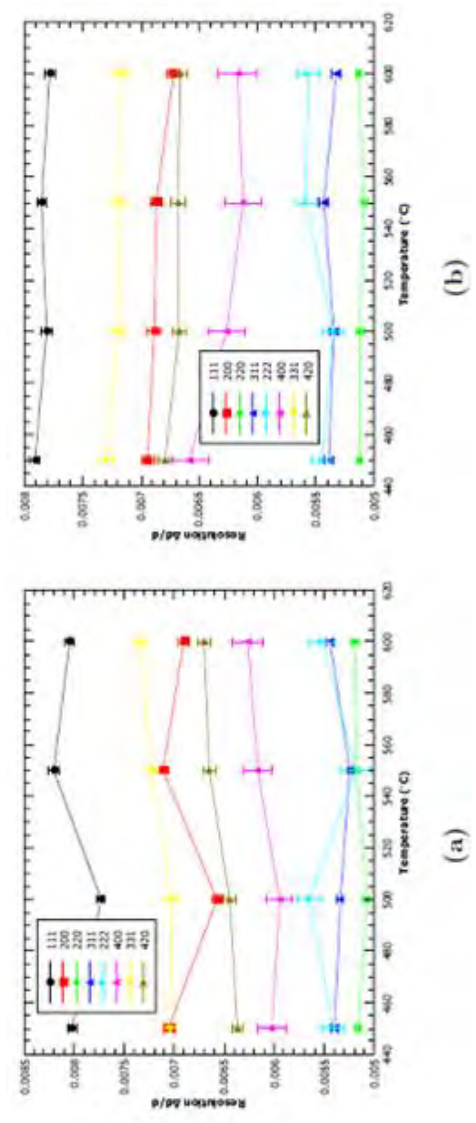


FIG. 16. Value of  $\Delta d/d$  calculated for the individual reflection as a function of temperature for samples ig800 (a) and ol304L (b).

## 2.5. Optimization of instruments for residual strain/stress measurements

Inspection of Figs 15 and 16 reveals that the values of resolution slightly increase with the increase of the temperature of the thermal treatment for the ig800 samples. In contrast to the ol304L the values of the resolution are rather constant or have a decreasing tendency with the increase of the temperature. It corresponds to the increase of the microstrain in the ig800 samples with increasing the temperature. This is in an agreement with the view on the macroscopic lattice strain which dramatically increases with the temperature of thermal treatment in the case of ig800 samples. The negative values of the lattice strain represent the movement of the reflections to higher angles (see Figs 17 and 18) and thus the  $d$ -spacing decreases which leads to compression forces in the sample. However, in the samples ol304L the evolution of the lattice strain is different. For the most of the reflections, except the 200 reflection, the  $d$ -spacing moves to the higher values and thus the material is in tension. The softest direction [200] follows the opposite way. The fluctuation of the intensity of the high  $d$ -spacing reflections can be due to the change of the grain and size distributions when the temperature of the thermal treatment is changed.

## 5. REMAINING WORK PLAN

For the last period of the CRP project there is necessity to prepare the publications, namely, related to the obtained results shown in chapters 2.2, 2.3 and 4. Also it is in plan to present the results at the international conferences. After succesful methodology results obtained with KAERI colleagues in the instrument development in the case of residual strain/stress diffractometer when the stresses can be effectively investigated in the welds of the thickness of 50 mm [5-9], our attentions is paid to a new field of testing of promising dispersive monochromators for high resolution powder diffractometry [10,11].

## 6. CONCLUSION

It could be stated that the participation in the CRP project has been very succesful. Together with the obtained experimental results it should be noted that withiin the collaborations NPI ASCR, v.v.i. provided one month training for dr. M. R. Muslih from BATAN to learn software package developed in the Neutron Physics Laboratory which permits to optimize performances of neutron scattering instruments, NPI provided Si crystal slabs for focusing monochromator in BARC Mumbai and KAERI Daejeon, NPI provided know-how related to a construction and employment of focusing monochromators based on cylindrically bent perfect crystals to CIA Beijing as well as know-how how to avoid a spurious surface effect in neutron diffraction strain/stress measurements to materials science diffractometer STRESS-SPEC at FRM-II.

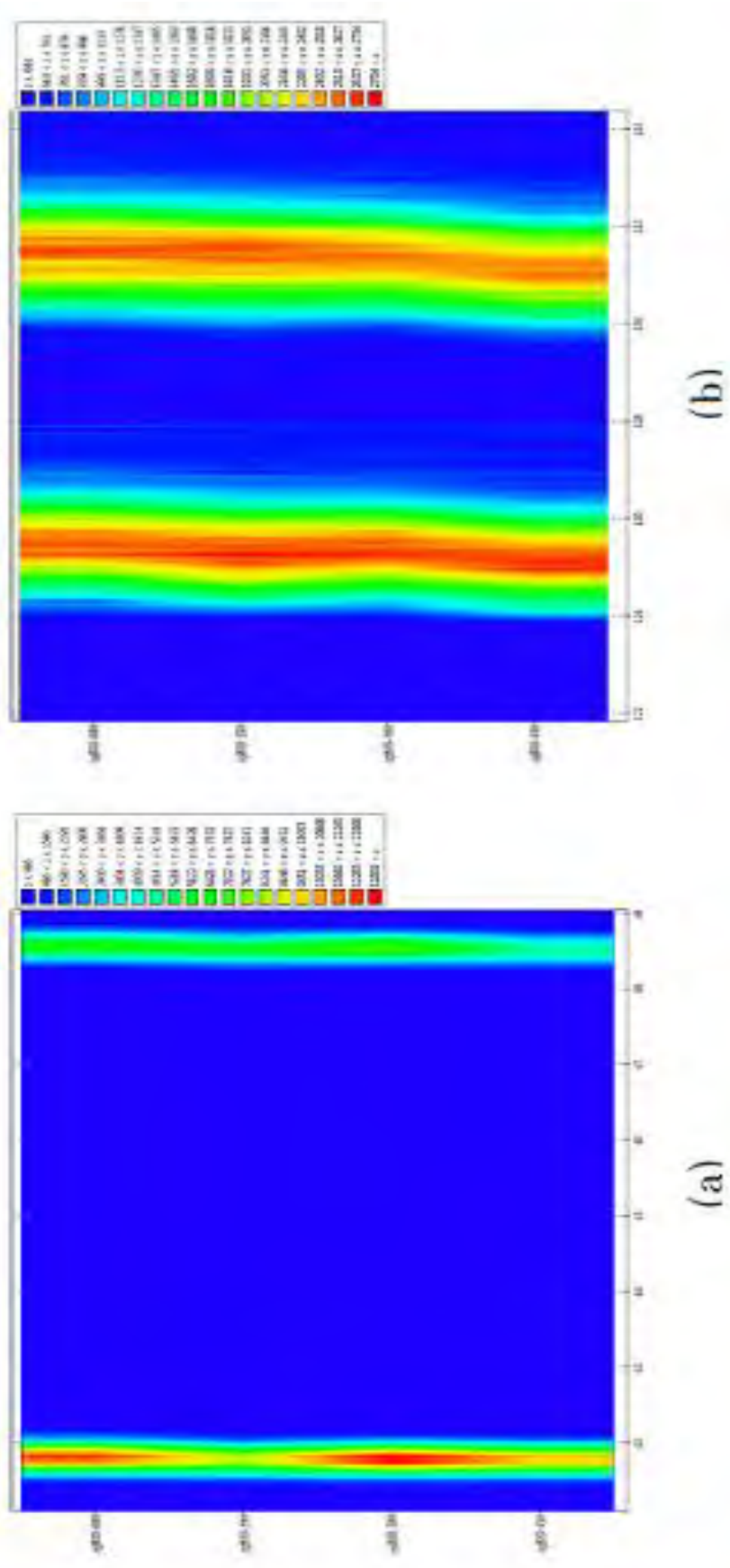


FIG. 17. Evolution of the position of the reflection with the temperature of the thermal treatment for the ig800 samples. The x axis corresponds to the diffraction angle. (a) 111 and 200 reflections; (b) 331 and 420 reflections.



## 2.5. Optimization of instruments for residual strain/stress measurements

### REFERENCES

- [1] MRAZ, L., et al. "Neutron diffraction analysis of residual strain/stress distribution in the vicinity of high strength welds", Book of abstracts of the ICEM14 Conference, held in Poitiers, France, July 4-9, 2010.
- [2] MRAZ, L., et al., "Identification of Weld Residual Stresses Using Diffraction Methods and their Effect on Fatigue Strength of High Strength Steels Welds", In Proc. of Int. Conf. ICRS9, Garmisch Partenkirchen, October 7-9, 2012, submitted to Materials Science Forum.
- [3] STRUNZ, P., et al., In-situ observation of morphological changes of gamma prime precipitates in pre-deformed single-crystal Ni-base superalloy, J. Appl. Cryst. **44** (2011), Part 5, 935.
- [4] GILLES, R., et al., In situ investigation with neutrons on the evolution of  $\gamma'$  precipitates at high temperatures in a single crystal Ni-base superalloy, Advanced Materials Research **278** (2011) 42.
- [5] SEONG, B.S., et al., Optimization of the bent perfect Si(111) monochromator, at small ( $\sim 30^\circ$ ) take-off angle for stress instrument, J. Appl. Cryst. **43** (2010) 654.
- [6] SEONG, B.S., et al., Unconventional Performance of a Highly Luminous Strain/Stress Scanner for High Resolution Studies, Materials Sc. Forum **681** (2011) 426.
- [7] WOO, W., et al., Neutron diffraction residual stress measurements in a thick weld by using the wavelength with lower total cross-section, Mater. Sc. Eng. A **528** (2011) 4120.
- [8] WOO, W., et al., Effect of wavelength-dependent attenuation on neutron diffraction stress measurements at depth in steels, J. Appl. Cryst. **44** (2011) 747.
- [9] WOO, W., et al., Neutron diffraction measurements of residual stresses in a 50 mm thick weld, Materials Sc. Eng. A **528** (2011) 4120.
- [10] MIKULA, P., et al., Double bent crystal dispersive arrangement for high resolution diffractometry, Journal of Physics: Conference Series **340** (2012) 012014.
- [11] MIKULA, P., et al., Experimental studies of dispersive double reflections excited in cylindrically bent perfect-crystal slabs at a constant neutron wavelength, J. Appl. Cryst. **45** (2012) 98.

## 2.5. Optimization of instruments for residual strain/stress measurements

### OPTIMIZATION OF NEUTRON BEAM TECHNIQUES FOR CHARACTERIZATION OF STRUCTURAL MATERIALS

S. SUTJARSO, T.H. PRIYANTO, M. R. MUSLIH

National Nuclear Energy Agency of Indonesia (BATAN)  
Kawasan Puspptek Serpong, Tangerang Selatan, Banten – Indonesia 15314  
Email: [sasok@batan.go.id](mailto:sasok@batan.go.id)

#### **Abstract.**

The result of the activities on the CRP project titled: Optimization of Neutron Beam Techniques for Characterization of Structural Materials has been reported. The activities consist of individual project which was proposed at the beginning of the project and collaborative works which is jointly carried out with the other members of the CRP. The individual project which is mainly focused on the optimization of the neutron diffractometer and neutron radiography has been successfully completed. The collaborative works which are mainly targeted to perform Round Robin exercise using VAMAS sample for neutron diffractometer and standard samples for tomography obtained from PSI have been carried out successfully. However, the texture measurement on Al alloys, applying data correction was not successfully achieved since the proper standard sample is not available and this is still needed for the the future plan.

## 1. INTRODUCTION

The Research Contract between the IAEA and the National Nuclear Energy Agency is made with reference No. 15991/RO with the title: Optimization of Neutron Beam Techniques for Characterization of Structural Materials. The contract period is from 2009 -12-16 until 2013-02-05. It was agreed upon the 1st RCM meeting that the programme work covers the individual projects and collaborative projects.

The individual projects are mainly focused on the optimization of performance of three neutron beam instruments i.e., the neutron diffractometer for residual stress, neutron diffractometer for texture analysis and radiography neutron. The programme works of the individual projects are as follows:

- Optimization of neutron tomography of the RN1.
- Design of radial collimator for the DN1 diffractometer.
- Design and fabrication of doubly focusing monochromator.

The collaborative efforts and results achieved consists of:

- Standardization of neutron tomography using tomographic phantom from the PSI.
- Round robin exercise of residual stress measurement using the VAMAS sample.
- Texture measurements on Al alloys, applying data correction obtained from standard sample.

Most of the programme works has been successfully carried out apart from the texture measurement which is still unable to obtain the appropriate normalized data due to the unavailability of a standard sample for this measurement. The standard sample of texture for neutron diffraction is still needed and it is included in the remaining work plan.

## 2.5. Optimization of instruments for residual strain/stress measurements

### 2. NEUTRON RADIOGRAPHY/TOMOGRAPHY

#### 2.1. Individual progress

Neutron tomography has been developed at the RSG-GAS reactor, Serpong. The configuration of the instrument is illustrated in Fig. 1 and the actual neutron radiography facility where the tomography was setup is shown in Fig. 2. Besides the CCD camera the system was also equipped with a rotary and translation table,  $^6\text{Li-ZnS}$  scintillation screen and high reflective  $\text{TiO}_2$  coated mirror. All components are enclosed within a dark box lined with lead and  $\text{B}_4\text{C}$  rubber acting as neutron shielding.

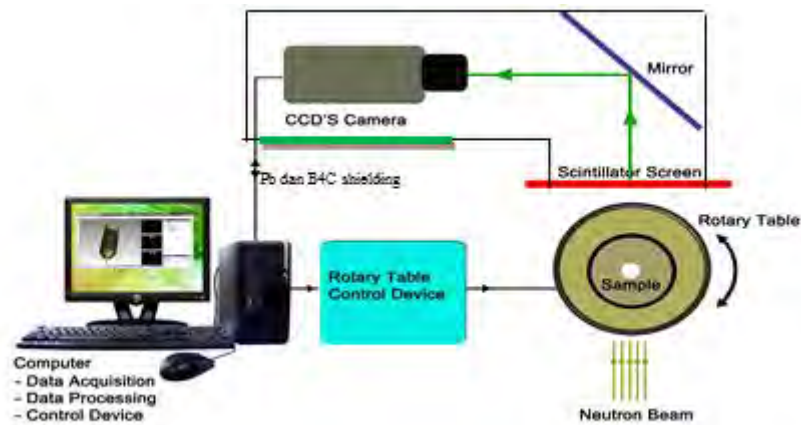


FIG. 1. Configuration of neutron tomography.



FIG. 2. The neutron radiography facility at the RSG-GAS reactor.

A low light CCD-camera iKon –M produced by the Andor technology has been chosen [1]. The pixel array format of this chip is  $1024 \times 1024$  pixels with a pixel size of  $(13.5 \times 13.5)$  micro meter. The Quantum Efficiency of the CCD-camera is 95% for wavelengths from 350-800 nm. The high precision CCD driver electronics provides 16-bit digitization (65535

## 2.5. Optimization of instruments for residual strain/stress measurements

gray levels). The deep cooling using peltier system keeps the CCD – chip at a temperature of about  $-95^{\circ}\text{C}$  to suppress dark current.

The data for tomography is obtained by rotating the object in small angular steps from  $0-180^{\circ}$  or  $360^{\circ}$  degree with an increment of 1 degree. The rotating table unit itself is mounted onto a 2-axis motion table used to position the sample precisely with regard to the CCD camera's field of view. The automatic sequence of rotating the sample and taking a transmission image is controlled using micro controller run under visual basic program. Tomographic reconstruction was carried out using commercially available reconstruction software, Octopus 8.5 which is based on a filtered back projection algorithm. The reconstructed images are visualized into 3D image using visualization software VGStudio 2.1.

The typical reconstruction images produced by this neutron tomography is shown in Fig. 3.

Figure 3 shows the sample of the ignition coil and neutron radiography image as well as the 3D reconstruction image of the object [2]. The vertical slice cut out from the reconstructed volume is able to reveal the internal structure of the object.

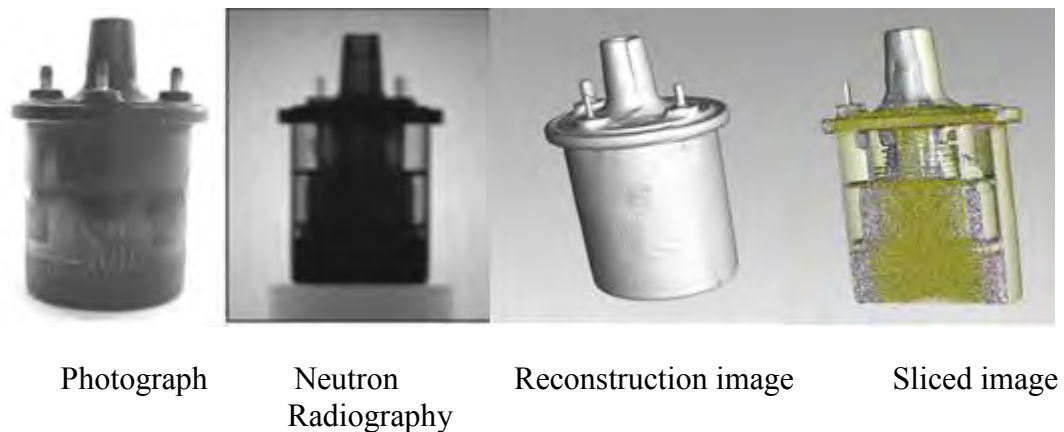


*FIG. 3. Neutron tomographic image of an ignition coil.*

## 2.2. Collaborative efforts; round robin exercise using the PSI sample

In a collaborative work the topic was focused on the standardization of neutron tomography. This is carried out by performing the Round Robin exercise standard samples i.e., “Contrast sample and Resolution samples”. The samples and the protocol were produced by the PSI and they were sent to several member countries to be measured and compared.

The contrast sample is a cylinder with a diameter of 30 mm made of aluminum with six holes with diameter 6 mm drilled in the axial direction. In each of these holes rods of polyethylene, nickel, iron, copper, lead, and aluminum are fitted [3]. A photograph of the sample is shown in Fig. 4 below. The measurement was carried out using the reactor power of 15 MW at the tangential beam tube S2 with the calculated L/D ratio of 83. Neutron flux at the sample position is  $10^6-10^7 \text{ n}\cdot\text{cm}^{-2}\cdot\text{s}^{-1}$  and it gives exposure time of 4 s per image. Lens of 50 mm/F1.4 was used for the CCD camera.

During the measurement the sample was placed at 10 mm away from the scintillator screen and it was rotated  $360^{\circ}$  and the image was taken every  $1^{\circ}$  rotation.

## 2.5. Optimization of instruments for residual strain/stress measurements

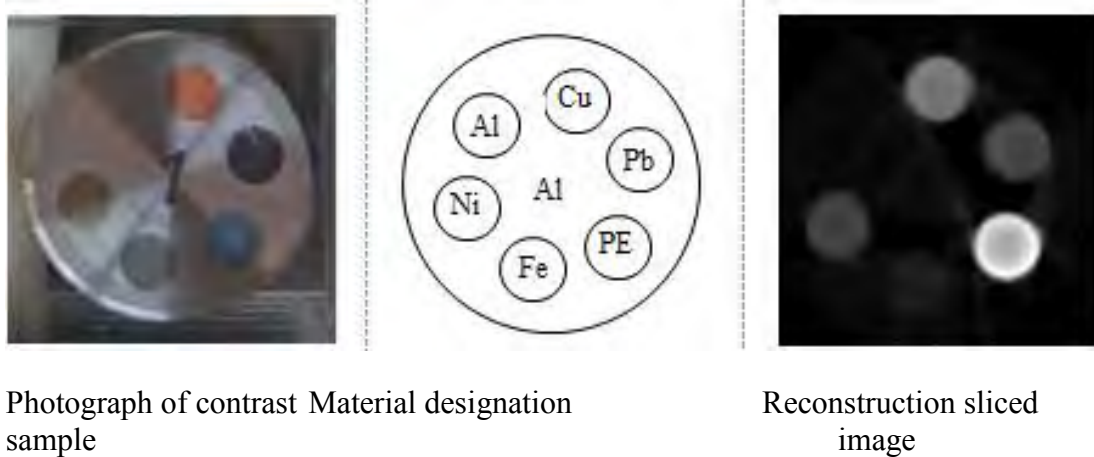


FIG. 4. Contrast sample and its reconstruction sliced image.

The resolution sample (Fig. 5) is composed of two rectangular blocks that can be attached to each other by two screws. One or more thin metal films can be placed between the two screw holes and thus create a small gap between the two blocks. The test set contains two material combinations: one sample (type A) is made of Al blocks with Cu films to produce a positive contrast gap and the other sample (type B) is made of Fe blocks with Al films to produce a negative contrast gap [3]. The film thickness is 20  $\mu\text{m}$  and it was put initially 10 foils and placed within the two blocks and its tomographic image was taken. The number of foils was reduced until the gap is no longer visible in the tomographic image.

Figure 6 shows the reconstruction sliced image of the resolution sample (type A) with the foils thickness of 200  $\mu\text{m}$ , 100  $\mu\text{m}$  and 40  $\mu\text{m}$ . Meanwhile for the resolution sample (type B) is shown in Fig. 7 for 200  $\mu\text{m}$  and 100  $\mu\text{m}$  only.



FIG. 5. Resolution sample.

Figure 6 reveals that the positive contrast gap resulted from foil Cu within the Al block is clearly visible from the tomographic image and as the number of foils is reduced it tends to fade away. The thickness of 40  $\mu\text{m}$  is the minimum gap that can be resolve in the tomographic image for this kind of sample.

## 2.5. Optimization of instruments for residual strain/stress measurements

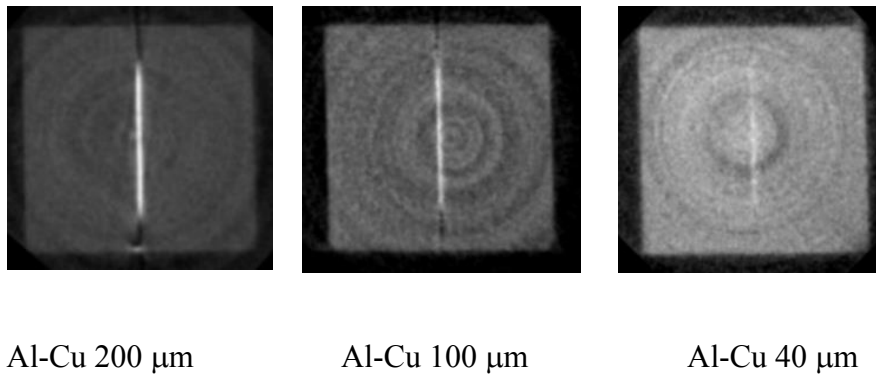


FIG. 6. The reconstruction sliced image of the resolution sample (type A).

Figure 7 show the similar result for the resolution sample (type B). The minimum gap which is visible in the tomographic image of this sample is 100  $\mu\text{m}$ .

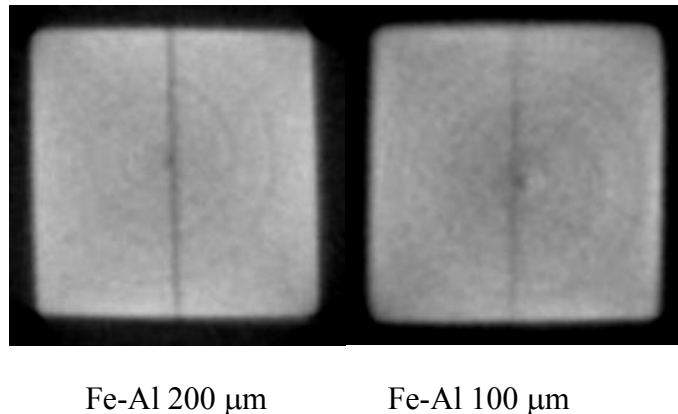


FIG. 7. The reconstruction sliced image of the resolution sample (type B).

## 3. RESIDUAL STRESS

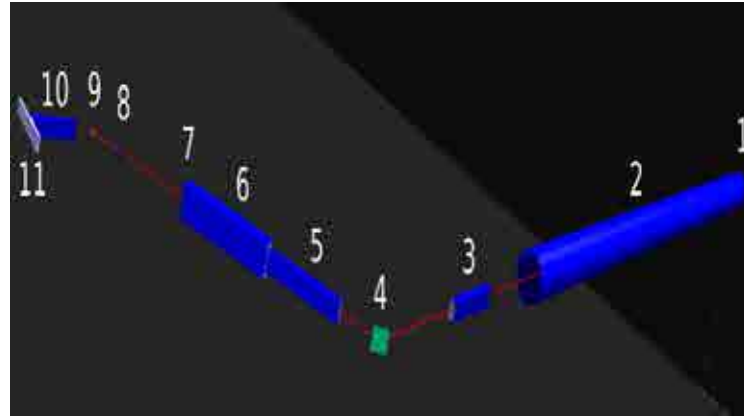
### 3.1. Individual progress

#### Design of radial collimator for DN1 diffractometer

The Monte-Carlo simulation has been done to design a radial collimator to be used for neutron diffractometer using SIMRES program package. The simulation was started by calculating the resolution of the installed diffractometer, DN1. The resolution based on the calculation is compared and adjusted with the resolution obtained by measurement using standard reference materials of silicon and nickel powder. The designed radial collimator is placed between the sample and detector to replace the component parallel collimator and slit attached in the previous configuration [4,5]. Radial collimator was simulated to have a wide range of 3 mm with a length of 210 mm.

The components of the DN1 are simulated using the configuration as show in Fig. 8. The resolution of the DN1 is calculated by changing the monochromator curvature from 3.3 m to 20 m and the result is shown in Fig. 9.

## 2.5. Optimization of instruments for residual strain/stress measurements



1. Neutron source 2. Beam tube 3. 1st collimator 4. Monochromator 5. 2nd beam tube  
6. 3rd beam tube 7. Slit #1 8. Slit #2 9. Sample 10. Radial collimator 11. Detector  
FIG. 8. The configuration of components of neutron diffractometer, DN1.

The resolution of DN1 obtained from measurement using standard silicon and nickel powder is shown in Fig. 10. It is found that the highest resolution is reached at 2 theta between  $70^\circ - 80^\circ$  which is in good agreement with the simulation i.e.  $76^\circ$ . Meanwhile the resolution itself differs slightly, from simulation it is  $7.8 \times 10^{-3}$  while from experiment  $4 \times 10^{-3}$ . Comparing the resolution curve in Fig. 9 and 10, it can be decided that the radius of horizontal curvature which will be using for the next calculation is 6.7 m which is associated with the curvature of  $0.15 \text{ m}^{-1}$ .

It can be concluded that the result of the Monte-Carlo simulation for the design of radial collimator is in good agreement with the simple analytical calculations which was done previously. The simulation reveals the radial collimator we made has a coverage of 3 mm at the distance of 91 mm.

The construction of the collimator was made based on the simulation result. The stretched mylar film (polyethylene) of 25 micron thickness spray coated with gadolinium oxide ( $\text{Gd}_2\text{O}_3$ ) was used as sollar slits (Fig. 11). The performance of the radial collimator was tested using the 2D detector and it was found that the improvement of the peak width is produced using the radial collimator compared with that of the absence of the collimator.

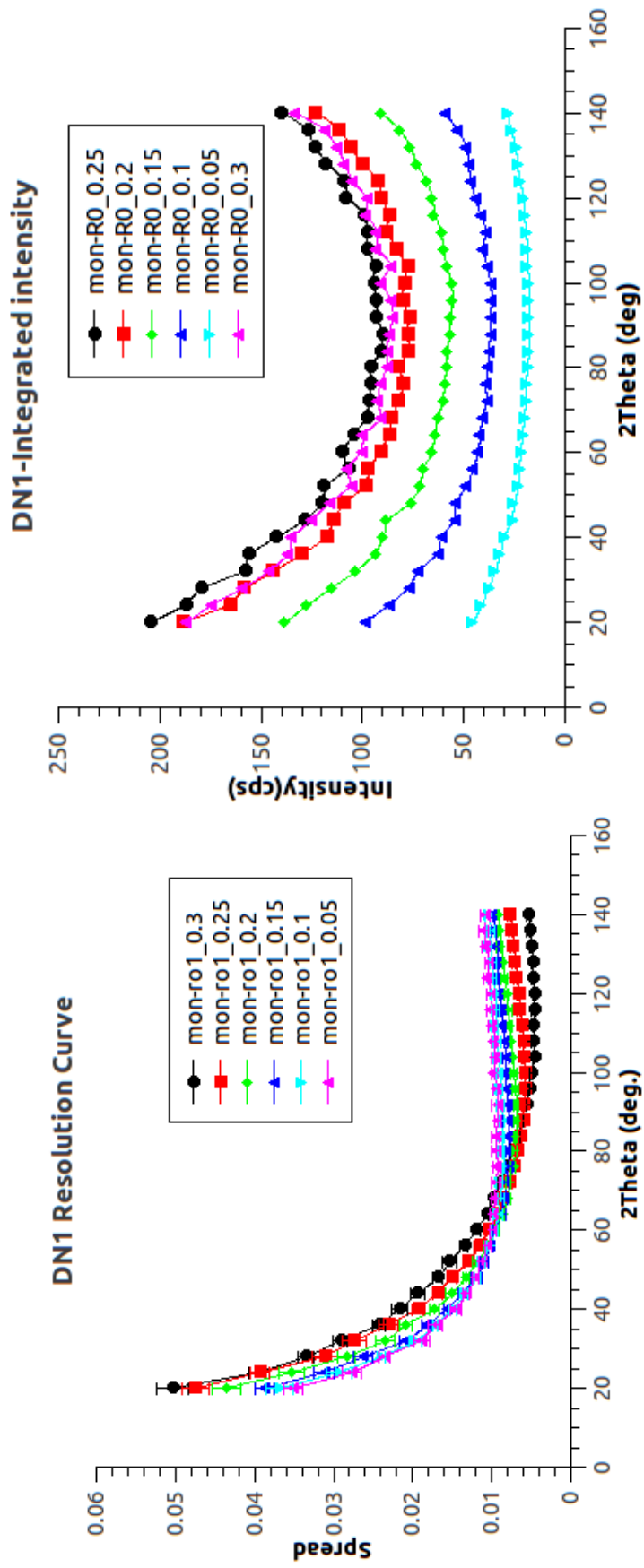


FIG. 9. Resolution curve (a) and Intensity (b) for various bending of monochromator crystal in the horizontal direction are from 3.3 up to 20 m associated with the curvature from 0.3 m<sup>-1</sup> up to 0.05 m<sup>-1</sup>. The lowest resolution for each curvature of 3.3 up to 20 m is 4.7.

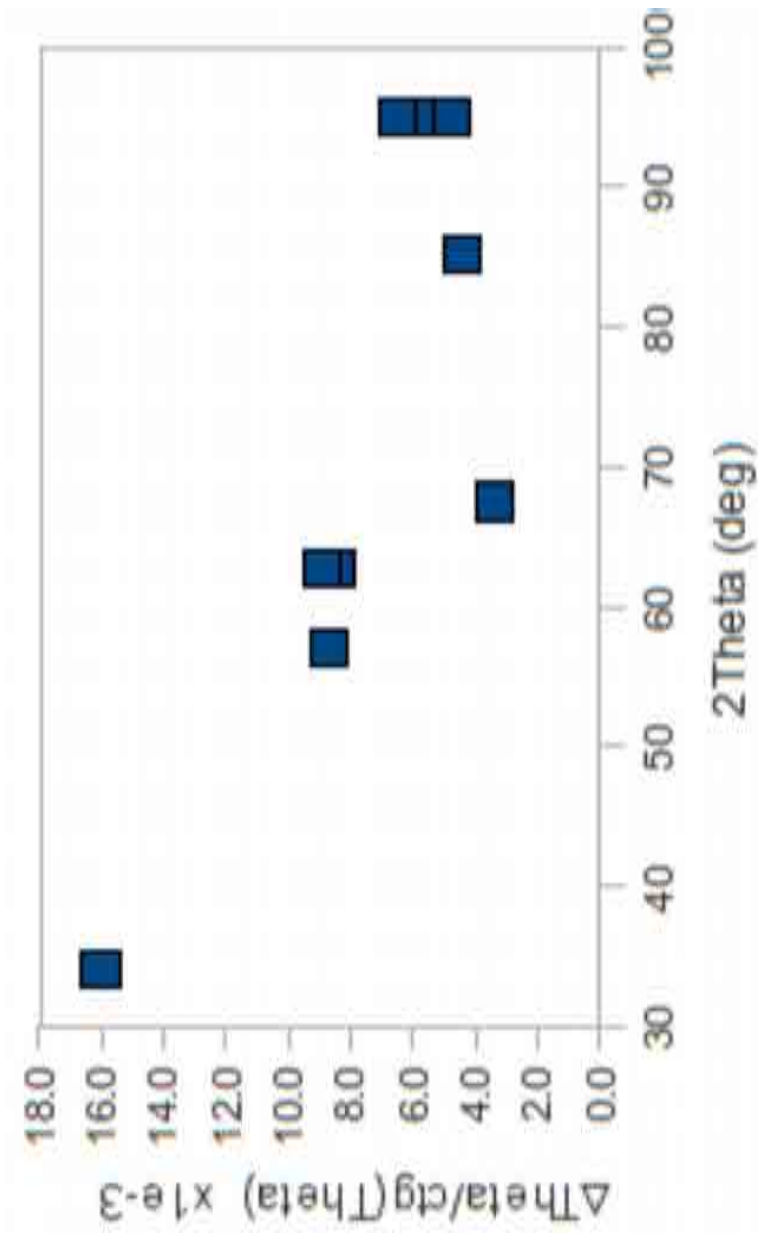


FIG. 10. The resolution of DNI measured using standard silicon and nickel powder.

The radial collimator is supported by goniometer with 3 axis, X, W and Rx.



FIG. 11. The radial collimator and its installation with the 2D detector.

## 2.5. Optimization of instruments for residual strain/stress measurements

### 3.2. Collaborative effort; round robin exercise using VAMAS sample

Round Robin exercise has been carried out using the VAMAS aluminium ring and plug specimen supplied by the JRC, Petten. The objective is to demonstrate the ability of the neutron diffractometer DN1 to measure the strain within the standard VAMAS shrink-fit aluminium specimen. The VAMAS specimen which was used in this exercise was specimen no 1. Evaluation was carried out at the  $hkl$  plane of (111), (200) and (311) for hoop and radial direction. Due to the existence of texture on the sample, (220) is the only plane that could be measured at axial direction. In the hoop and radial direction the measurement was carried out using slit with a dimension of  $2 \times 10$  (w  $\times$  h) mm<sup>2</sup> placed before and after the sample with the distance 100 mm toward the incident beam source and 50 mm toward the detector. In the axial direction the slit used was  $3 \times 3$  (w  $\times$  h) mm<sup>2</sup>.



FIG. 12. Neutron diffractometer for residual stress measurement DN1 installed at the beam tube S6 of the RSG-GAS reactor. Inset: position of VAMAS shrink-fit sample for radial direction measurement.

The measurement was carried out using wavelength of 0.185 nm which was calibrated using powder standard silicon NBS-640b. Residual strain within the sample for both radial and hoop direction has the same tendency and value measured with different  $hkl$  plane, as shown in Fig. 13. As for axial direction the measurement is only possible for (220) plane, due to the presence of strong texture inside the sample.

The measurement of (311) plane gives the best result at hoop and radial direction. This is due to the smallest irradiated gauge volume at this position, where diffraction angle of detector is  $97^\circ$ . As for (111) plane with diffraction angle of  $46^\circ$ , the scattered neutron came from large volume. This is very severe when the measurement point was in critical point such as boundary of ring and plug where the big difference strain is presence.

Residual stress measured in the VAMAS Round Robin Sample by the DN1 diffractometer shows a good agreement with the results obtained in other laboratories. Therefore it can be concluded that the DN1 neutron diffractometer is capable of producing residual stress data which is comparable with other facilities.

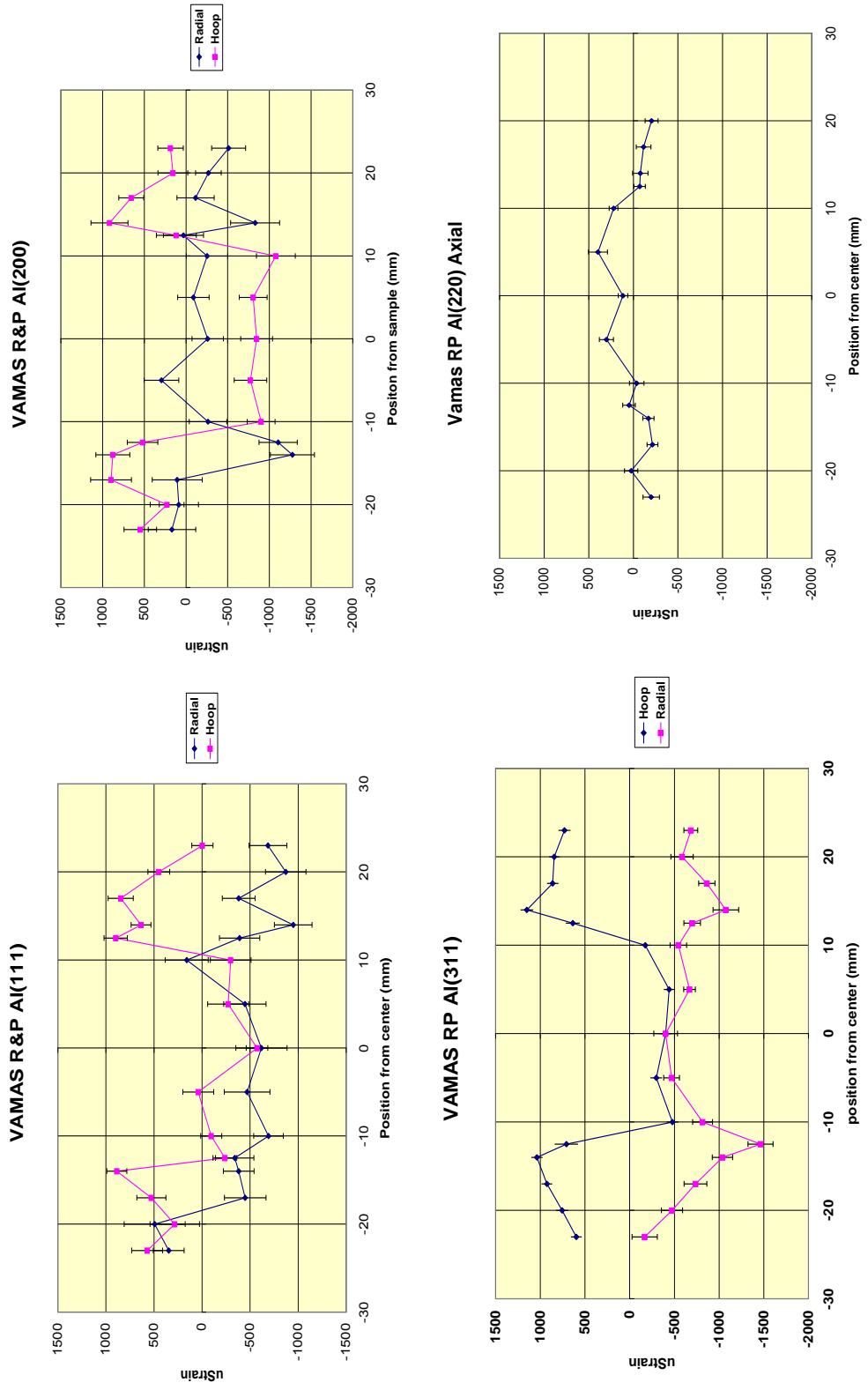


FIG. 13. Residual strain of VAMAS round robin sample for radial and hoop and axial direction, for hkl plane a. (111) b. (200) c. (311) and d. (220).

## 2.5. Optimization of instruments for residual strain/stress measurements

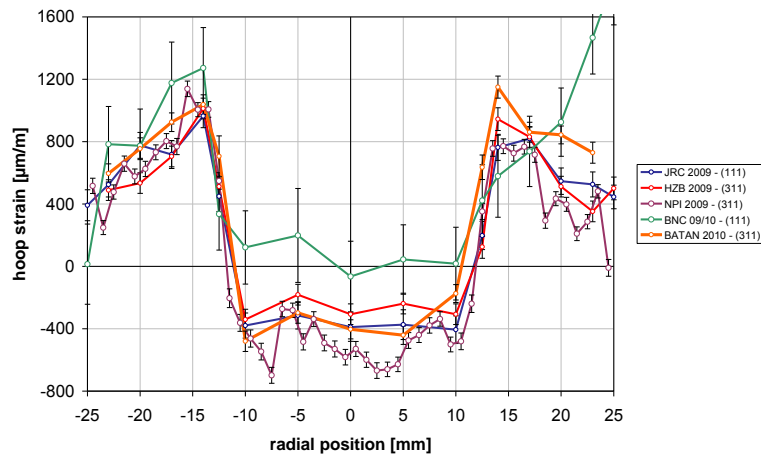


FIG. 14. IAEA Ring&Plug Round Robin Exercise; comparison of available hoop strain data [6].

## 4. TEXTURE

### 4.1. Individual progress

#### *Design and fabrication of doubly focusing monochromator*

A design of doubly bent monochromator crystal (DBMC) holder has been made using aluminium alloy. The holder is designed to hold 5 pieces of single crystal monochromator with a dimension of  $50 \times 20 \times 5 \text{ mm}^3$  each. Both ends of the monochromator crystals are gripped using crystal gripper and they are bent in horizontal and vertical direction using a screw provided. The crystals were labelled as crystal no. 1 to 5 from top to bottom, respectively. The crystal no. 1, 2, 4 and 5 were vertically bent and crystal no. 3 is kept flat since it is located at the center of the beam so no bending is necessary. Figure 15 is a design drawing of the monochromator holder and the adjustment device.

The triple axis spectrometer (TAS) was used for testing the monochromator crystal. The distribution of neutron beam reflected by silicon crystals was observed using Polaroid film FP-3000B. The distance from monochromator crystal to the focal point is made the same as the distance between monochromator and sample in the DN3. 2 theta axis of analyser is set at the elastic scattering position. DBMC holder is placed on the sample table as shown in Fig. 16. The observation was carried out at silicon crystal no. 4 (inset picture) and the distribution of neutron beam on crystal no.4 is shown in Fig. 17. To ensure that the reflection is from crystal no. 4 the crystal no.3 is covered by neutron absorber  $\text{B}_4\text{C}$ .

The doubly bent monochromator has been tested on the HRPD using nickel standard sample and the result is compared with the same sample taken previously by the hot pressed Ge(311) monochromator as shown in Fig. 18. However the result show that the diffraction pattern taken using the doubly bent monochromator is unable to produce the same diffraction pattern as the previous. This is due to the fact that the collimator, the detector efficiency as well as electronic system was not functioning properly as reported by the IAEA expert.

## 2.5. Optimization of instruments for residual strain/stress measurements

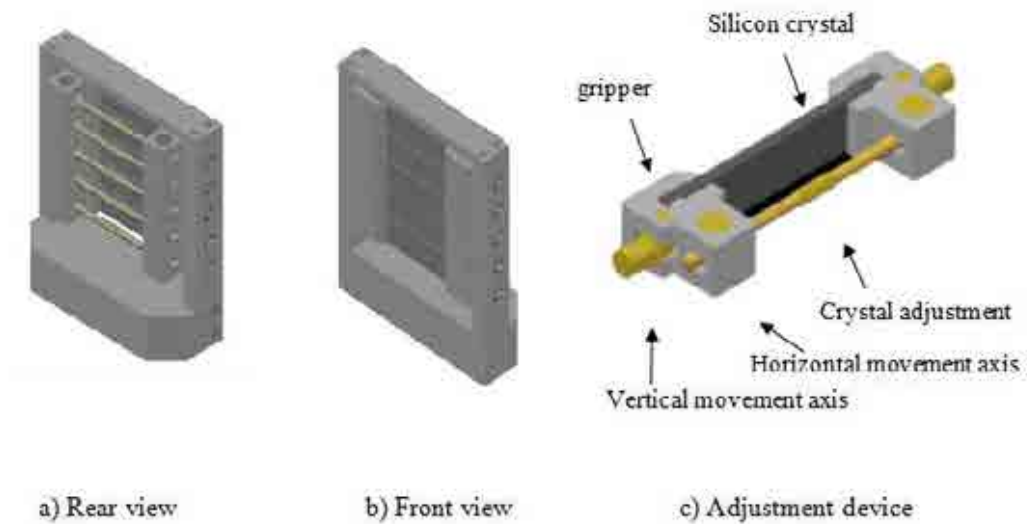


FIG. 15. A design drawing of monochromator crystal holder.



FIG. 16. DBMC set up on sample table of TAS and height adjustment using laser beam (red).

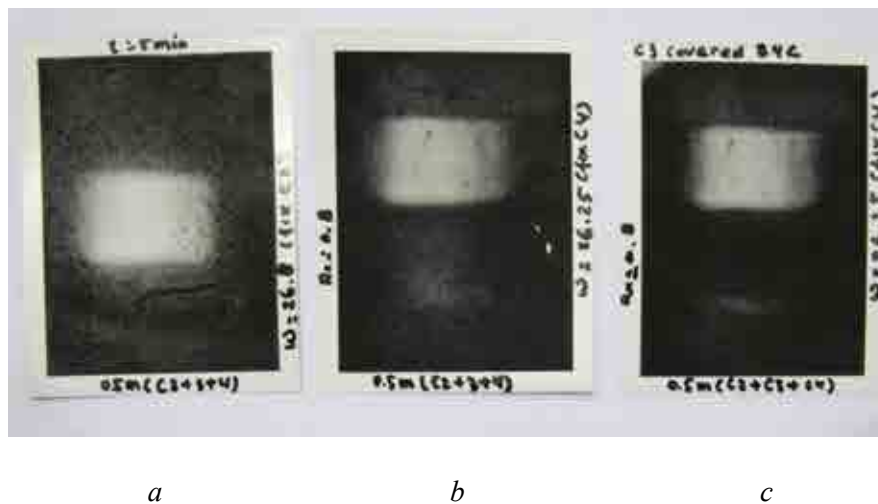
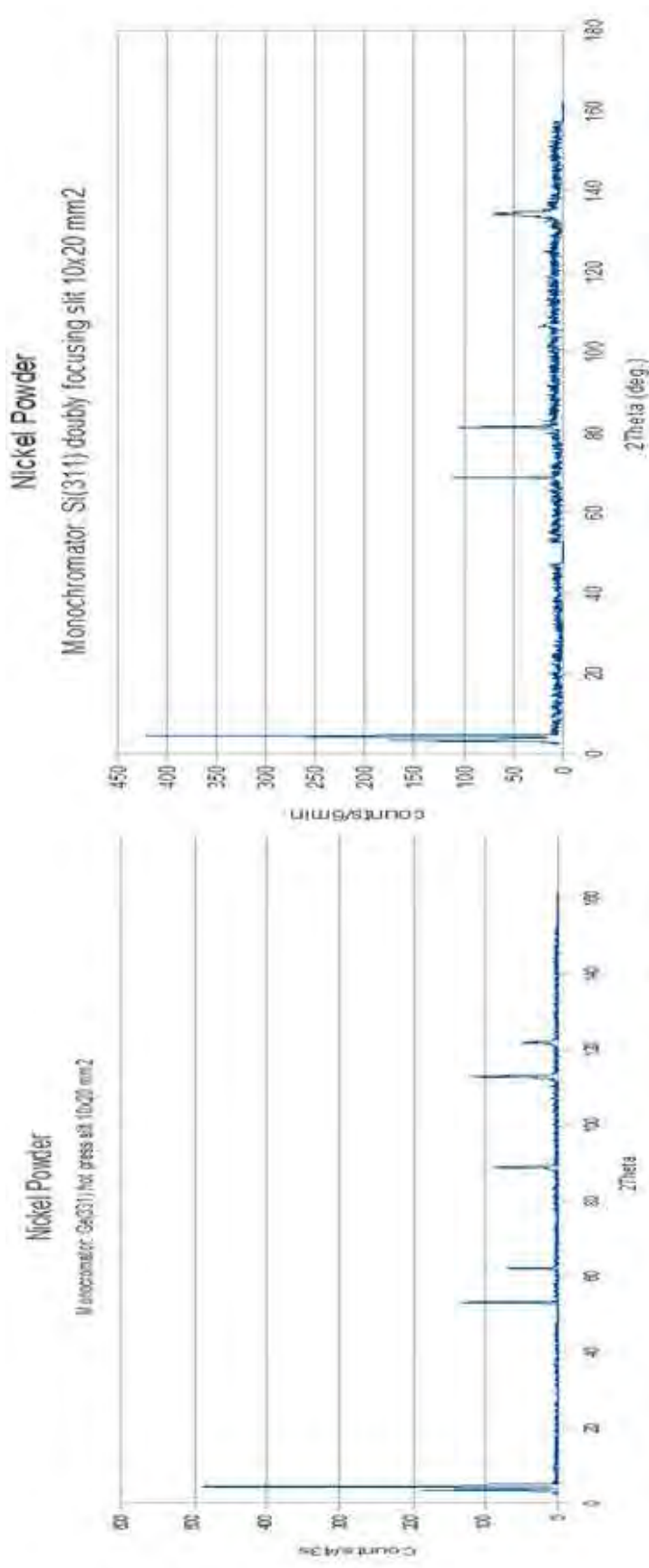


FIG. 17. The example of reflected beam by crystal no. 3 (a), crystal no.4 (b) and crystal no.4 with crystal no.3 covered by  $B_4C$  (c).



**a**

**b**

FIG. 18. Diffraction pattern of nickel sample using a hot pressed Ge(311) monochromator (a) and diffraction pattern of nickel sample using Si (311) doubly bent monochromator.

## 2.5. Optimization of instruments for residual strain/stress measurements

### 4.2. Collaborative effort

Texture measurements on Al alloys, applying data correction.

Texture measurement on Al alloys was planned to be carried out using standard sample obtained from the member of the CRP. However the expected standard sample was not able to obtain and an attempt to use another standard sample has been done using the X-ray copper reference sample SN-COA-472-011 from Bonet Company [7]. The sample consists of one powder and two massive samples prepared from commercial purity copper (*fcc* crystallographic lattice) in form of metal disks, 27 mm in diameter and about 6 mm thick.

Each sample is surrounded by an outside metal ring with a suitable colour marker (dot(s)) placed on its co-sample surface. To eliminate the aluminium effect from the Cu sample, the aluminium cover was taken out from the sample and two samples were used for neutron texture measurement, one is powder (non textured) with a thickness of 2 mm and another is Cu with triclinic sample symmetry with a thickness of 3mm. Measurement was performed using preset count mode. Monitor count is about 3500 cps. Measurement of defocusing effect was done using bonet Cu powder using preset count  $4 \times 10^5$ . Texture measurement was carried out at (111) and (200) Bragg peaks. MAUD software is used for texture analysis [8].

Texture measurement was performed in the range of  $0 \leq \phi \leq 360$  and  $0 \leq \chi \leq 90$ . Figure 19 shows reconstructed pole figure without defocusing and background correction and Fig. 20 shows reconstructed pole figure after corrected with defocusing, background and absorption factors. Linear absorption coefficient =  $0.19 \text{ cm}^{-1}$

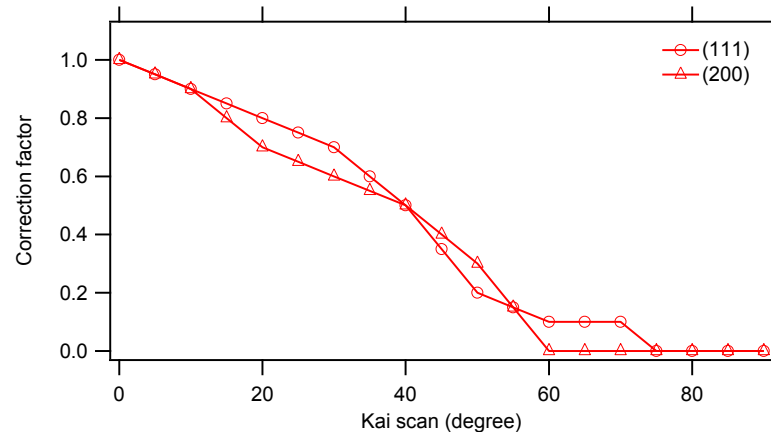


FIG. 19. Defocusing factor was taken from bonet Cu powder at (111) and (200) Bragg peak.

From experiment of defocusing effect, bonet bulk non texture sample with thickness of 2 mm and diameter of 20 mm is too thin for neutron defocusing effect experiment. By the use of minimum incoming beam slit ( $5 \times 5 \text{ mm}^2$ ), integrated intensity is gradually decrease and practically flat after  $\chi \geq 70^\circ$  for (111) plane and  $\chi \geq 60^\circ$  for (200) plane. So that defocusing effect and background of the sample must be taken into account and absorption factor as well. After it was corrected with these factors, reconstructed pole figures is shown in Fig. 21.

## 2.5. Optimization of instruments for residual strain/stress measurements

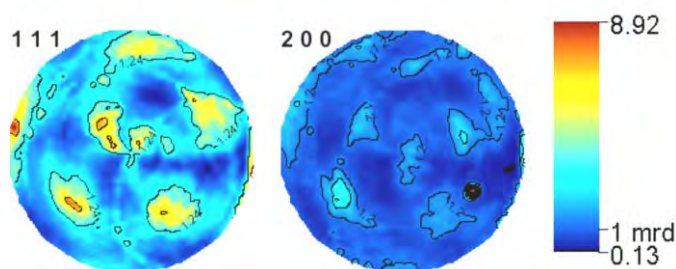


FIG. 20. Pole Figure (111) of copper sample with triclinic sample geometry without defocusing and background correction.

From experiment of defocusing effect, bonet bulk non texture sample with thickness of 2 mm and diameter of 20 mm is too thin for neutron defocusing effect experiment. By the use of minimum incoming beam slit ( $5 \times 5 \text{ mm}^2$ ), integrated intensity is gradually decrease and practically flat after  $\chi \geq 70^\circ$  for (111) plane and  $\chi \geq 60^\circ$  for (200) plane. So that defocusing effect and background of the sample must be taken into account and absorption factor as well. After it was corrected with these factors, reconstructed pole figures is shown in Fig. 21.

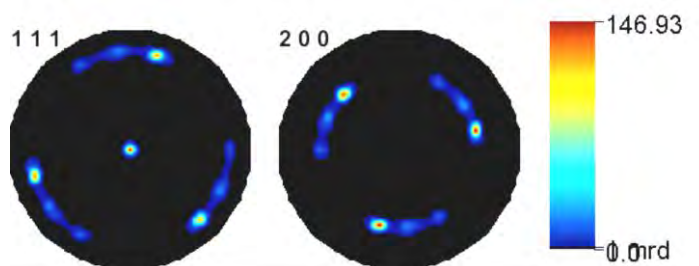


FIG. 21. Pole Figure (111) of copper sample with triclinic sample geometry after defocusing and background correction.

In association with the texture measurement recently it has been carried out the Round Robin exercise between BATAN and CIAE on the texture measurement of the Zircalloy sample. However since the measurement is in progress no experimental result can be shown in this report.

## 5. COLLABORATION BETWEEN INSTITUTIONS

Within the research contract period some collaborations between BATAN and other institutions within the CRP members have been done. Some of BATAN's researchers have visited NPI, Chech Republic, KFKI-AEKI, Hungary and JINR, Russia for learning about the Monte carlo simulation, Triple Axis Spectrometer and Detector system, respectively.

## 6. CONCLUSIONS

Programme works which were planned from the beginning of the project has been sucessfully carried out. Some of the neutron instruments have been optimized and the collaborative works with other member of CRP has been implemented i.e. Round Robin

## 2.5. Optimization of instruments for residual strain/stress measurements

exercises using VAMAS sample for neutron diffractometer and contrast and resolution samples for tomography are beneficial for standardization of these instruments. Normalization of texture data has not been achieved and an attempt to obtain the standard texture sample for neutron is being efforted.

### ACKNOWLEDGEMENT

Authors are thankful to the Government of Indonesia for the support with providing funds through DIPA project. We thank the IAEA for supporting this CRP project through financial and technical assistant. Special thanks to Pavol Mikula (NPI), Gyula Torok (AEKI), and Anatoly Balagurov (JINR) for assisting the scientific visit to their institutions and also thanks to Carsten Ohms, Eberhard Lehmann and Yuntao Liu for providing the sample for the Round Robin exercise.

### REFERENCES

- [1] ANDOR Technology, User Guide iKon-M, Version 1.2, August (2008).
- [2] SUTIARSO, BHAROTO, FAHRURROZI, SETIAWAN, JULIYANI, "3D neutron tomography in the RSG-GAS reactor for non destructive inspection of industrial components", Proceeding of National Seminar of Research and Nuclear Device Management, Yogyakarta, (2011) 252-254.
- [3] KAESTNER, A., LEHMANN, E., Quality Assessment for Neutron CT, Paul Scherrer Institut, Switzerland, (2012).
- [4] TORII, S., MORIAI, A., "The design of the radial collimator for residual stress analysis diffractometer at J-PARC" (in Japanese), JAEA-Technology 2005-004.
- [5] SAROUN, J., KULDA, J., "RESTRAX - a program for TAS resolution calculation and for scan profile simulation", *Physica B* **234-236** (1997) 1102-1104.
- [6] OHMS, C., Private communication on Round Robin exercise using VAMAS sample, 2011.
- [7] BONET A., Texture Reference Samples, Manual for Cu sample SN: COA-472-011, LaboSoft 2011, Product ID: 60-101.
- [8] LUTTEROTTI, L, MAUD Tutotial – Computing ODF using traditional pole figure using WIMV, (2000).



**2. RESULTS ACHIEVED**  
**2.6. EFFORTS TOWARDS**  
**STANDARDIZATION OF NEUTRON**  
**IMAGING**

## 2.6. Efforts towards standardization of neutron imaging

### IMPROVEMENT OF A NEUTRON TOMOGRAPHY FACILITY

R.PUGLIESI, R. SHOUERI, C. DOMIENIKAN, F. TOLEDO, M.L.G.ANDRADE

Nuclear and Energy Research Institute, IPEN-CNEN/SP.

Av. Prof Lineu Prestes 2242, Butanta,

CEP 05508-000 São Paulo – SP

Brazil

Email: [pugliesi@ipen.br](mailto:pugliesi@ipen.br)

#### Abstract.

A facility for neutron tomography was installed at the beam-hole #14, BH14, of IEA-R1 nuclear research reactor of IPEN-CNEN/SP. Its design was based on the design of the previous facility installed at BH08 of this same reactor. The main challenge was to ally, good performance to a minimal damage in the CCD sensor of the facility's video camera, caused by radiation. A tomography can be obtained in only 400s, with a spatial resolution of  $263\pm 35\mu\text{m}$  and the absorbed dose by the CCD is only 2.1 Sv(gamma) and 21 Sv(neutrons) per tomography. According to our last studies, it is possible to minimize still more the radiation damage in the CCD.

## 1. INTRODUCTION

The IPEN-CNEN/SP is a governmental institution which, since 1956, is devoted to the development and application of nuclear technology in Brazil, by making use of the 5MW pool type IEA-R1 nuclear research reactor. The neutron imaging activities in the Nuclear Physics Department of IPEN, began in 1987 and, in 1988, the working group has designed and constructed a neutron radiography facility which is operational since 1992 and is installed at the radial beam-hole, BH08. Between 1992 and 1998 the standard film as well as the track-etch imaging techniques were developed. In 1998, a real-time facility and a standard digital system for image processing were also installed. Between 2000 and 2008, the working group, has developed new imaging techniques by using low-energy electrons and alpha particles, generated by neutron beams, as penetrating radiation to inspect low thickness samples. In 2009 we started to install a neutron tomography (NT) facility in the same BH08 and at the end of 2010, the first tomography image was obtained. The main characteristics of the neutron beam at the irradiation position are shown in Table 1.

TABLE 1. CHARACTERISTICS OF THE NEUTRON BEAM AT THE IRRADIATION POSITION

thermal neutron flux	$10^6 \text{ n}\cdot\text{cm}^{-2}\cdot\text{s}^{-1}$
beam size	25 to 40 cm
mean energy	7 meV

## 2. THE NEUTRON TOMOGRAPHY FACILITY OF IPEN-CNEN/SP

Basically the facility consists of an automated rotating table coupled to a neutron imaging system and softwares for image reconstruction and image visualization. A tomography is obtained as follows: the sample is positioned at a rotating table and the transmitted intensity impinges a scintillator ( ${}^6\text{LiF-ZnS} - 18 \times 24 \text{ cm}^2$ ) forming an image which is captured by a cooled CCD video camera. In order to minimize damages at the CCD sensor caused by radiation, a high reflectivity plane mirror reflects the image to the camera which is positioned at  $90^\circ$  with respect to the neutron beam. The scintillator, the mirror and the camera

## 2.6. Efforts towards standardization of neutron imaging

are installed within a  $100 \times 30 \times 30 \text{ cm}^3$  aluminium light tight box. An electro-mechanical interface controls the table – camera set in such way that after the image be captured, the sample is rotated a small step of  $0.9^\circ$  and a new image is captured. Some details of the imaging system are shown in the Figs 1 and 2. After a complete rotation of  $360^\circ$ , 400 images are captured, the software Octopus is used for image reconstruction and the software VGStudio for 3D visualization of the internal structure of the sample. The overall time spent to obtain a tomography is about 1 hour. The light tight box, Fig. 2, is located inside a  $200 \times 100 \times 100 \text{ cm}^3$ , 7.5 cm (thickness) borated poly shielding, shown in the Fig. 3.

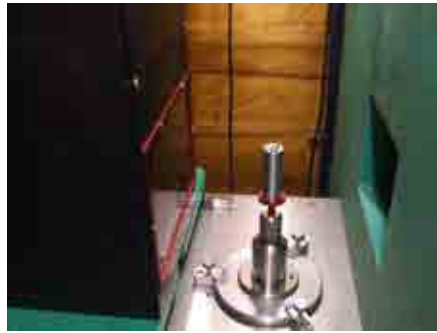


*FIG. 1. Tomography system: rotating table and scintillator.*



*FIG. 2. Tomography system: light tight box.*



*FIG. 3. Borated - poly shielding.*

## 2.6. Efforts towards standardization of neutron imaging

### 2.1. Irradiation time

The irradiation time to acquire each one of the 400 images for the tomography was determined by means of the curve that relates gray level - GL as functions of the irradiation time -  $T_i$ . The curve, shown in the Fig. 4, was obtained by performing irradiations in the direct beam (without sample) and reading the GL in the image, as functions of the irradiation time varying between  $2 < T_i < 15$  s. Seven points have been obtained and the GL of each point was evaluated by averaging the intensities of about 5,000 individual pixels. The standard deviations of the readings are inserted in the points and they ranged from 0.1% to 2% of the read value. A straight line was drawn between the points and the behavior of  $GL$  vs  $T_i$  is linear until about 12 s after which the pixel saturation takes place. For reconstruction, the images must be free of saturated pixels, therefore they must be acquired in the linear region. For the present data, a safe irradiation time that satisfies such requirement is about 10 s, that is, 80% of the maximal irradiation time that limits the linear region.

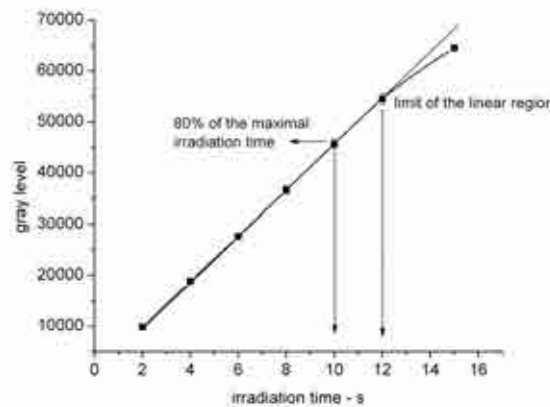


FIG. 4. Behavior of the gray level as functions of the irradiation time.

For this measurement the CCD is kept in a constant temperature of  $-20^{\circ}\text{C}$ , the CCD chip array was fixed to  $512 \times 512$  pixels, and the reactor power was 4.5 MW.

### 2.2. Spatial resolution

Usually it is quoted in terms of the total unsharpness- $U_t$ , consisting of the geometrical unsharpness- $U_g$  from the angular divergence of the neutron beam and the intrinsic unsharpness- $U_i$  from the detection system (scintillator, detection geometry, camera focus condition) and they are related by Eq. (1):

$$U_t^n = U_i^n + U_g^n \quad (1)$$

with  $1 < n < 3$

The total unsharpness was evaluated by scanning the gray level distribution in the image of a knife edge Gd foil ( $127 \mu\text{m}$ ) irradiated for  $\sim 8$  s, in a tight contact to the scintillator. Figure 5 shows the obtained distribution and the “Edge Spread Function” –  $ESF$  Eq. (2), fitted to the experimental data.

$$ESF = p_1 + p_2 \times \text{atan}(p_3(x - p_4)) \quad (2)$$

where  $x$  is the scanning coordinate.

## 2.6. Efforts towards standardization of neutron imaging

The obtained value was  $U_t = 347 \pm 26 \mu\text{m}$  and it corresponds to the full width at half maximum (FWHM) of the Line Spread function associated to Eq. (2) and is given by Eq. (3).

$$U_t = 2/p_3 \quad (3)$$

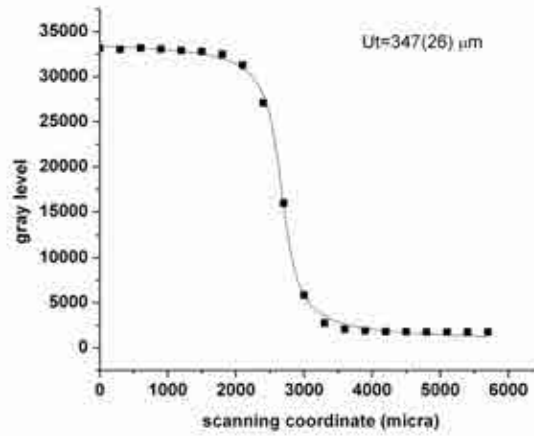


FIG. 5. Gray level distribution as functions of the scanning coordinate.

Since the Gd foil, was irradiated in tight contact with the scintillator ( $U_g \sim 0$ ) and  $U_t \sim U_i$ . The value for  $U_t$  results of the combined effect of: the scintillator, which because of the thickness of the scintillation layer of  $400 \mu\text{m}$ , limits the resolution to  $\sim 200 \mu\text{m}$ ; the detection geometry that limits the resolution to the effective pixel size of  $254 \mu\text{m}$ , evaluated for the camera - scintillator distance of  $60 \text{ cm}$ , a camera's field of view of  $13 \times 13 \text{ cm}^2$  (provided by the NIKON f1/1.2 58 mm lens), and a CCD chip array of  $512 \times 512$  pixels; the imperfect and subjective focusing procedure of the camera lens since it depends of the visual acuity of the technician. For this measurement the CCD was also kept in a constant temperature of  $-20^\circ\text{C}$ , the CCD chip array was fixed to  $512 \times 512$  pixels, and the reactor power was  $4.5 \text{ MW}$ .

## 2.3. Sensitivity to discern thickness

It is defined as the thickness change  $-\Delta x$  of the material, which is discernible by a gray level change  $-\Delta GL$  in the image. It was determined from the curve that relates  $GL$  as functions of the thickness  $x$ . The objects used in this measurement were step wedges manufactured in iron and Perspex with thicknesses varying between  $2 \text{ mm}$  and  $12 \text{ mm}$  in steps of  $2 \text{ mm}$ . The  $GL$  value for each step was evaluated by averaging the gray level intensities of about  $1,000$  individual pixels. The standard deviations of the readings are inserted in the points and they ranged from  $0.4\%$  to  $1\%$  of the read value. The behavior of  $GL$  vs  $x$  is given by the exponential function of Eq. (4).

$$GL = A \times \exp(-Bx) + C \quad (4)$$

The discernible thickness is given by Eq. (5) and can be evaluated as the derivative of Eq. (4):

$$\Delta x = \frac{\Delta GL}{-AB \cdot \exp(-Bx)} \quad (5)$$

## 2.6. Efforts towards standardization of neutron imaging

The plots of the sensitivity as functions of the object thickness are shown in Fig. 6 and the minimal discernible thickness for the studied materials were 0.33 mm (iron) and 0.2 mm (Perspex).

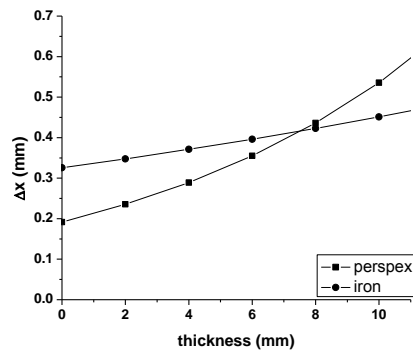


FIG. 6. Behavior of the sensitivity as functions of the object thickness.

## 2.4. 3D images

The figures below show some examples of 3D images obtained in this facility.

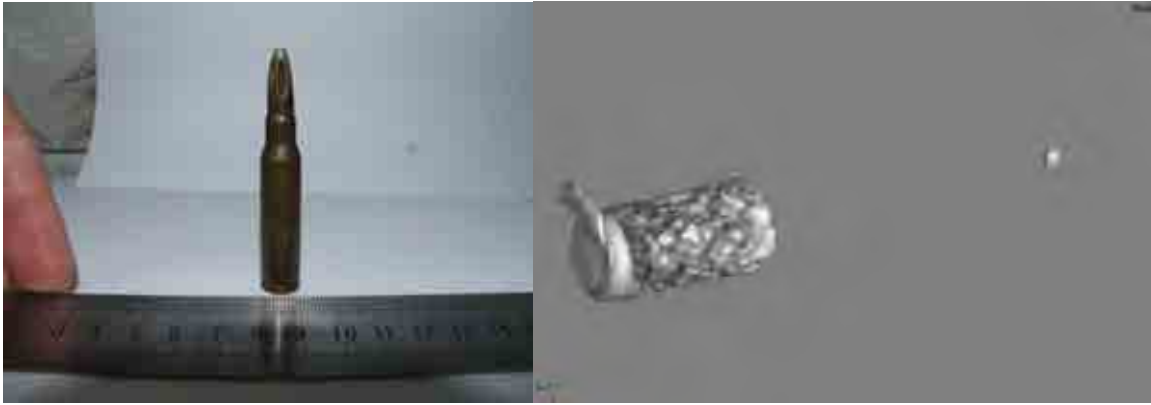


FIG. 7. (left) Aluminium case and insets (brass, steel and Perspex); (right) 3D image of the insets.



FIG. 8. (left) Pottery vase; (right) 3D image showing in detail the glue used in its restoration.

## 2.6. Efforts towards standardization of neutron imaging



*FIG. 9. (left) Gun bullet; (right) 3D image showing in detail the powder.*

After about three months in operation, a routine evaluation has revealed an abnormally high amount of damages in the camera's CCD, which are produced mainly by scattered neutrons. The dose rate at the camera position was about 1000  $\mu\text{Sv/h}$ , and about 1% of the pixels were damaged. As shown in the Fig. 10, the damages are like white spots superimposed to the image and for three reasons this amount is unexpectedly high: (i) this camera is commonly used in similar tomography facilities; (ii) the camera is surrounded by an appropriated radiation shielding; (iii) our old camera in use for several years in a similar radiation environment has accumulated less damage than the newer during these months. In spite the white spots can be eliminated from the image, either by lowering the CCD temperature or by image processing, most of them are permanent and the continuous use of the camera will continuously increase them until the CCD becomes useless. Therefore the irradiations were temporarily stopped and a study to minimize the radiation dose at the camera position was carried out. The major actions to be implemented would require changes in the neutron collimator and in the shielding of the facility and because of the limitations around the BH08, we transfer the tomography facility, to the BH14 of the same reactor.



*FIG. 10. Damages caused by radiation in the CCD sensor.*

## 2.6. Efforts towards standardization of neutron imaging

### 3. THE NEW FACILITY FOR NEUTRON TOMOGRAPHY OF IPEN-CNEN/SP

Figure 11 shows the BH14 before (left) and after (right) an old equipment be removed.



*FIG. 11. (left) Removing of the old equipment; (right) Area ready for use.*

The major actions implemented in the new facility were: (1) design a collimator (Fig. 12), which provides a neutron beam size of  $\sim 12\text{cm}$  at the irradiation position; (2) minimize the contribution of the scattered neutrons in air by using diaphragms, manufactured in borated polyethylene, positioned in the path of the beam (Fig. 13); (3) perform a precise alignment between the geometrical center of the beam – hole and the geometric center of the irradiation position, assuring a maximal illumination of the sample by the neutron beam (Fig. 14); (4) position the video camera and its shielding outside the irradiation position (Fig. 15); (5) improve the shielding close to the camera lens by using a light transparent boron glass filter; (6) reduce the thickness of every material close to the beam path to minimize neutron scattering; (7) use of beam limiters to perform fine adjustments in the size of the neutron beam.



*FIG. 12. (left) Parts of the new collimator; (right) mounting of the collimator.*

## 2.6. Efforts towards standardization of neutron imaging



*FIG. 13. Diaphragms in borated poly.*



*FIG. 14. Detail of the alignment by using a LASER.*



*FIG. 15. Camera positioned outside the irradiation position.*

Figure 16 (top) is a top view of the new facility which consists of three parts: (1) the most at left is the main shielding; (2) the central, inside which the irradiations are performed; (3) the most at right is the beam-catcher. Most of the material used as neutron shielding was borated polyethylene sheets. Figure 16 (bottom) shows details of the irradiation position.

## 2.6. Efforts towards standardization of neutron imaging

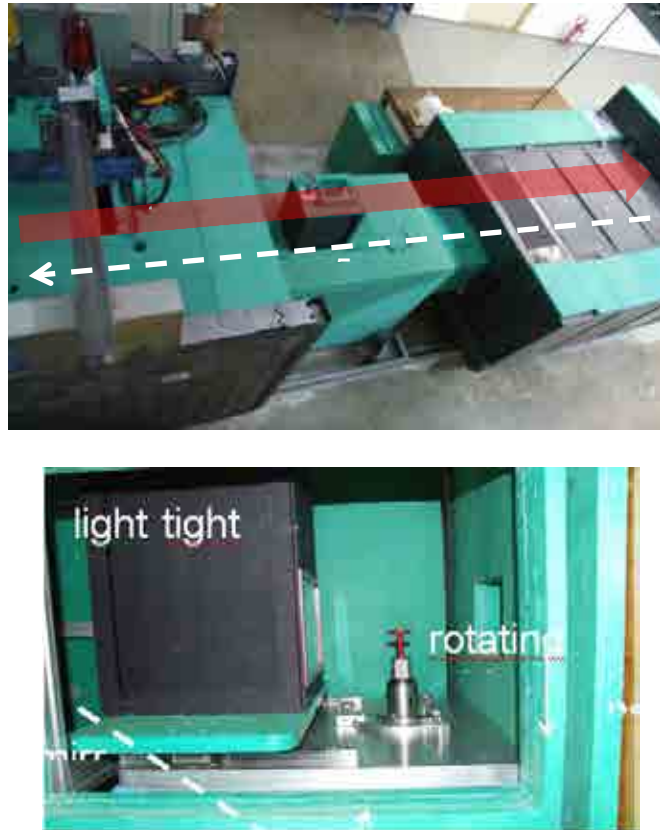


FIG. 16. (top) Top view of the facility's; (bottom) Details of the irradiation position. After implementation, the operational parameters of the new facility were evaluated according to the same procedures mentioned in 2.1 2.2 and 2.3.

### 3.1. Dose rate at the camera

The gamma and neutron dose rates at the camera position were measured resulting  $19 \mu\text{Sv/h}$  and  $189 \mu\text{Sv/h}$  respectively, for a neutron flux  $8 \times 10^6 \text{ n}\cdot\text{cm}^{-2}\cdot\text{s}^{-1}$  at the irradiation position.

### 3.2. Irradiation time

The curve that relates gray level - GL as functions of the irradiation time –  $T_i$  is shown in Fig. 17 and for the present data the irradiation time for the linear region is 1.0 s. Hence, the overall time to obtain all the 400 images for the tomography is about 400 s.

## 2.6. Efforts towards standardization of neutron imaging

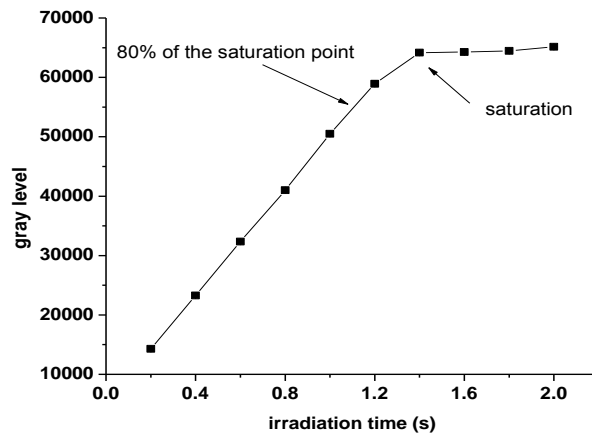


FIG. 17. Behavior of the gray level as functions of the irradiation time.

## 3.3. Spatial resolution

Since the present procedure to focus the lens depends of the visual acuity of the technician, it is subjective and the condition of perfect focus is very difficult, to be achieved. Therefore, in order to evaluate the resolution of the facility, several images of the same gadolinium foil, for several focus conditions, were captured. The Fig. 18 shows the distribution in which the best resolution was achieved and the obtained value was  $Ut = 263 \pm 35 \mu\text{m}$ .

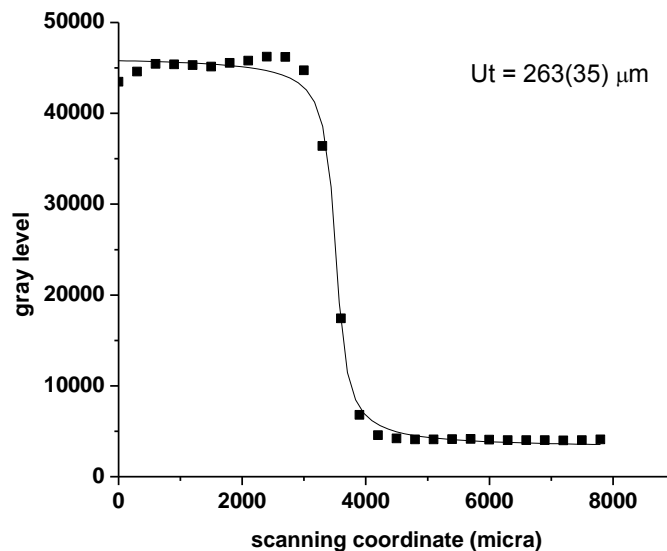


FIG. 18. Gray level distribution as functions of the scanning coordinate.

## 3.4. Sensitivity to discern thickness

The plots of the sensitivity as functions of the object thickness are shown in Fig. 19 and the minimal discernible thickness for the studied materials were 0.3 mm (iron) and 0.13 mm (Perspex).

## 2.6. Efforts towards standardization of neutron imaging

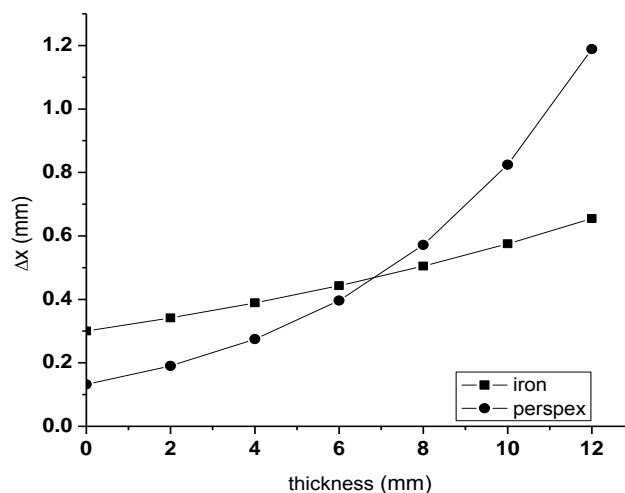


FIG. 19. Behavior of the sensitivity as functions of the object thickness.

Thus, according to these data, the present facility is an improved version of the previous one and its configuration has reached its maximum performance in terms of camera protection. Although the radiation dose rates in the CCD sensor were much reduced, one question still remains: it is possible to reduce it still more and ensure a safer camera's operational condition? In order to answer part of this question several cheap CCD cameras (used for surveillance), shown in Fig. 20, have been irradiated and the following important conclusions could be drawn:

- Epithermal neutrons are approximately 10 times more efficient than thermal neutrons to cause damages in the CCD.
- The contribution of scattered gamma radiation to the damages is negligible.
- The amount of damages caused in CCD is ~6 times greater with mirror than without mirror.

TABLE 2. THE MAIN CHARACTERISTICS OF BOTH NT FACILITIES

	BH-08	BH-14
thermal neutron flux(Au foil method)	$10^6 \text{ n} \cdot \text{cm}^{-2} \cdot \text{s}^{-1}$	$8 \times 10^6 \text{ n} \cdot \text{cm}^{-2} \cdot \text{s}^{-1}$
beam size	20 cm or 40 cm	1cm to 12cm
mean energy	7 meV	7 meV
gamma filter Bi	25 cm	25 cm
L/D ratio	~90	~90
spatial resolution	$347 \pm 26 \mu\text{m}$	$263 \pm 35 \mu\text{m}$
time spent per tomography	4000 s	400 s
dose at the camera per tomography	( $\gamma$ ) 54 $\mu\text{Sv}$ ; (n) 1111 $\mu\text{Sv}$	( $\gamma$ ) 2.1 $\mu\text{Sv}$ ; (n) 21 $\mu\text{Sv}$

## 2.6. Efforts towards standardization of neutron imaging

Based on the last conclusion, the answer to the question above is “yes”, it is possible to reduce more the radiation dose at the camera. It is necessary to substitute the present glass based mirror by a thin silicon based mirror to reduce the neutron dose at the camera from 21  $\mu\text{Sv}$  (see Table 2) to 3.5  $\mu\text{Sv}$  per tomography.



FIG. 20. Camera employed in the irradiation tests.

## 4. THE STANDARD SAMPLES PROVIDED BY PSI

The three standard samples provided by PSI, two for resolution and one for contrast measurements have been imaged in March/April, 2012 and they were sent back to PSI in April/2012. The obtained results by us and by several institutes were discussed during the meeting in Dubna-Russia May, 2013 resulting in several new suggestions regarding the data analysis procedure, specifically related the fitness of a Lorentzian function in the resolution data, as well as the use of some new standard samples manufactured in polyethylene for resolution evaluation.

## 5. CONCLUSIONS

By taking into account the original work plan, two activities were not yet concluded: design a collimator to provide a parallel neutron beam and tomograph samples relevant to nuclear energy sector.

However the main objective of the project, “the improvement of our NT facility”, was reached [1, 2].

## 6. NEXT STEPS

- Determination of the characteristics of the new facility, with Si-wafer based mirrors
- Tomograph typical samples relevant to nuclear energy sector.
- Cooperation IPEN-CNEN/SP (Brazil) - ITN (Portugal) in the study and development of a new collimator to provide a parallel neutron beam to reduce the irradiation time to half of the present time.

## **2.6. Efforts towards standardization of neutron imaging**

- Joint cooperation between Switzerland, South Africa, South Korea, Germany, USA, Indonesia and Brazil, to standardize the samples as well as the mathematical procedures for resolution and sensitivity evaluation of NT facilities.

### **REFERENCES**

[1] Stanjoev Pereira, R. et al, The neutron tomography facility of IPEN-CNEN/SP and its potential to investigate ceramic objects from the Brazilian cultural heritage, *Applied Rad. and Isotopes*, **75** (2013) 6–10.

[2] Pugliesi, R. et al. The new facility for neutron tomography of IPEN-CNEN/SP and its use for research and engineering purposes. In preparation.

## 2.6. Efforts towards standardization of neutron imaging

### TOWARDS STANDARDIZATION OF DIGITAL NEUTRON RADIOGRAPHY AND TOMOGRAPHY: SETUP CHARACTERIZATION AND APPLICATION IN POROUS MEDIA QUANTIFICATION

M. J. RADEBE\*, F. C. DE BEER\*, A. KAESTNER\*\*

\*Necsa(South African Nuclear Energy Corporation), P. O. Box 582, Pretoria, 0001, South Africa

\*\*Paul Scherrer Institute (PSI), Villigen, Aargau, Switzerland

#### Abstract.

Digital thermal neutron imaging (radiography and tomography) is a powerful non-destructive analytical tool and has demonstrated its importance in industrial- and research application world-wide. The standardization process, to certify digital thermal neutron imaging as a standard practice in industry, entails standardized test phantoms to be evaluated. Through the evaluation of the phantoms the spatial resolution and contrast of a thermal neutron digital imaging system can be determined in a controlled and standardized manner by accepting good practice in terms of scanning, data processing, data visualization and evaluation. Standard test phantoms are objects with physical features designed to test facility capabilities to reveal these features without any ambiguity. The good practice enables the acceptable assessment of different international digital thermal neutron imaging facilities for spatial resolution and contrast abilities. The purpose of this contribution is to establish good practice for the experimental setup, acquiring of 2-D digital projections and the reconstruction process of the 3-D digital images of standard test phantoms for spatial resolution and contrast. Results obtained from applying this suggested good practice on the contrast standard test phantom will be discussed.

Another challenge is that qualitative measurements using digital neutron imaging has been the more explored aspect than accurate quantitative measurements. The reason for this bias is that quantitative measurements require correction for background and material scatter, and neutron spectral effects. This work evaluates the capabilities of the QNI software package to produce accurate quantitative results on specific characteristics of porous media, and its role to non-destructive quantification of material with and without calibration. The work further complements QNI abilities by the use of different sample-detector distances (SDDs). Studies of the measurement of the effective percentage porosity of mortar samples using the calibrated attenuation coefficient of water, using QNI and the SDD principle, are reported.

## 1. INTRODUCTION

Digital thermal neutron imaging is a powerful non-destructive analytical tool and has demonstrated its importance in industrial- and research applications world-wide [1]. Yet standards for this analytical technique do not exist. Standardization for neutron radiography facilities is essential in that it establishes and enforces precision and accuracy in practices and measurements, as well as to create a basis to produce industrial- and commercial measurements in a same manner throughout the NR community across the globe [2]. The standardization process for 3-D neutron tomography started when test phantoms, one for spatial resolution and another for contrast were designed and development with the aid from the IAEA and through the assistance of the Paul Scherrer Institute in Switzerland. These phantoms were evaluated through the creation of good practice for the scanning process thereof, data processing, data visualization and evaluation. Standard test phantoms are objects with physical features and designed in such a way to test/determine facility capabilities to reveal these features without any ambiguity. The good practice enables the common acceptable assessment methodology for different international digital thermal neutron radiography facilities to obtain characteristics about their spatial resolution and contrast abilities.

This paper provides the standardized analytical procedure for projection acquisition and post processing of thermal neutron projections to images in three dimensional spaces (tomogram and slices in  $X$ -,  $Y$ -, and  $Z$  planes). This procedure is being discussed in the context of spatial resolution and contrast. One test sample for contrast, the Neutron Tomography Contrast (NTC), and two for spatial resolution, called Neutron Tomography Spatial Resolution (NTRS) PLUS and -MINUS are defined, tested at various facilities in the world; results discussed and will be introduced for adoption as standards to the NR community.

## **2.6. Efforts towards standardization of neutron imaging**

Digital neutron radiography also enables non-destructive quantitative measurements. The accuracy of these quantitative measurements is negatively affected by neutrons scattered from the surrounding material of the experimental chamber (background), the sample material as well as the neutron energy spectrum (spectral effect) of the neutron beam. The degree of correction effectiveness of these effects determines if calibration of material thickness is necessary or not. Calibration for material thickness is an important part of non-destructive quantitative measurements procedure, and its limitation is the availability of pure material under investigation. The calibration process is not effective for relatively thicker high scattering neutron material due to multiple scattering of neutrons and background scattering. Appropriate correction for these effects can lead to calibrations making it possible to predict material thickness of relatively thicker samples from transmitted intensity. While calibration is useful, it cannot always be conducted due to unavailability of a set of varying thicknesses of the material under quantification. In this case it is desirable to have accurate estimations of material thickness from transmitted patterns of neutrons using computational approaches such as Quantification of Neutron Images (QNI) software. This serves the purpose to have the theoretical calculated effective attenuation coefficient of the materials under investigation, comparable within a small error to the practical effective attenuation coefficient. The QNI software package has resulted from efforts to obtain accurate quantitative measurements from neutron radiographs through computational elimination of the effect of scattered neutrons from various sources on the radiographs, while the SDD variation principle has previously been demonstrated as means to eliminate material scatter effect [3,4]. The SDD was measured to the front side of the sample. The draft protocol for the non-destructive evaluation and testing of porous media in 2D with the aid of neutron radiography has been established [5]. The protocol dictates how the factors, affecting the accuracy of quantitative measurements using neutron radiography, are identified and then experimentally eliminated through applying the proposed standardized procedure. The protocol was tested and applied for the characterization of mortars and concrete. These materials is being considered as nuclear related materials, within the scope of this CRP as it is being used in the encapsulation of nuclear waste.

## **2. SAMPLES**

Through consultation, debate and discussion of various key role players within the NR community, several samples were identified, one for the testing and evaluation of the contrast obtained in a neutron tomography system (Neutron Tomography Contrast (NTC) phantom), as well as two samples for the testing and evaluation of the spatial resolution (Neutron Tomography Spatial Resolution (NTSR) phantom). In addition, the protocol for thecalibrated testing and evaluation of porous media in a form of a mortar and concrete samples were applied and tested.

### **2.1. NTC and NTSR test objects**

A set of NTC and NTSR samples designed and manufactured by Neutron Imaging and Activation group located at the Paul Scherer Institute (PSI) in Switzerland were made available for testing of contrast and spatial resolution of neutron tomography facilities respectively. Figures 1 and 2 show the design and photographs of the NTC and NTSR test objects respectively.

## 2.6. Efforts towards standardization of neutron imaging

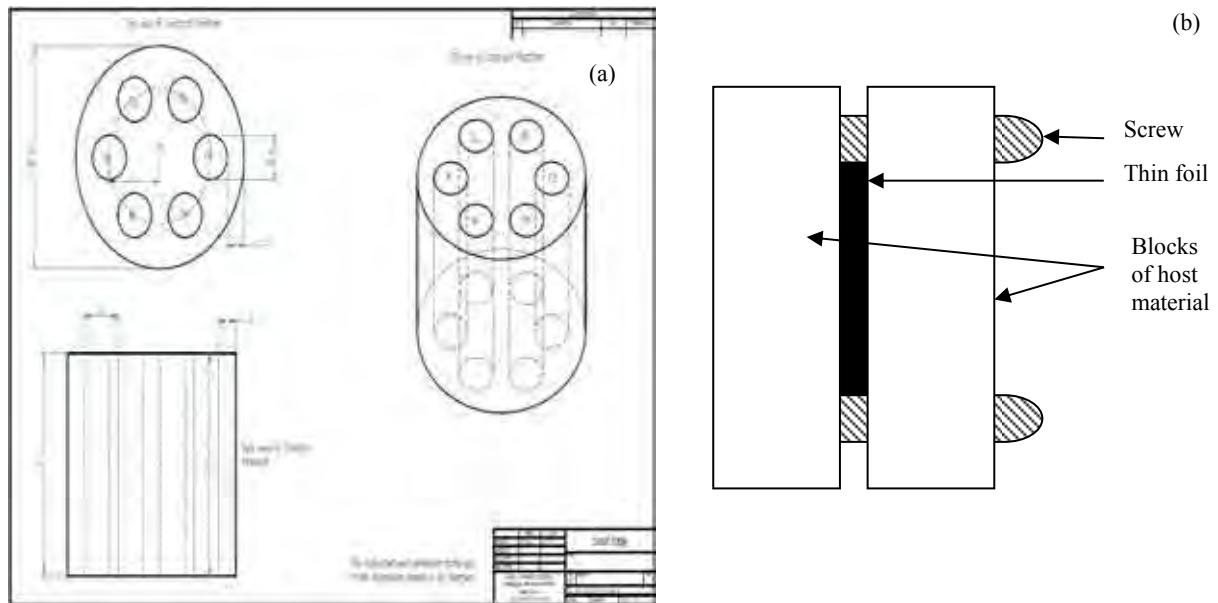


FIG. 1.(a) Design of the NTC standard developed by KAERI (Korea). (b) Side view of the NTRS standard design developed by PSI (Switzerland).

The NTC standard sample was designed by the Korean Atomic Energy Research Institute (KAERI). This NTC sample consists of 6mm diameter cylinders of Al, Cu, PE, Ni, Pb and Fe embedded in an Al cylinder of 30 mm in diameter. The contrast obtained by a specific NR system, was assessed in how easy the cylinders can be differentiated within the generated neutron 3D tomogram of the sample.

The NTRS standard sample was designed and manufactured by PSI, Switzerland. The spatial resolution of a NR system is being assessed through visualizing different sizes of an inclusion and/or a void in a solid piece of material. Each sample is made of two solid blocks ( $10 \times 20 \times 40 \text{ mm}^3$ ) fixed together by a set of screws, one at the bottom and another at the top. The NTRS MINUS (Figure 2) is based on matrix of Fe and the Al foil (Neutron transparent material – illusion of a void) between the two blocks, while the NTRS PLUS (Figure 2) is based on Al matrix and Cu foils (Neutron scattering materials – illusion of an inclusion). The space between the two blocks can be varied by inserting a number of 20-micron thick foils between the blocks.

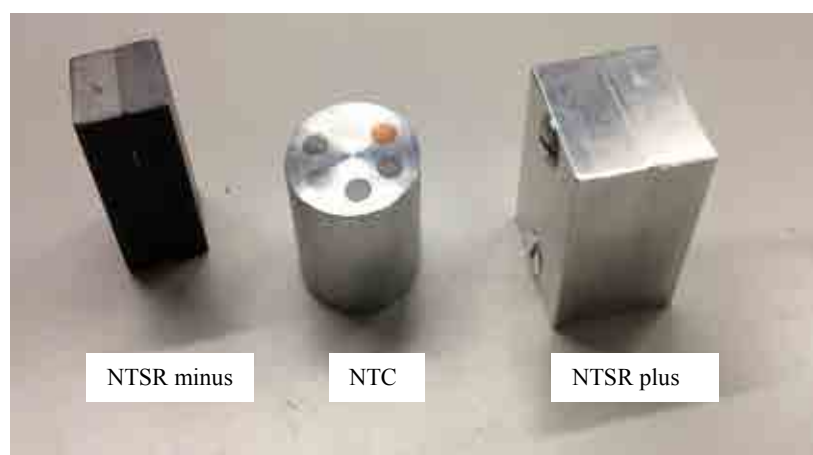


FIG. 2. A photograph of two NTRS (plus and minus) and one NTC test objects.

## 2.6. Efforts towards standardization of neutron imaging

### 2.2. Porous media quantification test objects

#### 2.2.1. Aluminum liquid sample holders

Aluminum containers of varying thicknesses were used to contain water samples for calibration purposes of the neutron attenuation coefficient for water as this calibrated parameter is needed in the quantification of porosity and water content within porous media such as concrete matrixes (Figure 3). Water, as high neutron scattering material, is used in porous media quantification as a contrast agent to enhance pores/voids normally not visible as empty spaces. The aluminum containers have the following thicknesses: 9.97 mm, 6.94 mm, 5.01 mm, 3.00 mm, 1.91 mm and 0.97 mm.



5.01 mm, 3.00 mm, 1.91 mm and 0.97 mm.

FIG. 3. Aluminum sample holders for different liquid thicknesses (total of 2 mm thick Al metal container).

#### 2.2.2. Porous media samples

For the demonstration of the effectiveness of the standardized calibration process, samples of choice were mortar and concrete samples of cylindrical and cubic shapes as shown in Figure 4.



FIG. 4. Examples of the concrete, mortar and cement paste samples saturated with liquid.

## 2.6. Efforts towards standardization of neutron imaging

### 3. EXPERIMENTS

Several experiments were conducted to evaluate the standardized procedures for the NCT, NTSR test objects, the procedure for standardised measurements of porous media and the evaluation of the quantum noise of neutron radiograph systems.

#### 3.1. Standardization procedures tested for setup characterization

The developed prescribed standardized procedures were applied at two digital neutron radiography facilities to obtain data for this purpose, namely the SANR facility in South Africa and the Swiss ICON facility [6, 7]. The SANR facility was used to obtain tomography projections for NTC and NTSR test objects and porous media radiographs, while the ICON facility was used to acquire radiography used for quantum noise characterization.

##### 3.1.1. Setup characterization and porous media quantification

The setup with a  ${}^6\text{Li}$  based scintillator screen, a CCD camera,  $\sim 1.2 \times 10^7 \text{ n}\cdot\text{cm}^{-2}\cdot\text{s}^{-1}$  and 150 collimation ratio was used. The SANR facility is a thermal neutron facility which was used to acquire projections of the test objects. The number of projections was calculated based on the Nyquist sampling theorem [9], Octopus reconstruction software used for 3D-reconstructions and ImageJanalytical software for analysis of cross sectional slices.

##### 3.1.2. Quantum noise

Open beam radiographs (Without samples), were used for the purpose of extracting the quantum noise of a particular NR system. Data used in this study was acquired at the cold neutron imaging beam line ICON [6] at the Swiss Spallation Neutron Source (SINQ). The midi setup was used with a 100micron thick  ${}^6\text{Li}$  based scintillator screen and a sCMOS camera and the 340 collimation ratio. The neutron flux was  $\sim 2 \times 10^7 \text{ n}\cdot\text{cm}^{-2}\cdot\text{s}^{-1}$ . The radiographs were acquired at varied exposures to investigate the empirical behaviour of quantum noise at gray values of 8000, 16500, 25000, 32000 and 40000 (corresponding to 2 s, 4 s, 6 s, 8 s and 10 s exposure time). The expected dynamic range for a 16 bit system is 0 to 65535. A set of 20 radiographs was acquired for each exposure time to allow the investigation of the quantum noise on the same field-of-view (FOV) from each of the 20 images. An open beam image is shown in Figure 5.

## 2.6. Efforts towards standardization of neutron imaging

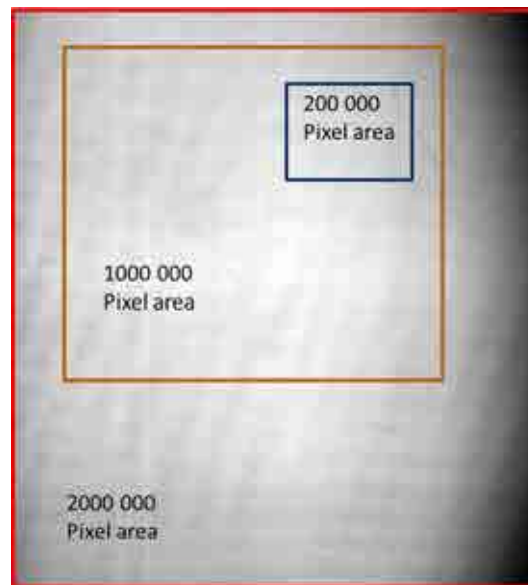


FIG. 5. Neutron computed radiograph of an open beam.

The pixel variation of the gray values within 20 images of each exposure time is the best way of conducting this work but at this stage the FOV (200 000, 1 000 000 and 2 000 000 pixel area) variation has been conducted for the purpose of establishing the principle. Each image can have noise from scintillation point spread function, thermal effects, dead pixel, gamma rays contribution, read out noise and quantization. Dead pixels and gamma rays noise components can be easily eliminated from neutron computed radiographs. The average of the FOV can be hugely influenced by these two latter noise components. The approach was to obtain the total quantum noise from the entire signal conversion chain by obtaining data from the FOV on each image of exposure time using the modal value as an indication of gray value without the negative effect of the dead pixels,  $\gamma$  rays.

## 4. RESULTS AND DISCUSSION

### 4.1. Setup characterization

#### 4.1.1. NTC-sample characterisation

This section presents the results of the examinations conducted to optimize scanning conditions and parameters on the NCT sample. Figure 6 presents the relative attenuation coefficients from a thermal neutron tomogram of the NTC standard obtained through a scanning protocol with 180 projections in  $180^\circ$  and without Fourier filtering. Figure 7 shows the effects of Fourier frequency filtering and sampling on contrast resolution in thermal neutron tomography. The cross-sectional image of the contrast phantom is shown in Appendix I, Figure A.1.

## 2.6. Efforts towards standardization of neutron imaging

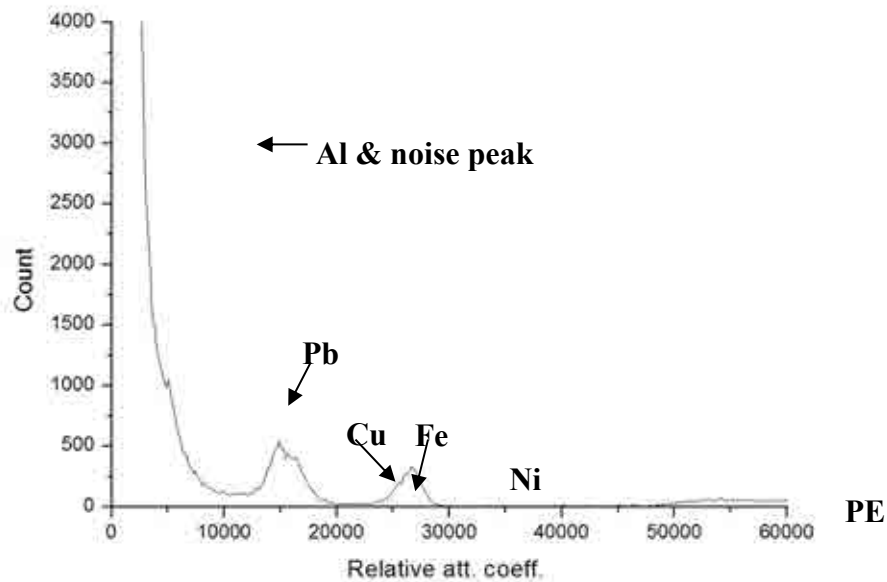


FIG. 6. Relative attenuation coefficients from a thermal neutron tomogram of the NTC standard without Fourier filtering and 180 projections in 180°. Peaks from left to right representing: background noise, Pb, Cu, Fe, Ni and PE.

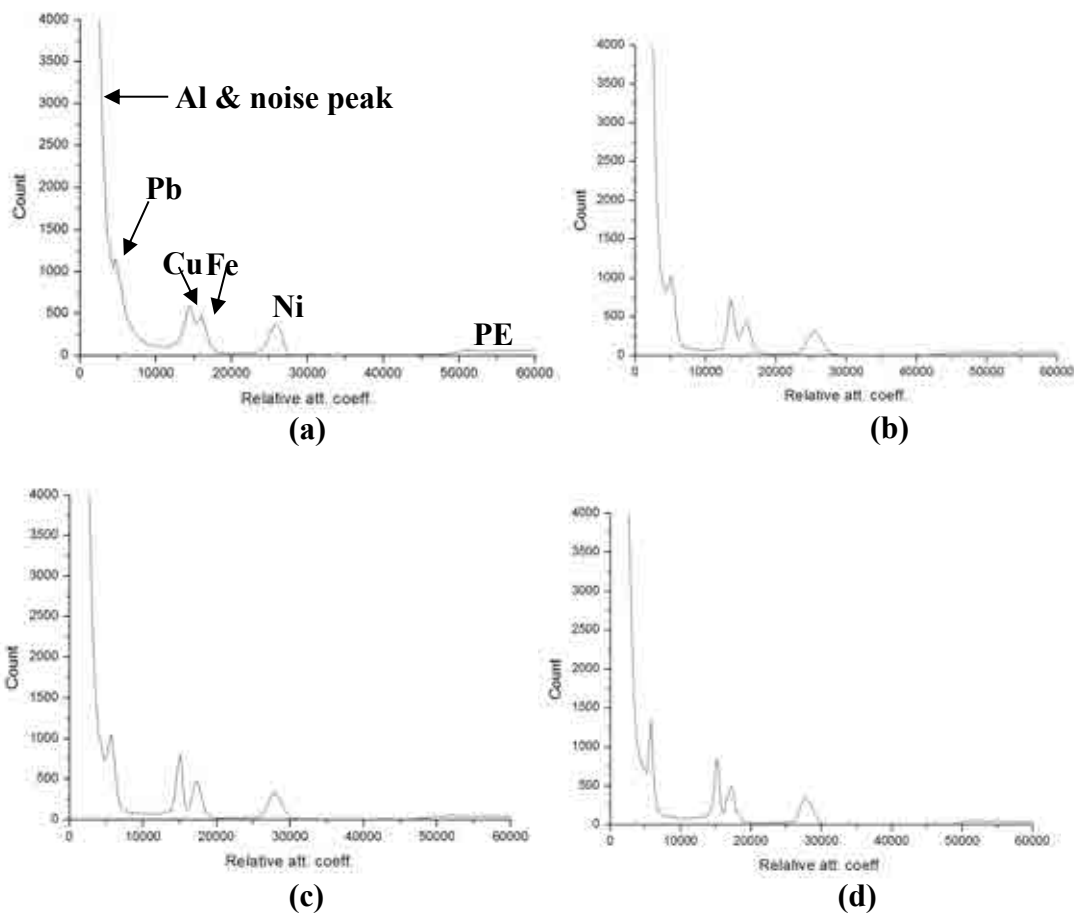


FIG. 7. Demonstration of the effect of the Fourier filter and effect of Sampling of the object during scanning.

## 2.6. Efforts towards standardization of neutron imaging

The results in Figure 7(a-d) are obtained by applying the recommendations of the standardized procedure in Appendix I. Figure 7(a) presents the effect of Fourier frequency filtering on resolution of Cu and Fe peaks from the scan of Figure 6. The NTC standard was then scanned to satisfy the Nyquist-Shannon sampling theorem in  $180^\circ$  and the results of that scanning protocol without Fourier frequency filtering is the resolution of Cu and Fe peaks, as well as the Pb peak from the Al and noise peaks (Figure 7(b)). Figure 7(c) presents the effect both the Nyquist-Shannon sampling theorem in  $180^\circ$  and the Fourier frequency filtering as the peaks become more separated and the materials thus more differentiated. The standard was then scanned to satisfying the Nyquist-Shannon sampling theorem in  $360^\circ$  and Fourier frequency filtering was applied (Figure 7(d)). The results of Figure 7(a) & (b) show better resolution of the Pb peak from the Al and noise peaks.

Figure 8 presents the photograph and reconstructed slice of the NTC test object. Figure 9 shows the results from evaluation of test samples for contrast (1x sample) which was received from PSI and successfully evaluated at Necs. Figure 9 presents contrast data from reconstructed slices sampled at the upper, central and lower regions of the NTC-sample according to the draft protocol developed at PSI [8]. The important feature of Figure 9 is the ability for thermal neutron to visualize all materials in the sample with the acceptable S/N ratio. The thermal beam facility shows results that can differentiate between all materials, of equal thicknesses, as presented in the contrast sample.

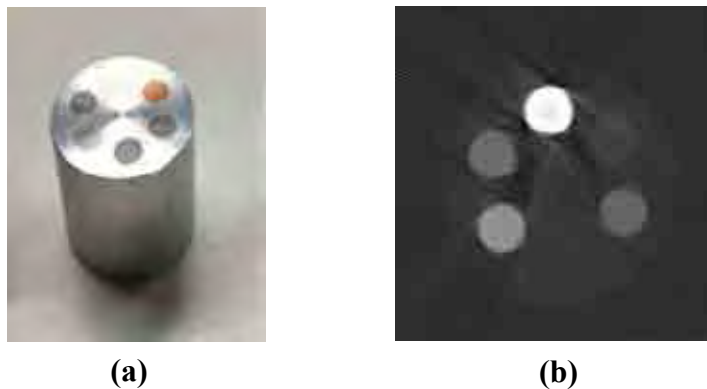


FIG. 8. (a) A picture of the NTC sample. (b) A thermal neutron reconstructed slice of the NTC sample.

## 2.6. Efforts towards standardization of neutron imaging

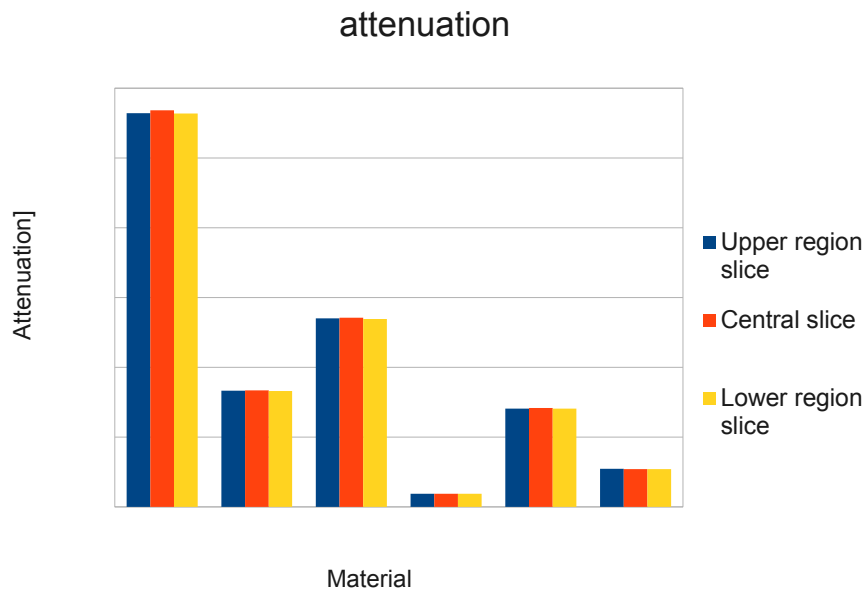


FIG. 9. Relative attenuation data for the contrast test sample.

### 4.1.2. NTSR-sample characterisation

A set of NTSR samples designed and manufactured by Neutron Imaging and Activation group located at the Paul Scherer Institute (PSI) in Switzerland were made available for testing of spatial resolution of neutron tomography facilities through visualizing different sizes of an inclusion and/or a void in a solid piece of material.

Figures 10 and 11 present the photograph and reconstructed slice of the NTSR test object for the NTSR-MINUS and NTSR-PLUS condition respectively. The SANR facility has a pixel size of 100 micron which is why the foils in the NTSR test object were accumulated to 100 micron. Presented in Figure 12 is the spatial resolution data from reconstructed slices of the NTSR-MINUS sample taken at the upper, central and lower regions of the according to the draft protocol. It can be seen that aluminum generally attenuates as much as the air does in this case. The reason for this is attributed to the scattering component of the steel contributing significantly to the transmission on the aluminum and air filled regions.

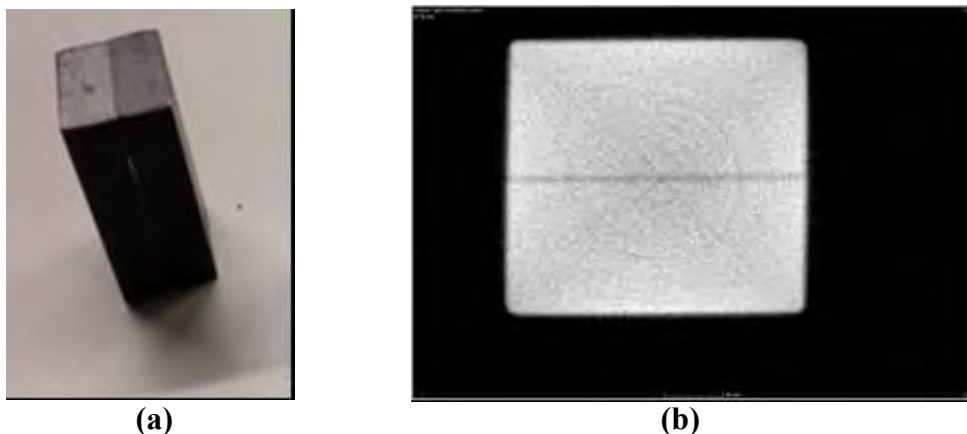


FIG. 10. (a) A picture of the NTSR-MINUS sample. (b) A thermal neutron reconstructed slice of the NTSR-MINUS sample.

## 2.6. Efforts towards standardization of neutron imaging

Figure 13 presents spatial resolution data of the NTSR-PLUS sample and it can be noticed that the bottom and top slices has significantly less attenuation than the center slice because the Cu doesn't extend to the top and bottom parts sampled.

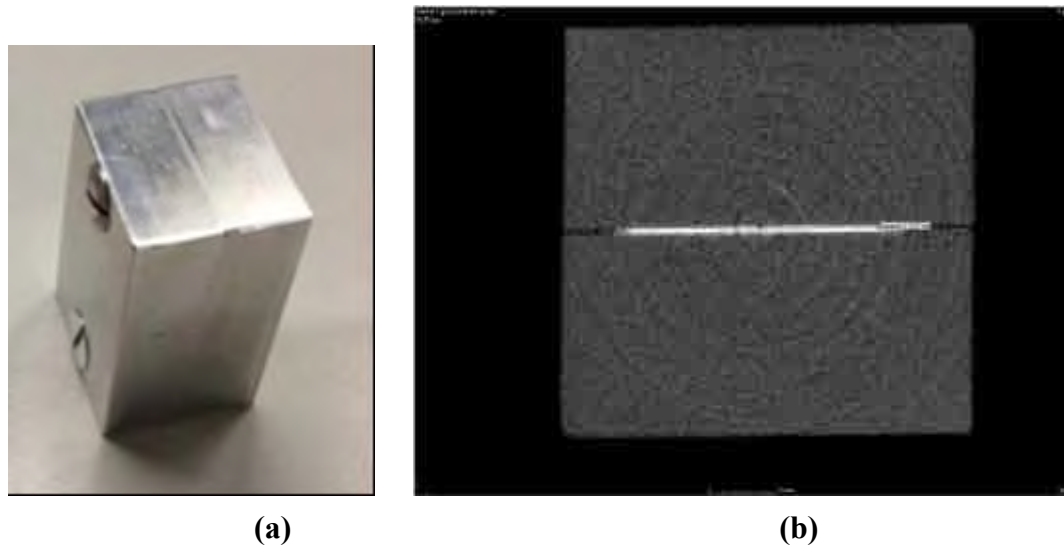


FIG. 11. (a) A picture of the NTSR-PLUS sample. (b) A thermal neutron reconstructed slice of the NTSR-PLUS sample.

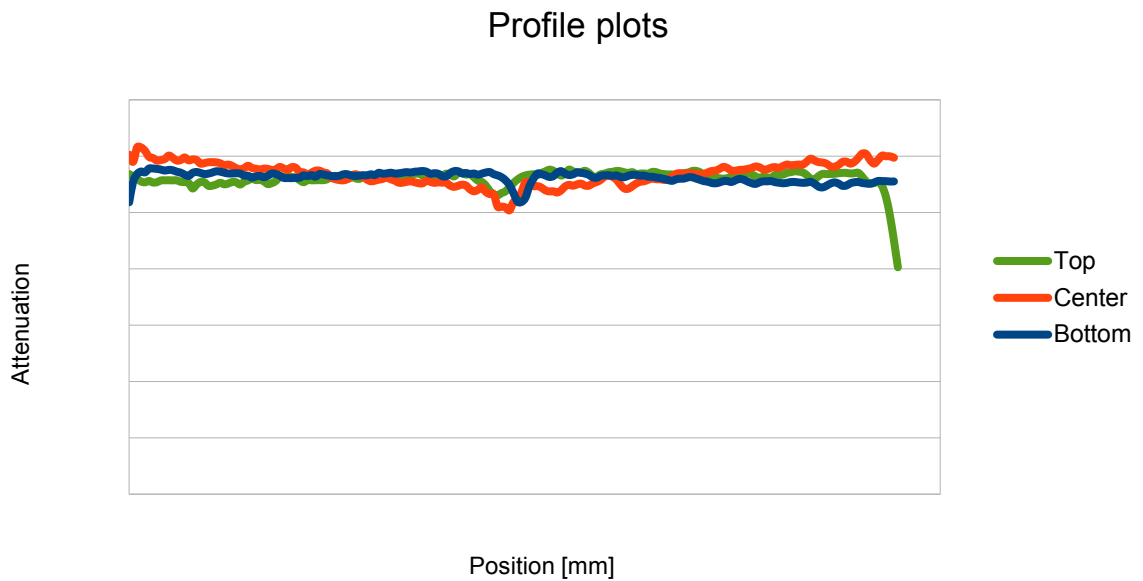


FIG. 12. Relative attenuation data (line profile of voxel values) for the NTSR-MINUS spatial resolution test sample (Al inclusion in Fe matrix).

## 2.6. Efforts towards standardization of neutron imaging

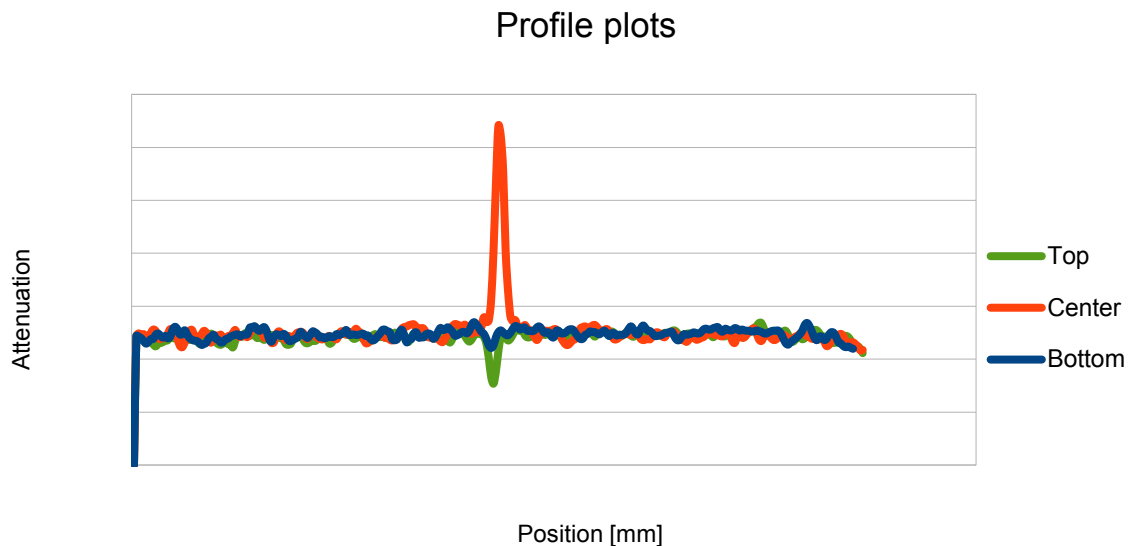


FIG. 13. Relative attenuation data (line profile of voxel values) for the NTSR-PLUS spatial resolution test sample (Cu inclusion in Al matrix).

### 4.2. Porous media quantification

Standardized experiments to test background scattering and sample scattering as a function of sample-detector distance (SDD) were designed and conducted. The QNI software package previously designed at PSI for the correction of neutron radiographs through inclusion of a scattering component to the digital data of each radiograph to achieve accurate quantitative measurements was also implemented.

Results of the thermal neutron attenuation of water samples before and after QNI correction at 20 mm, 50 mm and 80 mm SDD with the theoretical value of  $3.47 \text{ cm}^{-1}$  are compared in this section. The linearity of the calibration curves at difference SDD as well as with and without QNI was investigated.

#### 4.2.1. Water profiles

The data for the water profile was obtained from the line profile placed across the water visualised in the radiograph of the sample of 6.94 mm thickness in Figure 14. The profile data at 20 mm, 50 mm and 80 mm SDD are presented graphically as shown in Figures 15, 16 & 17 respectively. Figure 18 is the magnification of the overlapping region of the profiles at 80 mm SDD, showing the correction more clearly. The important feature of the plots is the flattening and dropping of the minima within the water region of the profile, showing the results of different corrections applied:

- a) No environmental and sample scattering correction
- b) No sample scattering correction (QNI- ENVIRON SCATTER & SPECTR. CORR.).
- c) Environmental and sample scattering correction (QNI- ENVIRON SCATTER, SPECTR. & SAMPLE SCATT. CORR.).

Generally, Figures 15, 16 & 17 show that minima differences before and after material scatter correction, decrease with the increase in SDD. Figure 18 shows a very little difference

## 2.6. Efforts towards standardization of neutron imaging

in minima before and after material scatter correction indicating negligible water scattering effect at a distance of 80 mm SDD.

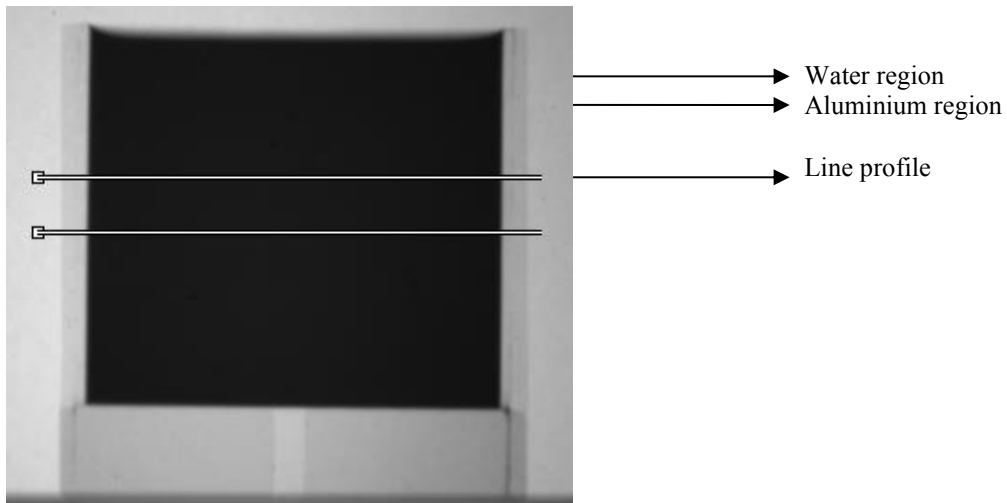


FIG. 14. Demonstration of the placement and extent of the line profile through 6.94 mm water contained aluminium holder.

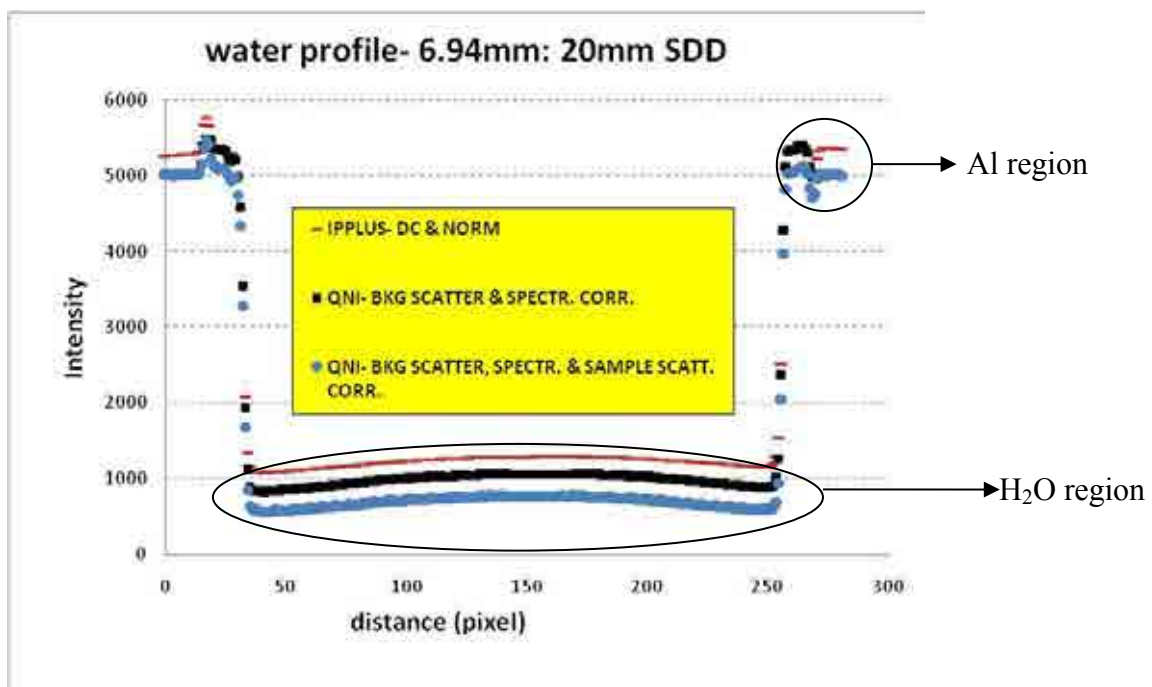


FIG. 15. Water profile curve of a 6.94 mm thick water sample at 20 mm after different QNI correction stages.

## 2.6. Efforts towards standardization of neutron imaging

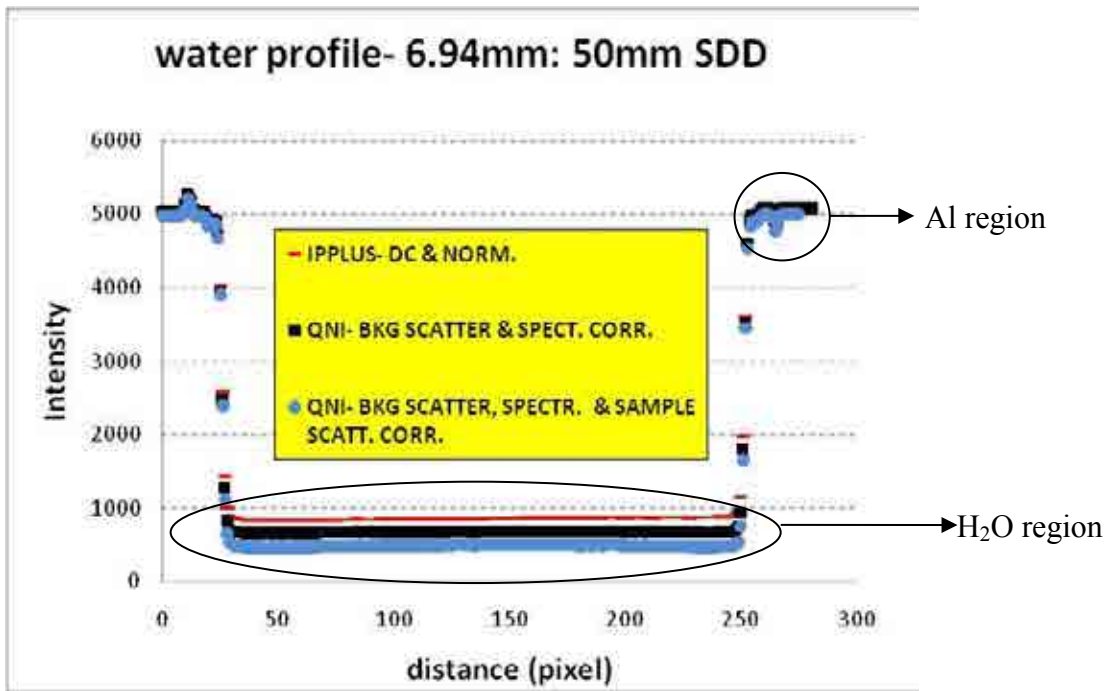


FIG. 16. Water profile curve of a 6.94 mm thick water sample at 50 mm before and after different QNI correction stages.

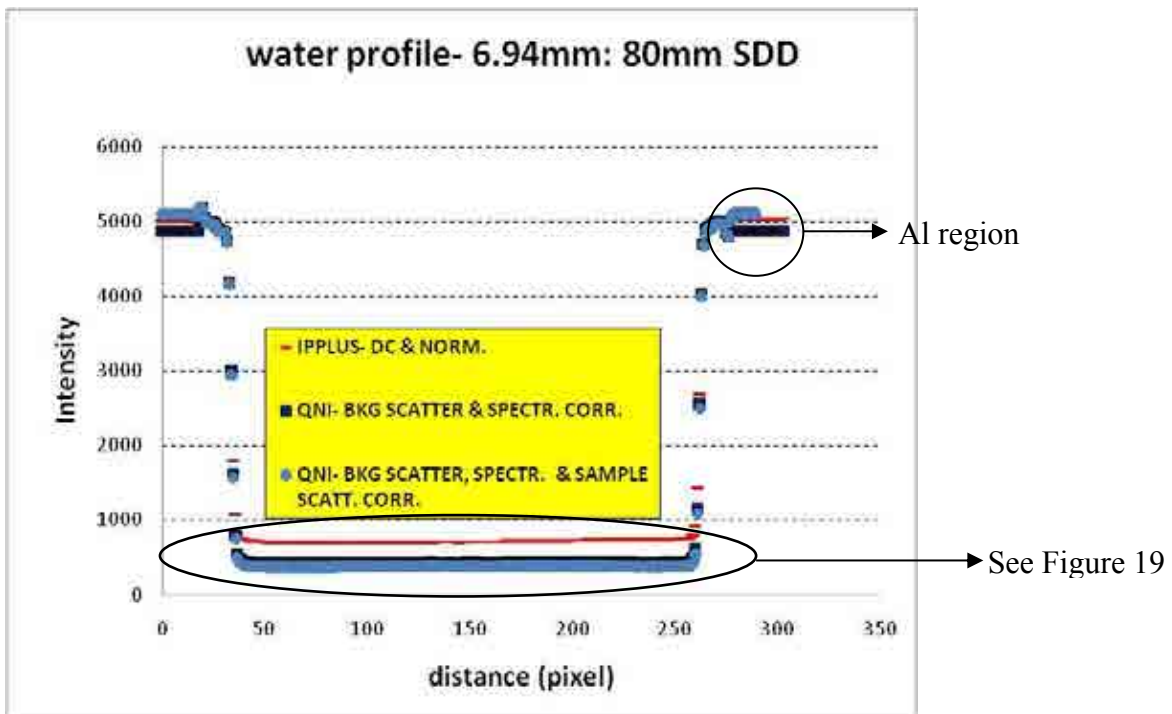


FIG. 17. Water profile curve of a 6.94 mm thick water sample at 80 mm before and after different QNI correction stages.

## 2.6. Efforts towards standardization of neutron imaging

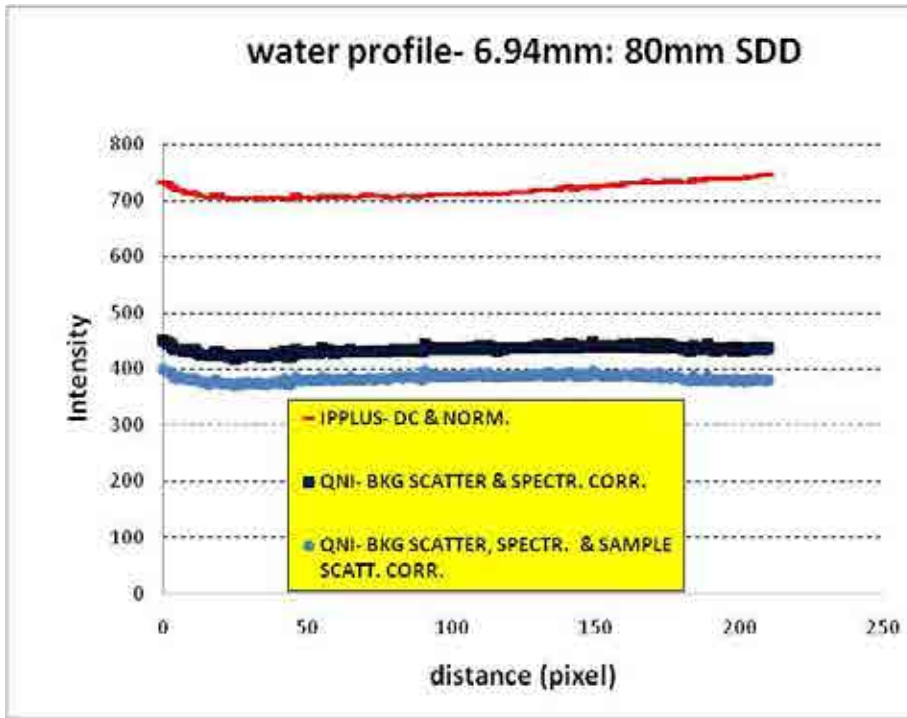


FIG. 18. Water profile curve of a 6.94 mm thick water sample at 80 mm SDD before and after different QNI correction stages- paying special interest on overlapping region.

### 4.2.2. Water thickness calibration

Results of all water thicknesses at SDDs 20 mm, 50 mm and 80 mm are presented, as water calibration curves, on Figures 19, 20 and 21 respectively. The important feature of these results is that, before QNI correction, the data adopts a polynomial fit (IPPLUS-DC & NORM) and after QNI correction a linear fit. This linear fit is very important because the gradient of this fit determines the attenuation coefficient of water which, according to theoretical evaluation there-of, should be the constant,  $3.47 \text{ cm}^{-1}$ .

From Eq (1):

$$\ln\left(\frac{I_0}{I}\right) = \sigma \cdot d \quad (1)$$

which corresponds with the general equation of the linear function Eq (2):

$$y = m \cdot x \quad (2)$$

where  $m$  is the gradient and hence is  $\sigma$

Each figure presents data set at a certain SDD from radiographs before and after different QNI correction procedures. The QNI corrections conducted are for environmental scattering, spectral effects and material scatter.

Results show that plots become more linear and approach the theoretical value as more QNI correction attributes are addressed.

## 2.6. Efforts towards standardization of neutron imaging

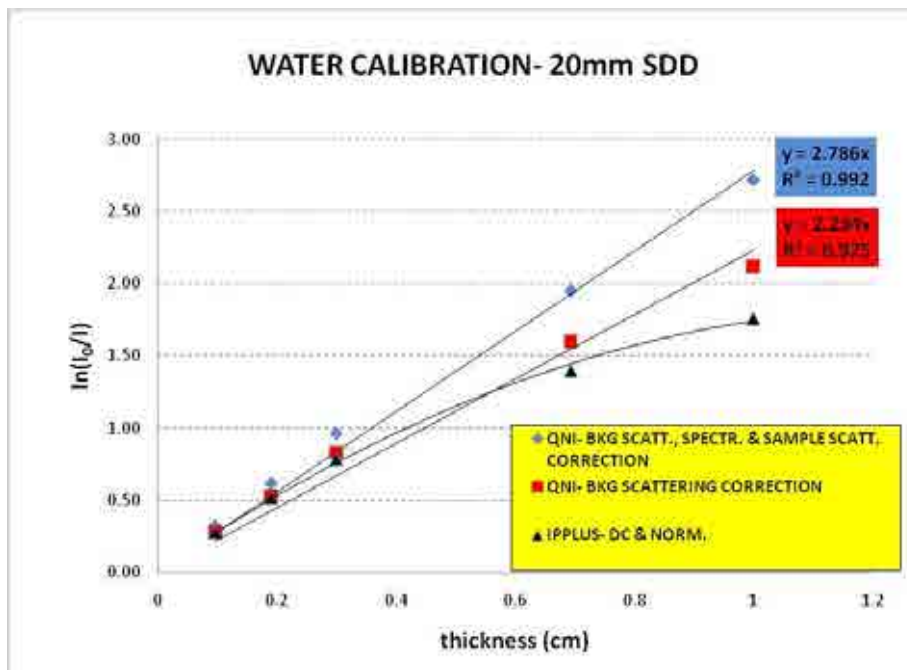


FIG. 19. Water thickness calibration curve after different QNI correction stages at 20 mm SDD.

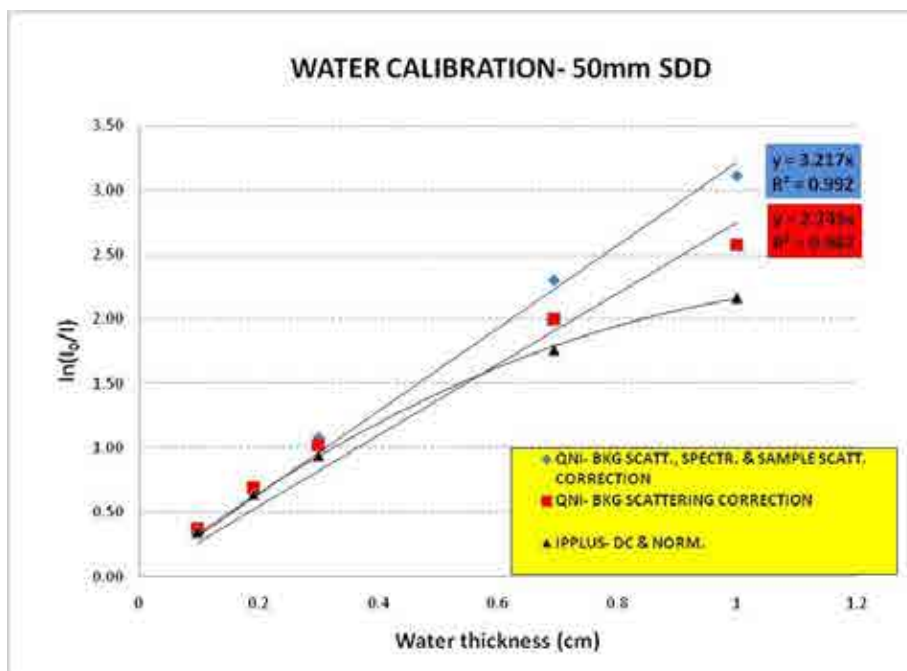


FIG. 20. Water thickness calibration curve after different QNI correction stages at 50 mm SDD.

## 2.6. Efforts towards standardization of neutron imaging

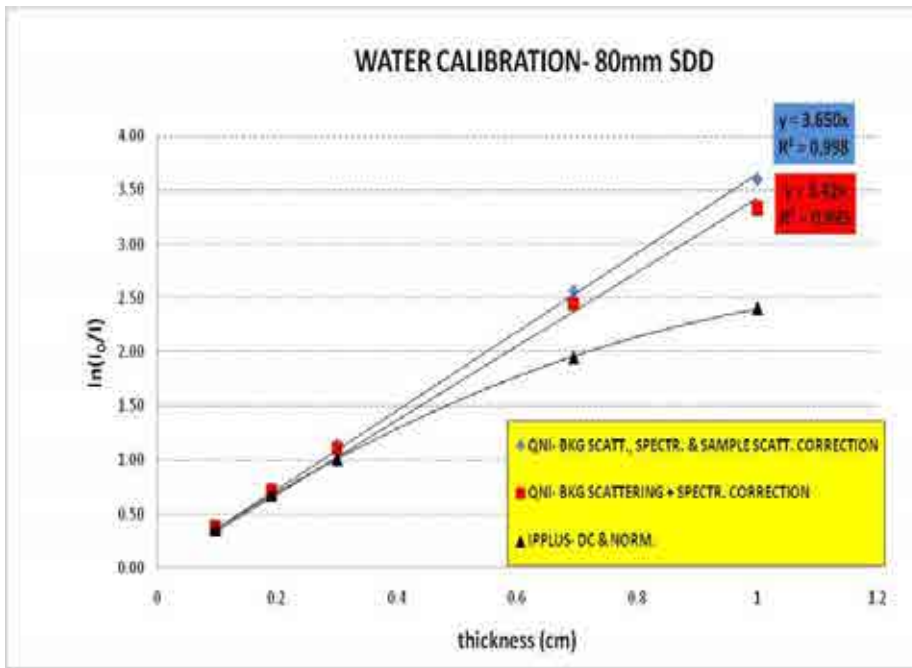


FIG. 21. Water thickness calibration curve after different QNI correction stages at 80 mm SDD.

It is noticed from Table 1 that the deviation of the water experimental linear attenuation coefficient from the theoretical value decreases with increase in SDD. Deviation from the theoretical value also decreases as more QNI correction attributes are corrected for, with the exception of 80 mm SDD where it increases with more QNI correction attributes.

TABLE 1. COMPARISON OF EXPERIMENTAL OBTAINED WATER THERMAL NEUTRON LINEAR ATTENUATION COEFFICIENT AND THE THEORETICAL VALUE FOR 20 MM, 50 MM & 80 MM SDDS

WATER: THERMAL NEUTRON LINEAR ATTENUATION COEFFICIENT (CM <sup>-1</sup> )					
SDD (mm)	THEORETICAL Value (cm <sup>-1</sup> )	QNI CORRECTIONS			
		Background scattering & spectral		Background scattering & spectral & sample scattering	
		Value (cm <sup>-1</sup> )	%dev. from theoretical	Value (cm <sup>-1</sup> )	%dev. from theoretical
20	3.47	2.23	35.73%	2.79	19.60%
50		2.75	20.75%	3.22	7.20%
80		3.42	1.44%	3.65	-5.19%

After three QNI correction attributes have been corrected for at 20 mm and 50 mm SSD, the experimental attenuation coefficient is still less than the theoretical value.

At 80 mm SDD the experimental attenuation coefficient is less than the theoretical value after the environmental scatter and the spectral effects are corrected for. When sample scattering (only the high water scattering) are included, the experimental attenuation coefficient exceeds the theoretical value. This shows that at 80 mm SDD background scatter and the spectral effects correction attributes are sufficient for the correction of radiographs.

## 2.6. Efforts towards standardization of neutron imaging

### 4.2.3. Percentage Porosity

This section compares results of %porosity as measured by NR with gravimetric values. The effect of QNI corrections on the results is investigated:

Gravimetric porosity was calculated using Eq-3:

$$\%porosity_{grav.} = \left( \frac{weight_{sat} - weight_{dry}}{weight_{dry}} \right) \times 100 \quad (3)$$

This section presents the %porosity data obtained from different concrete, mortars and cement paste samples of cylindrical and rectangular shapes. The results are obtained using the QNI corrections as those performed for water calibration.

The effect obtained with the QNI corrections on the NR %porosity results is indicated in Table 2.

At this stage of the investigation, the aim of this section was to show that QNI correction for water scattering can be effective even in complex systems, not to compare %porosity values at different SDD values. This is because material scatter of concrete, mortars and cement paste samples has not been corrected for yet.

The results show a great decrease in the % deviation between gravimetric- and NR percentage porosity results after QNI correction compared to NR %porosity results before QNI correction. As expected, results at 80 mm SDD show the least percentage deviation between gravimetric and NR percentage porosity results before and after QNI correction compared to 20 mm and 80 mm SDD.

TABLE 2.COMPARISON OF GRAVIMETRIC AND NR POROSITY RESULTS BEFORE AND AFTER QNI CORRECTION AT 20 MM & 80 MM SDD

SAMPLE ID	GRAVIMETRIC Value (%)	%Porosity (%) NEUTRON RADIOGRAPHY					
		OLD APPROACH IPPLUS With correction		NEW APPROACH with QNI CORRECTIONS			
		Value (%)	%dev. from grav.	Background scattering & spectral Value (%)	%dev. from grav.	Background scattering & spectral & sample scattering Value (%)	%dev. fromgrav.
SDD= 20mm							
Concrete-cylindrical No.2	45.6 ± 0.01	34.2 ± 0.3	25.0%	39.5 ± 0.3	13.4%	47.7 ± 0.3	4.6%
Concrete-cubic No.2	57.9 ± 0.02	45.5 ± 0.4	21.4%	55.1 ± 0.4	4.8%	58.8 ± 0.4	1.6%
SDD= 80mm							
Concrete-cylindrical No.2	34.3 ± 0.02	30.9 ± 0.2	9.8%	33.3 ± 0.3	2.7%	32.2 ± 0.2	6.1%
Concrete-cubic No.2	35.3 ± 0.02	32.2 ± 0.2	8.7%	35.4 ± 0.2	0.5%	33.8 ± 0.2	4.3%

### 4.3. Quantum noise

Figures 22 to 24 show the modegray values and average gray values of 20 images with 2 seconds exposure time obtained from 200 000, 1 000 000 and 2 000 000 pixel areas respectively. The important feature of these figures is how the mode captures the random

## 2.6. Efforts towards standardization of neutron imaging

character of the quantum noise without the effect of thermal or dead pixels or gamma rays noise. It is noticed that the average values increase towards the average of the mode gray values. This could be due to the thermal noise which increases with the period of use of the camera (number of images acquired). The averages and standard deviation for data in Figures 22 to 24 is shown in Figure 25.

The mode gray values for each of the five exposure times of 20 images each were then averaged and standard deviation calculated to give results of the relative fluctuation of the mode gray value for 20 images, this was done for three pixel areas (Figs 26 to 28). These relative fluctuation values are compared to theoretical values ( $\sqrt{\text{average of the modes}}$ ) obtained by dividing the square root of each average by its average (Poisson's law). Figure 29 presents averages and standard deviation for data in Figures 26 to 28. The important feature of these results is that the measured relative fluctuation increases with exposure time instead of the expected decreasing behaviour. It is noticed that the measured values begin to be more in agreement with the theoretical values with the increase of the quantum population.

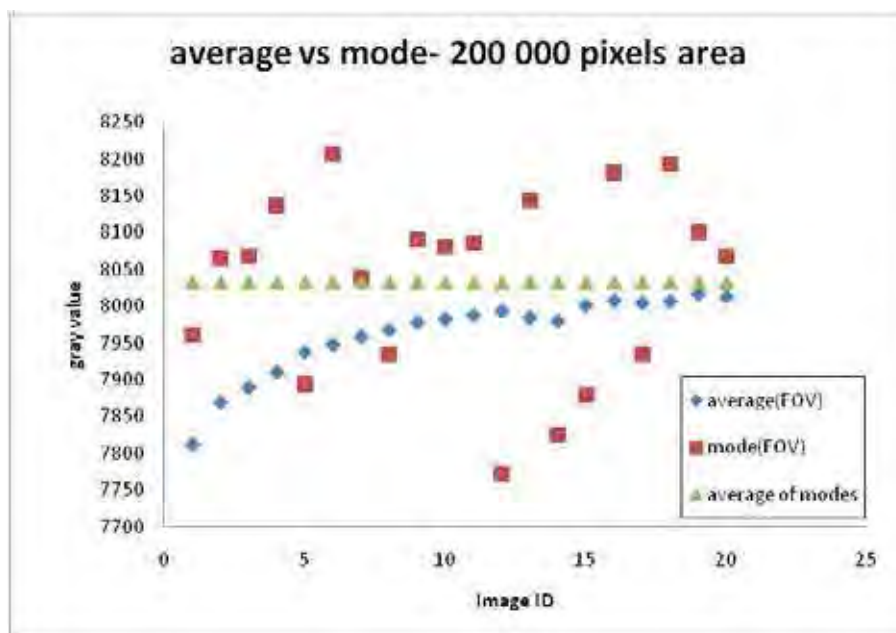


FIG. 22. Mode gray values and average gray values of 20 images with 2 seconds exposure time obtained from a 200 000 pixel area.

## 2.6. Efforts towards standardization of neutron imaging

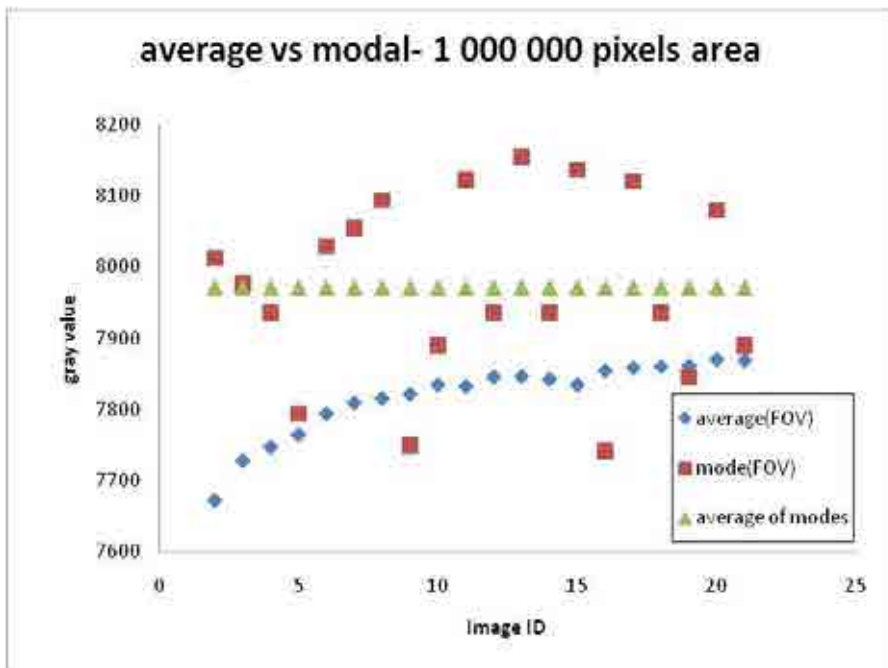


FIG. 23. Mode gray values and average gray values of 20 images with 2 seconds exposure time obtained from a 1 000 000 pixel area.

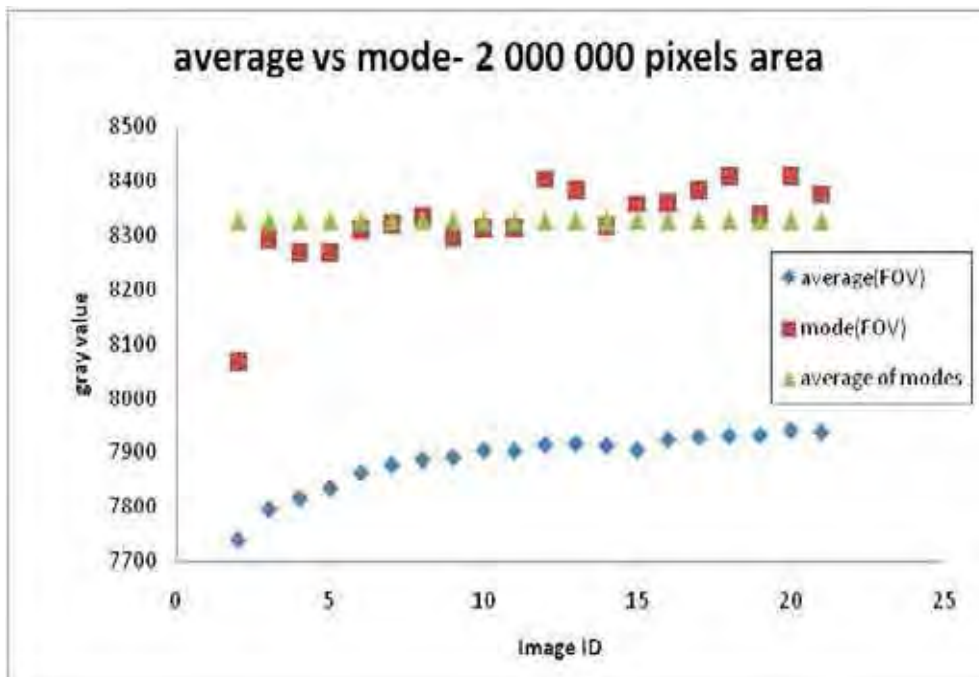


FIG. 24. Mode gray values and average gray values of 20 images with 2 seconds exposure time obtained from a 2 000 000 pixel area.

## 2.6. Efforts towards standardization of neutron imaging

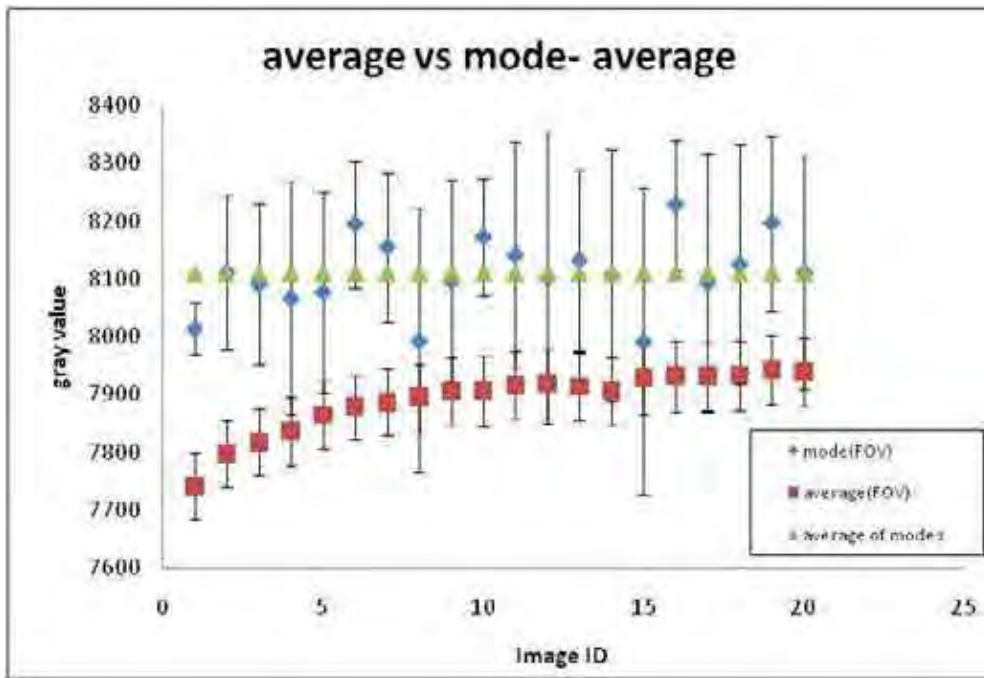


FIG. 25. Averages and standard deviation from mode gray values and average gray values of 20 images with 2 seconds exposure time sampled at three FOV pixel areas (200 000, 1 000 000 and 2 000 000 pixel area).

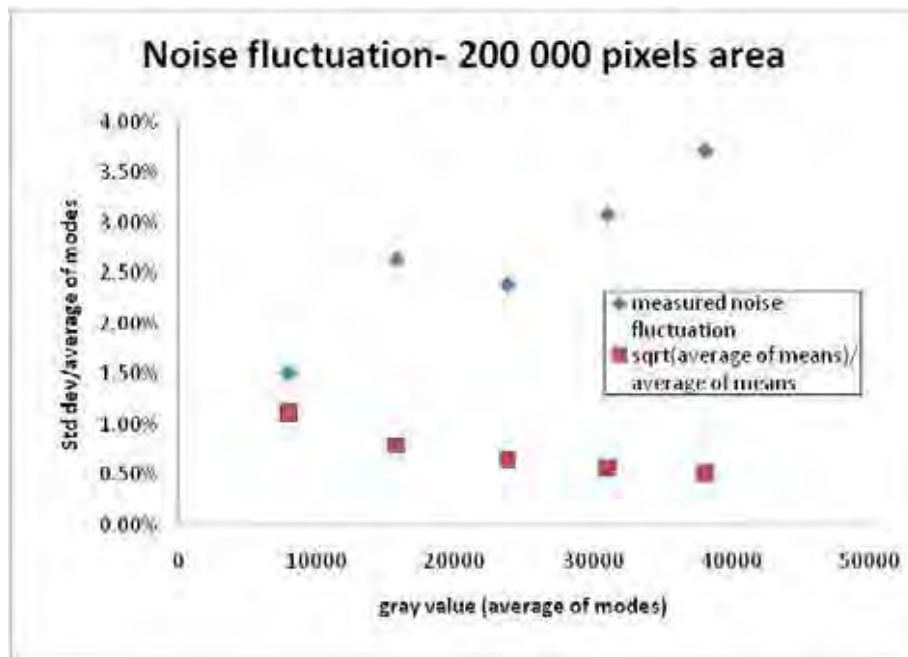


FIG. 26. Relative standard deviation (standard deviation/ mode gray value) from mode gray values of the five exposure (2 s, 4 s, 6 s, 8 s and 10 s) times of 20 images each obtained from a 200 000 pixel area. Relative fluctuation values are compared to theoretical values ( $\sqrt{\text{average of the modes}}$ ) obtained by dividing the square root of each average by its average.

## 2.6. Efforts towards standardization of neutron imaging

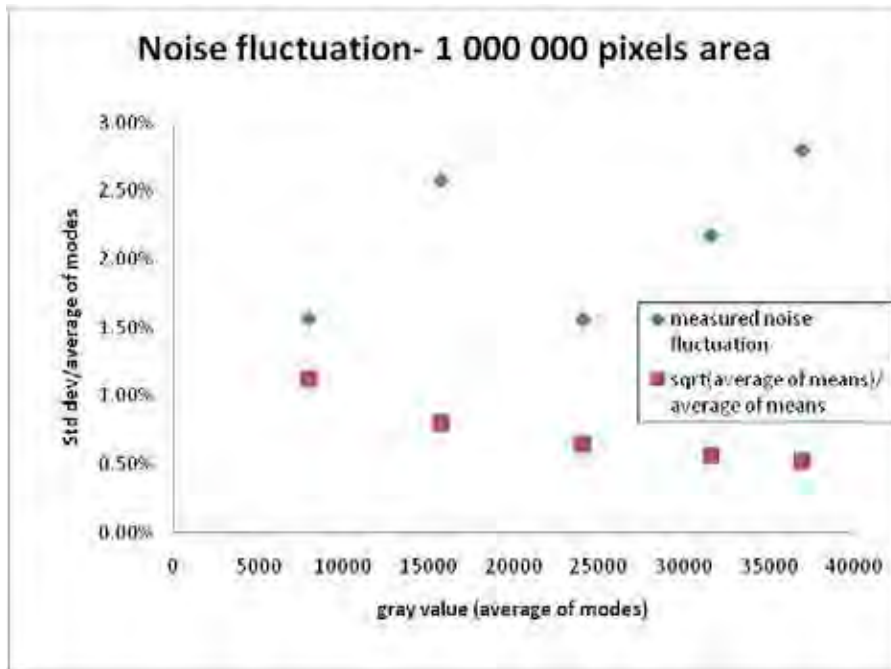


FIG. 27. Relative standard deviation (standard deviation/ mode gray value) from mode gray values of the five exposure times (2 s, 4 s, 6 s, 8 s and 10 s) of 20 images each obtained from a 1 000 000 pixel area. Relative fluctuation values are compared to theoretical values (sqrt[average of the modes]) obtained by dividing the square root of each average by it's average.

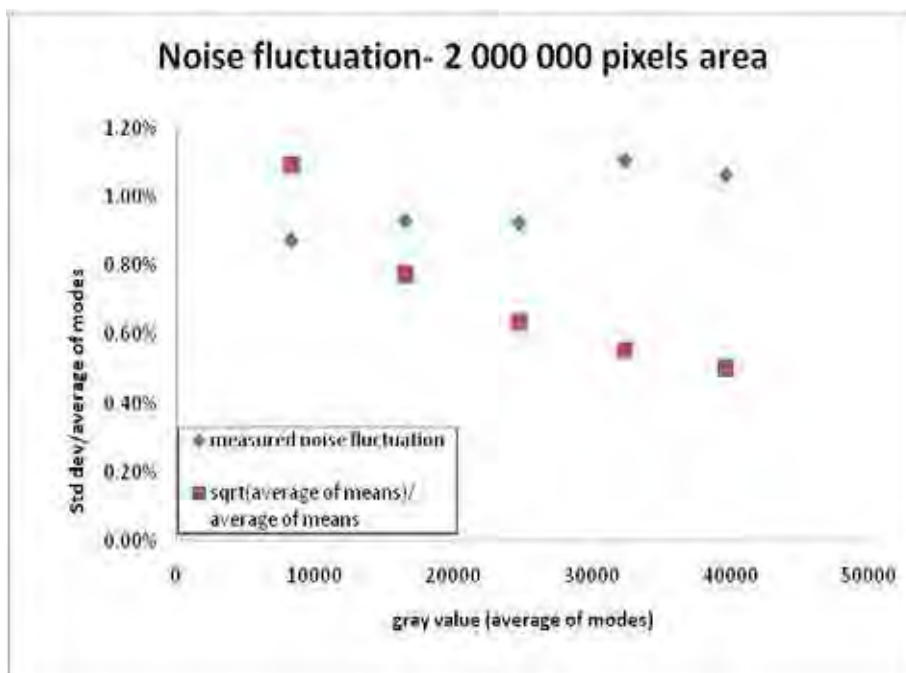


FIG. 28. Relative standard deviation (standard deviation/ mode gray value) from mode gray values of the five exposure times (2 s, 4 s, 6 s, 8 s and 10 s) of 20 images each obtained from a 2 000 000 pixel area. Relative fluctuation values are compared to theoretical values (sqrt[average of the modes]) obtained by dividing the square root of each average by it's average.

## 2.6. Efforts towards standardization of neutron imaging

## 7. CONCLUSIONS

Initial experiments in line with standardization for characterization of digital neutron imaging setups have been conducted. A few important parameters of NR –setups were investigated and with the aid of developed phantoms and procedures, quantified. This is the start of a development process for the characterization of NR facilities and the standardization of procedures for the 1-1 comparison of their performance.

The NTC test object proves to be sufficient for the characterization of contrast with the addition of standardized evaluation procedures for effective differentiation of materials which have approximate similar neutron attenuation properties. This will allow NR facilities, in the implementation of these procedures, to be more versatile in the evaluation of objects where similar kinds of materials are present within the object and quantified results are needed.

The NTSR test objects do not provide results without ambiguity new test objects are required. Recently suggested test objects are undergoing Matlab simulations to test their suitability.

Because of the relevance of porous media in the nuclear field of storage capabilities of nuclear waste, a draft procedure for good practice, to become a standard, with regard to quantification of porous media and application of the QNI software package has been established at Necsa. Further work is required to assess the effectiveness of the procedure and for establishment of the final procedure. Initial work shows potential for the procedure to provide results comparable to gravimetric data. Effectively, the quantification of the physical parameters of porous media such as porosity, which is frequently reported in open literature, can only be taken as true values when the results obtained was through following the standardized procedure according to the new proposed standard. It is recommended that repeatability tests, to streamline this standard procedure, should be conducted at a number of NR facilities.

The quantum noise affects the contrast lower boundary sensitivity by contribution of average base noise such that the dynamic range cannot be improved beyond this noise component. It also negatively affect contrast between materials of an object and spatial resolution by adding false fine defects which can be removed by averaging electronic filters and thereby also removing the fine features of the object under investigation. A simplified empirical method for measurement of quantum noise provides results which in agreement theoretically predicted absolute value of quantum noise. However theoretical predictions using Poisson's law have a negative slope while measurements show a positive slope. These are only preliminary results of a more detailed study, which in later stage will also be extended to neutron tomography.

## 2.6. Efforts towards standardization of neutron imaging

### REFERENCES

- [1] CONDON E. U. Basic Standards in Science. National Bureau of Standards.
- [2] BANHART J. Advance Tomographic Methods in Materials Research and Engineering. Oxford University press Inc., New York (2008).
- [3] N. KARDJILOV, F.C. DE BEER, R. HASSANEIN, E. LEHMANN, P. VONTOBEL, Nucl. Instr. and Meth. A **542** (2005) 336.
- [4] R. HASSANEIN, F.C. DE BEER, N. KARDJILOV, E. LEHMANN, Physica B **385–386** (2006) 1194.
- [5] RADEBE, M. J., Correction of neutron radiographs for quantitative application: Quantitative Neutron Imaging (QNI) software implementation at Necsca, Necsca internal document, RT-TVG-09/04, South Africa (2011) 1 – 34.
- [6] KAESTNER et al. (2011), The ICON beamline – A facility for cold neutron imaging at SINQ, NIMA, **659**(1), 387-393, doi: 10.1016/j.nima.2011.08.022.
- [7] DE BEER, F. C. Characterization of the neutron/X-ray tomography system at the SANR facility in South Africa. Nucl. Instr. Meth. Phys. A **542** (2005) 1-8.
- [8] KAESTNER A. P., LEHMANN E.H., Quality assessment for neutron CT, draft standard protocol (2012).
- [9] MILLER F. P., VANDOME A. F., MCBREWSTER J. Nyquistdash-Shannon Sampling Theorem. VDM Verlag, Dr. Mueller e.K (2010).

## 2.6. Efforts towards standardization of neutron imaging

### Appendix I

#### NECSA COMPILED PROTOCOL

##### 1. SCANNING PARAMETERS FOR NTC AND NTSR STANDARDS

Scanning protocol for neutron facilities is divided into flexible and fixed components. This is due to that not all parameters can be fixed as these facilities are constantly under development and hence unique - allowing freedom of customizing for best performance.

Flexible parameters:

Utilization of:

- A neutron beam.
- The highest available L/D ratio.
- Smallest Field-of-View (FOV) on the scintillator screen for the standard to fit e.g. 5cm × 5cm.

Detect:

- or with highest number of pixels array which will be used for nondestructive testing of the component: e.g. 20482 × 2048 pixels.
- Thinnest <sup>6</sup>LiF/ZnS scintillator for optimum spatial resolution performance and a <sup>6</sup>LiF/ZnS scintillator with high neutron efficiency for optimum contrast.

Fixed parameters:

- Number of projections:  $\pi \times \# \text{pixels}$  in 360 degrees, according to Nyquist-Shannon sampling theorem. #pixels are defined by the number of pixels that constitutes the widest horizontal dimension of the object to be imaged.
- Dynamic range: 70% or more of valid capacity (results in acquisition time and neutron flux).
- Sample-detector distance: 2cm from edge of sample to detector.
- Number of “Dark Current” (dc) radiographs: 15
- Number of Open beam (fl) radiographs: 15
- Sample position is recommended to be in centre of beam and rotation stage.

##### 2. RECONSTRUCTION PARAMETERS

The spatial resolution- and contrast needs for the reconstruction protocol for both the NTC and NTSR standards are different and are treated separately. This procedure describes application of the software package “Octopus” for reconstruction of cross-sectional slices from projections [4].

##### 3. NTC STANDARD

###### 3.1. Reconstruction of cross-sectional slices from projections.

*Image processing module*

- Enable automatic mode of spot filtering by inserting a -1 input.
- Normalize for beam fluctuation by selecting an AOI which is more 10 pixels thick and more than 100 pixels long in the open beam area – not to overlap with the sample.
- Enable automatic mode of ring filtering by inserting a -1 value input.
- Check box to create sinograms.

*Reconstruction module*

## 2.6. Efforts towards standardization of neutron imaging

### Scan geometry parameters

- Choose last angle to be 180°.
- Insert pixel size input:  $\text{Pixel size} = \frac{\text{FOV\_dimension (mm)}}{\text{No. of pixels}}$ .
- Right click on the rotation axis input space and click on “evaluate” under evaluation of parameters. Octopus will provide good results and select the best rotation axis automatically. Confirm if the chosen value gives the best image and select it, then click OK.

### Quality parameters

- First choose the regular Fourier Filter and increase numerical input in the Noise Filter Percentage slot until the visualized noise, which mimics the shape of the sample (Figure A.1) around the sample’s cross-sectional image, is minimum or disappears. Fourier frequency filtering is used to get rid of quantum noise which is tricky to remove from the digital image data. This process requires transforming the intensity domain to frequency domain. The trick is to make and observe signal of the same frequency as the random noise incorporated in the image disappear to know that the noise is removed from the image signal.

*Fig. A.1. Demonstration of the visual effect of the Fourier filter on image noise. (a) Before and (b) after Fourier filtering.*

- Uncheck the “**Apply Scaling Factor**” box to maintain sinograms scale from projections processing.
- Check the “**Apply Logarithm**” box to have the output numerical data on reconstructed image as integrated attenuation coefficient instead of transmission values.
- Choose no beam hardening correction under BHC method.
- Uncheck the “**Vertical Smoothing**” box.

### Output parameters.

- Choose after reconstruction option under scaling mode. The output type should be 16 bit, minimum gray value = 0 and maximum gray value= the largest value in the image (just drag the upper limit line to the end).
- Crop the reconstructed data as desired as long as the entire NTC standard image is complete.

## 4. NTRS STANDARD

### 4.1. Reconstruction of cross-sectionalslices from projections.

#### *Image processing module*

- Enable NO filtering.
- Normalize for beam fluctuation by selecting an AOI which is more 10 pixels thick and more than 100 pixels long. Octopus recommends a 10 pixels thick AOI.
- Enable automatic mode of ring filtering by inserting a -1 value input.
- Create sinograms.

#### *Reconstruction module*

##### Scan geometry parameters

- Choose last angle to be 180°.

## 2.6. Efforts towards standardization of neutron imaging

- Insert pixel size input:  $\text{Pixel size} = \frac{\text{FOV\_dimension}}{\text{No. of pixels}}$ .
- Right click on the rotation axis input space and click on evaluate under evaluation of parameters. Octopus will provide good results and select the best automatically. Confirm if the chosen value gives the best image and select it, then click OK.

### Quality parameters

- First choose the regular Fourier filter and keep the percentage at zero for a spatially sharp image.
- Uncheck the “**Apply Scaling Factor**” box to maintain sinograms scale from image processing.
- Check the “**Apply Logarithm**” box to have the output numerical data on reconstructed image as integrated attenuation coefficient instead of transmission values.
- Choose no beam hardening correction under BHC method.
- Uncheck the “**Vertical Smoothing**” box.

### Output parameters

- Choose after reconstruction option under scaling mode. The output type should be 16bit, minimum gray value= 0 and maximum gray value= the largest value in the image (just drag the upper limit line to the end).
- Crop the reconstructed data as desired as long as the entire NTRS standard image is complete.

## 2.6. Efforts towards standardization of neutron imaging

### NEUTRON TOMOGRAPHY STANDARDIZATION USING NTR AND NTC PHANTOM FOR INDUSTRY APPLICATION

C.M. SIM\*, HS.OH\*, T.J. KIM\*, M.RADEBE\*\*, A.P KAESTNER\*\*\*, E.H, LECHMANN\*\*\*

\*Korea Atomic Energy Research Institute, Daedeok-daero 989-111, Yuseong-gu, 305-353, South Korea

\*\*Necsa, Box 582, Pretoria, 0001, South Africa

\*\*\*Paul Scherer Institute (PSI), Villigen, Aargau, Switzerland

Email: [cmsim@kaeri.re.kr](mailto:cmsim@kaeri.re.kr)

#### Abstract.

The result of the activities on the CRP project titled: Standardization of neutron tomography imaging concept protocol and working procedures has been reported. The activities consist of individual project which was proposed at the beginning of the project and collaborative works which is jointly carried out with the other members of the CRP. The individual project which is mainly focused on the initiation of the standardization of the neutron tomography has been successfully completed. The collaborative works which are mainly targeted to perform Round Robin exercise using NTC-tomo contrast standard sample (KAERI) and NTR-tomo spatial resolution standard samples (ASTM, KAERI, and PSI) for building up tomography standardization have been carried out successfully. However, the measurement of Gd distribution in Al and the evaluation of hydride content in Zr alloy was not successfully achieved since the proper standard sample is not available and this is still needed for the future plan. The standardization of neutron tomography/neutron digital radiography would be indispensable for industry application expansion such as turbine blade, irradiated fuel, fossil, plant in soil, hydrogen fuel cell, and Li ion Battery. The initiation of the standardization of neutron tomography/neutron digital radiography has been successfully ignited since the CRP-1575.

## 1. INTRODUCTION

The research agreement between IAEA and KAERI was made with reference No. 15969 of the title: Application of neutron tomography for the measurement of Gd distribution in Al and evaluation of hydride content in Zr alloy. The agreement period is from 2009-12-16 until 2013-05-18. During the 2nd RCM meeting, the workscope of the individual projects and collaborative projects was re-coordinated since the proper standard sample for the measurement of Gd distribution in Al and the evaluation of hydride content in Zr alloy is not available.

The individual projects are mainly focused on the standardization of performance of neutron imaging of the individual projects are as follows:

- Standardization of neutron digital imaging (radiography/tomography) for turbine blade, irradiated fuel, fossil, plant in soil, hydrogen fuel cell, and Li-ion Battery

The collaborative efforts and results achieved consists of

- Standardization of neutron tomography using standard sample from ASTM-SI/KAERI-NTC, NTR/PSI-NTC, NTR.

## 2. NEUTRON RADIOGRAPHY/TOMOGRAPHY

### 2.1. Individual progress

Neutron tomography has been developed at the HANARO reactor [1], KAERI. The configuration of the instrument is illustrated in Fig.1 and the actual neutron radiography facility where the tomography was setup is shown in Fig. 2. Three CCD cameras (2048x 2048, 1340 x 1300), CMOS camera (100,000 fps) the system were equipped with camera controller, sample table (3 axis), auto sample changer, Li<sup>6</sup>-ZnS scintillator screen (200 μm-50 μm),

## 2.6. Efforts towards standardization of neutron imaging

Gd<sub>2</sub>O<sub>2</sub>S:Tb (20 μm) and first reflective Al+SiO<sub>2</sub>+TiO<sub>2</sub> coated mirror. The component is enclosed within a dark box lined with and B<sub>4</sub>C rubber acting as light tightening and neutron shielding.

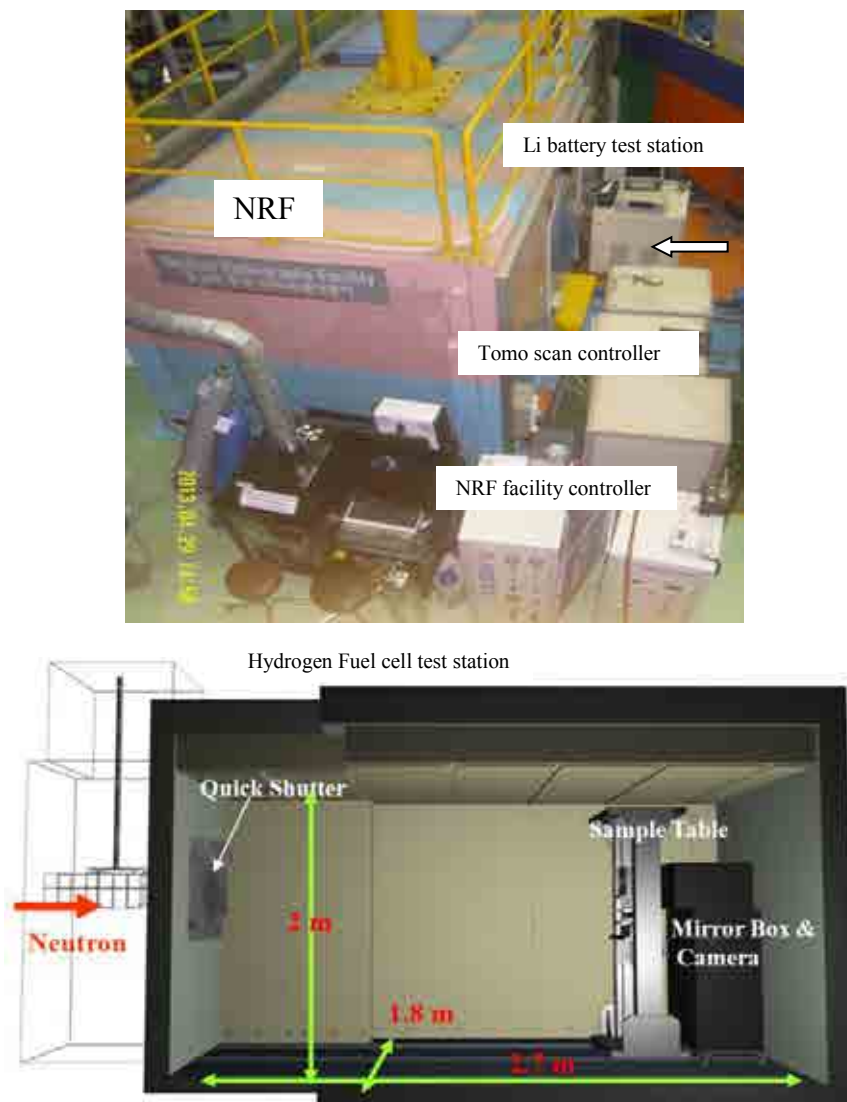


FIG. 1. Neutron radiography facility at HANARO research reactor.

The measurements were conducted at the thermal neutron imaging facility of the HANARO reactor. This facility has a mean energy of  $14 \pm 0.2$  meV, beam size of 35 cm x 45 cm, and intensity of  $5 \times 10^7$  n·cm<sup>-2</sup>·s<sup>-1</sup>, and L/D of 270. The detection tomography system is based on CCD camera of VersArray-1300FB and Andor Ikon with lens (85 mm, 135 mm and 200 mm) and uses a <sup>6</sup>Li and Gd based scintillator with a thickness of 150 μm (by 2009) and 50 μm (2010-Present) of PSI to convert neutrons to visible light with a wavelength of 440 nm.

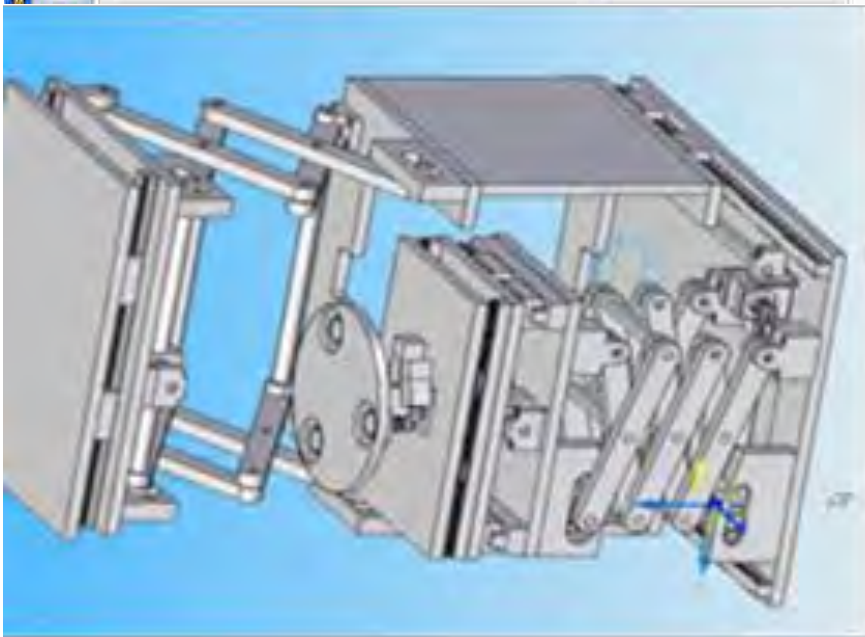
The field of view is 250 mm × 250 mm and the resulting images are 1340 × 1300 pixels. These parameters yield a pixel spacing (i.e., x-spacing and y-spacing) of 0.16 mm, a limitation related to spatial resolution. The tomographic volume was reconstructed using filtered back-projection algorithm using software tool Octopus version 8.0 and visualized by 3-D volume rendering software, VG Studio Max version 2.0.

## 2.6. Efforts towards standardization of neutron imaging

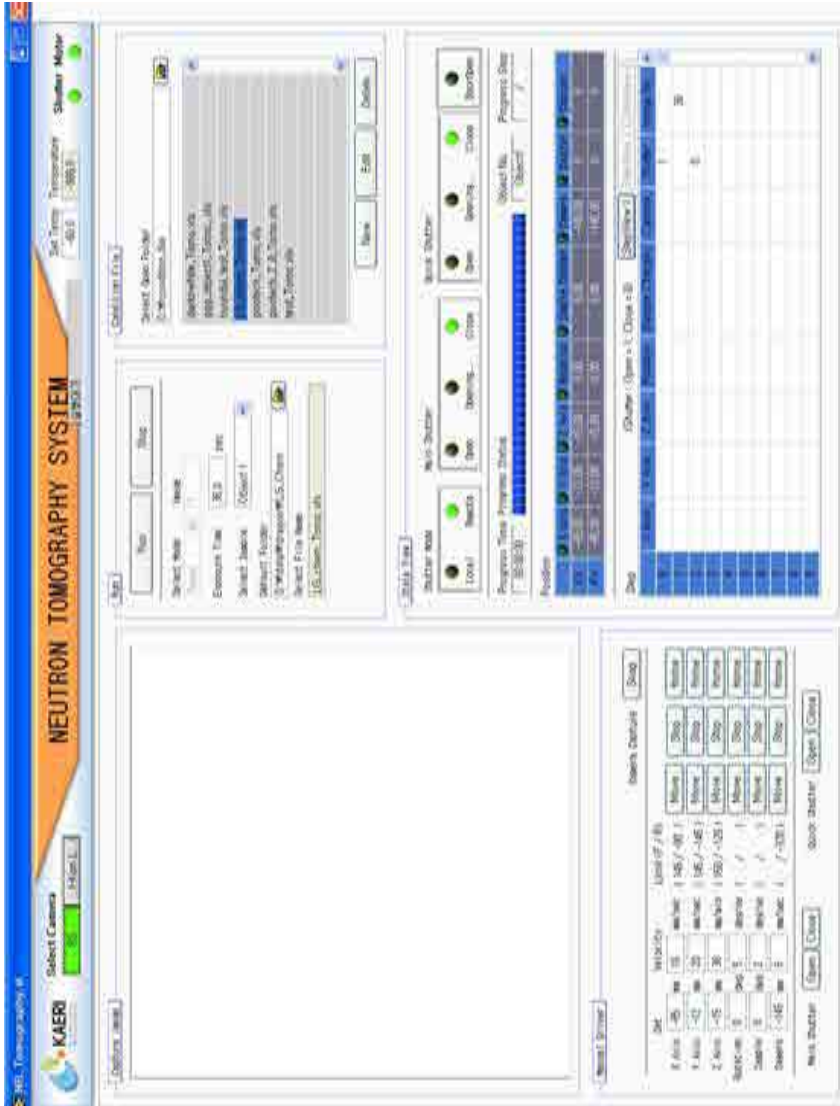
The data for tomography is obtained by rotating the object in small angular steps from 0-180° or 360° with an increment of 0.1°. The rotating table unit itself is mounted onto a 3-axis motion table used to position the sample precisely with regard to the CCD camera's field of view. The parameter of rotation angle, sample position, sample number, camera position, and exposure time are controlled by tomo-scan program of Lab View.

This report of Fig. 3 provides preliminary insight to the benefit and effectiveness of neutron radiography in identifying structural flaws that are otherwise undetected using other methods. The study was conducted at the neutron radiography facilities with an evaluation of turbine blades, a brazing joint of an engine after-burner, and a micro crack-calibration block. Shot balls exited internally on turbine blade (F100-700) are obvious on neutron image of SR-45 film. These parts were selected to undergo neutron radiography and tomography with Gd tagging [2]. As shown in Fig. 4, a transfer method of neutron radiography was developed to measure the size of the end plug and a gap of an intact K102L-2, the irradiated fuel of a ballooned K174L-3, a ballooned and ruptured K98L-3. A typical irradiation time of 25 min. was determined to obtain a film density of between 2 and 3 of SR X ray film with neutrons of  $1.5 \times 10^{11} \text{ n}\cdot\text{cm}^{-2}$ . To validate and calibrate the results, a RISO fuel standard sample, Cd plate and ASTM-BPI/SI were used. An activated latent image formed in the 100  $\mu\text{m}$  Dy foil was subsequently transferred in a dark room for more than 8 hours to the SR film which is a maximum of three half-lives. Due to the L/D ratio an unsharpness of 9.82-14  $\mu\text{m}$  and a magnification of 1.0003 were given. After digitizing an image of SR film, the ballooning gap of the plug was discernible by an H/V filter of image processing. The gap size of the ballooned element, K174L-3, is equal to or greater than 1.2 mm. The development of a transfer method played a pivotal role in developing high burn-up of nuclear fuel type [3].

As shown in Fig. 5, neutron tomography characterization, a new technology that can yield images with high contrast resulting from neutron interactions significantly with light materials like hydrogenous compounds, reveals a fully developed embryo that is fossilized within a thin (7.6 mm ~ 8.6 mm) calcite layer. Our combined skeletal and oological observations by neutron imaging suggest that this new embryo was a moderately robust basal titanosaur that retained several primitive features similar to *Erketu ellisoni*, a Somphospondyli from the Lower Cretaceous of the eastern Gobi [4].



a



b

FIG. 2. The neutron tomography system at the HANARO research reactor: a: auto sample changer/table(3-axis) b: Tomo scan program (camera control, sample table control, and sample changer control).

## 2.6. Efforts towards standardization of neutron imaging

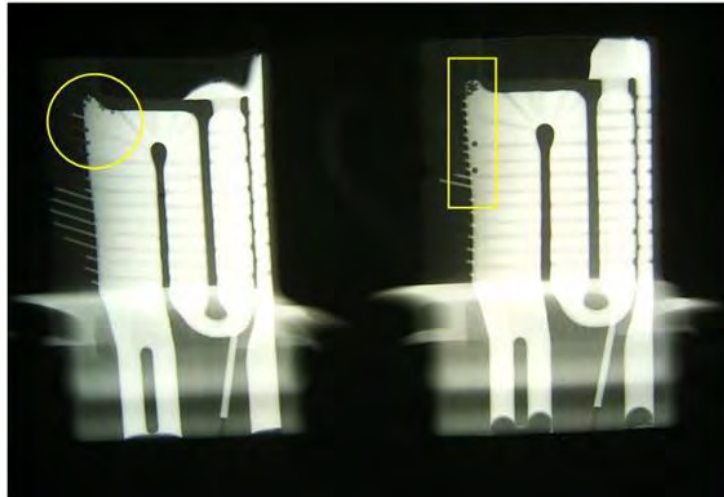


FIG. 3. Shot balls exited internally on turbine blade (F100-700) are obvious on neutron image SR-45 film (yellow circle, yellow rectangular).

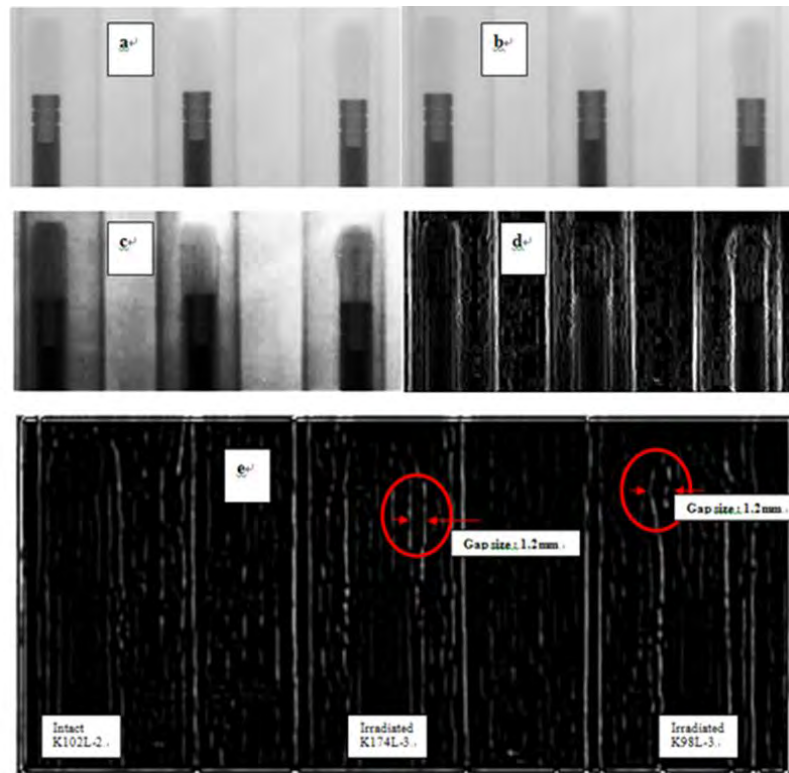
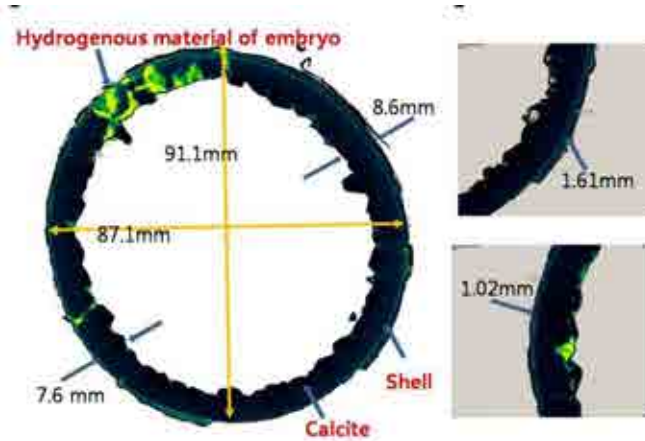


FIG. 4. a-e. a. ROI (Region of interest) image. b. Image removed image (Median filter/ edge observation). c. Enhancement image (Histogram equalization method). d. Sebel operator image (Use vertical filter-1). e: Laplacian gaussian image on K102L-2(left), K174L-3 (middle) and K98L (right).

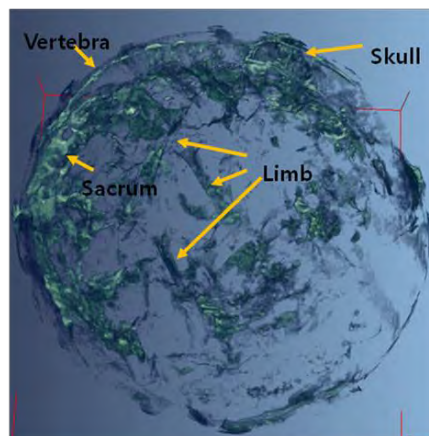
## 2.6. Efforts towards standardization of neutron imaging



(a)



(b)



(c)

*FIG. 5. (a) The egg has been diagenetically altered and partially filled with calcite crystals. The eggshell surface is not fractured implying little or no compression after being buried. (b) Neutron scan of X-Z axis, the relatively small spherical egg averages 87.07- 91.1 mm in diameter and the layer of calcite is preserved within a thin 7.6 mm ~ 8.6 mm. The egg shell thickness varies from 1.02- 1.61 mm. (c) Neutron scan imaging of the skull, sacrum, limbs and vertebra viewed by neutron tomography (-X-Z view).*

## 2.6. Efforts towards standardization of neutron imaging

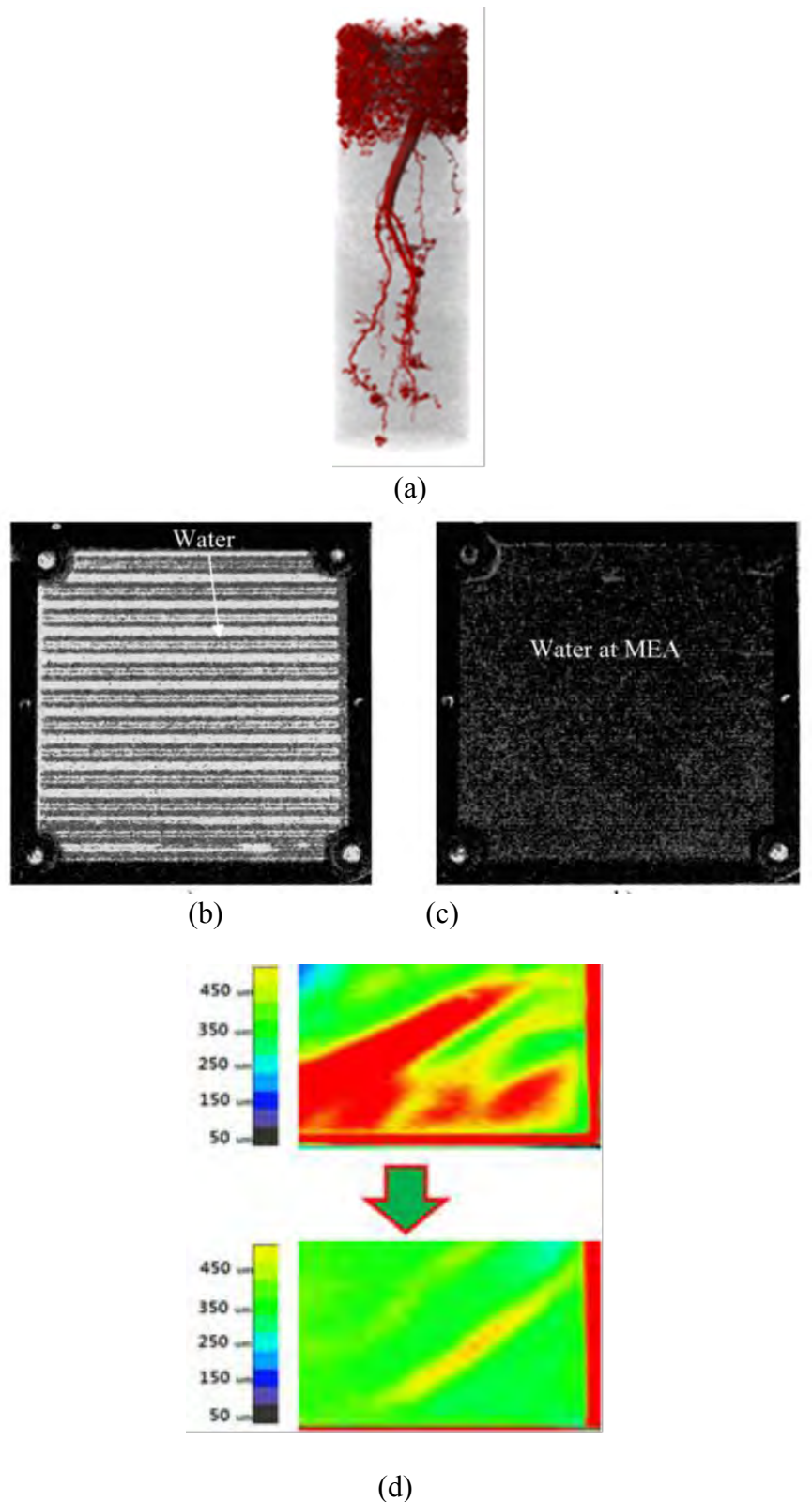


*FIG. 6. (a) Growing ginseng root embedded in soil was visualized with a resolution of 0.3 mm. Here we successfully visualized a whole ginseng root including 0.3 mm hairy ones in soil with tomography. (b-c) Neutron imaging on test results at the 3-parallel fuel cell serpentine flow field at 200 cc/min: b) Start and c) After 160 sec (d) Neutron imaging is powerful tool for the Li-ion battery research.*

As shown in Fig. 6a, a ginseng root is visualized as pseudo colouring image with resolution at 0.3 mm size. (4 year-old ginseng in the 5 cm diameter soil, thermal neutron flux

## 2.6. Efforts towards standardization of neutron imaging

$5 \times 10^7$ , L/D of 270, exposure time 10 sec per 1 projection, 200 projection, pseudo colouring image, VG studio). As shown in Fig.6a, the water removal characteristics at PEMFC were investigated under a different flow field design at same flow-rate (200 cc/min) by using the neutron imaging technique at the NRF, HANARO. The feasibility test was performed at first exposure room with a 4 sec exposure time. Fig. 6 b and c are test results of different flow field geometries. Fig. 6d is the imaging of Li-ion in association with the aging effect for wetting.

## 2.2. Collaborative efforts: round robin exercise using KAERI/ASTM/PSI sample

In a collaborative work the topic was focused on the initiation of the standardization of neutron tomography. This was carried out by performing the Round Robin exercise standard samples i.e., “(NTC) Contrast sample and (NTR) Resolution samples”. The samples and the protocol were produced by KAERI/PSI/Necsa and they were sent to several member countries to be measured and compared.

The contrast sample (KAERI) is a cylinder with a diameter of 30 mm made of aluminum with six holes with diameter 6 mm drilled in the axial direction. In each of these holes rods of polyethylene, nickel, iron, copper, lead, and aluminum are fitted. A photograph of the sample is shown in Fig. 7a. The measurement was carried out using the reactor power of 30 MW with the calculated L/D ratio of 270. Neutron flux at the sample position is  $10^7 \text{ n}\cdot\text{cm}^{-2}\cdot\text{s}^{-1}$  and it gives exposure time of 30 sec/image. Lens of 135 mm / F=2.0 was used for the CCD ( $1340 \times 1300$ , pixel size: 20  $\mu\text{m}$ , FOV= 11.8 cm  $\times$  6.5 cm) camera. During the measurement, the sample was placed at 87 mm away from the scintillator screen and it was rotated  $180^\circ$  and the image projection 600 was taken every  $0.3^\circ$  rotation with scintillator 50  $\mu\text{m}$ .

Figure 7 presents the relative attenuation coefficients from a thermal neutron tomogram of the NTC standard sample (KAERI) obtained through a scanning protocol with 600 projections in  $0.3^\circ$ . Fig. 7b is its reconstruction sliced contrast image of ①PE, ②Ni ③Pb, ④Fe, and ⑤Cu. Fig. 7c is the histogram of relative attenuation coefficients from a thermal neutron tomogram of the NTC standard sample(KAERI) with peaks from left to right: background noise and ③Pb, ⑤Cu, ④Fe, ②Ni and, ①PE. Figure 8 presents the resolution of wire diameter of 0.4 mm and slab thickness of 0.5 mm from the thermal neutron tomogram of the NTR standard sample (KAERI) obtained through a scanning protocol with 600 projections in  $180^\circ$  (Camera: Andor ( $2048 \times 2048$ ) Lens: 200 mm FOD: 5 cm  $\times$  5 cm, Exposure time: 120 sec / 1 image). Figure 9 presents the resolution 25  $\mu\text{m}$  of neutron tomogram image of the ASTM SI (sensitivity indicator) standard. The gap of 250  $\mu\text{m}$  can be oversized 370  $\mu\text{m}$  by scattering effect as shown in Fig. 9 c. Fig.10 presents the resolution 200  $\mu\text{m}$  of neutron tomogram image of Fe ball of the NTR standard sample (KAERI).

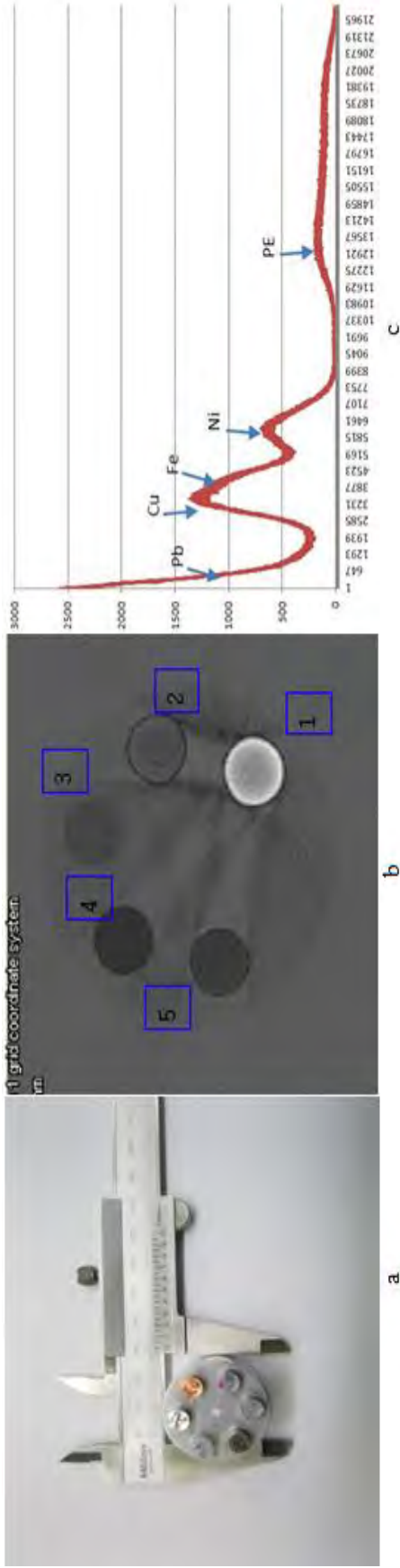


FIG. 7. a. Contrast sample(KAERI) b. its reconstruction sliced image (DPE), c. Histogram of relative attenuation coefficients from a thermal neutron tomogram of the NTC standard with Fourier filtering and 600 projections in 180°. Peaks from left to right: background noise and ③Pb, ④Cu, ④Fe, ②Ni and ①DPE.

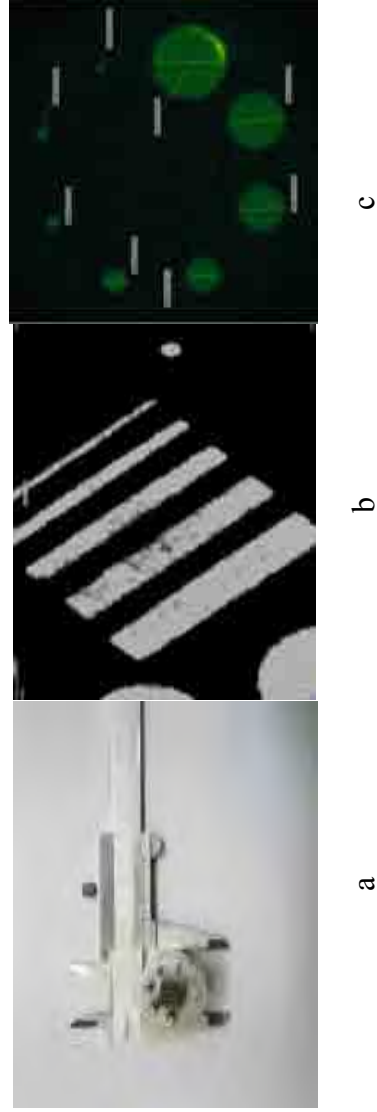


FIG. 8. a. Resolution sample(KAERI), b. Its reconstruction sliced image, slab thickness: 0.5 mm, 0.8 mm, 1.0 mm, 1.5 mm, and 2.0 mm. c. Its reconstruction sliced image wire diameter: 0.4 mm, 0.7 mm, 0.9 mm, 2 mm, 3 mm, 4 mm, 5 mm, and 6 mm.

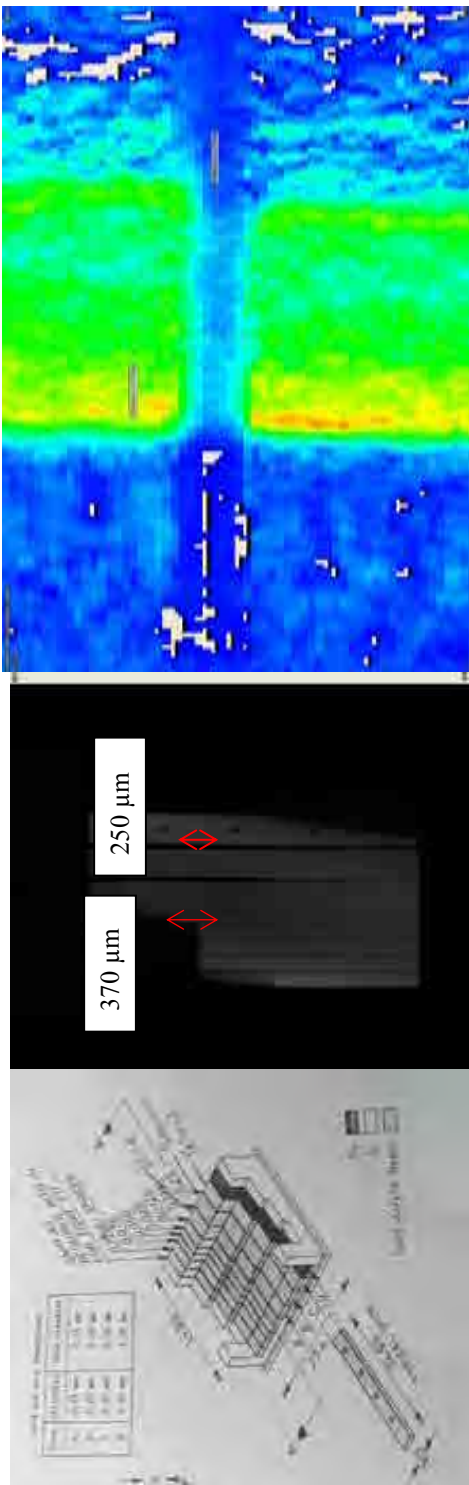


FIG. 9. a. SI sample (ASTM), its reconstruction sliced image. b. Its reconstruction sliced image 250  $\mu\text{m}$ , 100  $\mu\text{m}$ , 75  $\mu\text{m}$ , 50  $\mu\text{m}$ , and 25  $\mu\text{m}$ . c. Its reconstruction sliced image 250  $\mu\text{m}$  and overestimated size 370  $\mu\text{m}$ .



FIG. 10. a-b. Resolution sample of Fe ball (KAERI): 3 mm, 2 mm, 1 mm, 0.2 mm (KAERI), c. its tomo image.

## 2.6. Efforts towards standardization of neutron imaging

The resolution sample (PSI) is composed of two rectangular blocks that can be attached to each other by two screws. One or more thin metal films can be placed between the two screw holes and thus create a small gap between the two blocks. The test set contains two material combinations: one sample (type A) is made of Al blocks with Cu films to produce a positive contrast gap and the other sample (type B) is made of Fe blocks with Al films to produce a negative contrast gap [6]. The film thickness is 20  $\mu\text{m}$  and it was put initially 1 foil and placed within the two blocks and its tomographic image was taken. The number of foils was added until the gap is visible in the digital image with a rocking scan. A photograph of the sample is shown in Fig. 11. The measurement was carried out using the reactor power of 30 MW with the calculated L/D ratio of 270. Neutron flux at the sample position is  $10^7 \text{ n}\cdot\text{cm}^{-2}\cdot\text{s}^{-1}$  and it gives exposure time of 180 s/image. Lens of 200 mm /  $F = 4.0 \text{ mm}$  was used for the CCD ( $1340 \times 1300$ , pixel size: 20  $\mu\text{m}$ , FOV= 5.0 cm, SD = 87 mm) camera. During the measurement the sample was placed at 87 mm away from the detector.



FIG. 11. Resolution sample (PSI): Type A(Al+ Cu), Type B(Fe+ Al).

Figure 12 reveals that the positive contrast gap resulted from a foil Cu 20  $\mu\text{m}$  within the Al block is clearly visible from the tomographic image. The thickness of 40 mm is the minimum gap that can be resolved in the tomographic image for this kind of sample.

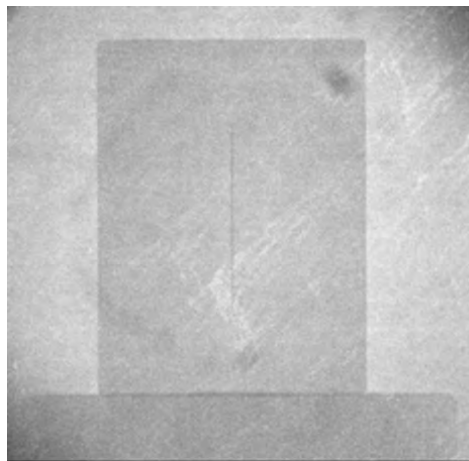


FIG. 12. The neutron radiography image of the resolution sample Al-Cu (foil) 20  $\mu\text{m}$  (type B).

Figure 13 show the similar result for the resolution sample (type B). The minimum gap which is visible in the tomographic image of this sample is 60  $\mu\text{m}$ .

## 2.6. Efforts towards standardization of neutron imaging

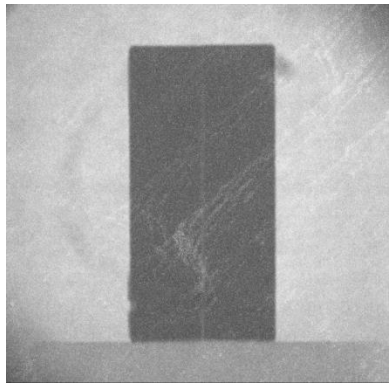


FIG. 13. The neutron radiography image of the resolution sample Fe-Al(Foil) 60  $\mu\text{m}$  (type A.).

## 3. CONCLUSIONS

The CRP project of neutron tomography standardization using NTR(neutron tomography resolution) and NTC(neutron tomography contrast) Phantom has been successfully carried out. The neutron tomography system has been optimized and the collaborative works with other member of CRP has been implemented i.e. Round Robin exercises using NTC and NTR samples for tomography are beneficial for neutron tomography standardization. The standardization of neutron tomography/digital neutron radiography would be helpful for industry application expansion such as turbine blade, irradiated fuel, fossil, plant in soil, hydrogen fuel cell, and Li-ion Battery. Reflected on film method standardization established at 1970, it would take a certain time beyond CRP-period. It is recommended that IAEA support be continued until connecting to standardization organization such as ASTM, EN, ISO. The initiation of the standardization of neutron tomography/neutron digital radiography has been successfully ignited since the CRP-1575.

## REFERENCES

- [1] SIM, C.M., et.al. Requirements of neutron tomography standardization for industrial application. *Key Engineering Materials* **6**, (2004) 270-273.
- [2] SIM, C.M., et.al. Detection of Hidden Shot Balls in a Gas Cooled Turbine Blade with an NRT Gadolinium Tagging Method, *Nuclear Instruments and methods in Physics Research A*, **605**, (2009) p. 175-178,(IP:1.1).
- [3] SIM, C.M., et.al. Measurement of Ballooning Gap Size of Irradiated Fuels Using Neutron Radiography Transfer Method and HV Image Filter. *Journal of the Korean Society for Nondestructive Testing*, **33**, 2, (2013) p. 198-204.
- [4] GRELLET-TINNER, SIM, C.M., KIM, D.H, OH, H.S., KARDJILOV, N. Description of the first lithostrotian titanosaur embryo *in ovo* with neutron characterization and implications for lithostrotian aptian migration and dispersion. *Gondwana Research* **20**, (2011), p. 621-629.
- [5] KIM, T.J., SIM, C.M., et. al., Experimental approaches for distribution and behaviour of water in PEMFC under flow direction and differential pressure using neutron imaging technique, *Nuclear instruments & methods in physics research section A* **600** (2008) p.325-327.(IP:1.1).
- [6] KAESTNER, A., LEHMANN, E., *Quality Assessment for Neutron CT*, Paul Scherrer Institut, Switzerland, 2012.